

**FABRICATION OF NANO JOSEPHSON JUNCTIONS USING THE  
FEMTOSECOND LASER TECHNIQUE ON HIGH -  $T_c$  SUPERCONDUCTING  
 $YBa_2Cu_3O_7$  THIN FILMS.**

by

**PATRICE OBINNA UMENNE**

**49920588**

submitted in accordance with the requirements for the degree of

**DOCTOR OF PHILOSOPHY: PHYSICS**

**FIELD OF SPECIALIZATION: MICRO-ELECTRONICS, SUPERCONDUCTING  
DEVICES, JOSEPHSON JUNCTIONS AND NANOTECHNOLOGY (98981)**

in the

Department of Physics

COLLEGE OF SCIENCE ENGINEERING AND TECHNOLOGY

**UNIVERSITY OF SOUTH AFRICA (UNISA)**

SUPERVISOR: PROF. VIJAYA SRINIVASU VALLABHAPURAPU

OCTOBER 2017

# DECLARATION AND COPYRIGHT

“I hereby declare that the:

**FABRICATION OF NANO JOSEPHSON JUNCTIONS USING THE FEMTOSECOND LASER TECHNIQUE ON HIGH -  $T_c$  SUPERCONDUCTING  $YBa_2Cu_3O_7$  THIN FILMS.**

“is my own original work submitted for the degree of Doctor of Philosophy: Physics, at the University of South Africa. All sources of materials that have been consulted or quoted are indicated and acknowledged by means of a comprehensive list of references.”

I further declare that I have not previously submitted this work, or part of it, for examination at Unisa for another qualification or at any other higher education institution.



-----  
Patrice Umenne

16<sup>TH</sup> October 2017

Date

# **CLASSIFICATION**

The content of this dissertation has been declared by UNISA as classified and confidential. All readers should hence ensure that they do not distribute information to third parties without the consent of the author and UNISA, because of the high potential intellectual value associated with the work.

# DEDICATION

This study is dedicated to the: Almighty God without whom I would not have been able to complete this work; my mother Mrs. Nadiejda Nikolaevna Umenne, my father Prof. Sampson Ikechukwu Umenne and my sister Irina Uzoma Umenne.

# ACKNOWLEDGEMENT

Firstly, I would like to thank all the academics, researchers and authors of all the published works that I referenced throughout the duration of this PhD work, without whom I would not have been able to get the necessary ideas and relevant points to be able to complete this PhD work.

Specifically I would like to acknowledge the following people:

1. Prof. Vijaya Vallabhapurapu Srinivasu my supervisor from the department of Physics (UNISA) for his original idea encapsulating this PhD work, critical guidance, continuous academic support, financial support for workshops, attendance of conferences, publications, equipment procurement and general academic grooming and development of myself as a researcher.
2. Dr. Herman Uys, from the national laser centre (CSIR) Pretoria, for all the time and effort he put in to teaching me and giving me the extensive training necessary to operate the femtosecond laser and the optical equipment that go hand in hand with the laser. Without this training, it would have been impossible for me to optimize the laser beam and fabricate the necessary constrictions.
3. Simon Lam and Jia Du, researchers from the Superconductivity research centre (CSIRO), Lindfield Australia, who facilitated my training in terms of the analysis of Josephson Junctions and the Josephson Effect. Without their research input and knowledge in the field of superconductivity and giving me the opportunity to make use of all the necessary equipment at the CSIRO, I would not have been able to complete this PhD work.
4. I would also like to acknowledge the contribution to this work of Ms Jeina Lazars from CSIRO, Australia for her assistance in placing Gold (Au) contacts during the photolithography process on the YBCO constrictions to facilitate I-V characterization and other tests for the Josephson Effect such as Shapiro on the samples.

5. I wish to express my gratitude to the University of South Africa (UNISA) for enabling me to complete my studies through them, make use of their facilities and also for all the financial support they have awarded me throughout the duration of this study.

# ABSTRACT

This PhD work involves the utilization of the femtosecond laser technique to fabricate the novel S-shaped Josephson Junctions on the high -  $T_C$  superconducting  $YBa_2Cu_3O_7$  thin films.

Initially, it was envisaged as the title states to fabricate nano sized Josephson Junctions using this femtosecond laser technique. However in this PhD work, micron sized (1 – 2  $\mu\text{m}$ ) and near nano sized (500 – 800 nm) Josephson Junctions where achieved.

The femtosecond laser technique involved optimizing the laser ablation spot size to the minimum size in order to facilitate the fabrication of small constrictions that form the Josephson Junction. The optimization of the laser ablation spot involved beam collimation and beam focusing processes using optical equipment.

In this PhD work, we designed a novel S-shaped Josephson Junction, which as the name implies is shaped like the letter “S”. The novel S-shaped Junctions where designed with the help of the G-code control systems programming language used to move the translation stage. The novelty stems from the fact that it is possible to regulate both the width and length of the constriction in the junction at the same time whereas in the standard shaped constrictions only the width of the junction can be regulated, the length is restricted to the laser ablation diameter.

At the beginning of the PhD work it was believed that due to the low pulse duration of the femtosecond laser which is specifically 130 femtoseconds, the constriction fabricated would not be exposed to localized heat from the laser and hence form an S-s'-S type Josephson Junction. However, after the completion of the research it was discovered that the length of time, the junction is exposed to heat from the laser depends not only on the pulse duration of the laser but also the feed rate of the translation stage, and the pulse repetition rate or the frequency of the laser. These other factors such as the laser feed rate which in this case is 333  $\mu\text{ms}^{-1}$  and the pulse repetition rate which is 1 kHz (1000  $\mu\text{s}$ ) in combination with the pulse duration of the laser in femtoseconds combine to expose the junction to the laser for a longer period than femtoseconds. As a result, the junction experiences thermal

degradation from the femtosecond laser. In the case of the near nano 816 nm wide Josephson Junction fabricated, the central part of the constriction was heated and normalized to form an S-N-S type Josephson Junction. While in the case of the micron sized 2.1  $\mu\text{m}$  wide Josephson Junction fabricated, the central part of the constriction was heated only slightly and an S-s'-S type Josephson Junction was formed.

The I-V characteristics, shapiro steps, critical current temperature dependence, critical current RF power dependence, normal resistance temperature dependence and  $I_C R_N$  temperature dependence curves are all shown and analyzed for the Josephson Junctions fabricated.

Finally, suggestions are given on how to fabricate Josephson Junctions using the femtosecond laser technique with minimal heating from the laser and on the technique that can be used to minimize the laser ablation spot size.

# PUBLICATIONS AND RESEARCH OUTPUTS RELATED TO THE PHD WORK.

1. Patrice Umenne, V.V Srinivasu, "Femtosecond-laser fabrication of micron and sub-micron sized S-shaped constrictions on high  $T_C$  superconducting  $YBa_2Cu_3O_{7-x}$  thin films : ablation and lithography issues", Journal of Materials Science: Materials in Electronics, April 2017, Volume 28, Issue 8, pp 5817-5826, <https://link.springer.com/article/10.1007/s10854-016-6253-z>. – **JOURNAL ARTICLE RELATED TO CHAPTER 3 IN PhD THESIS.**
2. Patrice Umenne, V.V srinivasu, "Constrictions fabricated on YBCO thin films using the femtosecond laser: Limiting factors", paper submitted to the conference of International Advances in Applied Physics and Materials Science, Turkey, 2017, to be published as a special issue in Acta Physica Polonica A. – **JOURNAL ARTICLE RELATED TO CHAPTER 4 IN PhD THESIS.**
3. Patrice Umenne, S. Lam, J. Du, and V. V Srinivasu, "Josephson Effect in the Micron and Submicron YBCO Constrictions Fabricated Using the Femtosecond Laser Technique," *J. Supercond. Nov. Magn.*, Oct. 2017. <http://link.springer.com/article/10.1007/s10948-017-4371-3> – **JOURNAL ARTICLE RELATED TO CHAPTER 5 IN PhD THESIS.**
4. Patrice Umenne, V.V Srinivasu, "Microwave power dependence of the I-V characteristics of submicron and micron YBCO constrictions", paper accepted at the 2<sup>nd</sup> International Conference on Condensed Matter and Applied Physics, ICC2017 Nov 24-25, 2017, Bikaner, India, to be published in the AIP (American institute of Physics) proceedings. – **PAPER RELATED TO CHAPTER 6 IN PhD THESIS.**
5. Patrice Umenne, V.V Srinivasu, "Micron sized constrictions fabricated using the femtosecond laser technique on  $YBa_2Cu_3O_{7-x}$  Thin films", accepted with minor revisions at Physica C, 9<sup>th</sup> January 2018. – **JOURNAL ARTICLE RELATED TO CHAPTER 7 IN PhD THESIS.**
6. **Patent filed:** International patent filed PTC Patent Application No. PCT/IB2017/051676 in the name of UNISA, Femtosecond laser based method for fabrication of micron- and nano constriction type structures on a  $YBa_2Cu_3O_{7-x}$  superconducting thin film. Official South African provisional patent number; 2016/01975.

# TABLE OF CONTENTS

DECLARATION AND COPYRIGHT .....	2
CLASSIFICATION.....	3
DEDICATION .....	4
ACKNOWLEDGEMENT .....	5
ABSTRACT .....	7
PUBLICATIONS AND RESEARCH OUTPUTS RELATED TO THE PHD WORK. ....	9
LIST OF FIGURES .....	18
LIST OF TABLES .....	27
KEYWORDS .....	28
LIST OF ABBREVIATIONS AND ACRONYMS.....	29
CHAPTER 1 .....	30
THE JOSEPHSON JUNCTION, THE JOSEPHSON EFFECT AND METHODS OF FABRICATION.....	30
1.1    INTRODUCTION TO SUPERCONDUCTIVITY.....	30
1.1.1    JOSEPHSON EFFECT .....	31
1.1.2    DC AND AC JOSEPHSON EFFECTS .....	32
1.2    VARIETIES OF JOSEPHSON JUNCTIONS .....	33
1.3    USES OF JOSEPHSON JUNCTIONS.....	34
1.4    WHY NANO JOSEPHSON JUNCTIONS? .....	35
1.5    PROBLEM STATEMENTS AND OBJECTIVES OF PHD WORK .....	35
1.5.1    PROBLEM STATEMENT 1 .....	35
1.5.2    PROBLEM STATEMENT 2 .....	35
1.5.3    PROBLEM STATEMENT 3 .....	36
1.5.4    PROBLEM STATEMENT 4 .....	36
1.5.5    PROBLEM STATEMENT 5 .....	36
1.5.6    OBJECTIVES OF PHD WORK .....	37
1.6    PROVING THE JOSEPHSON EFFECT.....	37
1.6.1    I-V CHARACTERISTICS .....	37
1.6.2    SHAPIRO STEPS.....	38
1.6.3    FRAUNHOFER DIFFRACTION PATTERN (DEPENDENCE OF $I_c$ ON THE MAGNETIC FIELD).....	39
1.6.4 $I_C$ VS TEMPERATURE DATA.....	40
1.7    METHODS OF FABRICATING JOSEPHSON JUNCTIONS .....	41
1.7.1    AFM – ATOMIC FORCE MICROSCOPY.....	41

1.7.2	SAMPLE MOSAIC NAVIGATION ASSISTED LASER ETCHING METHOD. ....	43
1.7.3	FOCUSED ION BEAM (FIB) METHOD.....	44
1.7.4	PHASE SEPARATION METHOD.....	45
1.7.5	FEMTOSECOND LASER.....	47
1.7.5.1	DETAILS OF FEMTOSECOND LASER .....	47
1.8	SCHEDULED ACTIVITY/PLAN FOLLOWED.....	47
1.9	REFERENCES.....	49
<b>CHAPTER 2</b>	<b>.....</b>	<b>52</b>
<b>MATERIALS AND METHODOLOGY</b>	<b>.....</b>	<b>52</b>
2.1	INTRODUCTION .....	52
2.2	YBCO THIN FILMS .....	52
2.2.1	METHOD USED TO FABRICATE THE YBCO THIN FILMS.....	53
2.2.1.1	THERMAL REACTIVE CO-EVAPORATION.....	53
2.2.2	TEMPERATURE DEPENDENCE OF THE SURFACE ( $R_s(T)$ ) RESISTANCE OF THE YBCO THIN FILMS. ....	54
2.3	THE FEMTOSECOND LASER .....	54
2.4	MAIN COMPONENTS OF THE FEMTOSECOND LASER .....	55
2.4.1	SERF™ FIBER LASER OPERARTION.....	55
2.4.2	ND : YAG PUMP LASER DIODE .....	56
2.4.3	TI : SAPPHIRE AMPLIFIER.....	57
2.5	THE OPERATION OF THE MAIN COMPONENTS OF THE FEMTOSECOND LASER.....	58
2.5.1	LASER LAMP (PUMP DIODE LASER AND THE ERBIUM DOPED FIBER) .....	58
2.5.2	SWITCHING THE LASER ON AND OFF .....	60
2.5.3	TIMING CONSOLE .....	61
2.5.4	THE PHYSICAL SHUTTER.....	63
2.5.5	THE OVERALL LASER PATH (REFLECTIVE MIRRORS AND IRIS APERTURES) .....	65
2.5.6	THE TRANSLATION STAGE .....	66
2.5.7	FOCUSING OPTICS (CONVEX LENS).....	67
2.6	SOFT MASK OF THE INITIAL CONSTRICTIONS MACHINED USING THE FEMTOSECOND LASER. ....	68
2.7	FACTORS THAT DETERMINE THE PARTIAL OR COMPLETE REMOVAL OF THE YBCO THIN FILM USING THE FEMTOSECOND LASER.....	69
2.8	INITIAL TEST CONSTRICTIONS MACHINED ON STEEL USING THE FEMTOSECOND LASER AND THE G-CODE PROGRAM USED FOR THE DESIGN.....	69
2.9	FINDING THE FOCUS POINT OF A LASER BEAM .....	71

2.10	FABRICATION OF THE MICROSTRIP LINES AND CONSTRICTIONS ON TEST METAL.....	72
2.11	MICRON, SUBMICRON AND NANO STRUCTURING YBCO THIN FILMS BY CHANGING THE LASER PULSE ENERGY .....	74
2.12	LASER ABLATION WIDTHS PRODUCED WITH VARYING LASER POWER ON A TEST STEEL SURFACE. ....	76
2.13	FACILITATING THE SUB-MICRON STRUCTURING OF MATERIALS BY USING THE LASER ABLATION THRESHOLD OF THE MATERIAL.....	78
2.14	FACTORS THAT DETERMINE THE NANOSTRUCTURING OF METALS .....	80
2.15	THE NOVEL S-SHAPED CONSTRICTION DESIGN THAT COULD BE USED AS A JOSEPHSON JUNCTION .....	81
2.16	PULSE ENERGY OF THE LASER .....	84
2.17	LASER BEAM SHAPING AND COLLIMATION PROCESS TO REDUCE LASER ABLATION SPOT SIZE.....	85
2.17.1	INTRODUCTION TO THE LASER BEAM COLLIMATION PROCESS.....	85
2.17.2	ACTUAL PROCESS OF COLLIMATING THE LASER BEAM AND THEN RE-FOCUSING TO A SMALLER SPOT SIZE.....	87
2.17.3	FOCUSING THE X-Y (AXIS) OF THE LASER SPOT ALONG THE Z-DIRECTION WITH THE SPHERICAL CONVEX LENS.....	90
2.17.3.1	ACTUAL PROCESS OF FOCUSING THE X-Y AXIS OF THE LASER SPOT.....	91
2.17.4	CONSTRICTIONS CUT ON TEST STEEL SAMPLES AFTER THE BEAM COLLIMATION PROCESS. ....	93
2.17.4.1	LASER POWER SET AT 483 mW .....	93
2.17.4.2	LASER POWER SET AT 223 mW .....	94
2.17.4.3	LASER POWER SET AT 37 mW .....	95
2.17.5	AFM IMAGES OF CONSTRICTIONS CUT ON STEEL AFTER THE BEAM COLLIMATION PROCESS. ....	95
2.17.5.1	LASER POWER SET AT 220 mW .....	95
2.17.5.2	LASER POWER SET AT 104 mW .....	97
2.17.6	AFM IMAGES OF CONSTRICTIONS CUT ON STEEL WITH THE LASER CONTROL TIMING SETTINGS CHANGED.....	98
2.17.7	FUTURE WORK.....	101
2.17.7.1	..... NEW CYLINDRICAL LENSES WITH LARGER APERTURES TO BE USED FOR THE BEAM COLLIMATION PROCESS.....	101
2.18	INITIAL CONSTRICTIONS FABRICATED ON THE YBCO THIN FILM.....	102
2.18.1	METHODS USED TO IMPROVE THE LASER ABLATION SPOT SHAPE. ....	104
2.18.2	AFM (ATOMIC FORCE MICROSCOPE) SCANNING OF THE CONSTRICTIONS.....	104

2.18.3	AFM IMAGES OF THE INITIAL CONSTRICTIONS FABRICATED ON THE YBCO THIN FILMS WITH A POORLY SHAPED LASER ABLATION SPOT. ....	107
2.18.3.1	CONSTRICTION FABRICATED WITH A LASER POWER SETTING OF 5 mW AND A SEPARATION DISTANCE BETWEEN THE LASER ABLATION SPOTS OF 90 $\mu\text{m}$ .....	108
2.18.3.2	CONSTRICTION FABRICATED WITH A LASER POWER SETTING OF 5 mW AND A SEPARATION DISTANCE BETWEEN THE LASER ABLATION SPOTS OF 60 $\mu\text{m}$ .....	109
2.18.3.3	CONSTRICTION FABRICATED WITH A LASER POWER SETTING OF 22.7 mW AND A SEPARATION DISTANCE BETWEEN THE LASER ABLATION SPOTS OF 60 $\mu\text{m}$ .....	111
2.18.3.4	CONSTRICTION FABRICATED WITH A LASER POWER SETTING OF 11.65 mW AND A SEPARATION DISTANCE BETWEEN LASER ABLATION SPOTS OF 25 $\mu\text{m}$ .....	112
2.18.4	ANALYSIS OF THE RESULTS .....	113
2.19	REFERENCES .....	115
<b>CHAPTER 3</b>	<b>.....</b>	<b>116</b>
<b>LITHOGRAPHY PROCESS DEVELOPED FOR THE FABRICATION OF THE NOVEL S-SHAPED CONSTRICTIONS ON <math>YBa_2Cu_3O_7 - x</math> THIN FILMS.</b>	<b>.....</b>	<b>116</b>
3.1	INTRODUCTION .....	116
3.2	LASER OPTICAL EXPERIMENTAL SETUP USED TO IMPROVE THE LASER ABLATION SPOT SHAPE.....	116
3.2.1	IRIS DIAPHRAGM (MANUALLY ADJUSTABLE APERTURE) .....	118
3.3	CONSTRICTION FABRICATED ON YBCO THIN FILM WITH THE IRIS APERTURE SET AT A DIAMETER OF 5 mm. ....	119
3.3.1	REASON FOR THE LASER SPOT HAVING AN UNWANTED EXTENSION.....	121
3.4	FUTURE WORK TO IMPROVE CONSTRICTION SHAPE.....	123
3.5	CONSTRICTION FABRICATED ON YBCO THIN FILM WITH THE IRIS APERTURE REDUCED TO A DIAMETER OF 2.55 mm.....	124
3.6	LITHOGRAPHY PROCESS AND G-CODE PROGRAM USED TO CONTROL THE MOVEMENT OF THE TRANSLATION STAGE IN THE DESIGN OF THE NOVEL S-SHAPED CONSTRICTIONS.....	126
3.6.1	LITHOGRAPHY DESIGN OF THE S-SHAPED CONSTRICTION. ....	127
3.7	MOVEMENT OF THE TRANSLATION STAGE IN THE X,Y,Z CO- ORDINATES.....	130
3.8	G-CODE PROGRAMMING LANGUAGE USED TO MOVE THE TRANSLATION STAGE WHILST CUTTING THE CONSTRICTIONS .....	131
3.8.1	ACTUAL G-CODE PROGRAM FOR CUTTING THE S-SHAPED CONSTRICTIONS. ....	131
3.9	EXPLAINING THE G-CODE PROGRAM USED AND THE ALGORITHM FOR THE DESIGN OF THE NOVEL S-SHAPED CONSTRICTIONS. ....	132
3.10	ENERGY DENSITY OF THE LASER AND DETERMINING THE PEAK LASER FLUENCE ABLATION THRESHOLD FOR YBCO THIN FILM. ....	134

3.10.1	FINDING THE PEAK LASER FLUENCE ABLATION THRESHOLD OF THE YBCO THIN FILM. ....	136
3.10.1.1	USING THE DIAMETER OF THE LASER ABLATION SPOT METHOD. ....	136
3.10.1.2	CRATER TOPOGRAPHY METHOD TO FIND THE PEAK LASER FLUENCE ABLATION THRESHOLD FOR VERIFICATION OF THE THRESHOLD VALUE. ....	138
3.11	IMPROVEMENTS IN THE OPTICAL EXPERIMENTAL SET UP AND CONSTRICTIONS MADE WITH NEW SET UP. ....	142
3.11.1	THE NEW OPTICAL EXPERIMENTAL SET UP. ....	142
3.11.2	KEYNOTE AREA: ....	144
3.11.3	AFM IMAGES OF THE CONSTRICTIONS FABRICATED WITH THE NEW AND IMPROVED OPTICAL SETUP. ....	145
3.11.3.1	PROBLEM ENCOUNTERED ....	146
3.11.3.2	CYLINDRICAL BEAM COLLIMATION LENSES CHANGED TO APERTURE DIAMETER 25 mm X 25 mm. ....	147
3.11.4	RESULTS OF USING THE COMBINATION OF THE LARGER APERTURE DIAMETER CYLINDRICAL LENSES AND THE OBJECTIVE LENS. ....	148
3.11.4.1	AFM IMAGES OF THE CONSTRICTIONS MADE WITH THE LARGER APERTURE CYLINDRICAL LENSES. ....	148
3.12	REFERENCES ....	151
<b>CHAPTER 4</b>	<b>.....</b>	<b>152</b>
<b>MICRON, SUB-MICRON AND NANO SIZED CONSTRICTIONS</b>	<b>.....</b>	<b>152</b>
4.1	INTRODUCTION ....	152
4.2	REPLACING THE OBJECTIVE PLANO CONVEX LENS (NA 0.25) WITH A SPHERICAL CONVEX LENS OF FOCAL LENGTH (30 mm).....	152
4.3	MICRON-SIZED CONSTRICTION ACHIEVED ON YBCO THIN FILM ....	153
4.3.1	SEPARATION DISTANCE BETWEEN LASER ABLATION SPOTS ( $SW$ ) OF 18 $\mu\text{m}$ IN G-CODE.....	153
4.4	MICRON-SIZED CONSTRICTION ACHIEVED ON THE YBCO THIN FILM.....	156
4.4.1	SEPARATION DISTANCE BETWEEN THE LASER ABLATION SPOTS ( $SW$ ) OF 17.5 $\mu\text{m}$ IN G-CODE.....	156
4.5	MICRON-SIZED CONSTRICTION ACHIEVED ON YBCO THIN FILM ....	160
4.5.1	SEPARATION DISTANCE BETWEEN THE LASER ABLATION SPOTS ( $SW$ ) OF 17 $\mu\text{m}$ IN G-CODE. ....	160
4.6	SUB-MICRON - SIZED CONSTRICTION ACHIEVED ON YBCO THIN FILM. ....	161
4.6.1	SEPARATION DISTANCE BETWEEN THE LASER ABLATION SPOTS ( $SW$ ) OF 16.5 $\mu\text{m}$ . ..	161
4.7	MICRON-SIZED CONSTRICTION FABRICATED ON YBCO THIN FILM. ....	164

4.7.1	SEPARATION DISTANCE BETWEEN THE LASER ABLATION SPOTS ( <i>SW</i> ) OF 16.5 $\mu\text{m}$ . ..	164
4.8	SUB-MICRON - SIZED CONSTRICTION FABRICATED ON YBCO THIN FILM.....	166
4.8.1	SEPARATION DISTANCE BETWEEN THE LASER ABLATION SPOTS ( <i>SW</i> ) OF 16 $\mu\text{m}$ .	166
4.9	SUMMARY OF CONSTRICTIONS FABRICATED, SCANNED USING AFM AND LABELLED ON THE YBCO THIN FILM. ....	168
4.10	METHOD USED FOR CLEANING THE THIN FILM SAMPLES AFTER LASER FABRICATION.	168
4.11	AFM IMAGES OF OTHER USEFUL CONSTRICTIONS FABRICATED. ....	170
4.12	SUMMARY OF THE ABOVE CONSTRICTIONS SCANNED IN AFM AND LABELLED ON THE THIN FILM .....	174
4.13	GEOMETRIC ANALYSIS OF CONSTRICTIONS FABRICATION. ....	174
4.13.1	SPECIFICATIONS OF CONSTRICTIONS FABRICATED .....	174
4.13.2	EXPERIMENTAL DETAILS.....	175
4.13.3	FACTORS THAT LIMIT THE FABRICATION OF NANO CONSTRICTIONS.....	175
4.13.4	CONSTRICTIONS FABRICATED.....	177
4.13.4.1	SUB-MICRON SIZED CONSTRICTION (500 – 1000 nm) .....	177
4.13.4.2	NANO CONSTRICTION (0 – 500 nm).....	179
4.13.4.3	SUB-MICRON SIZED CONSTRICTION (500 – 1000 nm) .....	180
4.13.4.4	MICRON-SIZED CONSTRICTION (ABOVE 1000 nm) .....	182
4.13.5	SUMMARY OF THE CONSTRICTIONS FABRICATED. ....	184
4.14	REFERENCES .....	184
<b>CHAPTER 5</b>	<b>.....</b>	<b>185</b>
<b>OBSERVATION OF THE JOSEPHSON-LIKE EFFECT IN THE VERY LONG SUPERCONDUCTING CONSTRICTIONS ON YBCO THIN FILMS.....</b>	<b>.....</b>	<b>185</b>
5.1	JOSEPHSON JUNCTION APPLICATIONS AND USING THE FEMTOSECOND LASER TO FABRICATE THE JOSEPHSON JUNCTIONS.....	186
5.2	EXPERIMENTAL DETAILS.....	187
5.2.1	PHOTOLITHOGRAPHY PROCESS AND PLACING GOLD (AU) CONTACT PADS ON THE YBCO TRACKS TO FACILITATE I-V MEASUREMENTS. ....	187
5.2.1.1	CLEANING THE SAMPLES.....	189
5.2.1.2	APPLYING PHOTORESISTOR.....	189
5.2.1.3	MASK ALIGNMENT .....	190
5.2.1.4	OXYGEN PLASMA.....	193
5.2.1.5	GOLD DEPOSITION.....	194
5.2.1.6	WIRE BONDING TO THE PCB HOLDER .....	197

5.2.1.7	SOLDERING THE PCB WITH THE SAMPLE TO THE NITROGEN IMMERSION PROBE AND I-V CHARACTERIZATION .....	199
5.2.2	LASER CUTTING SETTINGS AND SPECIFICATIONS OF THE JUNCTIONS THAT SHOWED THE JOSEPHSON EFFECT.....	203
5.2.3	RF CONNECTIONS FOR MEASUREMENT OF SHAPIRO STEPS .....	204
5.3	DISCUSSION.....	205
5.3.1	DIMENSIONS OF THE FABRICATED JUNCTIONS THAT SHOWED THE JOSEPHSON-LIKE EFFECT.....	205
5.3.2	CURRENT – VOLTAGE CHARACTERISTICS (IVC’S) OF THE CONSTRICTIONS.....	208
5.3.3	SHAPIRO STEPS.....	210
5.3.4	THE DEPENDENCE OF $IC$ ON RF POWER .....	213
5.3.5	CURRENT – VOLTAGE CHARACTERISTICS (IVC’S) AT VARYING TEMPERATURES AND THE CRITICAL CURRENT - TEMPERATURE DEPENDENCE CURVES.....	215
5.3.6	NORMAL RESISTANCE $R_N$ VS TEMPERATURE FOR THE JOSEPHSON JUNCTIONS..	218
5.3.7	$ICR_N$ PRODUCT VS TEMPERATURE FOR THE JOSEPHSON JUNCTIONS. ....	219
5.4	CONCLUSION .....	221
5.5	REFERENCES .....	222
<b>CHAPTER 6</b>	<b>.....</b>	<b>225</b>
	<b>THE EFFECT OF RF RADIATION ON THE CRITICAL CURRENT OF CONSTRICTIONS FABRICATED USING THE FEMTOSECOND LASER TECHNIQUE.....</b>	<b>225</b>
6.1	EXPERIMENTAL.....	226
6.2	RESULTS.....	226
6.2.1	THE CRITICAL CURRENT VS RF POWER CURVE FOR THE MICRON SIZED JOSEPHSON JUNCTION. ....	226
6.2.2	THE CRITICAL CURRENT VS RF POWER CURVE FOR THE SUB-MICRON SIZED JOSEPHSON JUNCTION. ....	228
6.2.3	PROOF OF THE A.C JOSEPHSON EFFECT IN THESE SAMPLES USING THE RF RADIATION.....	229
6.3	CONCLUSION .....	231
6.4	REFERENCES .....	232
<b>CHAPTER 7</b>	<b>.....</b>	<b>233</b>
	<b>SUPERCONDUCTIVE BRIDGES THAT DID NOT SHOW THE JOSEPHSON EFFECT; LIMITATIONS. .</b>	<b>233</b>
7.1	CURRENT – VOLTAGE CHARACTERISTICS OF ELECTRONICALLY SUPERCONDUCTIVE, RESISTIVE AND OPEN CONSTRICTIONS.....	234
7.1.1	SUPERCONDUCTIVE CONSTRICTION .....	234
7.1.1.1	SUB-MICRON BRIDGE (659.5 nm) .....	234

7.1.2	RESISTIVE CONSTRICTION.....	236
7.1.2.1	MICRON CONSTRICTION (1.49 $\mu\text{m}$ ).....	236
7.1.3	ELECTRONICALLY OPEN CONSTRICTION .....	238
7.1.3.1	MICRON CONSTRICTION (1.36 $\mu\text{m}$ ).....	238
7.2	CLASSIFICATION OF THE SUPERCONDUCTIVE BRIDGES.....	239
7.3	I-V CHARACTERIZATION OF THE CONSTRICTIONS.....	242
7.4	RESULTS: BRIDGES THAT DO NOT SHOW THE A.C JOSEPHSON-LIKE EFFECT.....	243
7.4.1	MICRON (A) CONSTRICTION .....	243
7.4.2	MICRON (B) CONSTRICTION .....	246
7.4.3	MICRON (C) CONSTRICTION .....	247
7.5	LIMITATIONS OF THE FEMTOSECOND LASER METHOD AND POSSIBLE IMPROVEMENTS .....	249
7.6	CONCLUSION .....	250
7.7	REFERENCES .....	250
<b>CHAPTER 8</b>	.....	<b>252</b>
<b>CONCLUSION</b>	.....	<b>252</b>
8.1	FUTURE WORK AND RECOMMENDATION .....	254
8.2	REFERENCES .....	255
<b>APPENDIX</b>	.....	<b>256</b>
	G-CODE PROGRAM TO FABRICATE THE S-SHAPED CONSTRICTIONS.....	256

# LIST OF FIGURES

Figure 1: Idealised sketch of a Josephson junction .....	31
Figure 2: Varieties of Junctions .....	33
Figure 3: A comparative description of device performance and power dissipation characteristics of various types of materials (semiconductors and superconductors) .....	34
Figure 4: I-V curve of a Nanoconstriction .....	38
Figure 5: Schematic of the basic test set up for Shapiro steps .....	38
Figure 6: Shapiro steps of a nanoconstriction and VTB after exposure to 14.427 GHz and 15.383 GHz microwave signal respectively .....	39
Figure 7: The effect of magnetic field on the critical current of the nanobridge .....	40
Figure 8: Critical current Vs Temperature of Nanoconstriction and VTB Bridge with linear fit .....	40
Figure 9: 3D AFM image of a nano bridge .....	42
Figure 10: AFM top view of the nano bridge or nano constriction. The horizontal distance between the marks in the profile defines the width of the constriction as 492.19 nm .....	42
Figure 11: (a) AFM picture of a laser-etched constriction width 1.64 $\mu\text{m}$ (b) submicron constriction width is 703 nm .....	44
Figure 12: FIB method side view of junction .....	45
Figure 13: Interface between [001] and [103] YBCO thin films and an insulative growth Y211 .....	45
Figure 14: nanoSQUID with a junction removed by FIB .....	46
Figure 15: current voltage characteristics (I-V) for a sample produced by soft nano-patterning width of 100 nm .....	46
Figure 16: Specifications of the superconductive YBCO thin films procured from ceraco and the cost as at 2014.....	53
Figure 17: Temperature dependence of the microwave surface resistance at 10.9 GHz of the YBCO thin films. ....	54
Figure 18: The schematic of the laser fiber oscillator.....	56
Figure 19: View of the laser YAG head structure and pump diode. ....	56
Figure 20: regenerative amplifier.....	57
Figure 21: Laser Source (Pump diode) .....	58
Figure 22: Pump laser control console for regulating lamp current.....	59
Figure 23: laser amplification section.....	60
Figure 24: Master controle console for Switching the laser ON/OFF. ....	61
Figure 25: Timing Console .....	62
Figure 26: Laser profile distribution on oscilloscope.....	62
Figure 27: Oscilloscope. ....	63
Figure 28: Shutter in open position. ....	64
Figure 29: Shutter closed.....	64
Figure 30: Reflective and guided path.....	65
Figure 31: Translation stage.....	66
Figure 32: Translation stage with the origin and axis lines sketched underneath. ....	67
Figure 33: Constriction design and microstrip lines.....	68

Figure 34: Microstrips lines with larger horizontal transitions.....	70
Figure 35: Microstrip lines with smaller horizontal transitions.....	70
Figure 36: Finding the focus point of laser.....	71
Figure 37: microstrip lines with constrictions.....	72
Figure 38: smaller constriction.....	74
Figure 39: Single pulse laser ablation .....	75
Figure 40: single pulse laser ablation with higher pulse energy .....	75
Figure 41: Laser power at 780 mW laser ablation width is 153 $\mu\text{m}$ . .....	76
Figure 42: laser power at 224 mW laser ablation width is 91 $\mu\text{m}$ .....	77
Figure 43: laser power at 137 mW laser ablation width is 89 $\mu\text{m}$ .....	77
Figure 44: laser power at 86 mW ablation width is 79 $\mu\text{m}$ .....	78
Figure 45: Ablation threshold of a laser beam .....	79
Figure 46: Laser fluences on the gold surface are increased .....	80
Figure 47: Dependence of the minimum structure size for different transparent materials on their band gap energy .....	81
Figure 48: Standard type of constriction.....	82
Figure 49: S-shaped constriction design.....	83
Figure 50: Constriction on steel with a width of 3 $\mu\text{m}$ .....	84
Figure 51: Beam collimation process consisting of a cylindrical diverging lens and a cylindrical converging lens. ....	86
Figure 52: Cylindrical lenses positioned at right angles to the direction of the axis to be blown up.....	87
Figure 53: 3-D view cylindrical lenses used to spread out and collimate the laser beam. ....	88
Figure 54: 2-D view of cylindrical lenses aligned in collimation set up.....	88
Figure 55: Gaussian beam optics simulator. ....	89
Figure 56: Test constriction cut on steel with a laser power setting of 483 mW. ....	94
Figure 57: Test constriction cut on steel with a laser power setting of 223.7 mW.....	94
Figure 58: Test constriction cut on steel with a laser power setting of 37.5 mW.....	95
Figure 59: AFM image showing the laser ablation width is 30.49 $\mu\text{m}$ at a power setting of 220 mW. ....	96
Figure 60: AFM image showing the constriction width is 30.89 $\mu\text{m}$ at a power setting of 220 mW. ....	96
Figure 61: AFM image showing the constriction length is 25.74 $\mu\text{m}$ at a power setting of 220 mW. ....	96
Figure 62: AFM image showing the laser ablation width is 25.75 $\mu\text{m}$ at a power setting of 104 mW. ....	97
Figure 63: AFM image showing the constriction width is 35.24 $\mu\text{m}$ at a power setting of 104 mW. ....	98
Figure 64: AFM image showing the constriction length is 15.05 $\mu\text{m}$ at a power setting of 104 mW. ....	98
Figure 65: AFM image of the constriction achieved with the Laser ablation spot size being 43.56 $\mu\text{m}$ the laser power setting is 190 mW.....	100
Figure 66: AFM image of the constriction achieved with a constriction width of 20.19 $\mu\text{m}$ , at a power setting of 190 mW. ....	100
Figure 67: New cylindrical lenses for beam collimation in the Gaussian beam simulation software. ....	102
Figure 68: Unwanted extension of the laser when its moved either in the forward direction or reverse direction viewed through the Atomic Force microscope (AFM). ....	103

Figure 69: Overall AFM atomic force microscope block. ....	106
Figure 70: Atomic Force Microscope scanning process with the cantilever tip over a constriction. ....	107
Figure 71: AFM image showing the Laser Ablation spot size is 31.68 $\mu\text{m}$ . ....	108
Figure 72: AFM image of the constriction showing constriction width is 60.19 $\mu\text{m}$ . ....	109
Figure 73: AFM image showing the Laser ablation spot size is 34.05 $\mu\text{m}$ . ....	110
Figure 74: AFM image showing constriction width is 30.49 $\mu\text{m}$ . ....	110
Figure 75: AFM image showing the constriction length is 53.46 $\mu\text{m}$ . ....	111
Figure 76: AFM image of a constriction showing the overlapping width to be 28.51 $\mu\text{m}$ . ....	112
Figure 77: AFM image showing the laser ablation spot size of the constriction is 62.96 $\mu\text{m}$ . .....	112
Figure 78: AFM image showing the overlapping area of the constriction to be 38.41 $\mu\text{m}$ . ....	113
Figure 79: Block diagram of the overall laser optical experimental set up used to cut the constriction. ....	117
Figure 80: Image of a Laser optical power meter based on a thermal power sensor. ....	117
Figure 81: Iris diaphragm with a manually adjustable aperture. ....	119
Figure 82: Overlapping length of constriction 30 $\mu\text{m}$ . ....	120
Figure 83: Poorly shaped focused laser ablation spot consisting of two laser ablation spots intertwined caused by spherical aberration of the laser light. ....	121
Figure 84: AFM image of the constriction showing the laser ablation spot size is 33.26 $\mu\text{m}$ . .....	122
Figure 85: AFM image of the constriction showing the constriction width to be 7.7 $\mu\text{m}$ . ....	123
Figure 86: AFM image showing a constriction fabricated with a laser power setting of 4.9 mW, iris aperture diameter 2.55 mm, constriction width of 1.989 $\mu\text{m}$ , separation distance between the laser ablation spots of approx. 17.8 $\mu\text{m}$ . ....	125
Figure 87: Design of the S-shaped constriction, Laser movement, Short movement factor (S.M.F), Long movement factor (L.M.F), Length Factor (L.F), the ablation strip lines, Length cons (constriction) and Width cons (constriction). ....	126
Figure 88: Normal constriction type, Length cons (constriction) and Width cons (constriction). .....	127
Figure 89: S-shaped constriction and ablation-strip lines captured beneath the cantilever tip of an AFM. ....	128
Figure 90: X, Y, Z directions for the movement of the translation stage and hence the relative movement of the laser. ....	130
Figure 91: AFM image scan of a laser ablation tunnel created during the fabrication of a constriction, laser power 2.7 mW, and laser ablation spot diameter 28.51 $\mu\text{m}$ , constriction width 2.376 $\mu\text{m}$ , length approx. 9 $\mu\text{m}$ . ....	136
Figure 92: A semi-logarithmic plot of the squared ablation diameter $D_2$ versus the peak laser fluence $F_0$ for YBCO on LAO substrate (red line is for the spline interpolation technique of curve fitting and the blue squares represents data points from Table 2, the peak laser fluence ablation threshold from the graph is approximately 0.824 J/cm <sup>2</sup> with (Fth, dia) method. ....	138
Figure 93: AFM image of a laser ablation spot tunnel created during the fabrication of a constriction, incident power 4.22 mW and maximum crater depth 146.2 nm. ....	139
Figure 94: A semi-logarithmic plot of maximum depth of the ablation craters $d_{\text{max}}$ versus the incident peak laser fluence $F_0$ for YBCO (red line for the spline fit and blue squares for the values from the Table 3, peak laser ablation threshold at x- intercept approximately 0.74 J/cm <sup>2</sup> with (Fth, dep) method. ....	140

Figure 95: Squared laser ablation diameter Vs Laser power (Laser power Threshold of YBCO thin film). .....	141
Figure 96: Overall optical experimental set up used to optimize the laser ablation spot. ....	143
Figure 97: AFM image of constriction showing the laser ablation spot size is 10.47 $\mu\text{m}$ . ....	145
Figure 98: AFM image of the constriction made showing the constriction width achieved is 2.59 $\mu\text{m}$ . .....	146
Figure 99: Cylindrical concave lenses of focal length of (-50 mm ) and Cylindrical convex lens with a focal length of (100 mm) aligned to collimate the laser beam. ....	147
Figure 100: 3-D view of the cylindrical diverging lenses of focal length (-50 mm ) and the cylindrical convex lenses of focal length (100 mm). .....	148
Figure 101: AFM image of the resulting constriction showing the laser ablation spot diameter of 7.344 $\mu\text{m}$ . .....	149
Figure 102: AFM image of the constriction showing the constriction width is 1.82 $\mu\text{m}$ . .....	150
Figure 103: AFM image showing the length of the constriction is 6.89 $\mu\text{m}$ . ....	150
Figure 104: AFM image of micron-sized constriction with ( $SW = 18 \mu\text{m}$ ) and an AFM scan area of 75 $\mu\text{m}$ X 75 $\mu\text{m}$ , showing a constriction width of 1.6 $\mu\text{m}$ . .....	153
Figure 105: AFM image of micron-sized constriction with ( $SW = 18 \mu\text{m}$ ) and an AFM scan area of 75 $\mu\text{m}$ X 75 $\mu\text{m}$ , showing a constriction width of 1.76 $\mu\text{m}$ . ....	154
Figure 106: AFM image of the micron-sized constriction with ( $SW = 18 \mu\text{m}$ ) and AFM scan area of 20.5 $\mu\text{m}$ X 20.5 $\mu\text{m}$ , showing a constriction width of 1.68 $\mu\text{m}$ . .....	155
Figure 107: AFM image of the micron-sized constriction with ( $SW = 18 \mu\text{m}$ ) and AFM scan area of 20.5 $\mu\text{m}$ X 20.5 $\mu\text{m}$ , showing the constriction length is 12.79 $\mu\text{m}$ . ....	156
Figure 108: AFM image of the micron-sized constriction fabricated with ( $SW = 17.5 \mu\text{m}$ ) and AFM scan area of 75 $\mu\text{m}$ X 75 $\mu\text{m}$ showing a constriction width of 1.58 $\mu\text{m}$ . ....	157
Figure 109: AFM image of the micron-sized constriction fabricated with ( $SW = 17.5 \mu\text{m}$ ) and AFM scan area of 75 $\mu\text{m}$ X 75 $\mu\text{m}$ showing a constriction width of 1.47 $\mu\text{m}$ . ....	158
Figure 110: AFM image of the micron-sized constriction fabricated with ( $SW = 17.5 \mu\text{m}$ ) and AFM scan area of 20.5 $\mu\text{m}$ X 20.5 $\mu\text{m}$ showing a constriction width of 1.39 $\mu\text{m}$ . .....	159
Figure 111: AFM image of the micron-sized constriction fabricated with ( $SW = 17.5 \mu\text{m}$ ) and AFM scan area of 20.5 $\mu\text{m}$ X 20.5 $\mu\text{m}$ showing a constriction length of 12.26 $\mu\text{m}$ . .....	159
Figure 112: Cross section taken of the constriction showing a constriction width of 1.39 $\mu\text{m}$ . .....	160
Figure 113: AFM image of the micron-sized constriction fabricated with ( $SW = 17 \mu\text{m}$ ) and AFM scan area of 20.8 $\mu\text{m}$ X 20.8 $\mu\text{m}$ showing the constriction width is 1.63 $\mu\text{m}$ . .....	161
Figure 114: AFM image of the sub micron-sized constriction fabricated with ( $SW = 16.5 \mu\text{m}$ ) and AFM scan area of 75 $\mu\text{m}$ X 75 $\mu\text{m}$ showing the constriction width is 1.06 $\mu\text{m}$ . .....	162
Figure 115: AFM image of the sub micron-sized constriction fabricated with ( $SW = 16.5 \mu\text{m}$ ) and AFM scan area of 14.6 $\mu\text{m}$ X 14.6 $\mu\text{m}$ showing the constriction width is 895.6 nm .....	163
Figure 116: AFM image of the sub micron-sized constriction fabricated with ( $SW = 16.5 \mu\text{m}$ ) and AFM scan area of 14.6 $\mu\text{m}$ X 14.6 $\mu\text{m}$ showing the constriction width is 858.3 nm. ....	163

Figure 117:	AFM image of the sub micron-sized constriction fabricated with ( $SW = 16.5 \mu m$ ) and AFM scan area of $14.6 \mu m \times 14.6 \mu m$ showing the constriction length is $9.66 \mu m$ .	164
Figure 118:	AFM image of the sub micron-sized constriction fabricated with ( $SW = 16.5 \mu m$ ) and AFM scan area of $75 \mu m \times 75 \mu m$ showing the laser ablation spot size is $15.82 \mu m$ .	165
Figure 119:	AFM image of the sub micron-sized constriction fabricated with ( $SW = 16.5 \mu m$ ) and AFM scan area of $16.7 \mu m \times 16.7 \mu m$ showing the constriction width is $1.231 \mu m$ .	165
Figure 120:	AFM image of the sub micron-sized constriction fabricated with ( $SW = 16 \mu m$ ) and AFM scan area of $75 \mu m \times 75 \mu m$ showing the overall constriction shape.	166
Figure 121:	AFM image of the sub micron-sized constriction fabricated with ( $SW = 16.5 \mu m$ ) and AFM scan area of $16.7 \mu m \times 16.7 \mu m$ showing the constriction width is $576.7 \text{ nm}$ .	167
Figure 122:	AFM image of the sub-micron-sized constriction fabricated with ( $SW = 16 \mu m$ ) and AFM scan area of $18.8 \mu m \times 18.8 \mu m$ showing the constriction width is $732.4 \text{ nm}$ .	167
Figure 123:	Thin film being cleaned in a sonicator	169
Figure 124:	Cleaned thin films in packaging	170
Figure 125:	AFM image of a sub-micron constriction of width $879.3 \text{ nm}$ fabricated with laser power $2.035 \text{ mW}$ , spherical convex lens ( $30\text{mm}$ focal length), scan area $17.6 \mu m \times 17.6 \mu m$ , separation distance between laser ablation spots ( $SW$ ) $16.5 \mu m$ , 5 <sup>th</sup> constriction on sample.	170
Figure 126:	AFM image of a sub-micron constriction of width $874.2 \text{ nm}$ fabricated with laser power $2.035 \text{ mW}$ , spherical convex lens ( $30\text{mm}$ focal length), scan area $19.6 \mu m \times 19.6 \mu m$ , separation distance between laser ablation spots ( $SW$ ) $16.5 \mu m$ , 3 <sup>rd</sup> constriction on sample.	171
Figure 127:	AFM image of a sub-micron constriction of width $813.1 \text{ nm}$ fabricated with laser power $2.035 \text{ mW}$ , spherical convex lens ( $30\text{mm}$ focal length), scan area $17.3 \mu m \times 17.3 \mu m$ , separation distance between laser ablation spots ( $SW$ ) $16.5 \mu m$ , 4 <sup>th</sup> constriction on sample.	171
Figure 128:	AFM image of a micron constriction of width $1.191 \mu m$ fabricated with laser power $2.035 \text{ mW}$ , spherical convex lens ( $30\text{mm}$ focal length), scan area $20.5 \mu m \times 20.5 \mu m$ , separation distance between laser ablation spots ( $SW$ ) $17 \mu m$ , 5 <sup>th</sup> constriction on sample.	172
Figure 129:	AFM image of a micron constriction of width $1.248 \mu m$ fabricated with laser power $2.035 \text{ mW}$ , spherical convex lens ( $30\text{mm}$ focal length), scan area $19.9 \mu m \times 19.9 \mu m$ , separation distance between laser ablation spots ( $SW$ ) $17 \mu m$ , 4 <sup>th</sup> constriction on sample.	172
Figure 130:	AFM image of a micron constriction of width $1.074 \mu m$ fabricated with laser power $2.035 \text{ mW}$ , spherical convex lens ( $30\text{mm}$ focal length), scan area $21.1 \mu m \times 21.1 \mu m$ , separation distance between laser ablation spots ( $SW$ ) $17 \mu m$ , 2 <sup>nd</sup> constriction on sample.	173
Figure 131:	AFM image of a sub-micron constriction of width $812.4 \text{ nm}$ fabricated with laser power $2.035 \text{ mW}$ , spherical convex lens ( $30\text{mm}$ focal length), scan area $22.4 \mu m \times 22.4 \mu m$ , separation distance between laser ablation spots ( $SW$ ) $16 \mu m$ , 3 <sup>rd</sup> constriction on sample.	173

Figure 132:	AFM image of a sub-micron constriction with a laser ablation spot diameter of 15.82 $\mu\text{m}$ , fabricated with laser power 2.035 mW, spherical convex lens (30mm focal length), scan area 75 $\mu\text{m}$ X 75 $\mu\text{m}$ , separation distance between laser ablation spots ( <i>SW</i> ) 16 $\mu\text{m}$ .	177
Figure 133:	AFM image of a sub-micron constriction with a constriction width of 549.3 nm, fabricated with laser power of 2.035 mW, spherical convex lens (30mm focal length), scan area 23.4 $\mu\text{m}$ X 23.4 $\mu\text{m}$ , separation distance between laser ablation spots ( <i>SW</i> ) 16 $\mu\text{m}$ .	178
Figure 134:	AFM image of a sub-micron constriction with a constriction length of 8.17 $\mu\text{m}$ , fabricated with laser power of 2.035 mW, spherical convex lens (30mm focal length), scan area 23.4 $\mu\text{m}$ X 23.4 $\mu\text{m}$ , separation distance between laser ablation spots ( <i>SW</i> ) 16 $\mu\text{m}$ .	178
Figure 135:	AFM image of a nano constriction with a laser ablation spot size is 15.53 $\mu\text{m}$ , fabricated with laser power of 2.035 mW, spherical convex lens (30mm focal length), scan area 75 $\mu\text{m}$ X 75 $\mu\text{m}$ , separation distance between the laser ablation spots ( <i>SW</i> ) 16 $\mu\text{m}$ .	179
Figure 136:	AFM image of a nano constriction with a constriction width of 394.8 nm, fabricated with laser power of 2.035 mW, spherical convex lens (30mm focal length), scan area 20.2 $\mu\text{m}$ X 20.2 $\mu\text{m}$ , separation distance between the laser ablation spots ( <i>SW</i> ) 16 $\mu\text{m}$ , 3 <sup>rd</sup> qubit.	179
Figure 137:	AFM image of a nano constriction with a constriction length of 7.53 $\mu\text{m}$ , fabricated with laser power of 2.035 mW, spherical convex lens (30mm focal length), scan area 20.2 $\mu\text{m}$ X 20.2 $\mu\text{m}$ , separation distance between the laser ablation spots ( <i>SW</i> ) 16 $\mu\text{m}$ , 3 <sup>rd</sup> qubit.	180
Figure 138:	AFM image of a sub-micron constriction with a laser ablation spot size of 15.82 $\mu\text{m}$ , fabricated with laser power of 2.035 mW, spherical convex lens (30mm focal length), scan area 75 $\mu\text{m}$ X 75 $\mu\text{m}$ , separation distance between the laser ablation spots ( <i>SW</i> ) 16.5 $\mu\text{m}$ , 2 <sup>nd</sup> qubit.	180
Figure 139:	AFM image of a sub-micron constriction with a constriction width of 881.2 nm, fabricated with laser power of 2.035 mW, spherical convex lens (30mm focal length), scan area 20.5 $\mu\text{m}$ X 20.5 $\mu\text{m}$ , separation distance between the laser ablation spots ( <i>SW</i> ) 16.5 $\mu\text{m}$ , 2 <sup>nd</sup> qubit.	181
Figure 140:	AFM image of a sub-micron constriction with a constriction length of 7.24 $\mu\text{m}$ , fabricated with laser power of 2.035 mW, spherical convex lens (30mm focal length), scan area 20.5 $\mu\text{m}$ X 20.5 $\mu\text{m}$ , separation distance between the laser ablation spots ( <i>SW</i> ) 16.5 $\mu\text{m}$ , 2 <sup>nd</sup> qubit.	181
Figure 141:	AFM image of a micron constriction with a laser ablation spot size of 15.23 $\mu\text{m}$ , fabricated with laser power of 2.035 mW, spherical convex lens (30mm focal length), scan area 75 $\mu\text{m}$ X 75 $\mu\text{m}$ , separation distance between the laser ablation spots ( <i>SW</i> ) 17 $\mu\text{m}$ , 4th qubit.	182
Figure 142:	AFM image of a micron constriction with a constriction width of 1.086 $\mu\text{m}$ , fabricated with laser power of 2.035 mW, spherical convex lens (30mm focal length), scan area 21.4 $\mu\text{m}$ X 21.4 $\mu\text{m}$ , separation distance between the laser ablation spots ( <i>SW</i> ) 17 $\mu\text{m}$ , 4th qubit.	183
Figure 143:	AFM image of a micron constriction with a constriction length of 7.211 $\mu\text{m}$ , fabricated with laser power of 2.035 mW, spherical convex lens (30mm focal length), scan area 21.4 $\mu\text{m}$ X 21.4 $\mu\text{m}$ , separation distance between the laser ablation spots ( <i>SW</i> ) 17 $\mu\text{m}$ , 4th qubit.	183

Figure 144:	Optical microscope (OM) image of a constriction made showing the heating fringe.....	186
Figure 145:	A sketch of the dimensions of the YBCO tracks containing the constrictions etched in the middle with the ablation striplines on the sides. The dimensions where done to create a soft mask to facilitate the photolithography process to place Gold (Au) contact pads on the YBCO tracks. ....	188
Figure 146:	Soft mask : gold (au) contact pads, one grid is 0.5 mm.....	188
Figure 147:	photoresistor application.....	189
Figure 148:	2-D profile showing the YBCO thin film and the photoresistor layer.....	190
Figure 149:	Hard mask used in the mask aligner tool.....	190
Figure 150:	Mask alignment tool. ....	191
Figure 151:	UV rays applied from the mask alignment tool after alignment with the hard mask .....	192
Figure 152:	The photo resist material removed in the sections where the gold (Au) pads will be applied. ....	192
Figure 153:	Oxygen plasma .....	193
Figure 154:	Oxygen plasma applied to clean the grooves where the gold (Au) contact pads are to be placed. ....	194
Figure 155:	Ion beam and gold deposition chamber. ....	194
Figure 156:	Control system for Gold deposition.....	195
Figure 157:	2-D profile image after the gold deposition process.....	196
Figure 158:	Photo resistor removed after cleaning in acetone leaving behind only the Gold (Au) contacts. ....	196
Figure 159:	The sample after gold deposition with a separation distance between the laser ablation spots ( <i>SW</i> ) 18.7 $\mu\text{m}$ – 18.3 $\mu\text{m}$ sample with 4-point gold contacts deposited. ....	197
Figure 160:	PCB holder with the YBCO thin film sample having gold contact points. ....	197
Figure 161:	Wire bonding machine .....	198
Figure 162:	(a) YBCO sample with 4-point gold contacts, wire bonded to the PCB holder, 162 (b) PCB holder mounted onto a nitrogen immersion probe. ....	199
Figure 163:	(a) The probe with sample immersed in liquid nitrogen, 163 (b) DC current source and DC voltmeter.....	200
Figure 164:	“SQUID” software from national instruments for plotting I-V characteristics of a constriction.....	201
Figure 165:	Image showing how each constriction is wire bonded to the PCB holder and then soldered to the nitrogen immersion probe. (wire connections).....	202
Figure 166:	Schematic of the sample I-V and RF measurement set-up. The sample is an YBCO thin film containing the laser etched constrictions.....	204
Figure 167:	RF connection coupled onto the one of the 4-point gold probes on the sample. ....	204
Figure 168:	(a) AFM image of the sub-micron constriction, 168(b) 3-D AFM image of the sub-micron constriction. whose width is defined between the (black) arrows as 816 nm. ....	205
Figure 169:	AFM Profile distribution of the sub-micron constriction, the width can be measured between the (black) arrows, and is 816 nm.....	206
Figure 170:	SEM image of the sub-micron constriction shows the width to be 816 nm between the red cursors, courtesy of CSIRO Australia Laboratory. ....	206

Figure 171:	(a) AFM image of the micron constriction, 171 (b) 3-D AFM image of the micron constriction whose width is measured between the black arrows is 2.1 $\mu\text{m}$ ..207	207
Figure 172:	AFM profile distribution of the micron constriction, the width measured between the (black) arrows, is 2.1 $\mu\text{m}$ .....207	207
Figure 173:	SEM image of micron sized constriction showing the width to be 2.1 $\mu\text{m}$ . .....208	208
Figure 174:	I-V characteristic for the sub-micron constriction measured at $T = 8.5 \text{ K}$ .....209	209
Figure 175:	I-V characteristic for the micron size constriction measured at Temperature $T=10 \text{ K}$ .....210	210
Figure 176:	Shapiro-like steps for the sub-micron sized constriction which was exposed to RF signal of frequency of 19.5 GHz, power strength -30 dBm and sample temperature of 8.5 K. ....211	211
Figure 177:	Shapiro-like steps of the micron-size constriction exposed to an RF frequency of 19.573GHz, signal power -12dBm and sample temperature of 25K. ....212	212
Figure 178:	I-V curves at different levels of RF signal power at a temperature of 8.5 K and a frequency of 19.5 GHz for the sub-micron constriction.....213	213
Figure 179:	I-V curves at varying levels of RF signal power, temperature of 6 K, RF signal frequency of 19.5 GHz for the micron sized constriction. ....214	214
Figure 180:	I-V curves for the sub-micron sized constriction at different temperatures. ....215	215
Figure 181:	I-V curves for micron sized constriction at different temperatures. ....215	215
Figure 182:	$IC$ versus $T/TCN$ plot for the sub-micron constriction. The solid red line is an exponential decay fit to the experimental data (solid squares) obtained for the 816 nm constriction. ....217	217
Figure 183:	$IC$ versus $T/TCN$ plot for the micron sized constriction, the solid line is a linear fit to the experimental data (solid squares) obtained for the 2.1 $\mu\text{m}$ constriction..217	217
Figure 184:	Normal Resistance $R_n$ Versus temperature for the sub-micron 816 nm constriction.....218	218
Figure 185:	Normal Resistance $R_n$ Versus Temperature for the micron 2.1 $\mu\text{m}$ constriction. ....219	219
Figure 186:	The $ICRN$ product curve for the micron 2.1 $\mu\text{m}$ Josephson junction. ....220	220
Figure 187:	$ICRN$ product curve for the micron 2.1 $\mu\text{m}$ Josephson junction. ....220	220
Figure 188:	Power dependence of the normalized critical current $ICN$ at the first shapiro step $n=0$ , for the Josephson junction 2.1 $\mu\text{m}$ wide, temperature 6 K and signal frequency 19.5 GHz. ....227	227
Figure 189:	RF power dependence of the normalized critical current $ICN$ at the first shapiro step $n=0$ , for the Josephson junction 816 nm wide, temperature 8.5 K and signal frequency 19.5 GHz. ....229	229
Figure 190:	Power dependence of the normalized Critical Current $ICN$ for the first shapiro step $n = 0$ , for the two Josephson junctions 816 nm and 2.1 $\mu\text{m}$ at a temperature of 7 K and signal frequency 19.5 GHz.....230	230
Figure 191:	I-V characteristic of the superconductive sub-micron bridge (659 nm). ....235	235
Figure 192:	SEM image of the 659 nm sub-micron bridge.....235	235
Figure 193:	I-V curve for the resistive micron constriction 1.49 $\mu\text{m}$ showing a straight line..236	236
Figure 194:	SEM image of the resistive micron constriction 1.49 $\mu\text{m}$ .....237	237
Figure 195:	Appropriate method of Storing fabricated Josephson junctions and SQUID devices. ....237	237
Figure 196:	I-V curve for the open micron constriction 1.36 $\mu\text{m}$ showing a hysteresis loop. 238	238
Figure 197:	SEM image of the electrically open micron constriction 1.36 $\mu\text{m}$ .....239	239

Figure 198:	Variety of possible sizes of dirty weak links and causes of the flow of supercurrent through them .....	241
Figure 199:	Set up for I-V measurement on the micron bridge samples using the circuit analysis software “SQUIDS” from national instruments. ....	242
Figure 200:	SEM image of 2.88 $\mu\text{m}$ micron bridge. ....	244
Figure 201:	I-V characteristic for the 2.88 $\mu\text{m}$ constriction (a) showing critical current to be 4.81 mA.....	245
Figure 202:	AFM profile of the 2.88 $\mu\text{m}$ constriction (a) showing the approximate height of the re-deposited particles to be 173 nm. ....	245
Figure 203:	SEM image of constriction (b) showing the width to be 1.72 $\mu\text{m}$ . ....	246
Figure 204:	I-V characteristic for the 1.72 $\mu\text{m}$ wide constriction (b) showing the critical current to be 1.77 mA at a temperature of 77 K.....	246
Figure 205:	AFM profile of 1.72 $\mu\text{m}$ wide constriction (b) re-deposited particles height is 151 nm. ....	247
Figure 206:	SEM image of the 1.69 $\mu\text{m}$ wide constriction (c). ....	248
Figure 207:	I-V curve of the 1.69 $\mu\text{m}$ constriction (c), showing the critical current to be 15.2 mA at a temperature of 77 K.....	248

# LIST OF TABLES

Table 1: Scheduled Activity for PhD Work. ....	48
Table 2: Finding the Peak laser fluence ablation threshold of YBCO thin film ( $F_{th}$ , $dia$ ) using the laser ablation spot diameter method.....	137
Table 3: Finding the Peak laser fluence ablation threshold of YBCO thin film ( $F_{th}$ , $dia$ ) using the laser ablation spot diameter method.....	139
Table 4: Objective Plano convex lenses with different parameters or specifications. ....	144
Table 5: Summarizing the constrictions fabricated so far, their widths measured in AFM, position on the thin films sample and the separation distances between the laser ablation spots ( $SW$ ) is given in the table.....	168
Table 6: Summarizing other useful constrictions fabricated, scanned in AFM showing the widths, position on the thin film, and the separation distance between the laser ablation spots ( $SW$ ).....	174
Table 7: Summary of constrictions fabricated in this sub-section with all specifications. ....	184
Table 8: Constrictions that showed the Josephson-like effect – dimensions, and their laser etching parameters.....	203
Table 9: Laser cutting parameters for each bridge. ....	242
Table 10: Constrictions sizes and their corresponding critical current.....	243

## KEYWORDS

JJ - Josephson Junction, femtosecond laser, beam collimation, shapiro steps, micron constrictions, submicron constrictions, nano constrictions, S-shaped constrictions, critical current, ablation threshold, peak laser fluence, aJ – attojoule, pJ – picojoule,  $T_C$ - critical temperature, normal resistance, RF power.

# LIST OF ABBREVIATIONS AND ACRONYMS

RF – (Radio Frequency)

S-s'-S - (Superconductor – geometrically reduced superconductor - Superconductor)

S-N-S – (Superconductor – Normal – Superconductor )

AFM – Atomic Force Microscope.

SEM – Scanning Electron Microscope.

SQUID – Superconducting Quantum interference Device.

YBCO – Yttrium barium copper oxide ( $YBa_2Cu_3O_7$ ).

G-code – Control language for CNC machines (RS-274).

LAO – Lanthanum aluminate ( $LaAlO_3$ ).

MgO – Magnesium Oxide.

Iris – Manually Adjustable Aperture.

NA – Numerical Aperture.

$I_c$  – Critical current.

$R_N$  – Normal Resistance.

$T_c$  – Critical Temperature.

# CHAPTER 1

## THE JOSEPHSON JUNCTION, THE JOSEPHSON EFFECT AND METHODS OF FABRICATION.

### 1.1 INTRODUCTION TO SUPERCONDUCTIVITY

Superconductivity occurs when you cool certain metals and alloys to very low temperatures, a phase transition occurs.

At this “critical temperature” the metal goes from what is called the normal state, where it has electrical resistance, to the superconducting state where there is essentially no resistance to the flow of direct electrical current. The newer high-temperature superconductors, which are made from ceramic materials, exhibit the same behaviour but at warmer temperature.

Above the critical temperature, the net interaction between two electrons is repulsive; below the critical temperature the overall interaction between the two electrons becomes slightly attractive. This slight attraction allows the electrons to drop into a lower energy state opening up an energy “gap”. In this energy gap electrons can move without being scattered by the ions of the lattice. When the ions scatter electrons then there is electrical resistance hence at this state there will be no electrical resistance and hence no voltage only the super current. There is however a maximum super current that can occur called the critical current. Above this critical current the material is normal and the current that flows is called a normal current. When the critical current is exceeded then a voltage will drop across the device, an A.C voltage which further reduces the critical current and causes even more normal current to flow.

So long as the current through the junction is less than the critical current the voltage is zero as soon as the current exceeds the critical current then the voltage is greater than zero and oscillates in time.

The Josephson effect is the phenomenon of super current i.e a current that flows indefinitely long without any voltage applied – across a device known as a Josephson Junction[1]. The Josephson’s Junction consists of two superconductors coupled by a weak link.

The Weak link can consist of a thin insulating barrier (superconductor-insulator-superconductor, or S-I-S), a short section of non-superconducting metal (S-N-S), or a physical constriction that weakens the superconductivity at the point of contact (S-s'-S). This project aims to fabricate the S-s'-S type constriction.

Detecting and measuring the change from one state to another is the heart of many applications for Josephson Junctions [2]-[6].

There is one other very important property: when a metal goes into the superconducting state, it expels all magnetic fields, as long as the magnetic fields are not too large.

### 1.1.1 JOSEPHSON EFFECT

The Josephson Effect is one of the macroscopic quantum phenomena of superconductivity. In it the current through a weak contact between two relatively bulky superconducting electrodes may contain a component  $I_S$  (supercurrent), which is dependent not on the voltage “ $V$ ” across the electrodes but on the phase difference [7] ( $\Phi_1 - \Phi_2$ ) between the two materials that sandwich the weak contact [8]. A Josephson junction can be seen in figure 1.

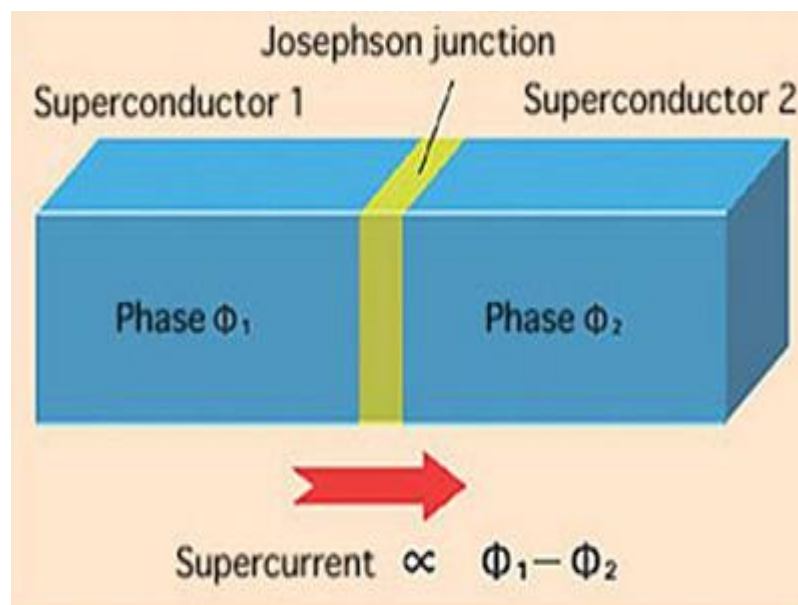


Figure 1 Idealised sketch of a Josephson junction [7]

Therefore based on this the phase difference is given by;

$$\varphi = \Phi_1 - \Phi_2 \quad (1)$$

Where  $\Phi_1$  and  $\Phi_2$  are the phases of the order parameter in the electrodes and  $\varphi$  is the phase.

In the simplest ("classical") case, the relationship  $I_S(\varphi)$  is sinusoidal;

$$I_S = I_C \sin\varphi \quad (2)$$

Where  $I_C$  is called the supercurrent amplitude or the critical current. The phase " $\varphi$ " is related to the voltage across the electrodes " $V$ " by the following expression in equation (3);

$$\frac{d\varphi}{dt} = \frac{2e}{\hbar} V \quad (3)$$

There is a significant difference between equations (2) and (3) which qualitatively describe the Josephson effect. Equation (2) is an approximate one, and various kinds of deviations of supercurrent from this dependence may be observed in a superconducting weak link of any type. The constant  $I_C$  involved in equation (2) is essentially dependent on the geometry and material of the weak link, the electrode material, temperature and other factors. In contrast, equation (3) is derived solely from the main principles of quantum mechanics and contains only fundamental constants.

### 1.1.2 DC AND AC JOSEPHSON EFFECTS

All the electrodynamic phenomena [8] taking place at the Josephson contacts are generally divided into stationary (d.c) and nonstationary (a.c) effects, depending on whether the variables, including the phase difference  $\varphi$ , change with time or not. If the phase  $\varphi$  remains constant (d.c effects), as directly follows from equation (3), the voltage across the junction is zero. At the same time, a nonzero supercurrent equation (2) can flow through the junction. In the dc case, this current must be constant in time and less than or equal to the critical current;

$$V = 0, \varphi(t) = \text{const}, I = I_S(\varphi), |I| \leq I_C \quad (4)$$

Among the nonstationary (ac) effects occurring when the phase changes with time, the most important are the Josephson oscillations (shapiro steps) which inevitably take place if the voltage "V" at the contact has a dc component  $\bar{V}$ . As follows from equation (3), in this case the phase  $\varphi$  contains a component that increases linearly with time at a rate;

$$\omega_V = \frac{d\varphi}{dt} = \frac{2e}{\hbar} \bar{V}, f_V = \frac{\omega_V}{2\pi} = \frac{2e}{h} \bar{V} \quad (5)$$

The supercurrent, therefore, oscillates in time at a frequency  $\omega_V$  directly proportional to  $\bar{V}$ . The proportionality factor ( $\frac{f_V}{\bar{V}} \approx 500 \text{ MHz}/\mu\text{V}$ ) is rather high; consequently, Josephson junctions are highly sensitive to the electromagnetic field. This proportionality factor and proof of the Josephson effect will be proven in the later chapters.

## 1.2 VARIETIES OF JOSEPHSON JUNCTIONS

There are different kinds of Josephson Junctions with respect to structure;

- (a) Tunnelling Junctions
- (b) Constriction
- (c) Point Contact

Tunnelling junctions are formed by surface contact; constriction, which is the structure to be implemented in this project, is formed by etching processes and point contact which is junctions formed by contact at a point. All this structures can be seen in figure 2.

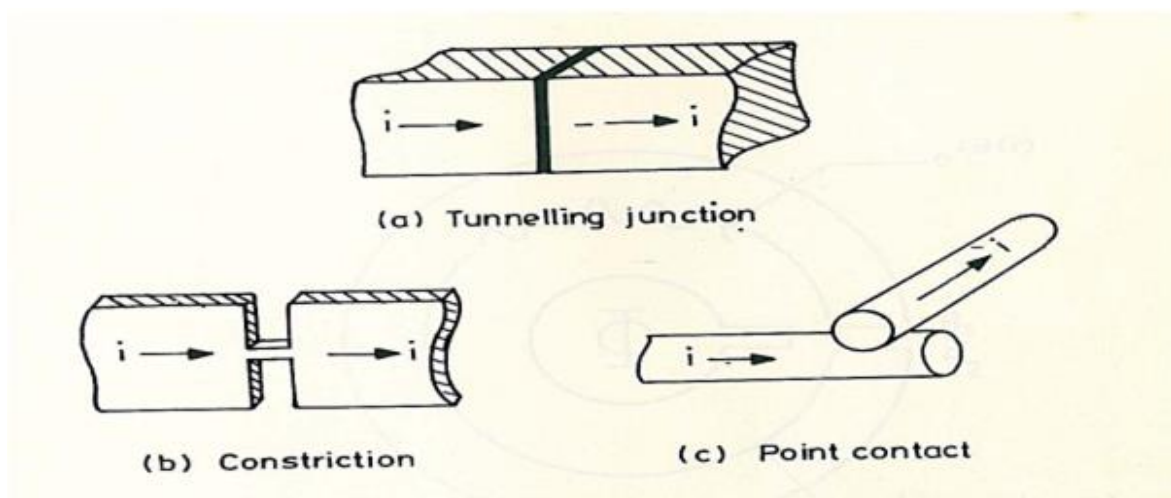


Figure 2 Varieties of Junctions [8]

### 1.3 USES OF JOSEPHSON JUNCTIONS

SQUIDS, or superconducting quantum interference devices, are very sensitive magnetometers that operate via the Josephson effect. They are widely used in science and engineering.

RSFQ digital electronics is based on shunted Josephson junctions. In this case, the junction-switching event is associated to the emission of one magnetic flux quantum that carries the digital information: the absence of switching is equivalent to 0, while one switching event carries a 1.

Josephson junctions are integral in superconducting quantum computing as qubits such as in a flux qubit or others schemes where the phase and charge act as the conjugate variables.

Lastly, Josephson Junctions have very low power dissipation as compared to other devices. Figure 3 shows that the superconducting Josephson junctions fall in the (aJ) region with respect to power consumption while semiconducting devices fall into the (pJ) region; which is several orders of magnitude larger. Therefore advancing methods in the fabrication of high- $T_C$  superconducting (HTS) JJ's open up doors for devices that consume low power [9].

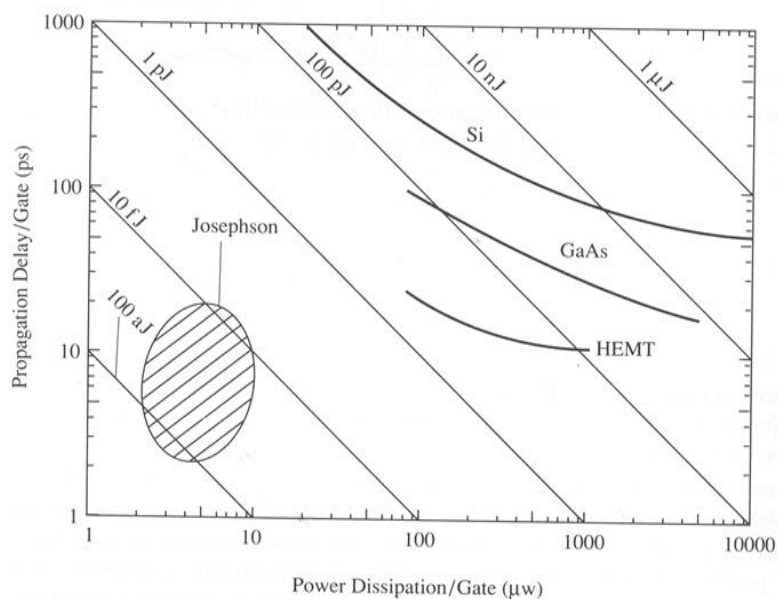


Figure 3 A comparative description of device performance and power dissipation characteristics of various types of materials (semiconductors and superconductors) [9]

## 1.4 WHY NANO JOSEPHSON JUNCTIONS?

Josephson Junctions are very useful for the fabrication of qubits. The advantages of Josephson junctions as qubits are twofold. First and foremost Josephson junctions have a low dissipation of energy hence a long coherence time, secondly when fabricating integrated circuits and using micro fabricating techniques it's possible to make use of a large number of JJ qubits [10]. In qubit design  $E_C \sim E_J$  where  $E_C$  is the charging energy and  $E_J$  is the Josephson energy, in order for this condition to be satisfied the device has to be in the nanoscale.

Josephson Junctions can be used to fabricate Nano-SQUIDS, which are useful in detection possibilities with respect to the magnetization of individual particles or molecular spins [10]. In the near field regime the spin sensitivity  $S_N$ , in terms of number of spins detected is expressed as  $S_N = 4r\Phi_{NS}/\alpha\mu_B\mu_0$ . Where  $r$ ,  $\Phi_{NS}$ ,  $\alpha$ ,  $\mu_B$ ,  $\mu_0$  are nanobridge width, SQUID flux noise, SQUID/dipole coupling factor, Bohr magneton, and vacuum permeability respectively. The spin sensitivity requires that the bridge dimensions be as small as possible preferably in the nano scale to pick up molecular spins.

## 1.5 PROBLEM STATEMENTS AND OBJECTIVES OF PHD WORK

### 1.5.1 PROBLEM STATEMENT 1

The main aim of this PhD work and the first problem to be solved is to fabricate a Josephson junction using the novel femtosecond laser technique. The femtosecond laser by itself is not novel by any means however using it to fabricate a Josephson junction is a novel technique. Other microsecond ( $\mu$ S) lasers [11-13] have in the past been used to fabricate Josephson junctions, but the femtosecond laser has never been used before. This problem would involve fabricating a Josephson junction using the femtosecond laser and then proving one is fabricated by using I-V characteristics, shapiro steps and RF effect on critical current.

### 1.5.2 PROBLEM STATEMENT 2

The second problem is that when using a laser technique in the fabrication of a Josephson junction especially when using the other microsecond lasers ( $\mu$ S) there is a tendency of the constriction fabricated being exposed to localized heating from the laser. This thermal degradation changes the weak link at the centre of the

Josephson junction from a superconductive phase to a normal one, thereby producing an S-N-S type Josephson junction instead of the preferred S-s'-S type junction. The S-s'-S type junction is a junction with a geometrically reduced s' superconductor sandwiched in the middle. By using the femtosecond laser which has a low pulse duration of 130 fs it is believed that the constrictions weak link would not be exposed to the thermal heating for any prolonged period of time and an attempt can be made to fabricate the preferred S-s'-S type junction.

### **1.5.3 PROBLEM STATEMENT 3**

The third problem to be solved is that of using the femtosecond laser to fabricate Josephson junctions in the nanoscale or nano dimensions. That is the Josephson junctions fabricated should preferably be in the dimension range of (0 – 500 nm). The reason for attempting to make Josephson junctions in this scale has already been mentioned in section 1.4 above and is related to the high sensitivity of sensors made from nano sized Josephson junctions. In addition, constrictions or weak links in the nano scale are more likely to show the Josephson effect as specified in [8] by Ikharev et al.

### **1.5.4 PROBLEM STATEMENT 4**

An attempt will be made to fabricate a novel S-shaped constriction to be used as a Josephson junction. This S-shaped constriction as the name implies is shaped like the letter "S" and differs from the standard constriction type junctions in that it's possible to regulate both the width and the length of this constriction at the same time during fabrication, which will be explained in chapter 3 in detail. Again the novelty stems from the fact that this type of constriction has never been designed before.

### **1.5.5 PROBLEM STATEMENT 5**

The last problem is partially related to problems 1 and 3. This problem is related to making use of the femtosecond laser for the fabrication process and the desire of making a Josephson junction in the nanoscale. In order to make use of the femtosecond laser technique for fabrication of Josephson junctions the laser beam spot has to be shaped, optimised and reduced in size to produce a small laser ablation spot which is conducive for cutting constrictions in the nano dimension. Therefore, a laser beam shaping and collimation process has to be developed in order to optimize the laser beam spot for the machining process.

### **1.5.6 OBJECTIVES OF PHD WORK**

The Josephson Junction has already been made before and its properties have been extracted using several methods [10]-[14]. The main aim of this project is to make use of a novel approach the femtosecond laser technique to fabricate the Josephson Junctions. The idea behind using this method is that it is very quick and uses ultra-fast pulses of laser 130 fs in etching the material. It has a very short wavelength 775 nm. The short wavelength would allow very small junction sizes to be produced in the order of 400 nm and the short pulse duration would enable junctions to be produced without heating the constriction in manufacturing. With other laser etching methods when the constriction size decreases from micron to submicron levels there will be excessive local heating which changes the YBCO phase in the constriction into a non-superconducting normal phase [11]. If the superconducting phase can be achieved then the Junction made will be homogenous without a normal phase.

Josephson effect may then be analysed by using I-V measurements, Shapiro steps,  $I_c$  versus magnetic field, the critical current versus temperature relationship and the critical current versus RF power and then compare this to Junctions fabricated using other techniques. Finally, if possible the fabricated nano-junction can be applied in an electrical sensor capacity such as a magnetic sensor.

## **1.6 PROVING THE JOSEPHSON EFFECT**

The following experiments shall be done to establish the Josephson's effect in the fabricated JJ's.

### **1.6.1 I-V CHARACTERISTICS**

As an example figure 4 shows the typical I-V curve of a nanoconstriction produced by the AFM technique. Although the I-V curve can be used as proof that a Josephson's junction is produced in this case it shows a bit of rounding near the knee of the curves which can be attributed to flux flow not the Josephson's effect.

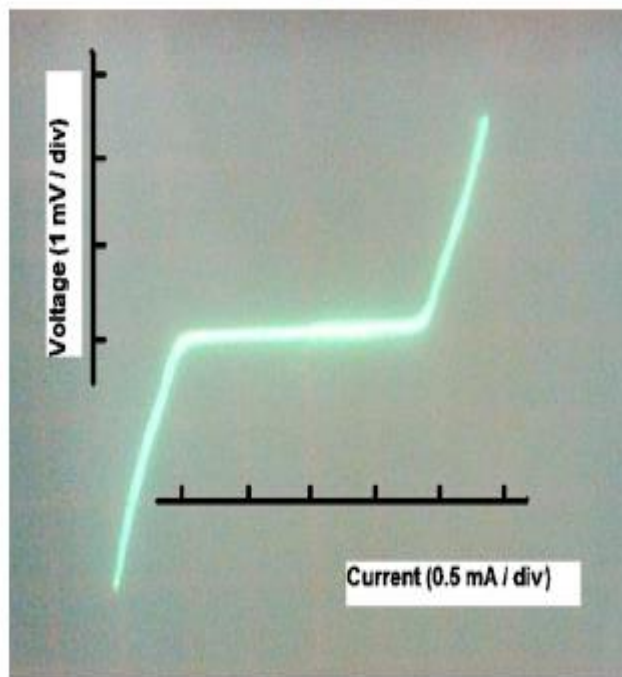


Figure 4 I-V curve of a Nanoconstriction [10]

### 1.6.2 SHAPIRO STEPS

Figure 5 shows the schematic of the basic test set up to test the device for Shapiro steps at  $T = 57.1$  K and frequency of 9.073 GHz.

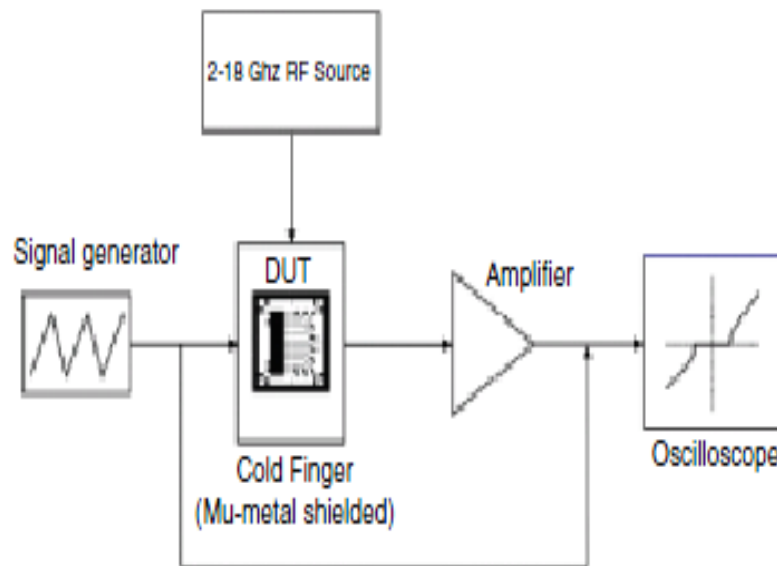


Figure 5 Schematic of the basic test set up for Shapiro steps [11]

Shapiro steps give a positive evidence of the Josephson's effect when they occur. Figure 6 shows the typical steps produced by the constant width nanobridge and those produce by the VTB – Variable Thickness Bridge, by Elkaseh et al [10].

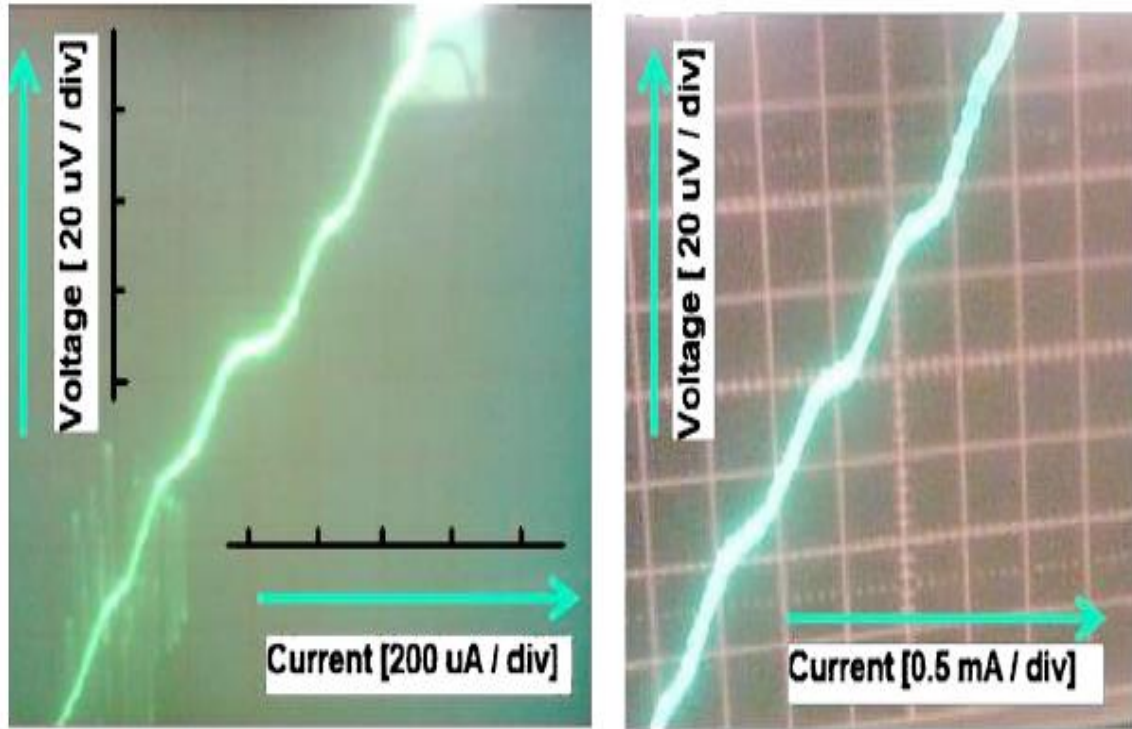


Figure 6 Shapiro steps of a Nanoconstriction and VTB after exposure to 14.427 GHz and 15.383 GHz microwave signal respectively [10].

The formula that can be used to define the step voltages is given below by;

$\left(\frac{e}{h}\right) = n\left(\frac{f_s}{2V_0}\right)$  Where  $e/h$  is the fundamental electronic charge divided by Planck's constant,  $f$  is the microwave frequency,  $V_0$  is the step voltage and  $n$  is an integer.

### 1.6.3 FRAUNHOFER DIFFRACTION PATTERN (DEPENDENCE OF $I_c$ ON THE MAGNETIC FIELD)

When a magnetic field is applied in the plane of a junction a uniform junction would show the famous fraunhofer behaviour shown by the relation in equation (6):

$$I_c \cong \frac{|\sin\left(\frac{\Phi}{\phi_0}\right)|}{\frac{\Phi}{\phi_0}} \quad (6)$$

which would be a true evidence of the Josephson's effect. Here  $\Phi$  is the flux density and  $\phi$  is the flux quantum expressed in Gauss per centimetre square.

For example figure 7 shows the  $I_c$  versus applied magnetic field ( $B$ ) relationship for the nanoconstriction and VTB. In the case of the uniform thickness constriction a good fraunhofer – type diffraction pattern is obtained. This shows the homogeneity of the junction.

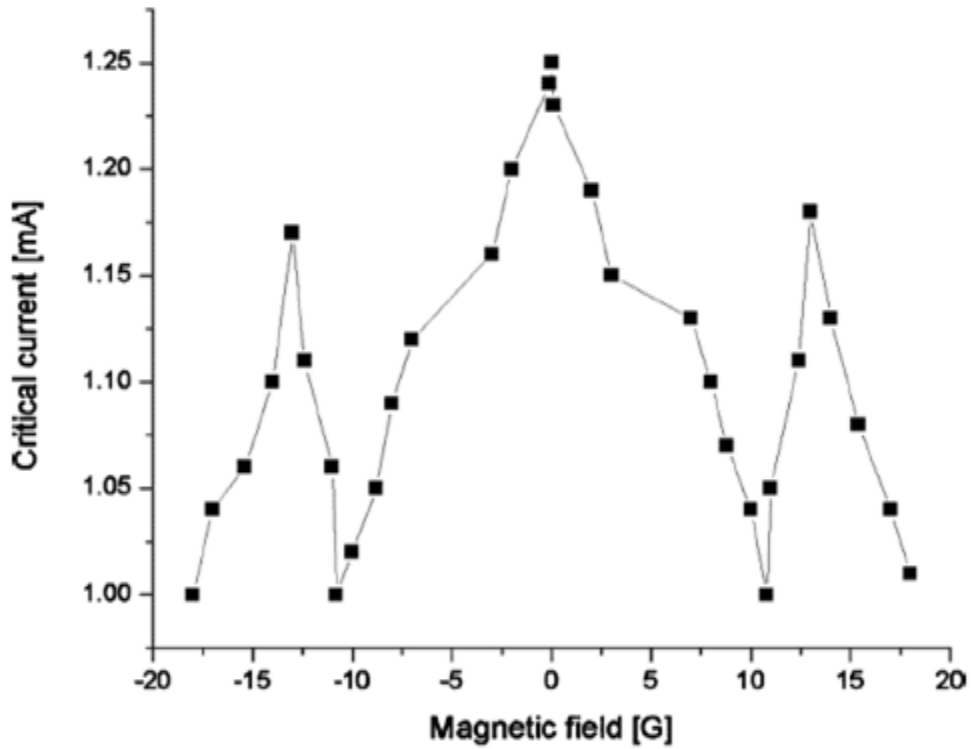


Figure 7 The effect of magnetic field on the critical current of the nanobridge [10]

#### 1.6.4 $I_C$ VS TEMPERATURE DATA

In a constriction, type Josephson Junction the  $I_C$  Vs temperature Data exhibits straight line behaviour [10] as shown in figure 8.

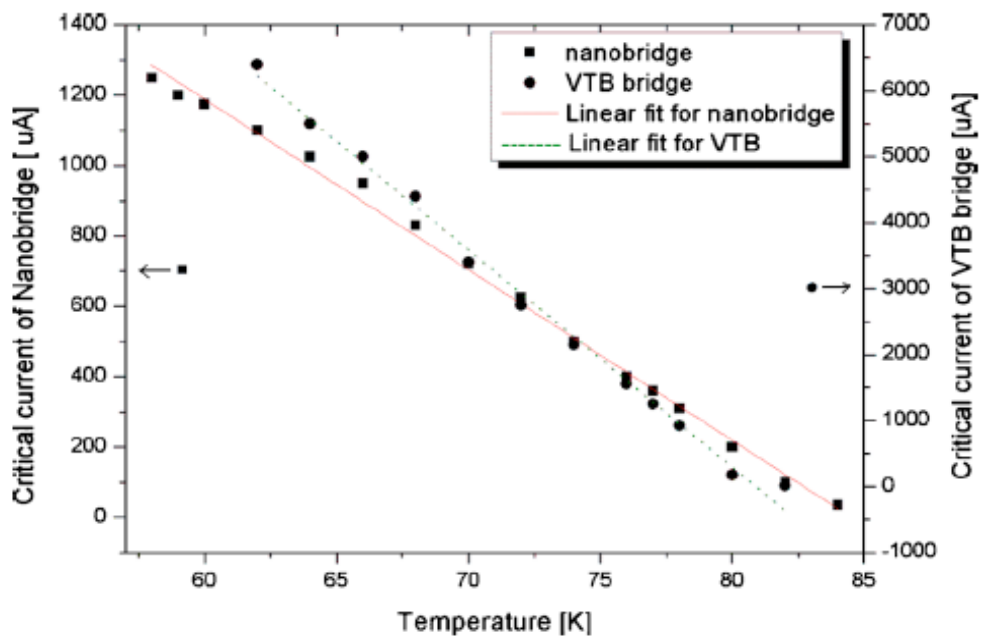


Figure 8 Critical current Vs Temperature of Nanoconstriction and VTB Bridge with linear fit [10]

$I_C$  Versus  $T$  data is also important to understand the constriction type JJ's behaviour. We will be doing detailed measurements of  $I_C$  versus  $T$  on our fabricated JJ's.

## **1.7 METHODS OF FABRICATING JOSEPHSON JUNCTIONS**

Many methods have been utilized in the past to fabricate Josephson Junctions some of which include;

- AFM-Atomic Force Microscopy [10],[14]
- Sample mosaic navigation assisted Laser Etching method [11]
- Focused ion beam (FIB) [15],[16]
- Phase separation technique [17],[18]

Most of these methods mentioned utilise a bit of thermal heat to cut or etch away the unwanted materials when fabricating the junctions such that a certain amount of thermal heating occurs at the junction hence the heating changes the temperature of the material and makes it normal in some sections rather than a homogenous superconducting material. This would make the flow of electrons across a normal material not a superconducting one and hence we may not have the Josephson effect. Briefly describing some of the methods already listed above in the following sections:

### **1.7.1 AFM – ATOMIC FORCE MICROSCOPY**

Atomic force microscopy (AFM) can be used as a lithography tool, to produce nanoconstrictions of width say 492 nm, length 660 nm and thickness of film 100 nm [10].

In the paper mentioned above the method was used to fabricate a constant thickness bridge and a variable thickness bridge (VTB). Subsequently properties such as I-V measurements, Shapiro steps and magnetic influence on the critical current were extracted from the junctions.

The method involves using 100-120 nm thin films of YBCO grown on MgO substrate by inverted magnetron sputtering. The surface roughness is about 6 nm. The measured  $T_C$  is about 92 K. The YBCO thin films are patterned into 8-10  $\mu\text{m}$  width micro strips using argon milling.

Subsequently “The tip of the AFM is vertically displaced on the YBCO surface with a loading of 11  $\mu\text{N}$ . To obtain a constriction width  $W$ , the tip is placed at the centre of the stripling it’s then displaced by  $W/2$  to the left side on the strip line. It is then driven into the YBCO film surface and ploughed on the same line until the left edge is reached” [10]. The process is repeated back and forth several hundred times. The tip velocity is about 4  $\mu\text{m/s}$ . The same ploughing process is done on the right side.

Figure 9 shows the constant thickness nano bridge produced using the AFM technique. The width of the junction can be seen in figure 10 and is about 492 nm.

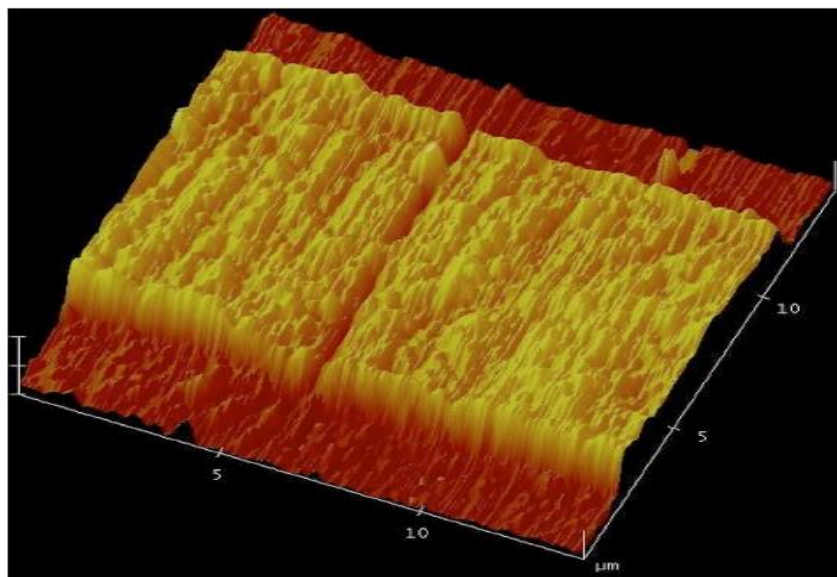


Figure 9 3D AFM image of a nano bridge [10]

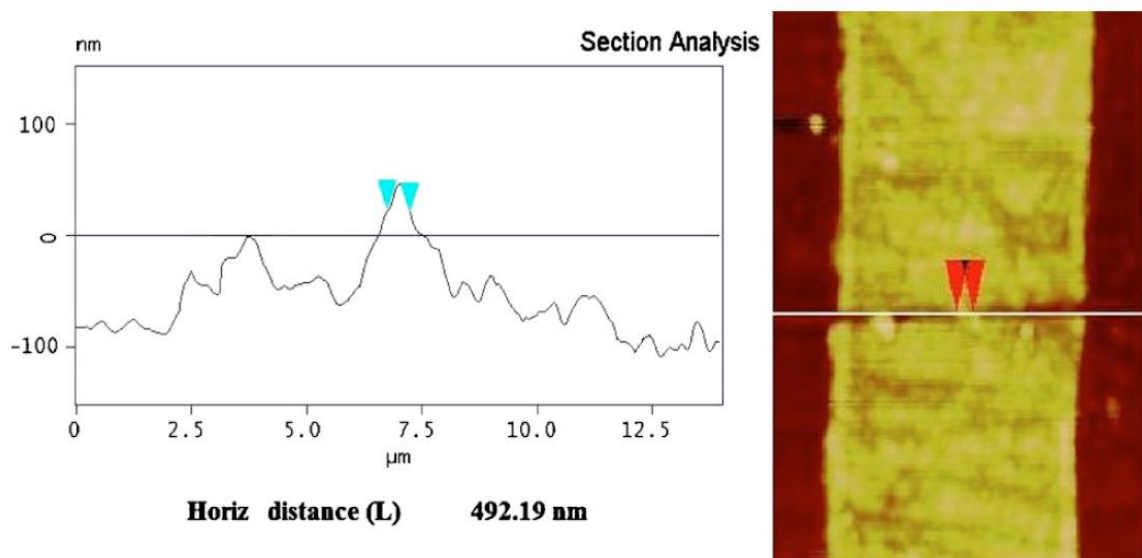


Figure 10 AFM top view of the nano bridge or nano constriction. The horizontal distance between the marks in the profile defines the width of the constriction as 492.19 nm [10]

### 1.7.2 SAMPLE MOSAIC NAVIGATION ASSISTED LASER ETCHING METHOD.

The laser method involves making use of a new wave 213 nm laser system [11], equipped with high-precision submicron resolution sample mosaic navigation system. This is used to laser etch and fabricate planar submicron-size Josephson junctions on YBCO thin films. The widths are measured by atomic force microscopy (AFM) and they are about 0.7 to 1.4  $\mu\text{m}$ . In the case of micron-sized junctions the measured critical current dependence on temperature is a linear relationship, whilst for submicron constrictions the dependence is an exponential decay type. This is consistent with diffusive long S-N-S junction behaviour. It is believed that the observed behaviour can be ascribed to laser heating of the constriction material changing the superconducting phase to a normal one. This is something we assume will not occur when the femtosecond laser will be used to fabricate the sub-micron sized junctions.

The laser etching method can be used to fabricate High  $T_c$  superconducting (HTS) Josephson junctions.

“Inverse cylindrical magnetron (ICM) sputtering is used to deposit 150 nm thick YBCO films on MgO. The surface roughness as measured using atomic force microscopy (AFM) is approximately 9nm. The film is patterned into 4-10  $\mu\text{m}$  strips by argon-ion milling. Using the new wave 213 nm laser system with submicron resolution the laser beam is guided from the edges of the each YBCO strips, ablating and etching from both sides of the edges [11]. The constrictions are washed in an ultrasonic bath of acetone in order to remove the re-deposited material. The laser beam movement rate is about 5  $\mu\text{m s}^{-1}$ .

Figure 11 shows the Josephson junctions produce using this method at micron and submicron sizes.

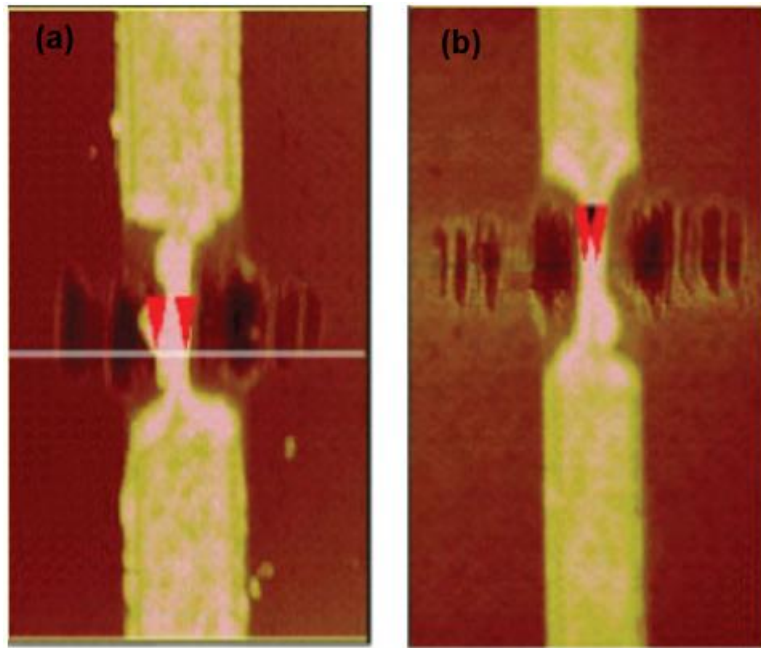


Figure 11 (a) AFM picture of a laser-etched constriction width 1.64  $\mu\text{m}$  (b) submicron constriction width is 703 nm [11]

As the constriction size decreases from micron to submicron level using this method, the laser due to excessive local heating, changes the YBCO phase in the constriction region into a non-superconducting normal phase. The constriction becomes an S-N-S junction as a result not a Josephson junction.

### 1.7.3 FOCUSED ION BEAM (FIB) METHOD

This method involves the utilization of electrodes that generate an ion beam to cut the material in etching the junctions.

In this method as seen in [19] the Ferromagnetic thin film ( $Pt_{1-x}Ni_x$ ) is deposited on an Nb layer using DC magnetron sputtering. The thickness of the Nb layer is about 225 to 350 nm and the thickness of the Ferromagnetic layer is about 20 to 30 nm. The deposited multilayer is patterned into micro strips using a photolithography tool called Ar<sup>+</sup> milling. The width of the micro strips produced is about 6  $\mu\text{m}$ . “A wedge holder is use to rotate the strips so that they can lie parallel and then perpendicularly to the beam” [19].

Initially the electrodes are used to produce junctions that have a width of 0.5  $\mu\text{m}$ , then when they are parallel to the beam the width is reduced to between 80 nm and 300 nm. Figure 12 shows the side view of the junction produced using such a method.

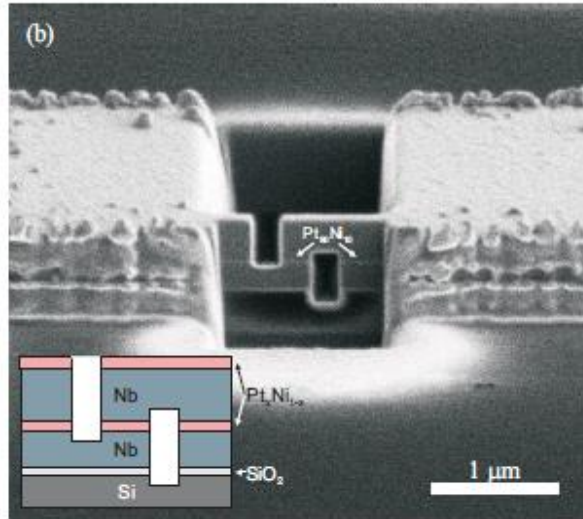


Figure 12 FIB method side view of junction [19]

#### 1.7.4 PHASE SEPARATION METHOD

When the junction size is reduced it puts severe limit retaining its superconductive properties. In this method, the junctions are realized by using the biepitaxial grain boundary technique [20]. This involves producing an interface between YBCO thin film with a [001] grain orientation and a YBCO thin film with a [103] grain orientation subsequently a YBCO thin film which is an insulating phase is introduced during the thin film growth. The competition between the superconductive and insulating phases during thin film growth produces the junctions. Figure 13 shows the interface produced between the [001] and the [103] YBCO thin films with the insulation growth that produces the junction whilst figure 14 shows a nanosquid produced from two junctions whilst the 3<sup>rd</sup> junction is removed by the FIB technique.

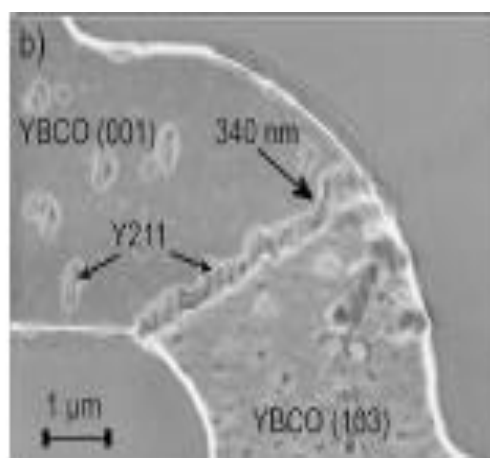


Figure 13 Interface between [001] and [103] YBCO thin films and an insulative growth Y211 [20]

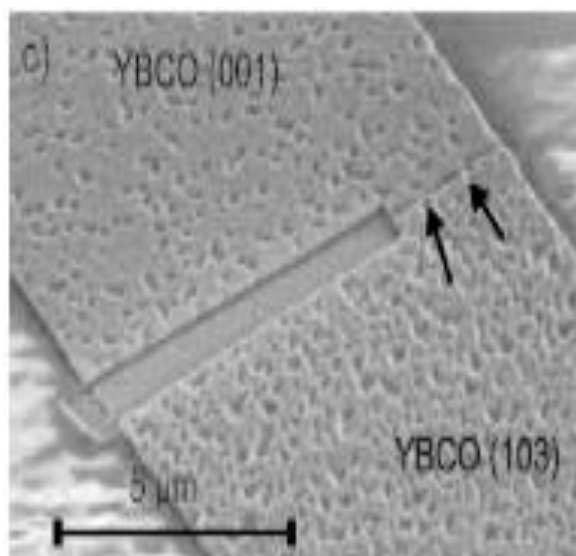


Figure 14 nanoSQUID with a junction removed by FIB [20]

Using this method also eliminates thermal heating in making the junctions. The junction width is about 185 nm to 275 nm. Figure 15 shows the I-V characteristic obtained from this method. The knee of the curves does not show much rounding rather it is a sharp corner which shows that Josephson junctions are produced without heating.

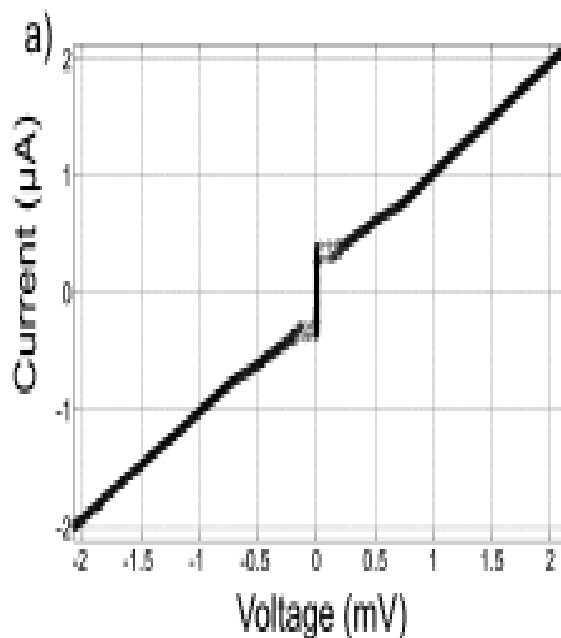


Figure 15 current voltage characteristics (I-V) for a sample produced by soft nano-patterning width of 100 nm [20]

### **1.7.5 FEMTOSECOND LASER**

The definition of LASER is “Light Amplification by Stimulated Emission of Radiation”. This method uses ultra-fast pulses of a pulse duration of up to  $130 \times 10^{-15} \text{ s}$  that is 130 femtoseconds. The short duration pulses may allow easy manufacture of junctions in the order of nanometres without thermal heating of the constriction, which makes the constriction normal. The femtosecond laser etches away the material at the constriction without applying thermal energy like most of the other methods.

#### **1.7.5.1 DETAILS OF FEMTOSECOND LASER**

“Drilling or machining of holes and channels in the low micrometer regime in various materials is of interest in many research and industrial applications. Precision femtosecond laser micro machining has been widely demonstrated to produce minimal thermal damage to the work piece material, the ability to produce very small spot sizes and allows removal rates of tens to hundreds of nanometres depth per pulse. This kind of precision can be very useful in removal of thin layers, drilling small features or producing well-defined small structures. “The ablation process results in minimal melting and therefore even plastics can be processed” using this method [21]. As a result of this the femtosecond laser would be used to cut small constrictions on YBCO thin films that would later be used to prove the presence of the Josephson effect.

## **1.8 SCHEDULED ACTIVITY/PLAN FOLLOWED**

Scheduled activity would involve etching the Josephson nanoconstrictions on the YBCO thin films at the CSIR, national laser facility. Subsequently measurements will be taken from the junctions such as I-V, C-V characteristics at the applied physics laboratories at UNISA and at CSIRO research centre at Lindfield Australia.

Comparison would be made between the properties of junction made using the femtosecond laser to junctions fabricated by other methods such as AFM.

In addition, the influence of a magnetic field on the junction will also be taken into consideration. Table 1 below gives a summary of the scheduled activity for the PhD work.

Table 1 Scheduled Activity for PhD Work.

Activity	Time period	Details
<b>PhD Registration</b>		
<ul style="list-style-type: none"> <li>• <b>PhD registration</b></li> </ul>	End of 2011	<ul style="list-style-type: none"> <li>• Completed</li> </ul>
<b>Proposal Writing</b>		
<ul style="list-style-type: none"> <li>• <b>Proposal writing</b></li> <li>• <b>Literature review</b></li> </ul>	2012	<ul style="list-style-type: none"> <li>• Proposal writing.(DPSET04)</li> <li>• Literature review</li> </ul>
<ul style="list-style-type: none"> <li>• <b>Oral presentation proposal defence</b></li> </ul>	Beginning 2013	Registered for PhD thesis. (TPHY01).
<b>Methodology, Field Work Data collection</b>		
<ul style="list-style-type: none"> <li>• <b>Femtosecond laser work at CSIR</b></li> </ul>	September 2013-December 2013	<ul style="list-style-type: none"> <li>• Etching of Micros trip lines using femtosecond laser on metal. Prototype testing of G-code program for cutting constrictions.</li> </ul>
<ul style="list-style-type: none"> <li>• <b>Femtosecond laser work at CSIR, Pretoria</b></li> </ul>	February 2014-December 2014	<ul style="list-style-type: none"> <li>• Re-registered for PhD thesis</li> <li>• International Conference presentation based on femtosecond laser work in India GESM 2014.</li> <li>• Beam shaping of the femtosecond laser. NANO constriction Fabrication.</li> <li>• Femtosecond laser ablation of constriction type Josephson Junctions at CSIR Pretoria on YBCO thin films.</li> </ul>
<ul style="list-style-type: none"> <li>• <b>CSIRO Research facility Lindfield Australia</b></li> <li>• I-V measurements at 77K in Liquid nitrogen</li> <li>• Shapiro steps measurements in Helium gas</li> <li>• Magnetic field measurements.</li> </ul>	August –October 2015	<ul style="list-style-type: none"> <li>• I-V measurements on constrictions made.</li> <li>• Junction analysis</li> <li>• SEM imaging.</li> <li>• Shapiro step measurements at CSIRO Lindfield research centre in Australia.</li> </ul>
<b>Results and Analysis</b>		
<ul style="list-style-type: none"> <li>• <b>Journal publications</b></li> </ul>	January 2016 –December 2016	<ul style="list-style-type: none"> <li>• Written five articles on the fabrication process and results.</li> <li>• Poster presentation at conference ICSM 2016, April 2016, Fethiye, Turkey.</li> <li>• Published one article on the fabrication process of constrictions in the Journal of material science;materials in electronics (first online December 2016).</li> </ul>
<b>Conclusion</b>		
<ul style="list-style-type: none"> <li>• <b>Thesis Write-up</b></li> </ul>	2017	<ul style="list-style-type: none"> <li>• Write-up and compile Thesis report.</li> <li>• Published second article in the journal of superconductivity and novel magnetism on the Josephson Effect. (First online October 2017)</li> </ul>

## 1.9 REFERENCES

- [1] Josephson's Junctions –Wikipedia the free encyclopaedia.
- [2] Donald G. McDonald, Robert L. Peterson, Clark A. Hamilton, Richard E. Harris and Richard L. Kauz, "Picosecond Applications of Josephson's Junctions", IEEE Transactions On Electron Devices, Vol. Ed-27, No.10, October 1980.
- [3] D.V Averin, "Quantum Computing and Quantum Measurement with Mesoscopic Josephson Junctions", Department of Physics and Astronomy, SUNY at Stony Brook, February 1, 2008.
- [4] Theodore Van Duzer, Charles W. Turner, "Principles of Superconductive Devices and Circuits, Second Edition", Book, 15th August 2002.
- [5] Di Iorio, M. S. Yoshizumi, S. Yang, K-Y. Zhang, J. Maung, M. "Practical high Tc Josephson junctions and dc SQUIDs operating above 85 K," Applied Physics Letters, vol.58, no.22, pp.2552-2554, Jun 1991.
- [6] R. Gross, P. Chaudhari. D. Dimos, A. Gupta, and G. Koren, "Thermally Activated Phase Slippage in High-  $T_c$  Grain-Boundary Josephson's Junctions", physical review Letters Volume 64, Number 2, 8<sup>th</sup> January 1990.
- [7] John Macfarlane, "Superconductivity at CSIRO (Sydney) 1969 – 2009, Australian Physics, Volume 47, Number 2, March/April 2010.
- [8] Book Chapter, K.K Likharev, "Superconducting weak links", American Physical Society, 1979.
- [9] H. Hayakawa, Eds. Steven, T. Ruggiero and David A. Rudman, "Superconducting Devices", Academic Press, INC, (1990) 103.
- [10] A. A. O Elkaseh, W.J Perold, and V.V Srinivasu, "Josephson nanoconstrictions made by AFM plowing of  $\text{YBa}_2\text{Cu}_3\text{O}_{7-x}$  films", Journal of Applied Physics 108,053914, 14<sup>th</sup> September 2010.
- [11] U Buttner, G L Hardie, R Rossouw, V V Srinivasu and W J Perold, "Fabrication of Submicron YBCO Josephson junctions by a sample mosaic

navigation assisted laser etching process”, Superconductor Science and Technology 20, S426-S429, 18<sup>th</sup> October 2007.

- [12] I. Barbooy *et al.*, “Micro-Raman spectroscopy of laser processed YBa<sub>2</sub>Cu<sub>3</sub>O<sub>7- $\delta$</sub>  thin films” J. Appl. Phys. **110**, 033912 (2011).
- [13] A. Jukna *et al.*, “Laser processed channels of easy vortex motion in YBa<sub>2</sub>Cu<sub>3</sub>O<sub>7- $\delta$</sub>  films” Appl. Phys. Letter, **87**, 192504 (2005).
- [14] Song Insang, Kim Byong Man, Park Gwangseo, “Fabrication of a Josephson’s junction using an Atomic Force Microscope”, Applied Physics Letters, Volume 76, issue 5, 2000.
- [15] J.C Macfarlane, J.C Gallop, D. Cox, J. Beyer, D. Drung, T. Schurig, “Measurement And noise Performance of Nano-superconducting-Quantum-Interference devices fabricated by Focused Ion Beam”, Applied Physics letters, Volume 92, Issue 19, pp 192507-192507-3, May 2008.
- [16] V.M. Krasnov, O. Ericsson, S. Intiso, P. Delsing, V.A. Oboznov, A.S. Prokofiev, V.V. Ryazanov, “Planar S–F–S Josephson junctions made by focused ion beam etching”, Physica C: Superconductivity, Volume 418, Issues 1–2, 15 January 2005, Pages 16-22, ISSN 0921-4534.
- [17] Shi Y, Hasan T, Babu NH, Torrisi F, Milana S, Ferrari AC, Cardwell DA, “Synthesis of YBa<sub>2</sub>Cu<sub>3</sub>O(7- $\delta$ ) and Y<sub>2</sub>BaCuO<sub>5</sub> nanocrystalline powders for YBCO superconductors using carbon nanotube templates”, ACS Nano.,6(6), 5395-403, 26<sup>th</sup> June 2012.
- [18] Klie RF, Buban JP, Varela M, Franceschetti A, Jooss C, Zhu Y, Browning ND, Pantelides ST, Pennycook SJ, “Enhanced current transport at grain boundaries in high-T(c) superconductors”, Nature, 435(7041), 475-478, 26<sup>th</sup> May 2005.
- [19] T.Golod, H. Frederiksen and V.M Krasnov, “Nb-PtNi-Nb Josephson’s Junctions Made by 3D FIB Nano-Sculpturing”, Journal of Physics: Conference Series 150 (2009) 052062.

- [20] D. Gustafsson, H. Petterson, B. Iandolo, E. Olsson, T. Bauch and F. Lombardi, "Soft Nanostructuring of YBCO Josephson's Junctions by Phase Separation", *NANO letters*, 10, 4824-4829, November 2010.
- [21] a du Plessis, J Steyn, H Burger, M Theron, LR botha, "Precision femtosecond laser micro machining: a new facility for South Africa", CSIR National laser Centre, 2012.

# CHAPTER 2

## MATERIALS AND METHODOLOGY

### 2.1 INTRODUCTION

The main steps in the methodology component of the PhD work include the following:

1. Dry etching of micro strip lines to separate one constriction from another this is done by using the femtosecond laser to etch away the micro strips.
2. Fabricating micron, sub-micron and nano sized S-shaped constrictions using the femtosecond laser.
3. Atomic Force Microscopy (AFM), scanning electron microscopy (SEM), optical microscopy (OM) – using these facilities to take images of the resulting constrictions to establish the dimensions of the Josephson junctions made.
4. Using the I-V system rack, SQUID software instruments, DC voltage meter, DC current source, RF signal generator at CSIRO, Lindfield, Australia to take I-V measurements, Shapiro steps and fraunhofer diffraction pattern to establish the presence of Josephson junctions on the constrictions fabricated.

### 2.2 YBCO THIN FILMS

The YBCO thin films were procured from Ceraco ceramic company GmbH. The YBCO superconductive thin films procured had the following specifications. Each thin film had a dimension of 10 mm X 10 mm X 0.5 mm. Of these 12 thin films came on an LAO substrate and the other 12 thin films were procured on an MgO substrate. The thin films had only one side polished with YBCO on the substrate. It is a single sided YBCO thin film with the thickness of the YBCO being 200 nm (0.2  $\mu\text{m}$ ) on the surface the rest is the substrate 499.8  $\mu\text{m}$ . On the surface, the dimension of the YBCO superconductive material is 9 mm X 9 mm. Figure 16 shows the cost of purchasing the YBCO thin films used and their specifications.

<b>INVOICE</b>			
Qty	Description	Unit Price EUR	Ext. Price EUR
12	9×9 mm YBCO film, single sided 200 nm, S-type, on 10x10x0,5 mm LaAlO <sub>3</sub> substrate, one side polished	97.00	1,164.00
12	9×9 mm YBCO film, single sided 200 nm, S-type, on 10x10x0,5 mm MgO substrate, one side polished	104.00	1,248.00
	Packaging, shipping, insurance	120.00	120.00
<b>Total</b>		<b>EUR</b>	<b>2,532.00</b>

Figure 16 Specifications of the superconductive YBCO thin films procured from ceraco and the cost as at 2014.

The thin films chosen are the S-type smooth matrix useful for the manufacture of SQUIDS. The critical temperature of the YBCO thin film used is  $T_c = 87$  K which is relatively high.

## 2.2.1 METHOD USED TO FABRICATE THE YBCO THIN FILMS.

### 2.2.1.1 THERMAL REACTIVE CO-EVAPORATION

In this case the YBCO thin films used for the project were fabricated by using the thermal reactive co-evaporation technique. This technique can be achieved by using two setups. The first set up involves intermittent deposition of the material and reaction with oxygen using a heater, which rotates the substrate in and out of an oxygen pocket. In this set up, the substrate is rotated and the oxygen pocket is held in a fixed position. This method allows deposition on substrates that are not very large, for example, substrates on a circular area of 23 cm diameter. This method can be used to increase the productivity rate, by increasing the rate at which samples are moved in and out of the oxygen pocket. However, this leads to a loss of quality. In the second setup and the one that was actually used for our samples. The substrate is held in a fixed position while the oxygen pocket is set in linear reciprocation (rotated). This method can be used for larger substrates that cannot be rotated. It can be used on a square of 20 X 20 cm<sup>2</sup>. In this method both the productivity rate and the quality of the sample produced is enhanced.

## 2.2.2 TEMPERATURE DEPENDENCE OF THE SURFACE ( $R_s(T)$ ) RESISTANCE OF THE YBCO THIN FILMS.

The temperature dependence of the microwave surface resistance for the YBCO thin film used from Ceraco GmbH is depicted in figure 17. The dotted red graph represents the YBCO on LAO substrate that was utilised for the purposes of this PhD. From this graph we can tell that the surface resistance of the YBCO increases to a high resistance in ( $m\Omega$ ) at a critical temperature of about 87 K. Above this temperature the YBCO ceases to be superconductive.

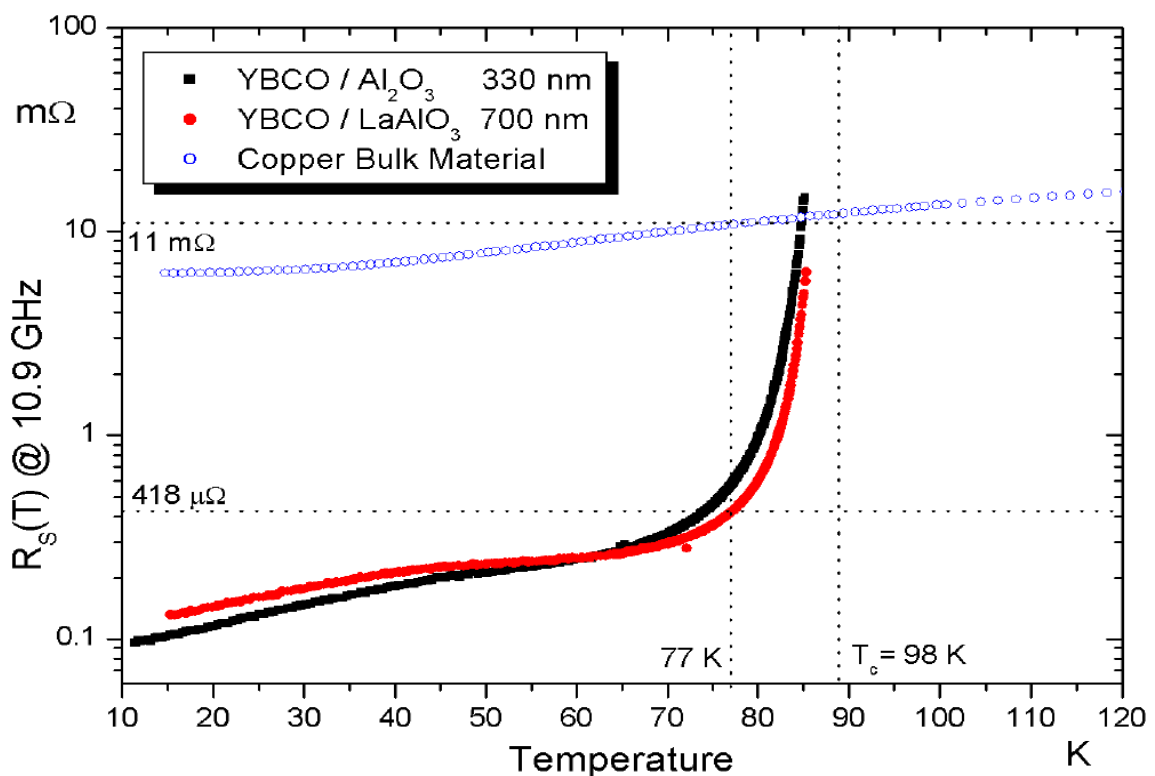


Figure 17 Temperature dependence of the microwave surface resistance at 10.9 GHz of the YBCO thin films.

## 2.3 THE FEMTOSECOND LASER

The definition of LASER is “Light Amplification by Stimulated Emission of Radiation”. The femtosecond laser is a laser that has a low pulse duration in the range of femtoseconds specifically in this case 130 fs. The wavelength of the laser is 775 nm, the power output ranges from (0 - 1000 mW) and the pulse repetition rate ranges from (1 – 2 kHz).

## 2.4 MAIN COMPONENTS OF THE FEMTOSECOND LASER

The Main components of the femtosecond laser are the ErF/SErF fiber oscillator, the Ti:Sapphire regenerative amplifier and the frequency-doubled Nd:YAG diode pump laser, extracted from [1].

### 2.4.1 SErF™ FIBER LASER OPERARTION

The femtosecond laser (SErF™) is based on the fiber ring “Stretched Pulse” laser developed at MIT by the group of Professors E.P. Ippen and H.A Haus. The basic design is that of a unidirectional, polarization rotation additively pulse mode-locked (APM) fiber laser which uses Erbium doped fiber (ErF) as the gain medium. The output wavelength of the femtosecond laser (SErF) is centered on 775 nm. The system is designed to provide hands-off performance once it has been set up in a standard optics laboratory environment. The pump source for the laser is an all solid-state fiber-coupled laser diode (Nd:YAG diode) operating at approximately 980 nm.

The femtosecond laser (SErF) contains the following components:

1. A laser diode and associated control electronics.
2. An active fiber ring laser.
3. Some bulk optics used for polarization control, output coupling and wavelength control.
4. A compressor to eliminate residual dispersion of the output pulses.
5. A temperature-stabilized periodically poled lithium niobate (PPLN) frequency doubler.

These components are summarized in figure 18;

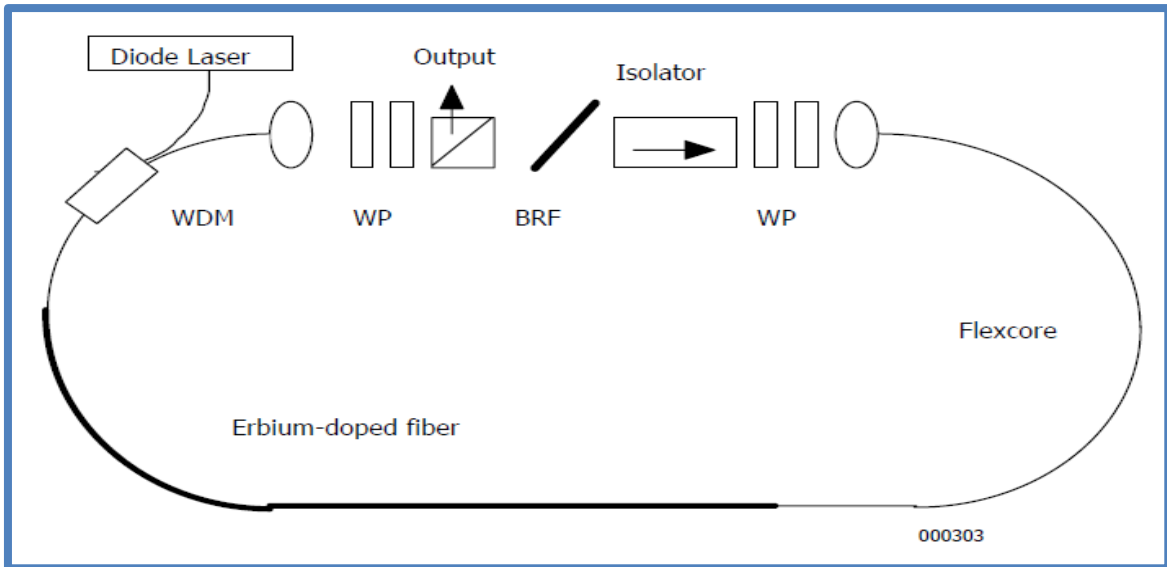


Figure 18 The schematic of the laser fiber oscillator.

### 2.4.2 ND : YAG PUMP LASER DIODE

This component acts as the source of the laser light. The crystalline wave guiding material which forms the active medium for this part of the laser is yttrium-aluminium-garnet ( $Y_3Al_5O_{12}$ ) doped with the rare earth metal ion neodymium ( $Nd^{3+}$ ) to form the Nd:YAG structure as described in [2]. There is also a  $AlGaAs$  LED Diode used to generate light to pump the  $Nd$  ions out of the YAG material. These ions collide with the surface to generate light energy that passes through the (SErF) fiber oscillator, which acts as the gain medium. The sketch of the Nd : YAG Pump laser diode can be seen in figure 19.

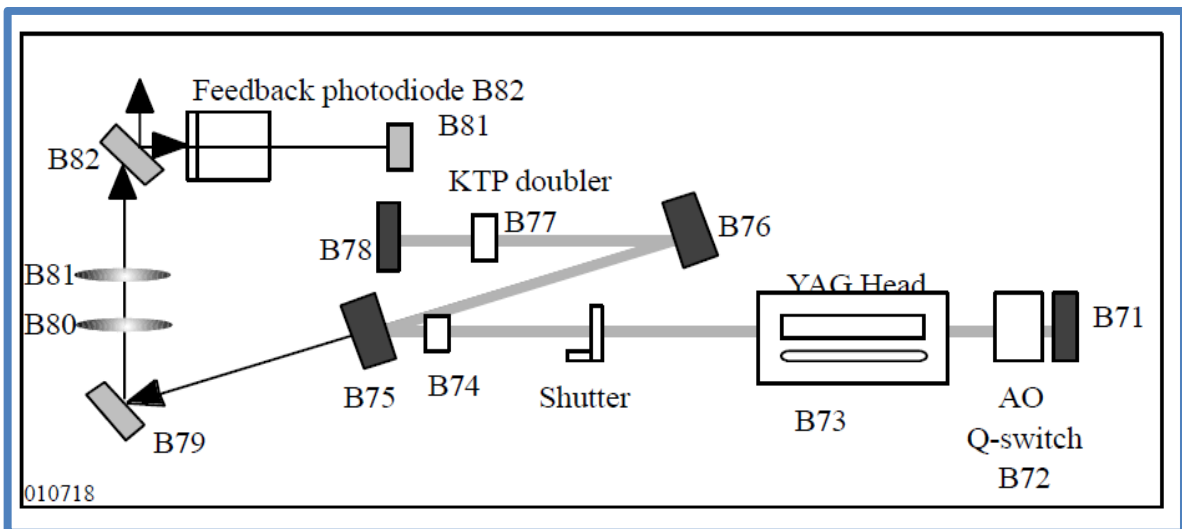


Figure 19 View of the laser YAG head structure and pump diode.

### 2.4.3 TI : SAPPHIRE AMPLIFIER

This component is an amplifier that re-generates the laser light emitted and coming from the fibre oscillator. The regenerative amplifier was factory aligned. It should not require any realignment after installation with the following exceptions:

- Optimization of the timing
- Optimization of the seed injection

The sketch in figure 20 shows the Ti:Sapphire Amplifier.

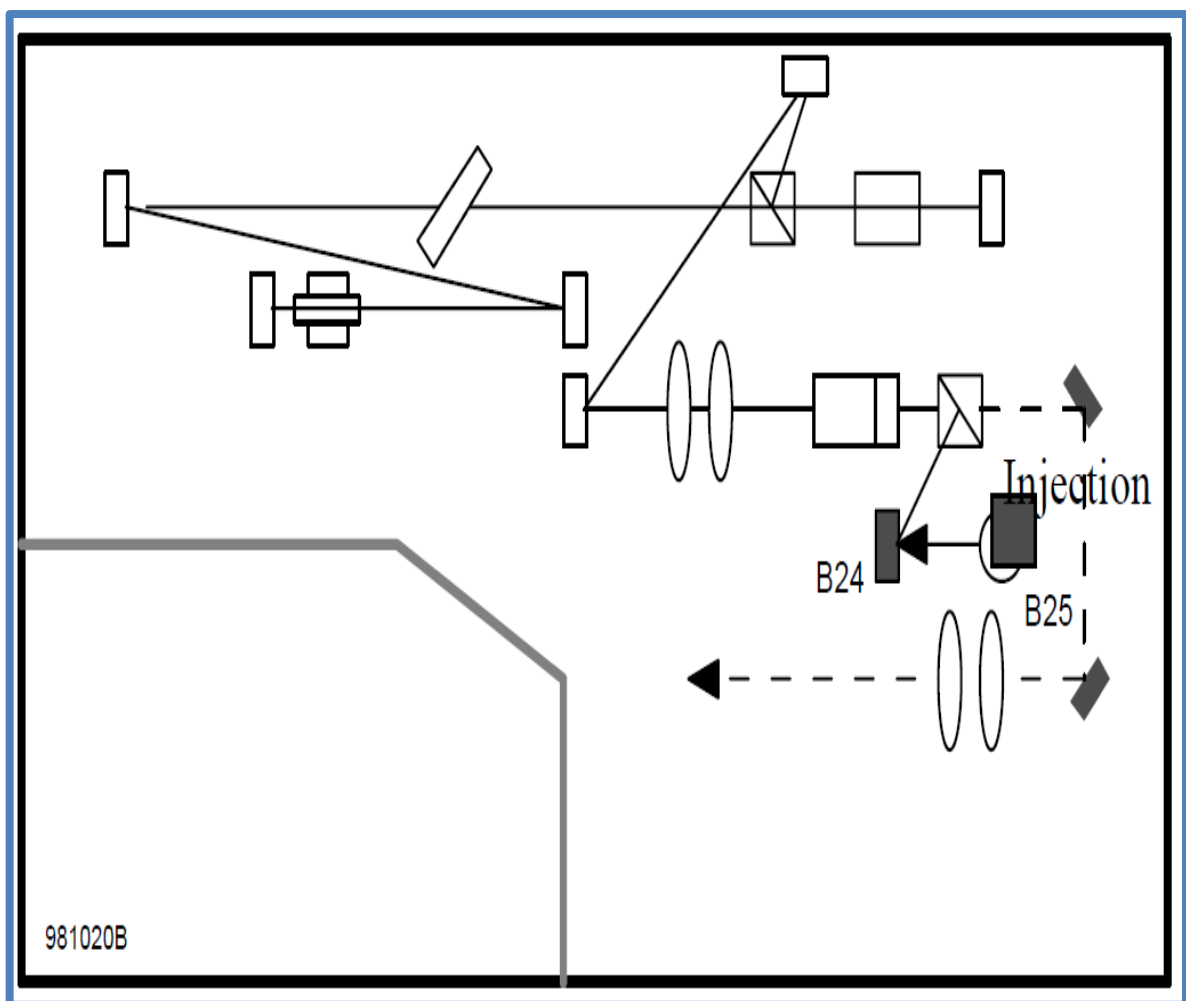


Figure 20 regenerative amplifier

The Laser beam width coming from the output of the amplifier is approximately  $9850 \mu\text{m}$  (9.85 mm).

## 2.5 THE OPERATION OF THE MAIN COMPONENTS OF THE FEMTOSECOND LASER

### 2.5.1 LASER LAMP (PUMP DIODE LASER AND THE ERBIUM DOPED FIBER)

The laser generation part is where the laser is produced and the power of the laser is generated. Essentially the laser lamp (pump diode laser and erbium-doped fiber) lies here. The lamp current can be controlled in this section from the pump laser control console.

As can be seen from figure 21 the laser lamp (pump diode) lies in this box. The lamp current can be seen to be 28 A and can be controlled from the pump laser control console shown in figure 22.



Figure 21 Laser Source (Pump diode)

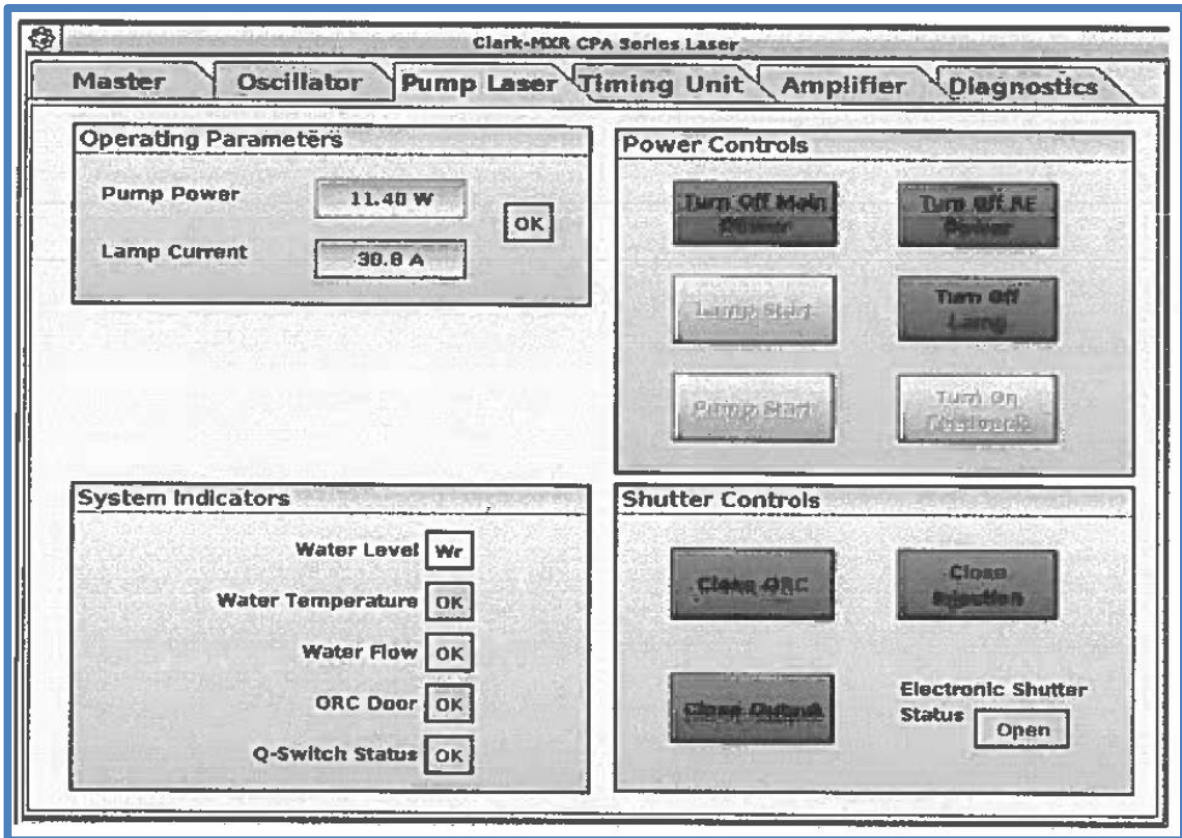


Figure 22 Pump laser control console for regulating lamp current

The pump laser interface or control console centre shown in figure 22 can be used to regulate the lamp current, which should be gradually stepped up but should not exceed 30 A. The laser lamp power should not exceed about 8 W. These settings are deemed necessary to prevent the lamp from burning after a short period. If the lamp is consistently kept at a lamp current of 30 A it quickly burns out. Therefore, the lamp current should be kept steady at about 28 A.

In addition, this interface shows the system indicators if the water temperature is fine or not circulating around the lamp current. This would give a red warning light if something is wrong.

In the re-generative amplifier section seen in figure 23 the power of the laser is amplified by a Ti:Sapphire amplifier before being guided out of the box. The oscilloscopes are used to indicate if the laser pulse has the right amplification (peak power) and to show the laser profile shape. Subsequently the laser beam is manually released by using the black shutter before being utilized for machining.

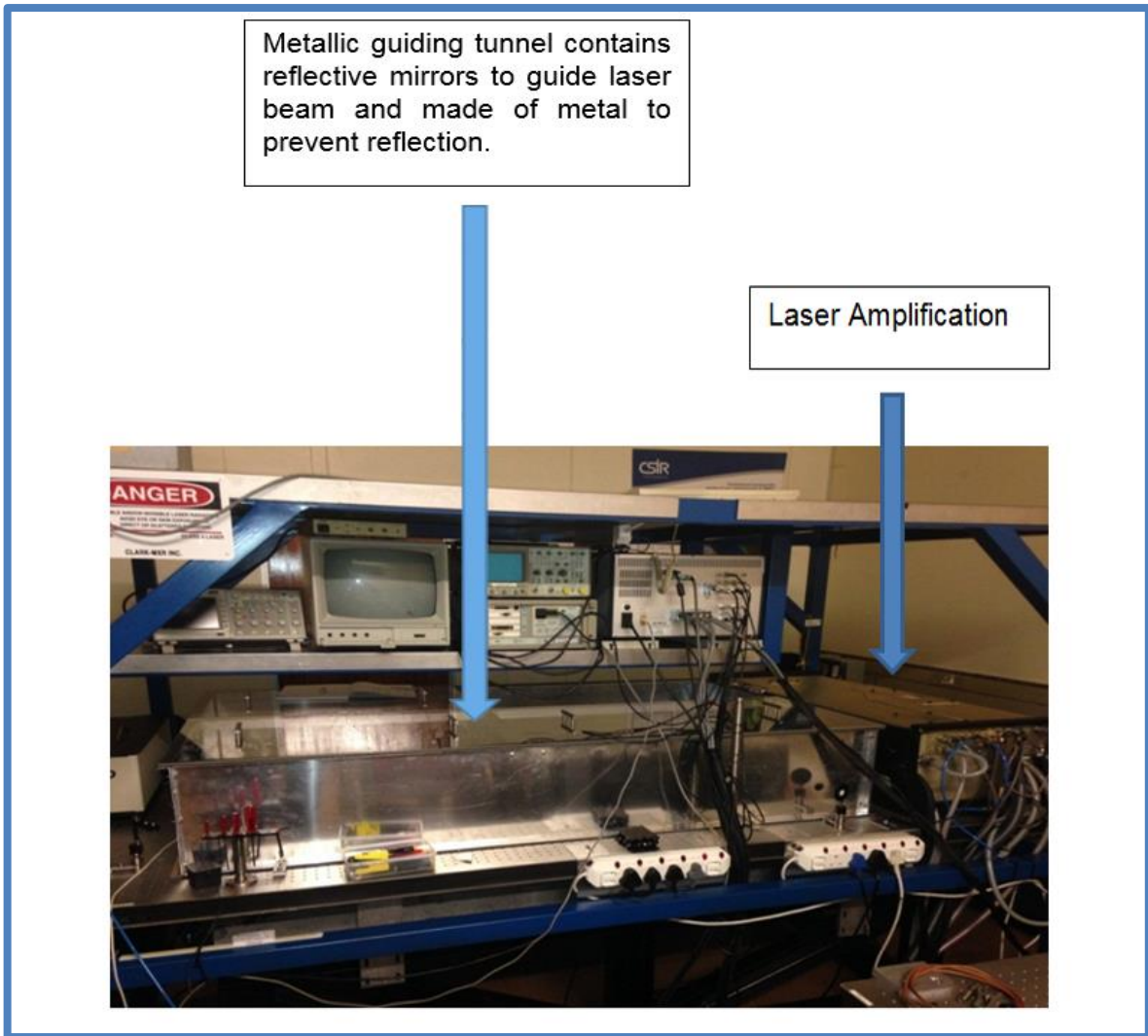


Figure 23 laser amplification section

### 2.5.2 SWITCHING THE LASER ON AND OFF

In figure 24 below one can see the Master control console used to stop and start the system. It also allows one to set the power output of the laser from approximately 0 mW up to a power output of 1 W or 1000 mW. The pulse repetition rate can also be set using this interface from 1 – 2 kHz.

There is a button to open the electronic shutter for the laser, such that the laser beam can be released. This electronic shutter is regulated by pressing the “close output switch”.

Finally, the interface shows the status of the lasers individual components such as the pump laser, the amplifier, the system status if they are okay or not. If one of the components is not okay the system gives a warning with a red light on the system indicator.

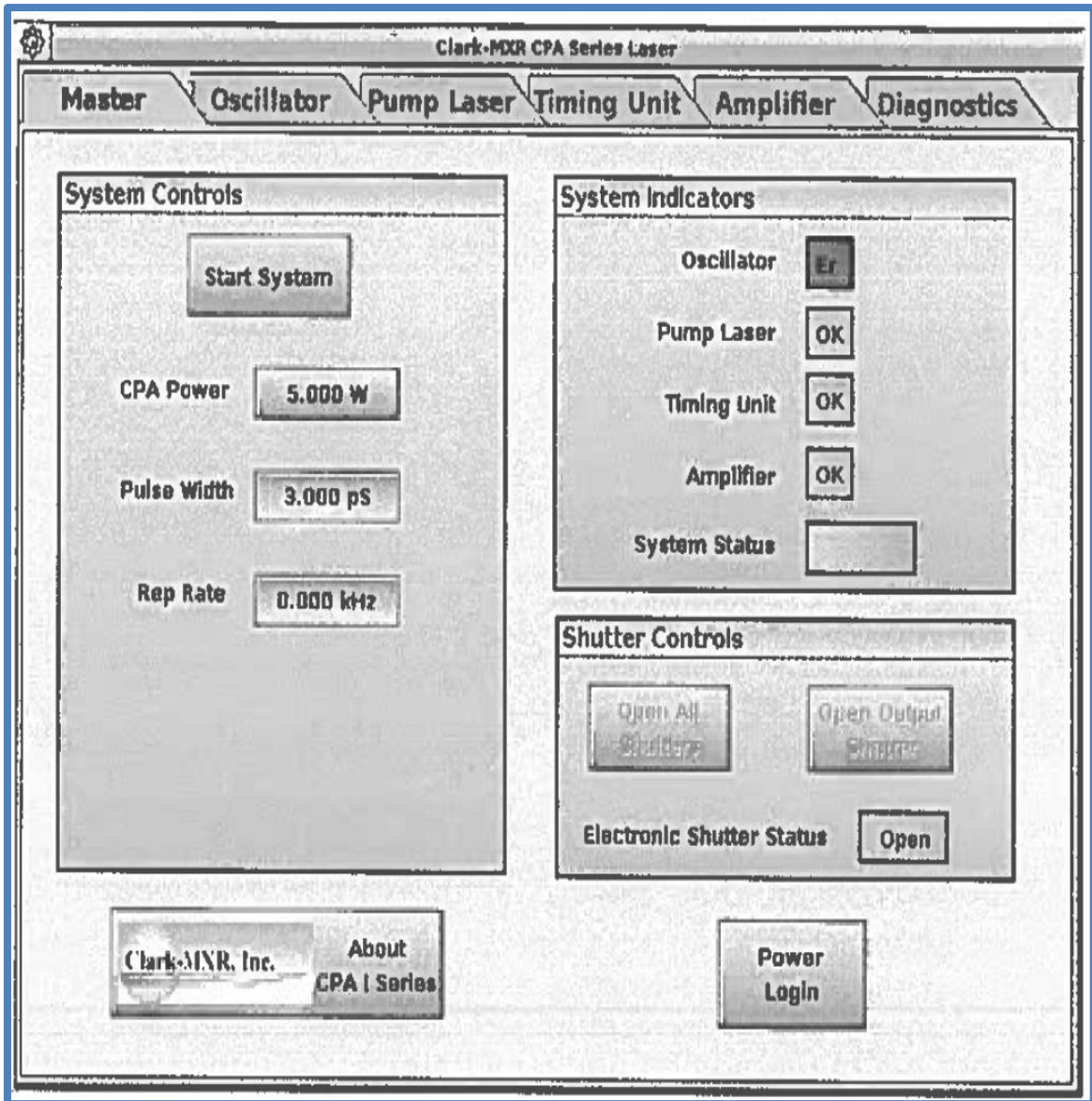


Figure 24 Master control console for Switching the laser ON/OFF.

### 2.5.3 TIMING CONSOLE

The timing console has 3 delay controls, Delay 1, Delay 2 and Delay 3, the values are in hexadecimal. These delay switches can be manipulated to achieve a phase lock between the master (pump diode laser) and the fibre oscillator frequency. When this occurs then the maximum power will be released from the laser source. Such that when the output power is set to 1000 mW it will release precisely that. The timing console can be seen in figure 25;

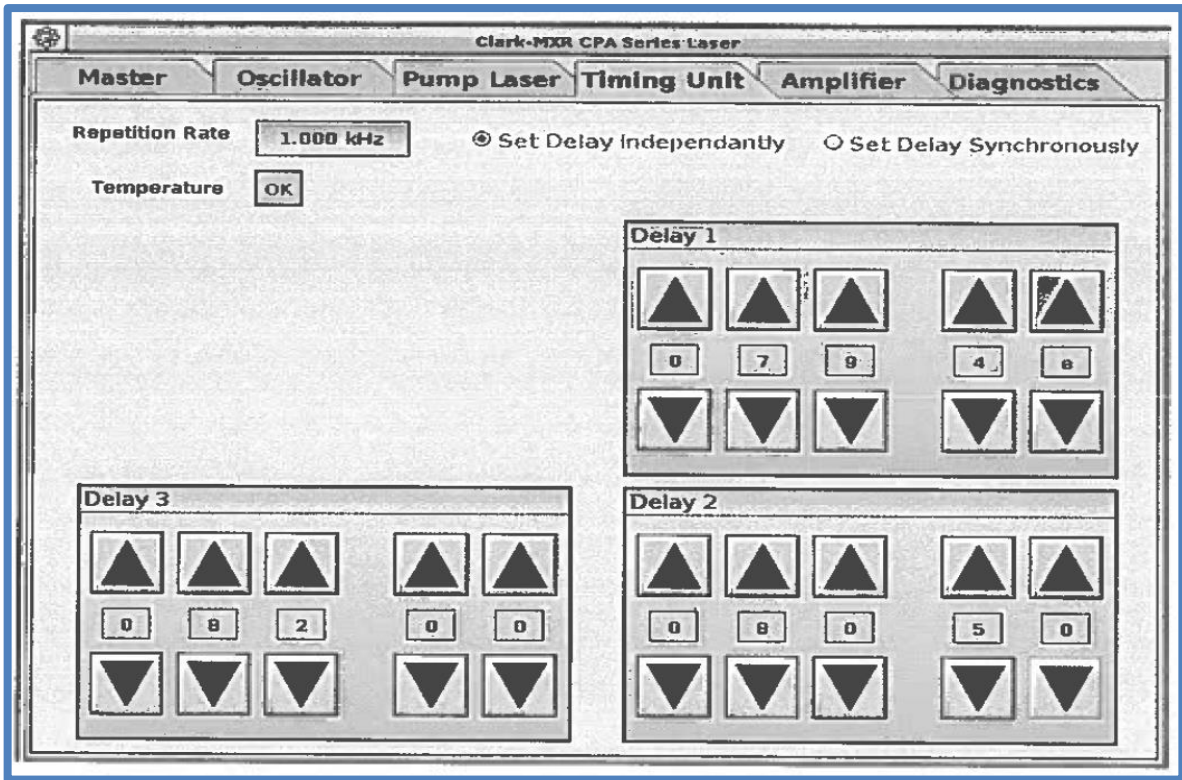


Figure 25 Timing Console

In order to determine if a lock is achieved or the right power is being released from the laser, you need to look at the laser profile or distribution curve on the oscilloscope connected to the laser source. This can be seen in figure 26.



Figure 26 Laser profile distribution on oscilloscope.

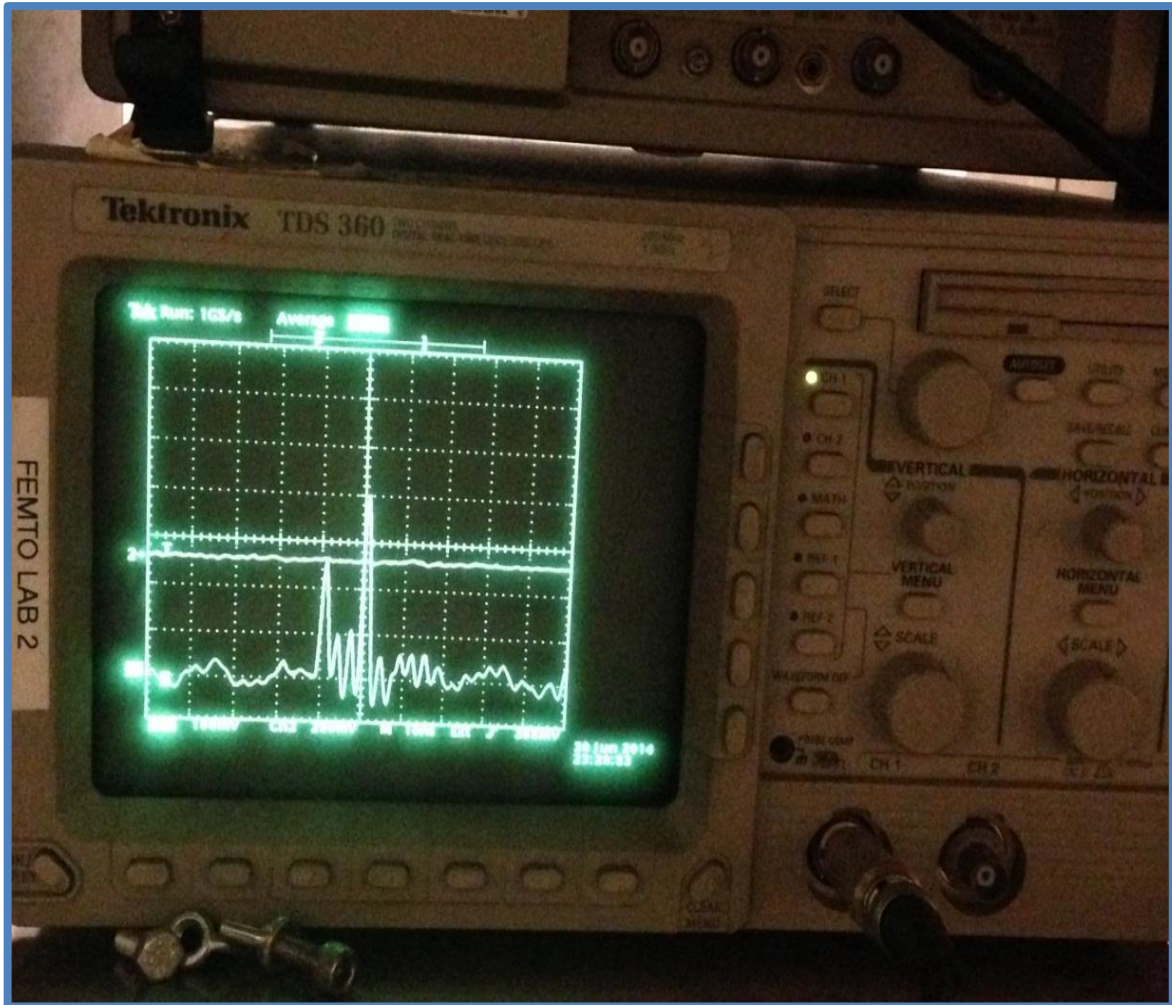


Figure 27 Oscilloscope.

Normally when the timing is set correctly, the central peak amplitude on the laser profile will increase to a maximum. Giving maximum power from the laser. There may be two side peaks or bands whose amplitudes should be reduced to a minimum as can be seen in figure 26 and 27.

#### 2.5.4 THE PHYSICAL SHUTTER

The physical shutter is made of black rubber-like material that enables one to open and close the physical aperture that controls the laser beam coming out of the guiding tunnel. The black rubber-like material would absorb the laser beam rather than let it pass through only when its in an upright position.

Once the laser generation section is switched on and the laser beam is produced, to control the laser beam coming out of the guiding tunnel you can use the physical shutter to open and close the aperture through which the laser beam comes out of the guiding tunnel.

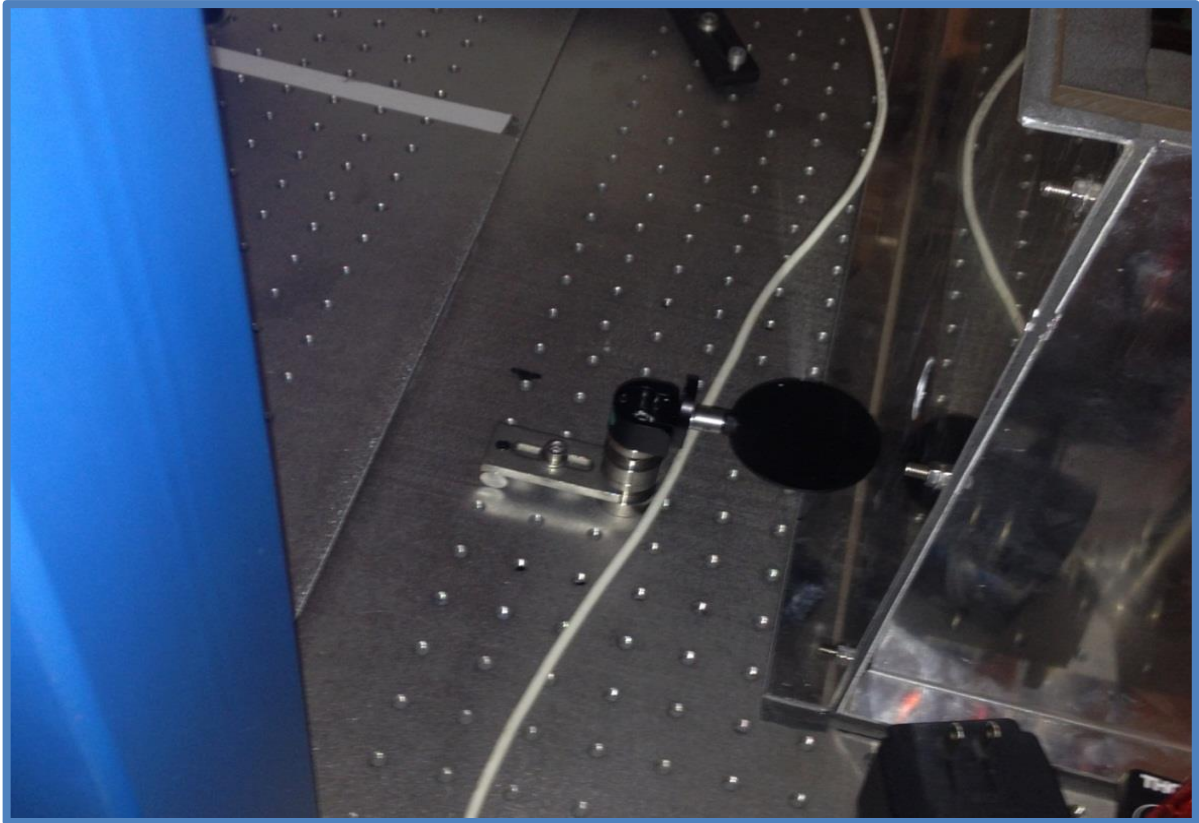


Figure 28 Shutter in open position.

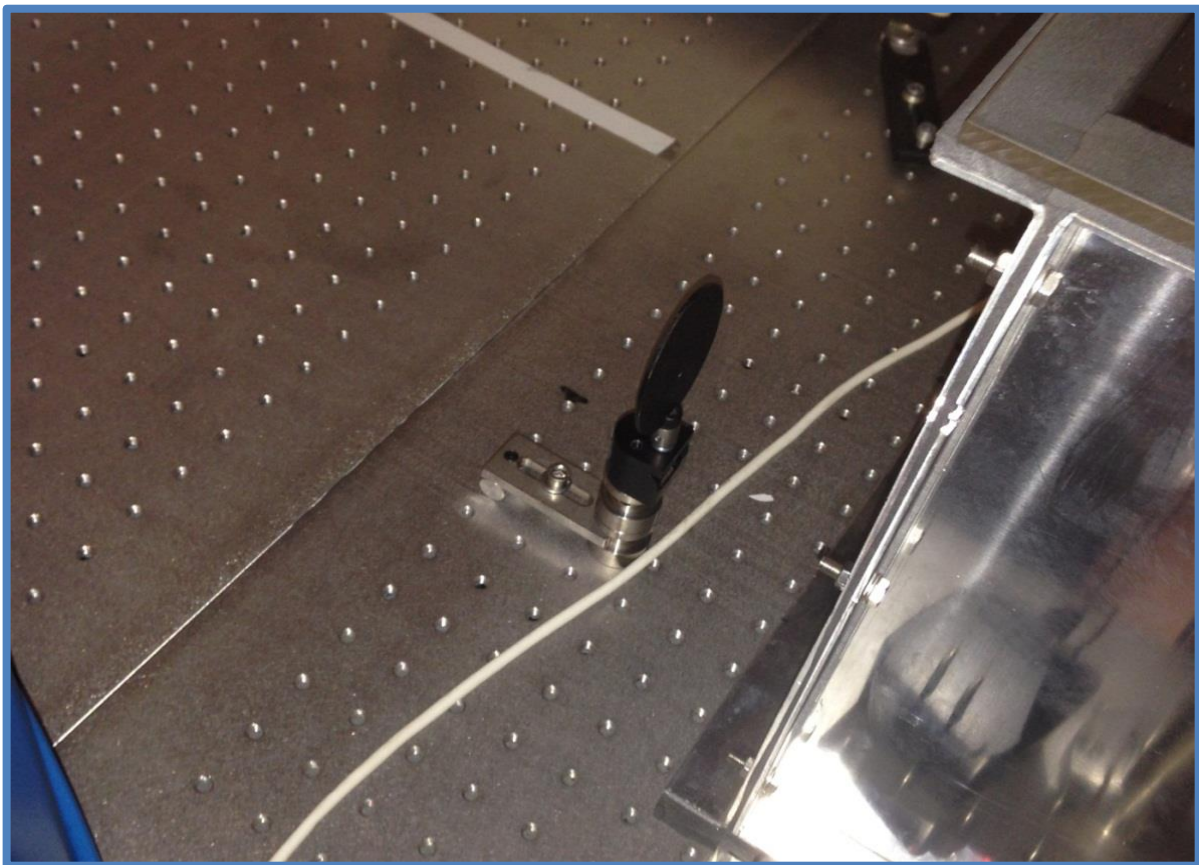


Figure 29 Shutter closed.

As can be seen in figure 28 and 29 the shutter blocks the laser beam generated in the laser lamp (pump laser diode) section. It has two positions when the shutter is open as in figure 28 and when the shutter is closed as in figure 29. When the shutter is closed, the beam cannot exit the generation box and hence the laser beam cannot be used.

### 2.5.5 THE OVERALL LASER PATH (REFLECTIVE MIRRORS AND IRIS APERTURES)

Outside the generation box when the shutter is open the laser follows a predetermined path guided by mirrors which reflect the beam and send it in a specific path as can be seen in figure 30.

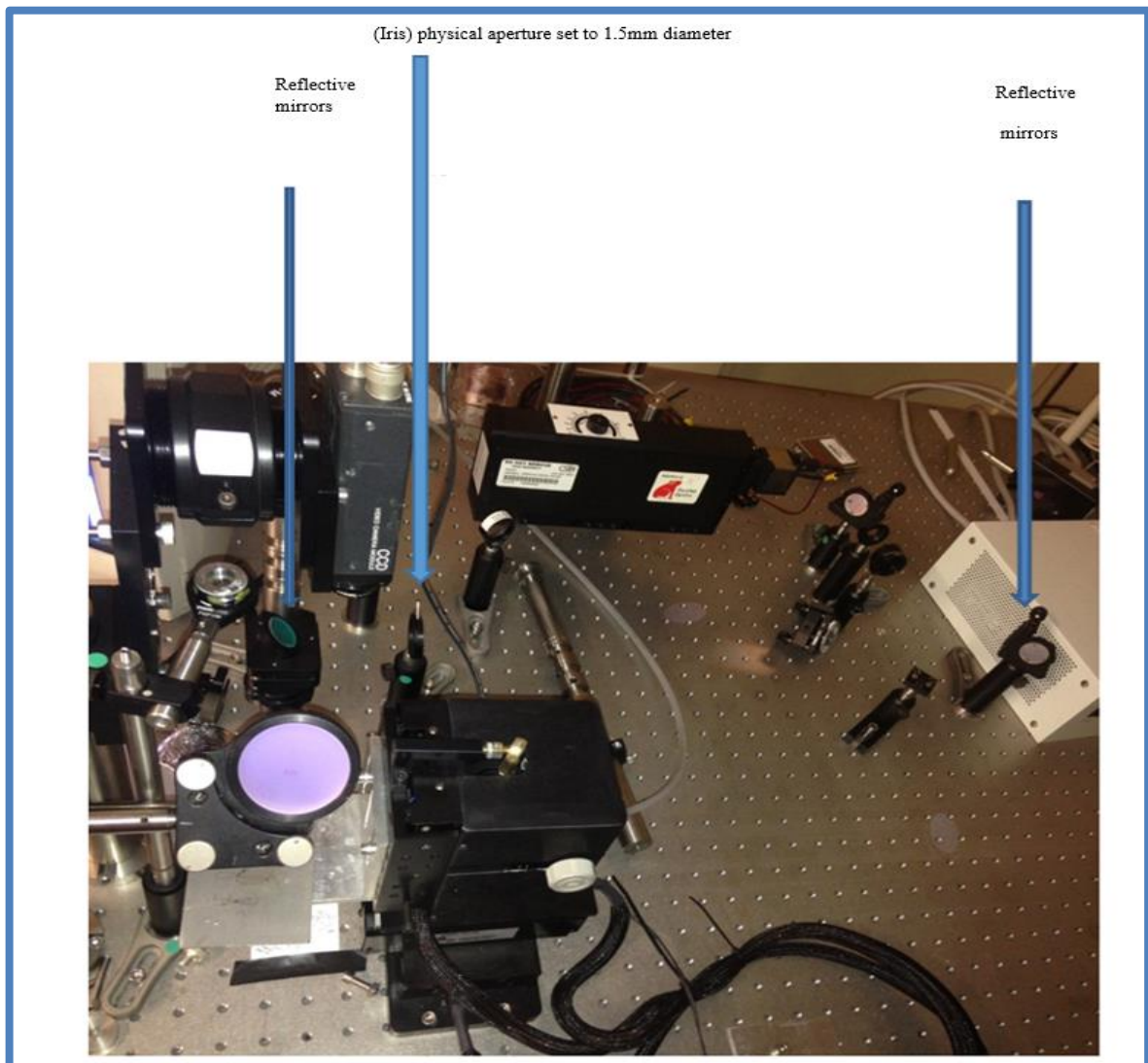


Figure 30 Reflective and guided path.

The laser beam travels and is reflected by mirrors until it reaches another shutter and an iris aperture. The aperture width of the iris can be regulated to shut out the beam completely. Finally, it reaches a lens that focuses the beam onto a translation stage.

### 2.5.6 THE TRANSLATION STAGE

The translation stage consists of a platform together with an argon gas compressed mechanical part that moves the platform in 3 dimensions (X, Y, Z). The platform holds the job piece that is being machined.

The translation stage can be programmed in G-Code to move the piece being machined in such a way as to allow the laser cut intricate patterns on the job piece. In other words, the laser itself is held stationary above the sample while the translation stage is moved according to the G-code. The translation stage works together with a reflective mirror held in place above it and a focus lens that focuses the beam onto the job sample.

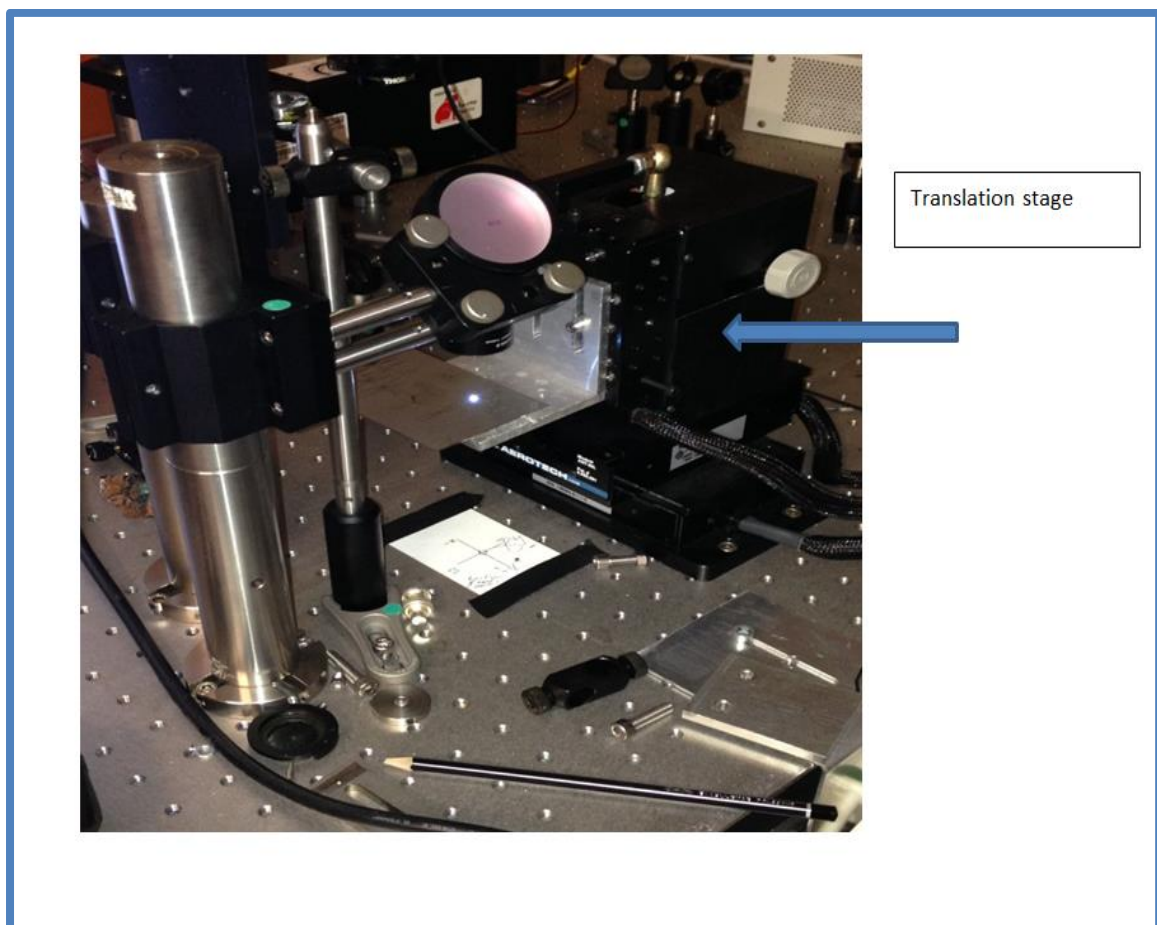


Figure 31 Translation stage.

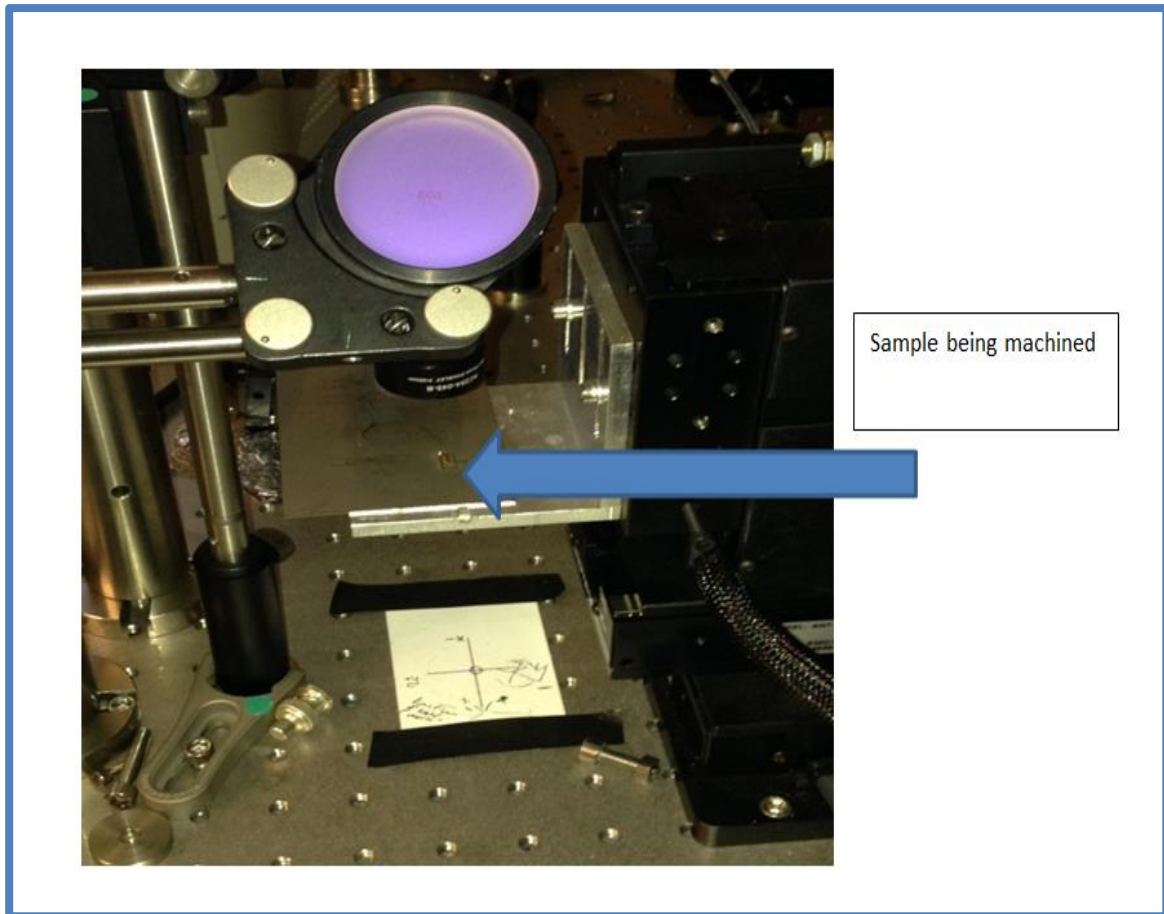


Figure 32 Translation stage with the origin and axis lines sketched underneath.

As can be seen in figure 31 the beam is focused onto the translation stage holding the job piece. In figure 32, an actual pattern is cut or machined on the metal test sample. The origin of the X-Y co-ordinates is shown below the platform.

### 2.5.7 FOCUSING OPTICS (CONVEX LENS)

After the reflective mirrors, the laser beam is focused onto the translation stage for machining the sample by using a lens. This is done either by using a conventional spherical convex lens of a specific focal length or by using an objective Plano convex lens with a specific numerical aperture. The spherical convex lens used had a focal length of either 45 mm or 30 mm. The shorter the focal length of the lens the higher the focusing power of the beam and can therefore produce a smaller ablation spot size from the laser source. The objective lens used had a numerical aperture of NA 0.25 and a X 10 magnification. This tends to focus the beam more than the normal spherical convex lens and thus produces a smaller laser ablation width.

## 2.6 SOFT MASK OF THE INITIAL CONSTRICTIONS MACHINED USING THE FEMTOSECOND LASER.

The diagram in figure 33 shows a sketch of the soft mask that was initially designed to make constrictions. The micro strip lines were used to separate one constriction from another electronically. The initial constriction design was a standard type where the width of the constriction could be controlled easily but the length was restricted to the laser ablation spot size.

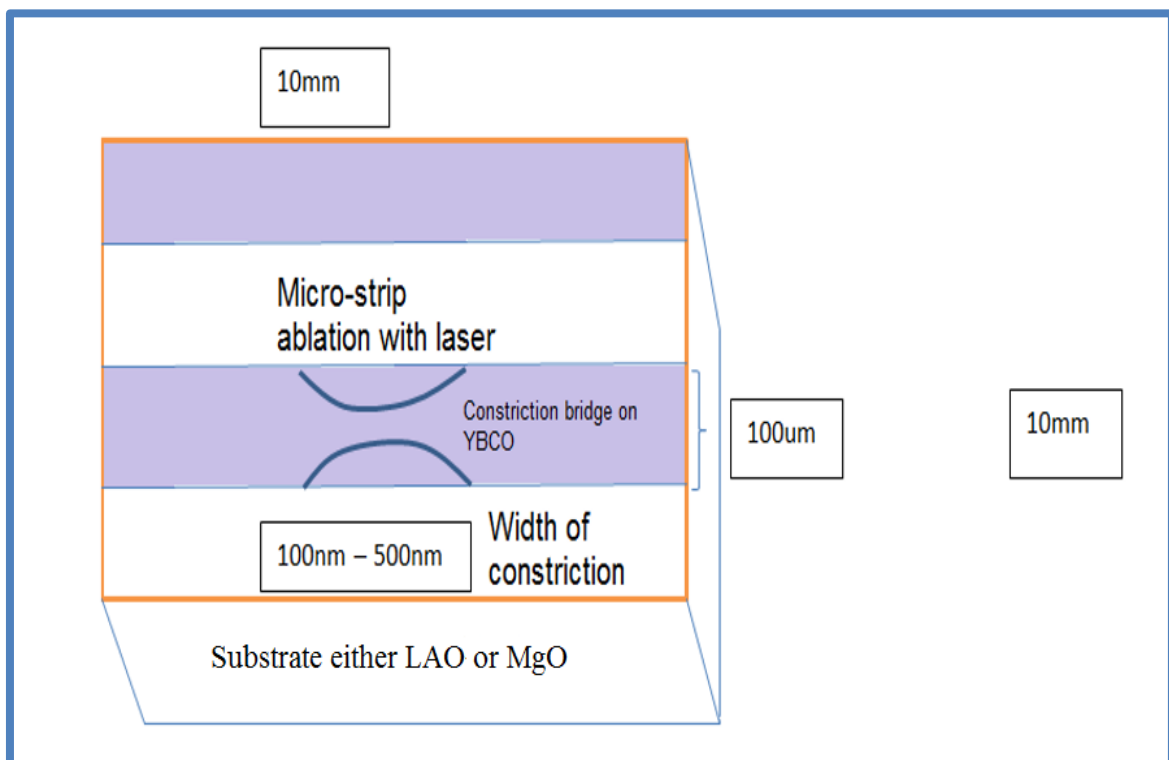


Figure 33 Constriction design and microstrip lines.

The width of the strips containing the constriction will be about 100  $\mu\text{m}$  wide. In between one constriction and the next there will be sections with the thin film completely removed by dry milling with the laser, leaving only the substrate of the thin film (micro strip lines). The method for doing this would be to use the femtosecond laser itself to machine the thin film (dry etching).

The objective would be to machine the micro strip lines on both sides of a constriction by using a laser beam of about 50  $\mu\text{m}$  diameter. Then move the laser into the YBCO strip and out from both sides leaving a constriction or bridge of about 100-500 nm wide.

## **2.7 FACTORS THAT DETERMINE THE PARTIAL OR COMPLETE REMOVAL OF THE YBCO THIN FILM USING THE FEMTOSECOND LASER.**

Some of the factors that determine the complete or partial removal of the thin film material include:

1. Laser feed rate.
2. Fluence of the laser related to the laser power and the ablation profile of the material used [3].
3. Numerical aperture of the objective lens, which is related to the lens focusing power and line width [3].

## **2.8 INITIAL TEST CONSTRICTIONS MACHINED ON STEEL USING THE FEMTOSECOND LASER AND THE G-CODE PROGRAM USED FOR THE DESIGN.**

A G-code program was written to move the translation stage of the femtosecond laser. During the design of the constrictions, code was written for the microstrip lines that were used to separate one constriction from the other and for the constriction itself. Initially when cutting the microstrip lines, the laser horizontal movements were made large to see if the laser could be used to completely remove the thin film as can be seen in figure 34. Subsequently the laser horizontal movements were reduced in spacing as can be seen in figure 35. By doing so the top YBCO material in the microstrips is etched away with the femtosecond laser.

For the section, which contains the constriction itself, the laser was utilised to cut incisions into the thin film to form small constrictions.

In figure 34 the first instance the dimensions were increased for visibility to see the constriction well and show control with the G-code program. The width of the removed thin film surface (microstrip lines) was 4 mm, moving in horizontal transitions of 0.4 mm, whilst the width of the constriction area was 2 mm, with incisions of 0.8 mm both sides leaving a constriction width of 0.4 mm or 400  $\mu\text{m}$ . This practice was initially performed on metal to prevent damage of the YBCO samples, which are very expensive to purchase.

In figure 35, the second instance the completely ablated metal section (microstrip lines) had a width of 2 mm and by moving vertically up and down the metal surface is removed with horizontal transitions of 0.2 mm. The constriction area had a width of 1 mm and the incisions are about 0.4 mm on both sides making a constriction of 0.2 mm about 200  $\mu\text{m}$ . This can be seen in the figure 35.

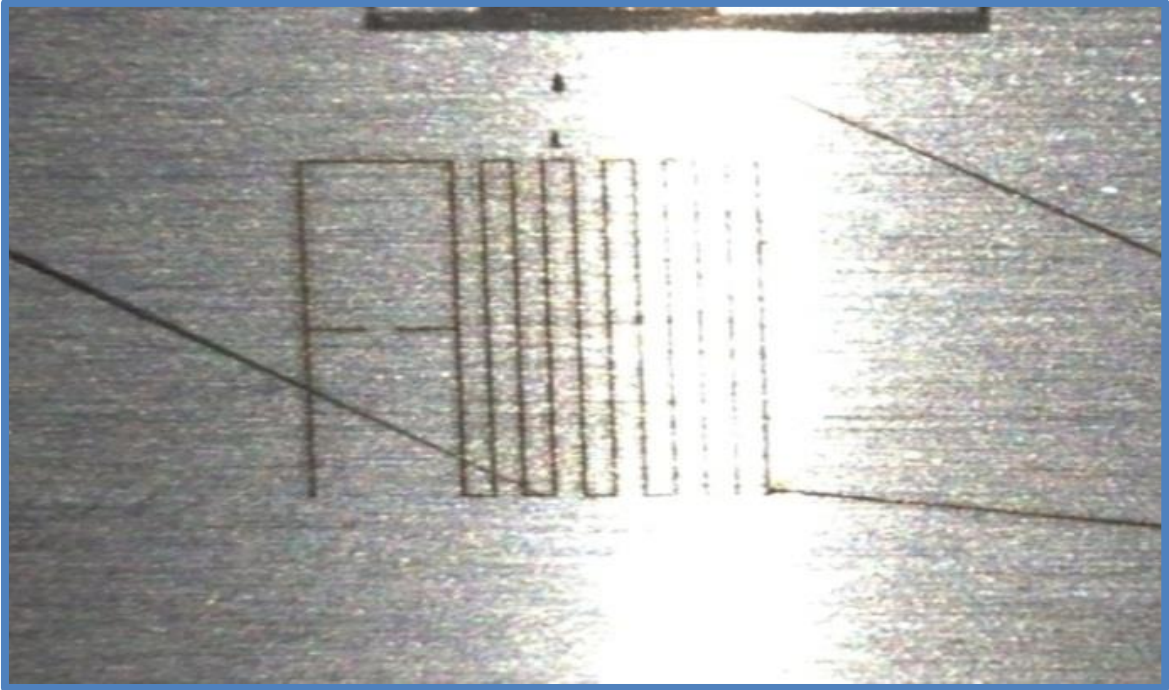


Figure 34 Microstrips lines with larger horizontal transitions

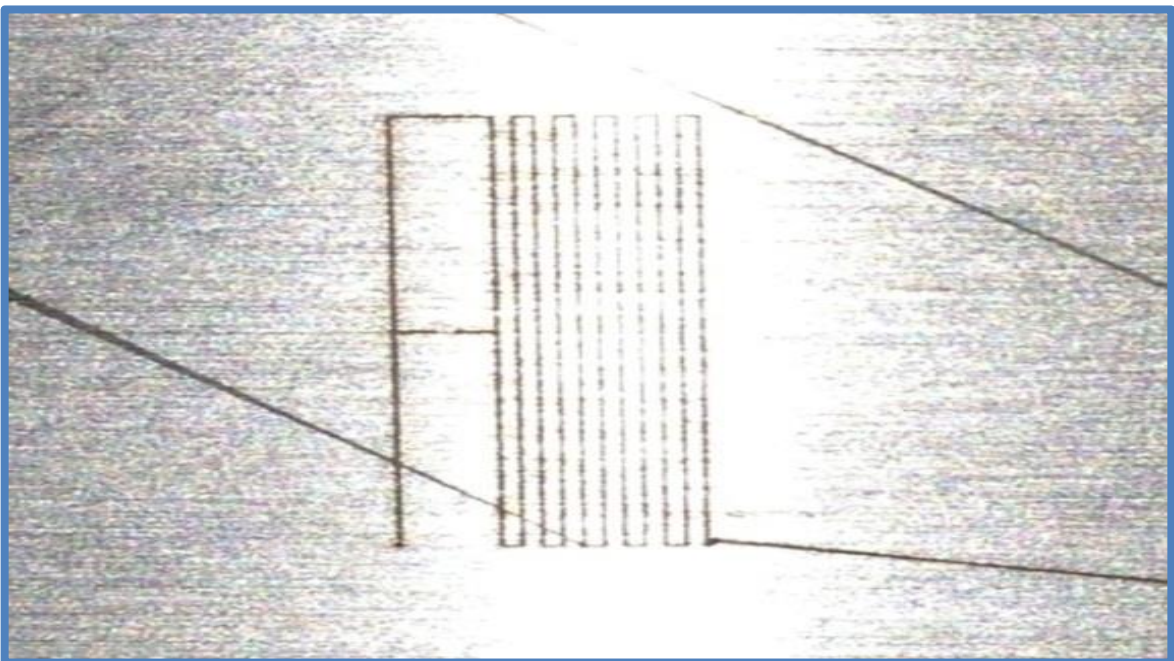


Figure 35 Microstrip lines with smaller horizontal transitions

## 2.9 FINDING THE FOCUS POINT OF A LASER BEAM

It is important to find the focus point of a laser beam because this will enable the laser to cut at the highest power and to cut with the narrowest beam width or smallest spot size.

The procedure involves moving the translation stage of the laser manually in steps along the Y-axis and then vertically up along the Z-axis producing holes on a metal that will show the focus point of the laser. The focus point of the laser will generally drill the smallest hole.

When focusing the laser the holes drilled must pass through the focus point (smallest hole drilled), this is visible because the holes go from the largest spot size through to the smallest spot size and back to the largest spot size again as can be seen in figure 36. So essentially, you chose the smallest hole drilled as can be seen in figure 36. You make horizontal movements along the Y-axis and vertical movements along the Z-axis, then you take note of the position (co-ordinate) along the Z-axis where the laser is focused (smallest hole drilled) and set the translation stage to that vertical (co-ordinate) position before you start actually cutting the constrictions. To control the translation stage there is a software interface that can be used to control the manual movement of the translation stage and control the programmed movement of the translation stage with the help of the G-code programming language.

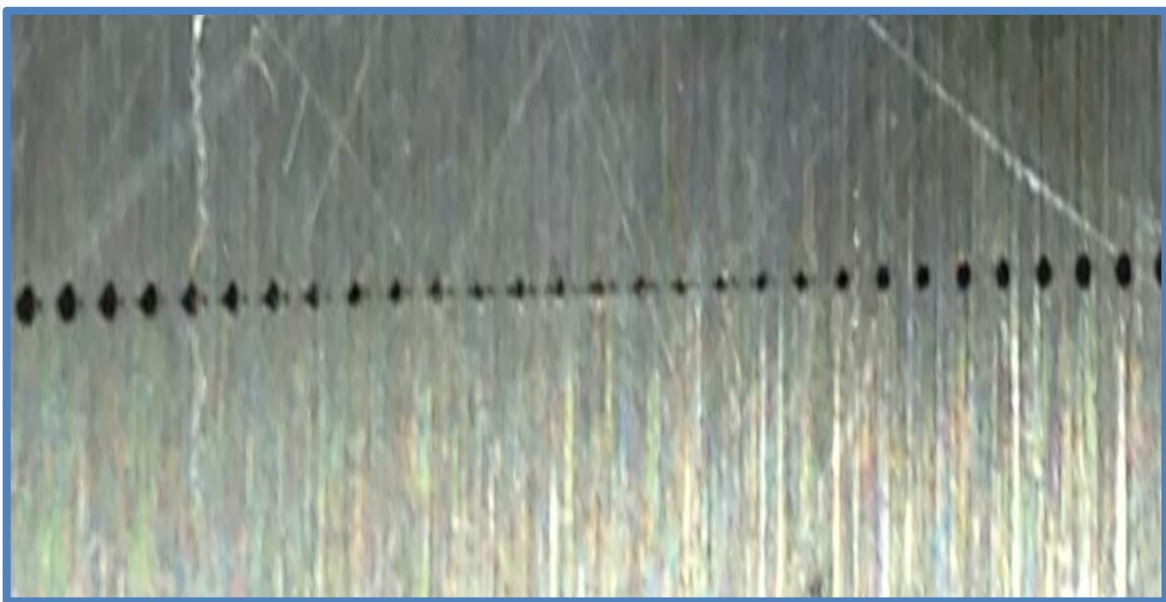


Figure 36 Finding the focus point of laser.

## 2.10 FABRICATION OF THE MICROSTRIP LINES AND CONSTRICTIONS ON TEST METAL

The microstrip lines were cut on metal by;

1. Reducing the movement along the horizontal Y-axis down to  $20\ \mu\text{m}$  such that complete ablation or removal of the thin film from the surface occurs.
2. Creating a loop within the code that enables 5 microstrip lines and 5 constrictions to be fabricated.
3. The incisions were made on both sides of the strip lines to produce a junction of about  $50\ \mu\text{m}$ . However using the dimensions of the beam width (laser ablation spots) being around  $50\ \mu\text{m}$  it's estimated that the constrictions produced in the centre of the ablation spots were much smaller about  $10\ \mu\text{m}$ . However this needs to be confirmed by taking images with an (OM) optical microscope or by using an (AFM) Atomic force microscope.

The diagram in figure 37 shows the microstrip lines (ablation patches) that were cut to separate one constriction from another. The constrictions can be seen as scratch lines in between the ablation patches in figure 37.

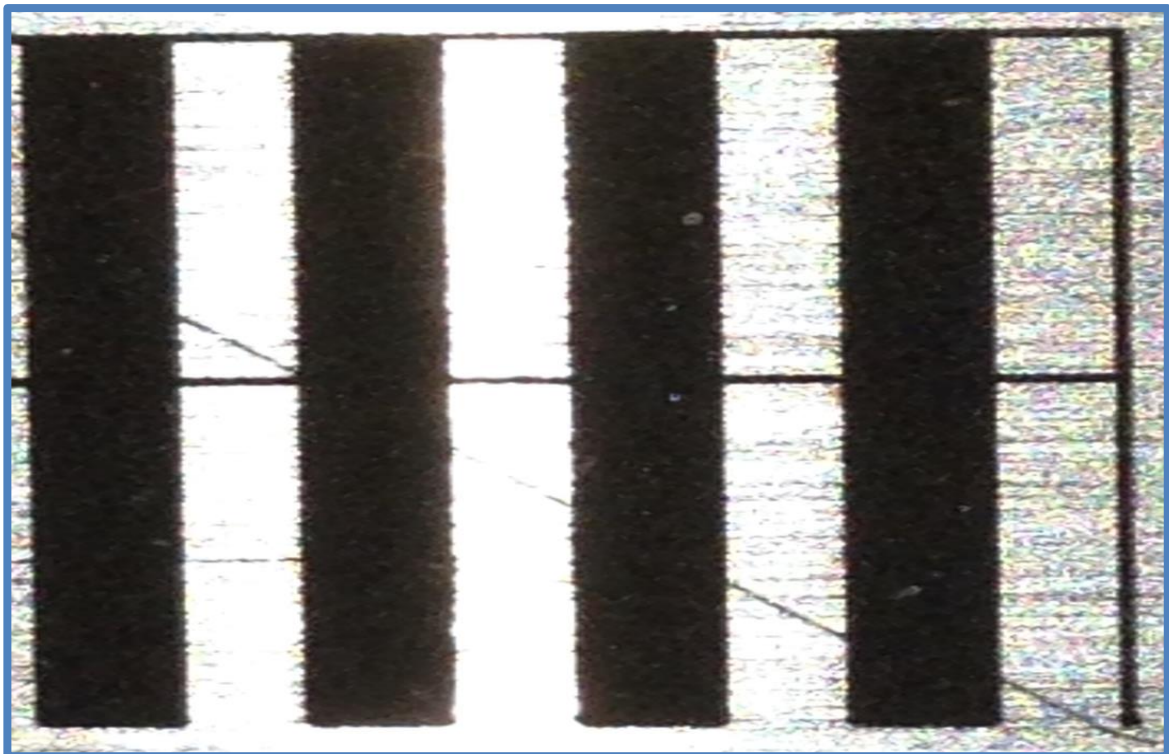


Figure 37 microstrip lines with constrictions.

Subsequently the G-code program was modified in the last experiment to make the horizontal adjacent movements in the ablation process to about 10  $\mu\text{m}$  from 20  $\mu\text{m}$ . This is done to make sure that the top layer of the metal is completely removed. However, this was deemed unnecessary at this point in search of complete removal of the YBCO thin film surface in the strip line.

An attempt was made to reduce the constriction width from 50  $\mu\text{m}$  to 20  $\mu\text{m}$ .

Initially there was a problem doing this as the laser tended to cut across and remove or clip the constriction. However the laser was refocused, smaller ablation spots were achieved and very small constrictions widths were made (20  $\mu\text{m}$ ).

The constrictions were viewed on an (OM) optical microscope, better images can be obtained on an (AFM) atomic force microscope.

Generally, it was difficult to work with the laser at the beginning because it seemed as though the power of the laser was divided into two pulses rather than centred. To make sure the whole laser power goes into the one central pulse, one needs to play around with the delay switches or timing console to ensure that a phase lock is achieved between the master and oscillator frequency. The phase lock will ensure that when the laser is set to an output power of 1 W, that it is issuing exactly that power.

The laser power was varied such that as the laser power is reduced then smaller beam widths and laser ablation spots are achieved. With smaller ablation spots it's possible to cut relatively smaller constrictions. That is, the beam width of the laser becomes smaller as the power of the laser is reduced meaning that a smaller constriction could be cut. The output power of the laser was varied from 800 mW to 500 mW to 350 mW.

The diagram in figure 38 shows the microstrip lines produced with constrictions 20  $\mu\text{m}$  wide in between.

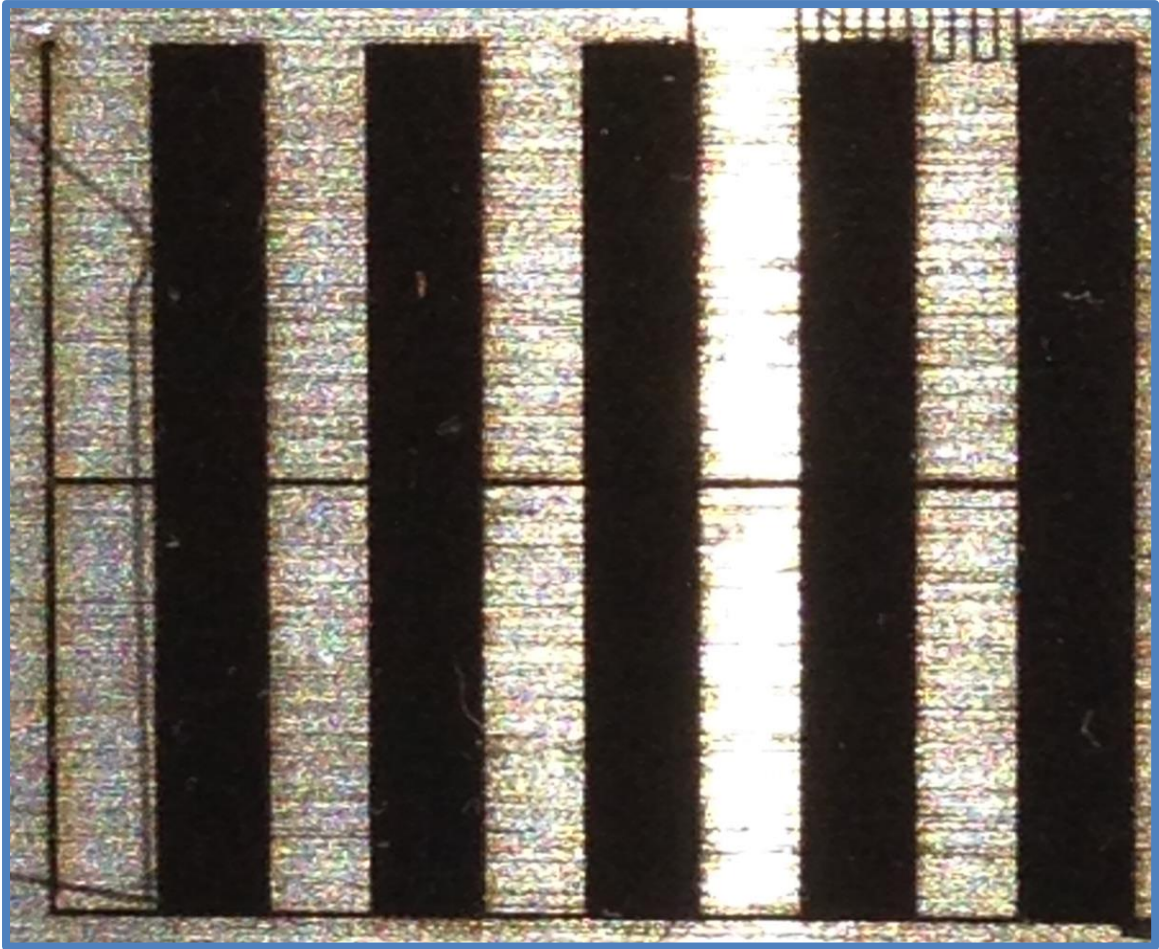


Figure 38 smaller constriction.

The brownish red colour is due to the partial removal of the metal surface during ablation. This is related to the power of the laser being applied not being sufficient. For complete removal or ablation, the power of the laser can simply be increased.

## **2.11 MICRON, SUBMICRON AND NANO STRUCTURING YBCO THIN FILMS BY CHANGING THE LASER PULSE ENERGY**

It is possible to fabricate nano structures in the region of 100 - 200 nm. This can be done by varying the laser pulse energy. As can be seen in the paper by [3] (Korte et al, 2003). There is the low energy regime, in this regime the ablation process is usually accompanied by the formation of small bubbles as can be seen in figure 39 [3]. At higher pulse energies, a molten ring around the holes and small droplets can be observed. When the laser pulse energy grows, the size of the hole drilled increases as can be seen in figure 40 [3].

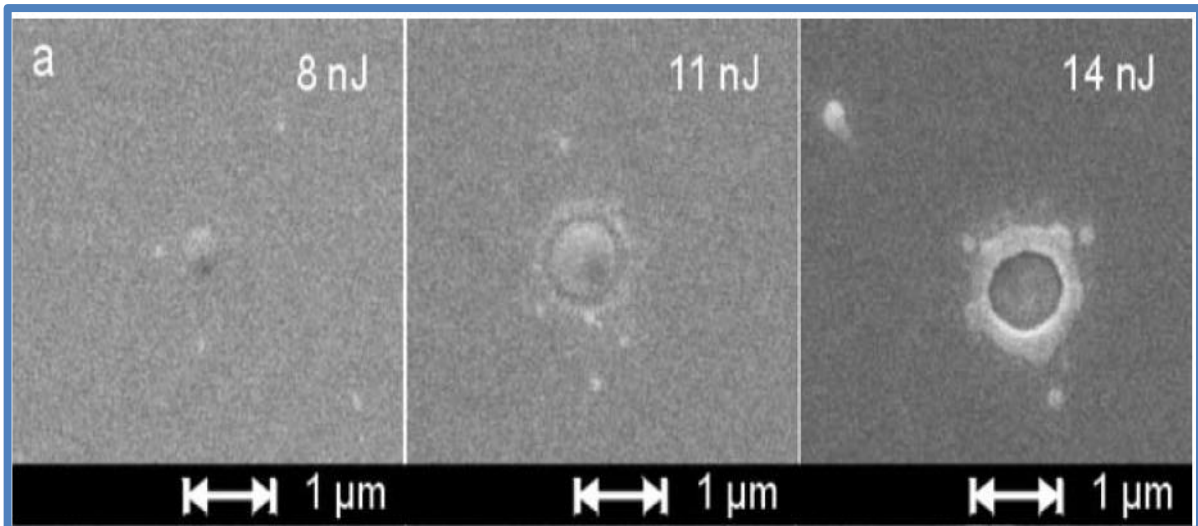


Figure 39 Single pulse laser ablation [3].

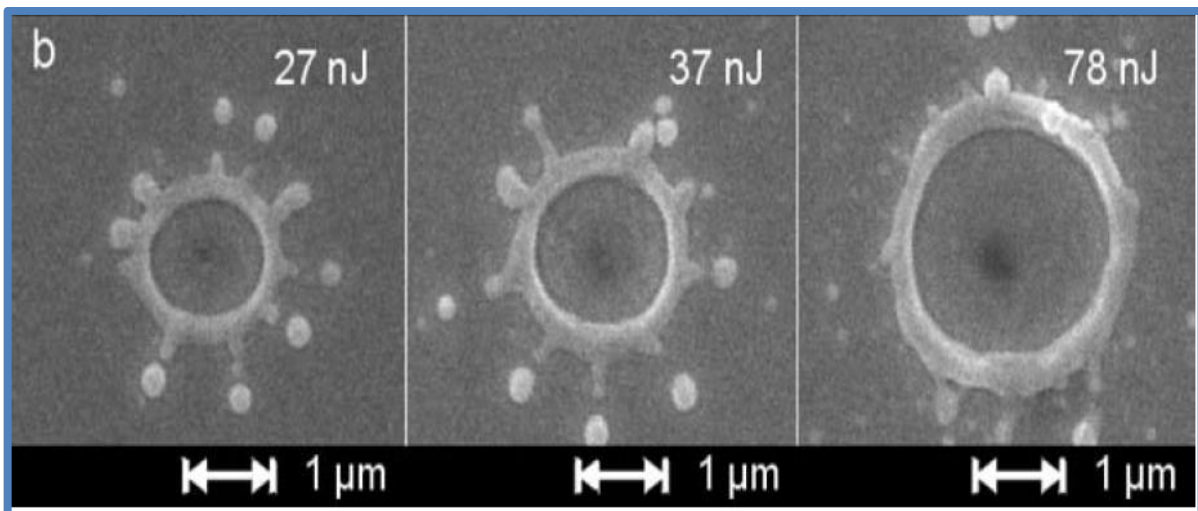


Figure 40 single pulse laser ablation with higher pulse energy [3].

$$P_{AVG} = E \times Hz \quad (1)$$

In equation (1), " $P_{AVG}$ " is the average power output from the laser source, "E" is the pulse energy of the laser and "Hz" the repetition rate of the laser pulse or frequency of the laser. According to equation (1) if you want to reduce the pulse energy one can keep the average power of the laser fixed and increase the frequency or repetition rate of the laser or keep the repetition rate fixed at 1 kHz for example and reduce the average power effluent from the laser source. In this case the power range is from 0 – 1000 mW and the frequency range is from 1 – 2 kHz.

Reducing the energy of the pulse will reduce the beam width, the ablation spot size of the laser and the diameter of the hole that is being drilled as you can see in both figure 39 and 40 [3].

## 2.12 LASER ABLATION WIDTHS PRODUCED WITH VARYING LASER POWER ON A TEST STEEL SURFACE.

In order to verify the above-mentioned theory that the lower the laser energy applied to the sample the smaller the size of the ablation spot. The following experiment was performed; the power output of the laser beam was varied and the resulting ablation widths were measured under the (OM) optical microscopes as follows. The laser power was set at 780 mW, 224 mW, 137 mW, 86 mW applied to cut prototype constrictions on metal surfaces and the corresponding ablation widths were measured and compared. The results can be observed in the figures below. From figures 41 to 44 as the laser power is reduced from 780 mW to 86 mW, the laser ablation width reduces from 153  $\mu\text{m}$  to 79  $\mu\text{m}$ . Therefore, this result validates the theory in [3].

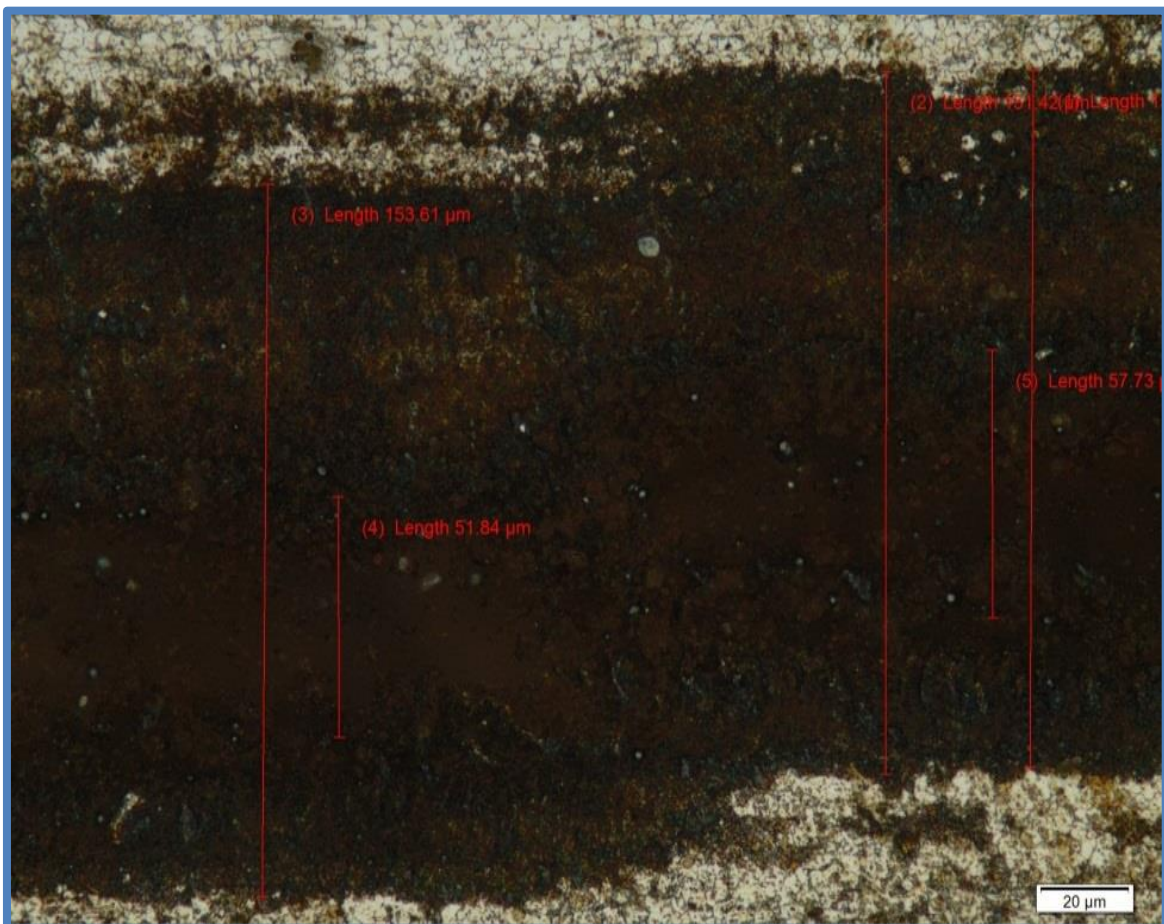


Figure 41 Laser power at 780 mW laser ablation width is 153  $\mu\text{m}$ .

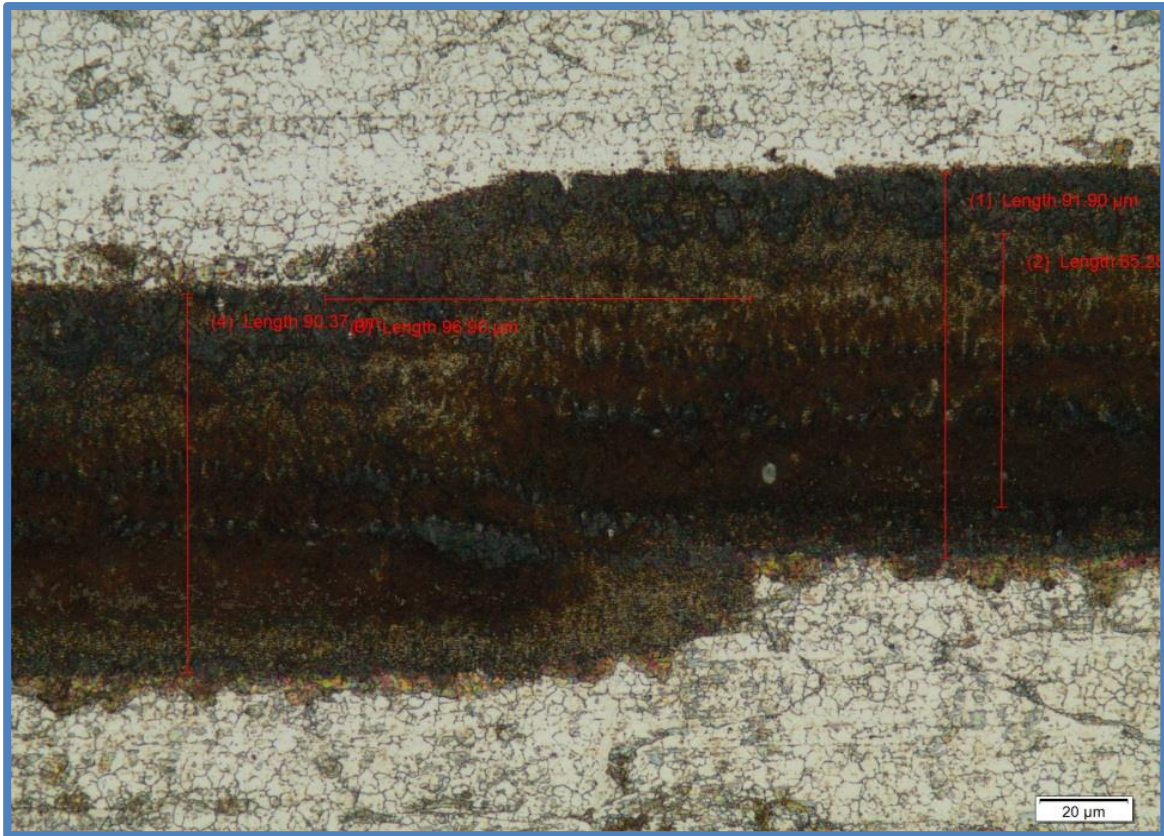


Figure 42 laser power at 224 mW laser ablation width is 91  $\mu\text{m}$ .

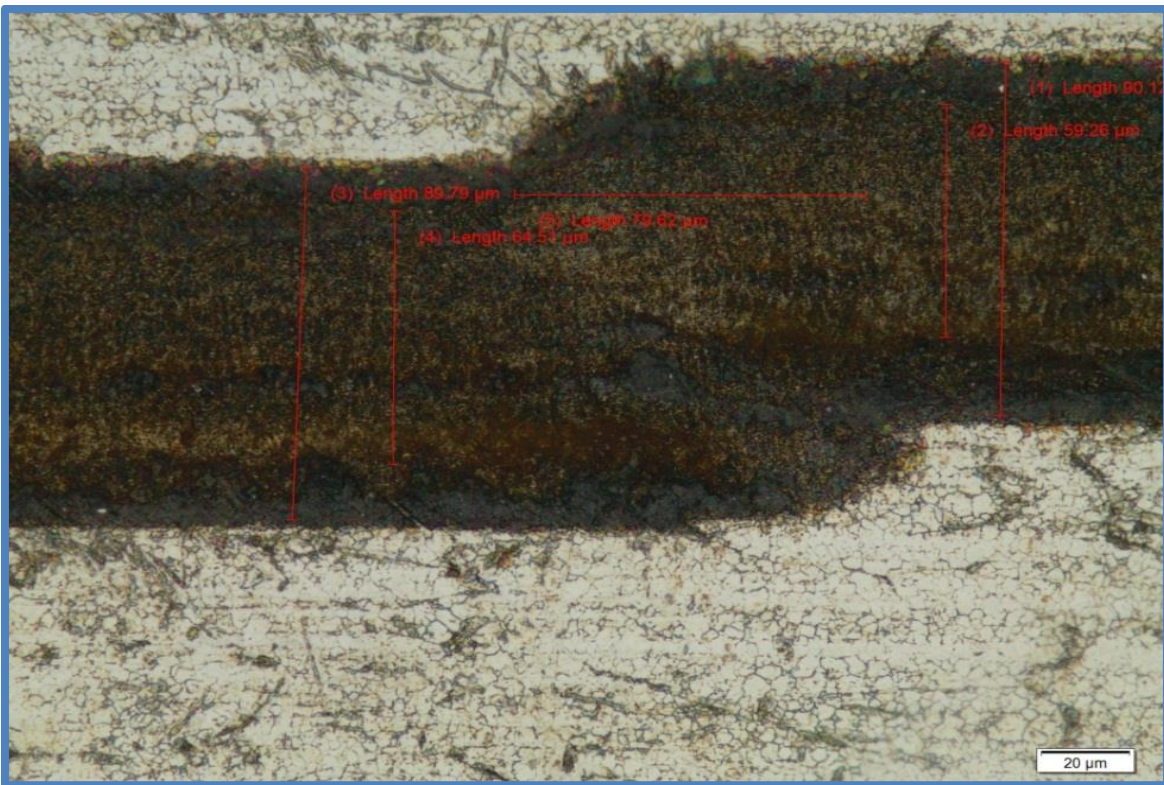


Figure 43 laser power at 137 mW laser ablation width is 89  $\mu\text{m}$ .

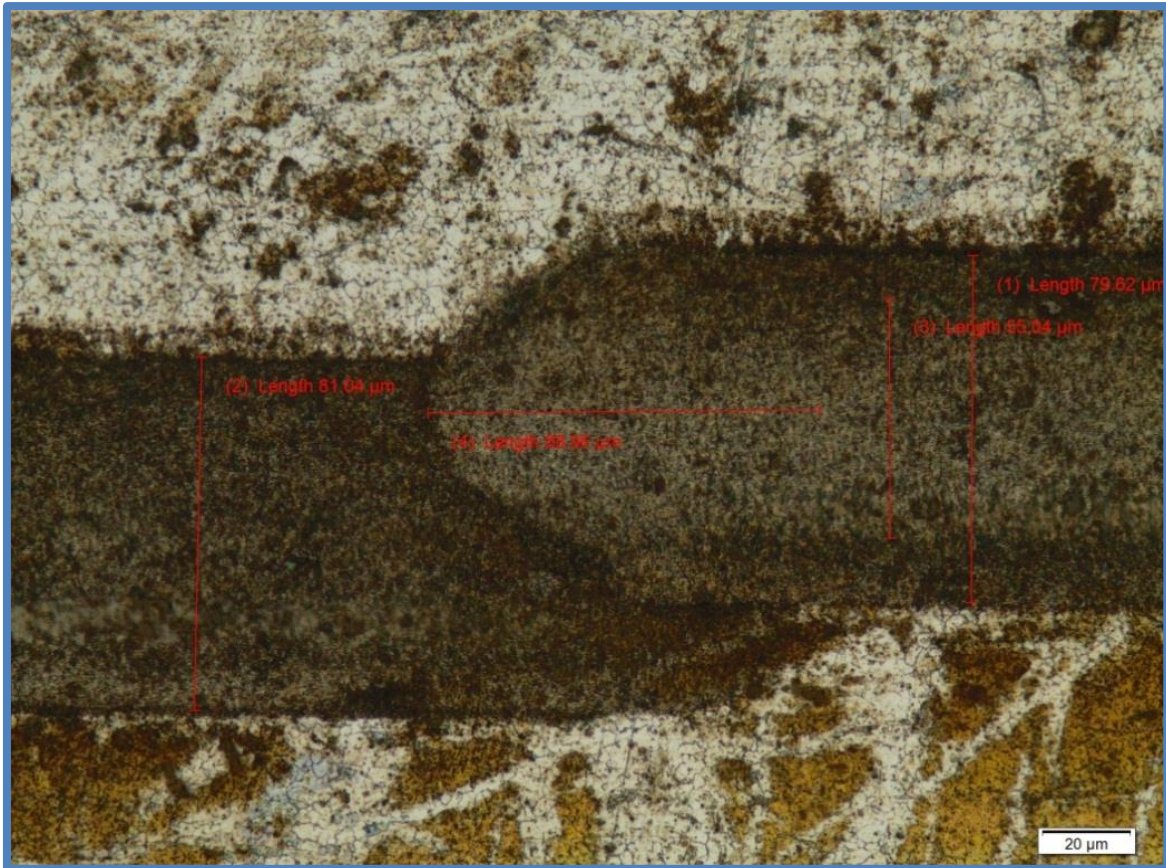


Figure 44 laser power at 86 mW ablation width is 79  $\mu\text{m}$ .

## 2.13 FACILITATING THE SUB-MICRON STRUCTURING OF MATERIALS BY USING THE LASER ABLATION THRESHOLD OF THE MATERIAL.

Every laser has a profile distribution or what one refers to as a Gaussian profile distribution as can be seen in figure 45. The peak of this Gaussian distribution will vary depending on the laser power released from the source, the energy of the laser and laser fluence or energy density. Generally, the cumulative energy of the laser will be the total area of the Gaussian profile distribution underneath the curve area. Different materials have different ablation thresholds with respect to a specific laser i.e the minimum amount of energy or power required to just begin removing some of the surface material of that sample with the laser (ablation). To make the ablation spot of the laser, which is removing the material as small or minute as possible one needs to set the laser power or energy such that the profile distribution is just slightly above the ablation threshold of that particular material as can be seen in figure 45. In this figure, one of the Gaussian profile distribution of the laser just slightly eclipses

the horizontal ablation threshold line. If vertical lines are then plotted downwards from there to the X- axis one will see that the resulting ablation spot size is minimum.

It is possible to drill very small holes; submicron holes by choosing the peak laser fluence slightly above the ablation threshold of the laser see figure 45 [3].

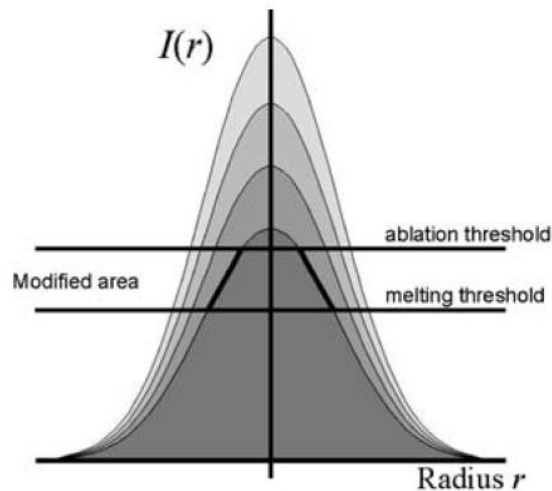


Figure 45 Ablation threshold of a laser beam [3].

Working slightly above the ablation threshold is possible by varying the pulse energy of the laser before the laser is focused unto the material sample. In this case, only the central part of the beam can ablate the material and it becomes possible to produce sub-micron structures.

Using equation (2) from [3],

$$F = F_0 \exp\left(-\frac{d^2}{d_0^2}\right) \quad (2)$$

Where " $d_0$ " the ablation width (laser spot size after ablation) or in some few cases the beam diameter, " $F$ " is the laser fluence which is essentially the energy of a pulse per unit area of application and " $F_0$ " is the peak laser fluence possible.

According to equation (2), the larger the fluence the larger the diameter of the hole that can be drilled. This can be observed in figure 46 [4], laser fluence in joules per centimetres squared is increased then the diameter of the laser ablation beam size increases and hence the diameter of the hole drilled in gold thin film [4] increases and also leads to the formation of a droplet due to some thermal heating.

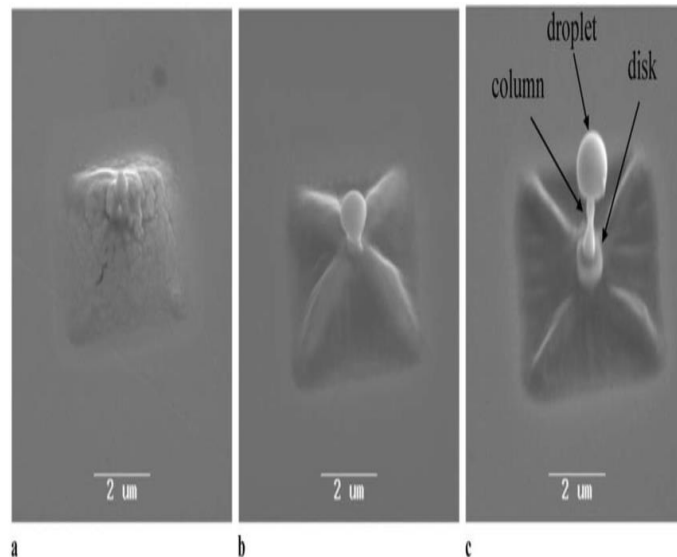


Figure 46 Laser fluences on the gold surface are increased [4].

## 2.14 FACTORS THAT DETERMINE THE NANOSTRUCTURING OF METALS

The minimum structure size that can be produced by femtosecond laser pulses is determined by equation (3) from [3];

$$d = k\lambda/NAq^{1/2} \quad (3)$$

Where " $\lambda$ " is the radiation wavelength, " $NA$ " is the numerical aperture of the objective lens used or the focusing optics, and  $k$  is a proportionality constant. Generally, when the numerical aperture of the lens is increased in the set up then the diameter of the structure produced can be reduced.

Also  $q$  is related to the energy band gap of the material, the higher the energy band gap of the material the smaller the size of the structure that can be produced, this can be seen in figure 47 [3].

For this project the femtosecond laser has a radiation wavelength " $\lambda$ " of 775 nm, and the objective lens used has an " $NA$ " of 0.25. Certain materials are better suited for nano structuring depending on their energy band gap [3]. What about YBCO? **"Answer"** The (in plane) energy gap of YBCO is 20 meV [5] while there is also a sub-gap energy band of 12 meV.

In YBCO the energy gap between the conduction band and valence band can get to as low as 5 meV [5]. Based on this energy band gap and by using the graph in figure 47, the limit on the constriction size that can be fabricated on YBCO material and still hold up without collapsing, will be about 450 nm. As we will later observe the structures that I made had a sub-micron limit of about 800 nm for the constrictions width as the YBCO crystals tended to collapse after this.

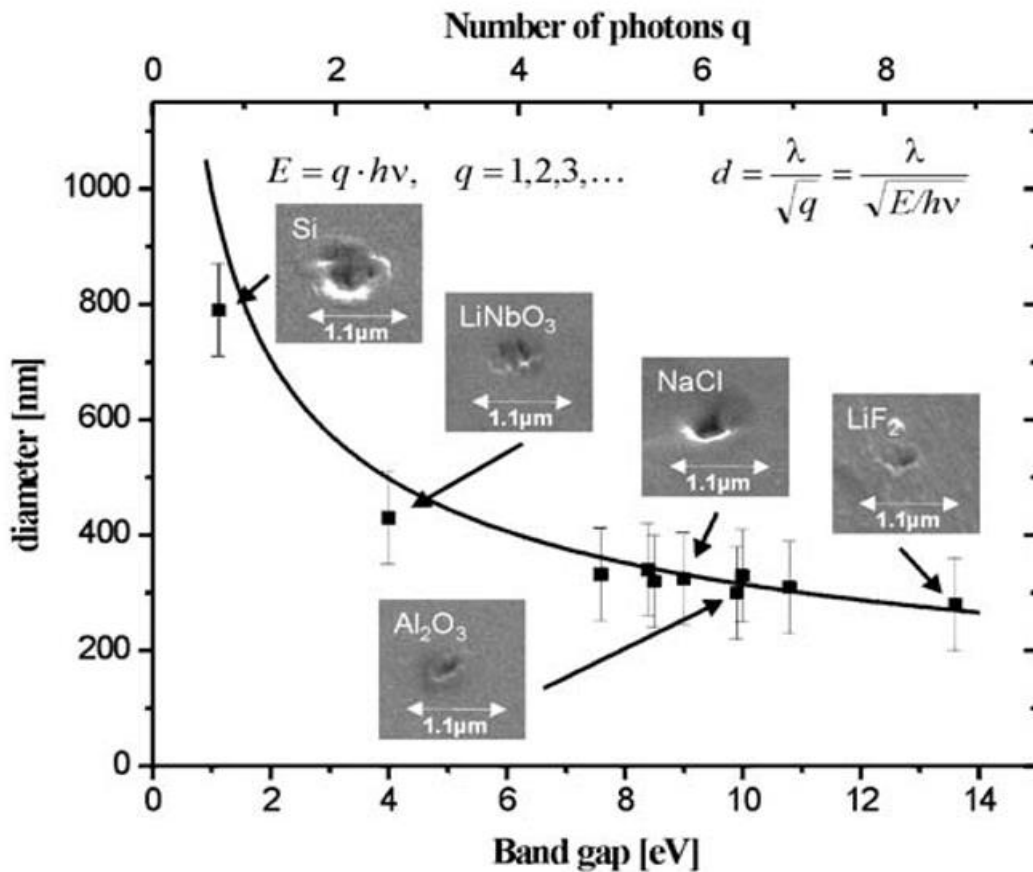


Figure 47 Dependence of the minimum structure size for different transparent materials on their band gap energy [3]

## 2.15 THE NOVEL S-SHAPED CONSTRICTION DESIGN THAT COULD BE USED AS A JOSEPHSON JUNCTION

A proposal was made for a new S-shaped structure to be cut on the YBCO thin film material. The need for the structure arose because of the need to control the width and the length of the constriction at the same time. In the standard type of constrictions as can be seen in figure 48, it is only the width of the constriction that can be controlled the length of the constriction is restricted to the laser ablation width as can be seen in figure 48. Which is not the best scenario.

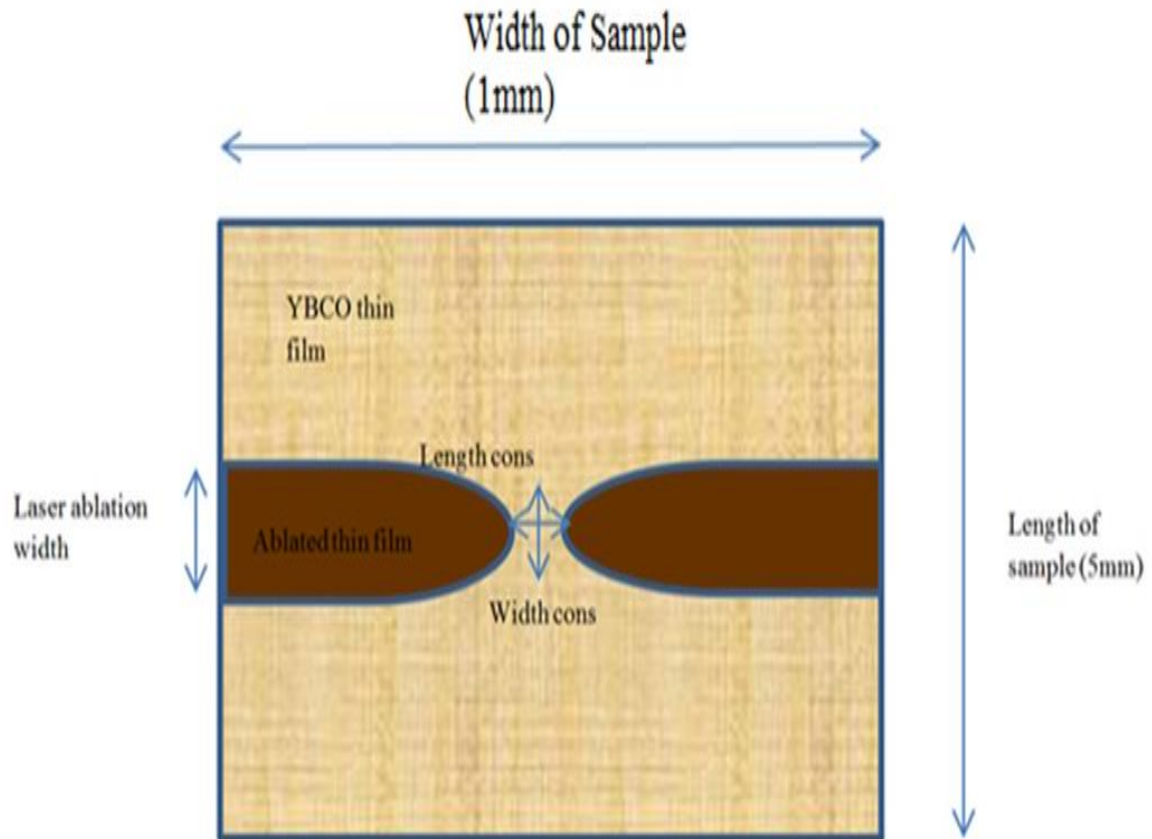


Figure 48 Standard type of constriction.

The diagram in figure 49 shows the shape of the novel S-shaped constriction that was designed and machined using the G-code programming language to control the movement of the translation stage. In the S-shaped constriction, it is possible to regulate both the width and the length of the constriction.

$S_W$  represents the separation distance in G-code between the centres of the laser ablation spots. The beam width refers to the laser ablation width of the laser beam. Therefore, according to equation (4) one can calculate the width of the constriction.

$$S_W - \text{beam width (laser ablation width)} = \text{width of constriction} \quad (4)$$

The beam width puts a restriction factor on the width of the constriction that can be fabricated. But with the S-shape for the constriction it may be possible to overcome this problem. The reason for this is that the width of the constriction that can be fabricated depends on the laser ablation width. The smaller the laser ablation width the smaller the width of the constriction that can be fabricated.

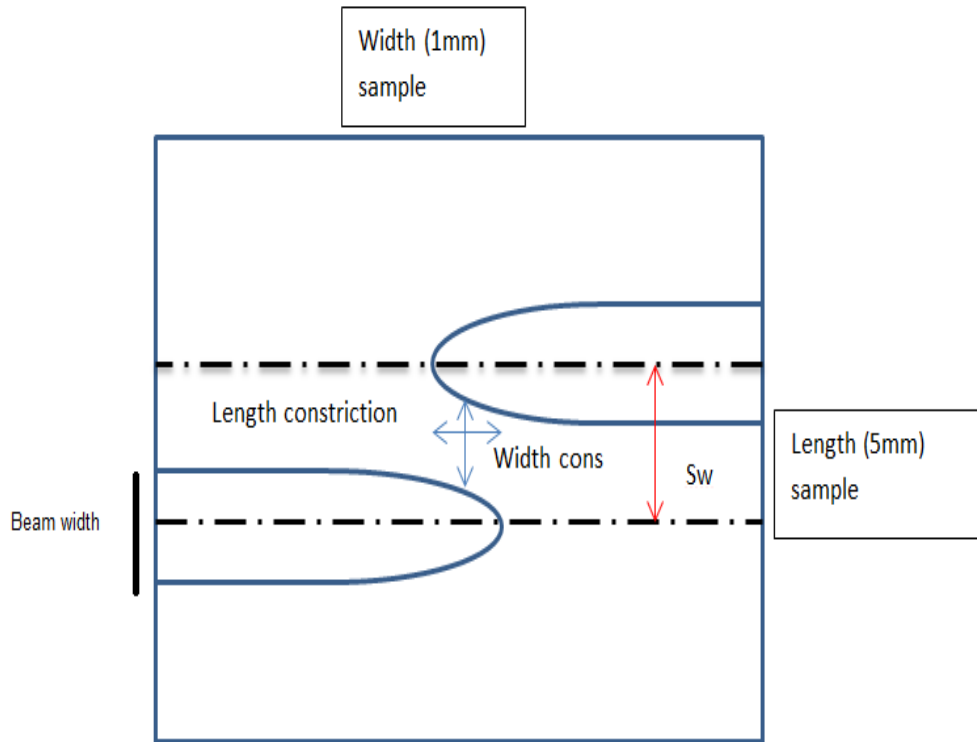


Figure 49 S-shaped constriction design.

This S-shaped design was utilised to cut test constrictions on metal at the national laser centre (CSIR) in Pretoria, South Africa. In the one scenario, a spacing of 70  $\mu\text{m}$  was set between the laser ablation beams in the G-code program and the beams still overlapped and created no junctions. The spacing was then set to 80  $\mu\text{m}$  from the centre of one beam to the other and the beams just touched. It was concluded that the beam width (laser ablation width) of the laser was about 80  $\mu\text{m}$  with the current laser settings.

Finally, the spacing was adjusted to cut a constriction size of about 2  $\mu\text{m}$ . This was done by separating the laser ablation spots by 82  $\mu\text{m}$ . That this dimension was achieved was verified by measuring the width of the constriction by using the atomic force microscope (AFM).

Subsequently by varying the power of the laser, it was possible to make S-shaped constrictions on steel plates with a width of about 3  $\mu\text{m}$  as can be seen in figure 50.

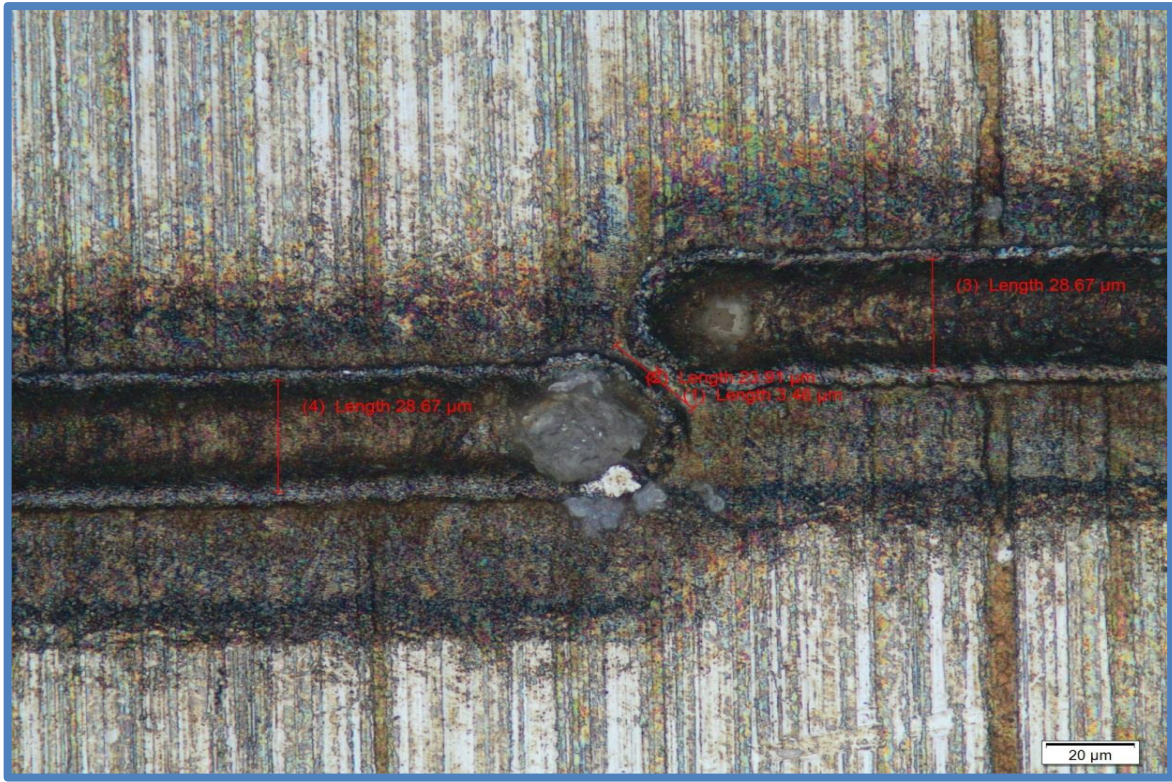


Figure 50 Constriction on steel with a width of 3 μm.

## 2.16 PULSE ENERGY OF THE LASER

The femtosecond laser has a very short pulse length (duration) of 130 femtoseconds, a wavelength of 775 nm, a power range of 0 to 1000 mW and a frequency range setting of 1 kHz-2 kHz but it was operated at 1 kHz from the control console.

Using the formula in equation 5

$$P_{AVG} = E_{pulse} * Pulse_{rep.rate}(freq) \quad (5)$$

Where  $P_{AVG}$  is the average power effluent from the laser set on the control interface,  $E_{pulse}$ , is the energy per pulse of the laser and  $Pulse_{rep.rate}(freq)$  is the pulse frequency repetition rate of the laser set on the control interface as well.

In most optimum instances, the laser power incident on the thin film sample was set at about 2.1 mW. The reason being that at this power the top layer of the YBCO thin film is just removed or ablated. The thin film has a thickness of 200 nm. The frequency of operation is set at 1 kHz. This calculates to 2.1 μJ of energy reaching the sample using equation 5. The lower the energy applied the smaller the size of the laser ablation width or laser ablation spot size drilled on the sample.

This results in very high peak powers of 16.2 MW with relatively low pulse energy, according to the formula in equation 6 below;

$$E_{pulse} = P_{PEAK} * t \quad (6)$$

Where  $P_{PEAK}$  is the peak power of the laser not the average power and  $t$  is the pulse duration in femtoseconds.

In an example when 1000 mW is applied out of the laser then the energy per pulse is about 1 mJ, with this energy value the peak power produced using equation 6 is about 7.7 GW.

Due to the reduced pulse, energy when 2.1 mW is applied to the sample one would expect low thermal heating of the device during the cutting of the material.

The reason why we want to utilise the femtosecond laser to fabricate the Josephson junction is because the low pulse duration length and the reduced thermal heating can prevent normalization of the superconductive material used for the fabrication of the Josephson junction, however that this actually happens still has to be proven in experiment.

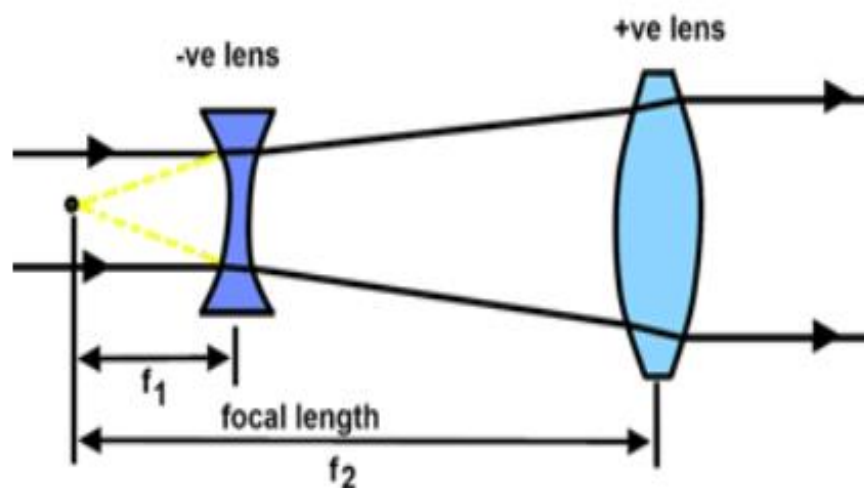
## **2.17 LASER BEAM SHAPING AND COLLIMATION PROCESS TO REDUCE LASER ABLATION SPOT SIZE.**

### **2.17.1 INTRODUCTION TO THE LASER BEAM COLLIMATION PROCESS.**

The Beam collimation process is explained in this sub-section. Beam collimation involves spreading out, blowing up or expanding a beam and then making it parallel (collimating) it. The reason for doing this is in two part. The first reason is because the laser beam spot is elliptical with the X-axis smaller than the Y-axis, and there is a need to expand the X-axis. Secondly because there was an idea that by blowing up the laser spot before using a convex lens to converge it, could possibly produce a smaller ablation spot for the fabrication of nano junctions. After the beam collimation process was complete the constrictions where initially fabricated on a steel surface in order to test the results of the beam collimation process before applying the fabrication process on the expensive and highly limited YBCO thin films.

Beam collimation involves spreading out or blowing up an incident laser beam waist and then making the resulting bigger beam waist parallel, sort of like in a telescope. This can be seen in figure 51 where the beam is initially spread out by the cylindrical diverging lens and then subsequently made parallel by the cylindrical converging lens. The cylindrical lenses are slightly different from the spherical lenses in that they are half the sphere in a spherical lens. In the specific case of my beam collimation experiment, a cylindrical diverging lens of focal length of -12.5 mm and a cylindrical converging lens of focal length of 25 mm were utilized. When the beam is collimated then the beam lines should not meet (converge) in theory no matter how far the beam is sent across a room. That is the beam rays stay parallel. If the beam rays stay parallel, then the beam spot will remain the same size after collimation no matter how far the beam travels across a room.

The lenses used for this process are cylindrical lenses half of spherical lenses as can be seen in figure 51 and 52. Cylindrical lenses are used because we only want to spread out a certain direction the X-axis of the laser beam spot. The reason for doing this is that the original laser beam spot is elliptical in shape with the X-axis of the spot being smaller than the y-axis. With cylindrical lenses, you can spread out the axis that is perpendicular to the normal axis (direction) of the cylindrical lenses themselves.



**Galilean Collimator**

Figure 51 Beam collimation process consisting of a cylindrical diverging lens and a cylindrical converging lens.

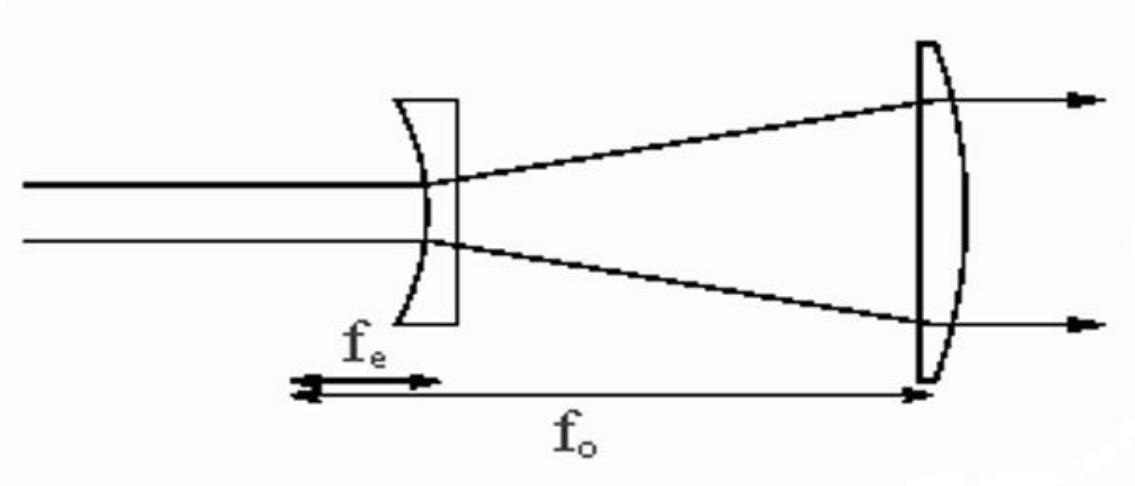


Figure 52 Cylindrical lenses positioned at right angles to the direction of the axis to be blown up.

Hence, as you will be able to see in figure 53 and 54 the cylindrical lenses are placed at right angles or 90 degrees to the vertical X-direction of the laser spot.

Another point of interest is that in order to collimate the beam the separation distance between the lenses has to be specific along the beam path. That is the beam only collimates when the lenses are separated by a specific distance. When the ratio of the focal length between the diverging lens in this case -12.5 mm and the converging lens in this case 25 mm is 2 then the separation distance between the lenses should be approximately the focal length of the first lens in this case 12.5 mm. In the process of beam collimation, the cylindrical diverging lens is positioned first to spread out the beam and then the cylindrical converging lenses are placed last.

### 2.17.2 ACTUAL PROCESS OF COLLIMATING THE LASER BEAM AND THEN RE-FOCUSING TO A SMALLER SPOT SIZE.

Essentially the beam spot coming out of the laser source is elliptical and not spherical or round. It is approximately 9.85 mm wide along the Y-direction and slightly narrower along the X-directions. It is in some proportions narrower in the X-axis or X-direction than in the X-direction. The assumption is that it's narrower by a factor of about 2 or 1.5.

Hence, there is a need to expand the beam in the X-direction using a beam expander, making the beam round or spherical or the same in both directions and then subsequently collimate the beam or make it parallel.

To achieve this, we have utilised a cylindrical diverging lens or concave lens with a focal length of -12.5 mm to spread out the beam first in the X-direction and then a cylindrical convex lens with a focal length of 25 mm to collimate the beam in the X-direction and make it parallel. These lenses have a physical aperture dimension of 10 X 10 mm.

Subsequently we will refocus the beam with a spherical convex lens to make the spot size smaller again to cut the thin films in the appropriate proportions to get to the nano or sub-micron scale. The spherical convex lens will refocus all the directions X and Y, in the same way. The setup and alignment of the cylindrical lenses to collimate the beam can be seen in figure 53 and 54.

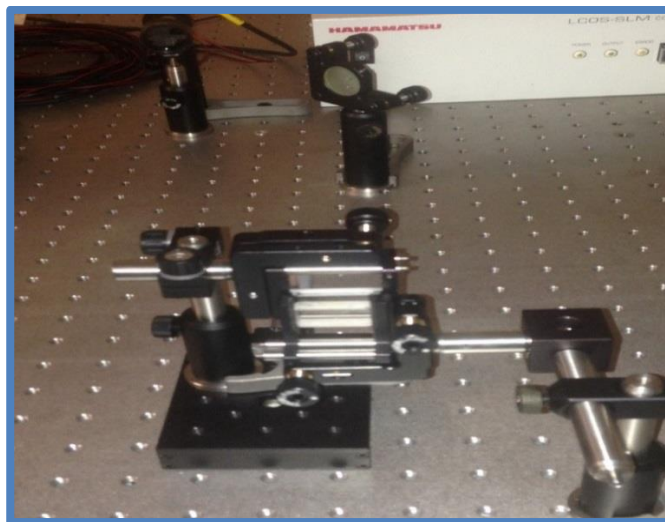


Figure 53 3-D view cylindrical lenses used to spread out and collimate the laser beam.



Figure 54 2-D view of cylindrical lenses aligned in collimation set up.

Before the cylindrical diverging and converging lenses are set up to collimate the laser beam, we need to get an estimate distance between the lenses at which they should be positioned so that the beam can be made exactly parallel. In order to achieve this a software simulator is used to simulate the exact situation. The lenses focal lengths are chosen and then positioned in the Gaussian beam simulator at different distances from each other until the beam becomes parallel. According to the Gaussian, beam simulator in figure 55 the beam initially spreads out and then it is collimated, made parallel, before it is refocused. From the Gaussian, beam simulator we can see that the two cylindrical lenses should be separated by approximately 12.5 mm.



Figure 55 Gaussian beam optics simulator.

The laser input beam waist placed in the simulator for simulation purposes only is about 180 μm, but in reality its much more about 9850 μm. In the simulator, the laser beam waist initially drops to 9.8 μm then its spread out to 360 μm by the diverging lens in the X-direction. That is from 180 μm to 360 μm a factor of 2 after collimation. The lenses are rotated to a position of 90 degrees perpendicularly to the X-direction in the setup. To spread out a direction the cylindrical lens has to be perpendicular to that direction and 180 degrees to the direction that remains unchanged.

Therefore, the lenses are aligned at 90 degrees to the X-direction, which must be spread out and 180 degrees to the Y-direction, which remains unchanged.

The cylindrical converging lens collimates the beam and the spherical converging lens following the set up focuses the beam to a spot size of 11  $\mu\text{m}$ . Therefore, we started with an input beam blown up to a waist size of 360  $\mu\text{m}$  and ended up with a laser beam waist of 11  $\mu\text{m}$ . A reduction by a factor of about 32.7 times. In reality with an input beam waist of 9850  $\mu\text{m}$ , we expect an output beam waist of 301  $\mu\text{m}$ . This depending on the focal length of the converging lens or the focusing power of the objective lens used at the end of the setup and its distance from the collimation lenses. In this simulation, a convex lens of 45 mm was used at the end of the setup. However, this is just a simulator to give an approximate idea of what may occur. When we make both axis the same then the laser spot becomes more or less spherical in shape with a diameter of 9850  $\mu\text{m}$  at the input. In reality, the beam may not be focused to a much smaller size than 775 nm at the output because this is limited to the diffraction limit of the laser beam, which has a wavelength of 775 nm.

### **2.17.3 FOCUSING THE X-Y (AXIS) OF THE LASER SPOT ALONG THE Z-DIRECTION WITH THE SPHERICAL CONVEX LENS.**

During the beam collimation process, it is necessary to focus the X-Y axis of the now spherical laser ablation spot. This is because during the collimation process the X and Y-axis of the laser spot are not focused the same way by the spherical convex lens or not by the same amount along the Z-axis. Hence, it is important to find the same focus point for the X and Y-axis of the laser spot along the Z-direction. When the same focus point is found for both the X and Y-axis of the laser spot then you would also get the correct separation distance between the cylindrical lenses, which achieves this. Therefore, the same focus point for the X-Y axis of the laser spot is obtained by varying the separation distance between the cylindrical lenses along the Z-direction.

The X - axis and the Y - axis of the laser spot are focused by the spherical convex lens in both directions, because the lens is spherical and not cylindrical. Subsequently you must operate the cutting at the point where both the focus point of the X - direction and the Y - direction coincide along the Z - axis (that is are the same).

The spherical convex lens must focus the X and Y direction the same way as mentioned above. This can be achieved by playing around with the separation distance between the diverging cylindrical lens and the convex cylindrical lens.

#### **2.17.3.1 ACTUAL PROCESS OF FOCUSING THE X-Y AXIS OF THE LASER SPOT.**

Initially the distance between the two lenses is set to 16.5 mm on the micro meter screw gauge fastened to the prototype board and holding the diverging cylindrical lens as a reference point as can be seen in figure 53. The origin setting on the micrometer screw gauge is 20 mm. This means that the actual distance between the lenses with this setting is  $(20 \text{ mm} - 16.5 \text{ mm} + 10 \text{ mm} = 13.5 \text{ mm})$ . Taking into consideration that the separation distance between the lenses should be measured from the centre of the two cylindrical lenses. Such that the combined thickness of the two lenses is about 10 mm measured with a calliper. Hence the actual separation distance between the centre of the lenses is about 13.5 mm. With this setting (variation along the Y-axis is done) the focus point is found by varying the movement along the Y-axis and the Z-axis and then drilling holes. Then checking for the smallest hole made (focus point) and looking to see if both the X-axis of the laser spot and the Y-axis of the laser spot are both focused the same or are in their smallest dimension on that spot.

With the separation distance between the lenses set at 13.5 mm it is found that for the Y-axis of the laser spot the focus is at a position of 0.1 mm along Z - direction and the focus point for the X – axis of the laser spot is at a position of -3.5 mm along the Z-direction. This means the Y and the X-axis of the laser spot are not focused at the same position along the Z – direction. Therefore, this separation distance between the cylindrical lenses for the collimation process cannot be used.

Then the micrometer screw gauge is set to a value of 17.0 mm, which transpires to a separation distance of  $(20 \text{ mm} - 17 \text{ mm} + 10 \text{ mm} = 13 \text{ mm})$  between the lenses. With this setting the focus for the Y-axis of the laser spot is achieved at a position of 0.1 mm along the Z-direction and the focus for the X-axis of the laser spot is achieved at a position of 2.0 mm along the Z–direction.

Again, the X and Y-axis of the laser spot are not focused at the same position along the Z-direction for this setting. Hence this separation distance is not used either.

**KEYNOTE :**

*Then the micrometer screw gauge is set to a value of 17.5 mm which produces a separation distance of  $(20\text{ mm} - 17.5\text{ mm} + 10\text{ mm} = 12.5\text{ mm})$  between the lenses. With this setting, the focus point for both the X and Y-axis of the laser spot is found to be the same at a position of 0.3 mm along the Z-direction. This is the setting utilised to separate the cylindrical lenses to achieve a near perfect collimation for the laser beam. The focal length of the (first lens) cylindrical diverging lens is -12.5 mm this coincides with the spacing set between the lenses of 12.5 mm at which beam collimation is achieved. Therefore, the spacing between the lenses required to collimate a beam should be equal to the focal length of the first cylindrical diverging lens, if the ratio between focal lengths of the two lenses is equal to a factor of 2.*

Finally for testing purposes the micro meter screw gauge is set to a value of 18 mm which means a separation distance of  $(20\text{ mm} - 18\text{mm} + 10\text{ mm} = 12\text{ mm})$  between the lenses. For this setting the focus for the Y - axis of the laser spot is found to be at a position of 1.1 mm along the Z-direction and the focus for the X - axis of the laser spot is found to be at a position of - 2.0 mm along the Z – direction. The focus point for the X and Y-axis of the laser spot are not at the same position therefore this setting is also not utilized.

With the X and Y- axis of the laser spot focused, the laser can now be used to cut constrictions. Subsequently images will be taken with an optical microscope (OM) and the Atomic force microscope (AFM) to show that the laser ablation spot generated after the laser is focused becomes more round rather than elliptical.

In summary when you have two lenses a cylindrical diverging lens of focal length - 12.5 mm and a cylindrical converging lens of focal length 25 mm with a ratio of 2 between the focal lengths of these two lenses. Then to achieve beam collimation with these lenses the separation distance between the two lenses has to be the absolute value of the focal length of the first diverging lens -12.5 mm.

After the beam collimation process was completed, a spherical convex lens of focal length 45 mm was used to focus the beam and then cut constrictions on the sample.

#### **2.17.4 CONSTRICTIONS CUT ON TEST STEEL SAMPLES AFTER THE BEAM COLLIMATION PROCESS.**

After the design of the S-shaped constriction was completed and the beam collimation process was perfected then initial constrictions were cut on steel samples made available at the national laser center at CSIR, Pretoria South Africa.

The reason for initially using steel to fabricate the constrictions was to test the design and coding process of the S-shaped constrictions before applying it to the real superconductive YBCO material. This material is very expensive about R40000 for 24, 10 mm X 10 mm samples. Hence, it was deemed necessary to perfect the design process of the constrictions on steel before applying it to YBCO.

The other point to take note of is that the ablation threshold for steel is different from that of the YBCO material. For steel, the laser starts to cut or ablate at a power of about 50 mW as will be seen later while for YBCO thin film the ablation threshold is as little as 1 mW. The ablation threshold for these materials was determined through trial and error and by making repetitive cuts to see at what power is the surface material completely removed.

As a result, constrictions were cut on steel at different levels of laser power namely; 483 mW, 223.7 mW, 97.3 mW and 37.5 mW. The following images taken with an optical microscope (OM) show the achieved S-shaped constrictions fabricated on steel. By varying the levels of laser power it becomes possible to verify the theory obtained from literature that as the level of laser power decreases and therefore the laser energy applied decreases then the size of the laser ablation spot cut on a material will decrease.

##### **2.17.4.1 LASER POWER SET AT 483 mW**

At this power, setting of 483 mW the laser ablation width is 40  $\mu\text{m}$ , the width of the constriction is 37  $\mu\text{m}$  and the separation distance between the centre of the laser ablation spots set in the G-code program is 82  $\mu\text{m}$  as can be seen in figure 56. The separation distance is occupied by the laser ablation width of 40  $\mu\text{m}$  and the width of the constriction 37  $\mu\text{m}$ .

Therefore we can conclude that the;

*width of the constriction =*

*separation distance between the laser ablation spots – laser ablation widths (7)*

In practice, this equation is not achieved exactly.

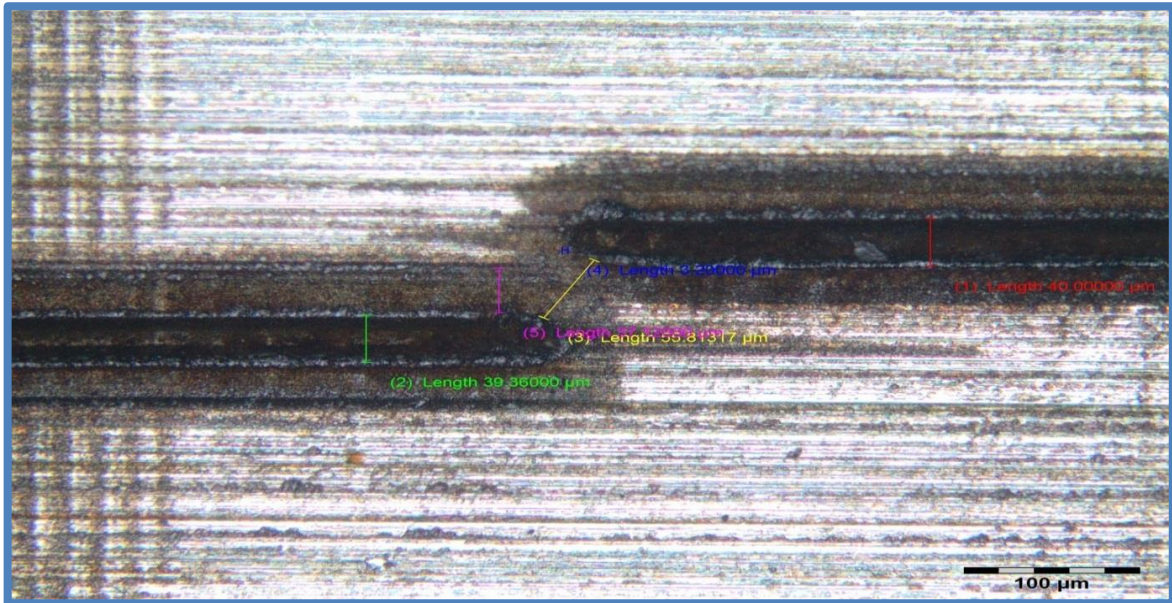


Figure 56 Test constriction cut on steel with a laser power setting of 483 mW.

#### 2.17.4.2 LASER POWER SET AT 223 mW

Figure 57 shows that when the power is reduced to 223 mW the ablation width drops to 30 μm.

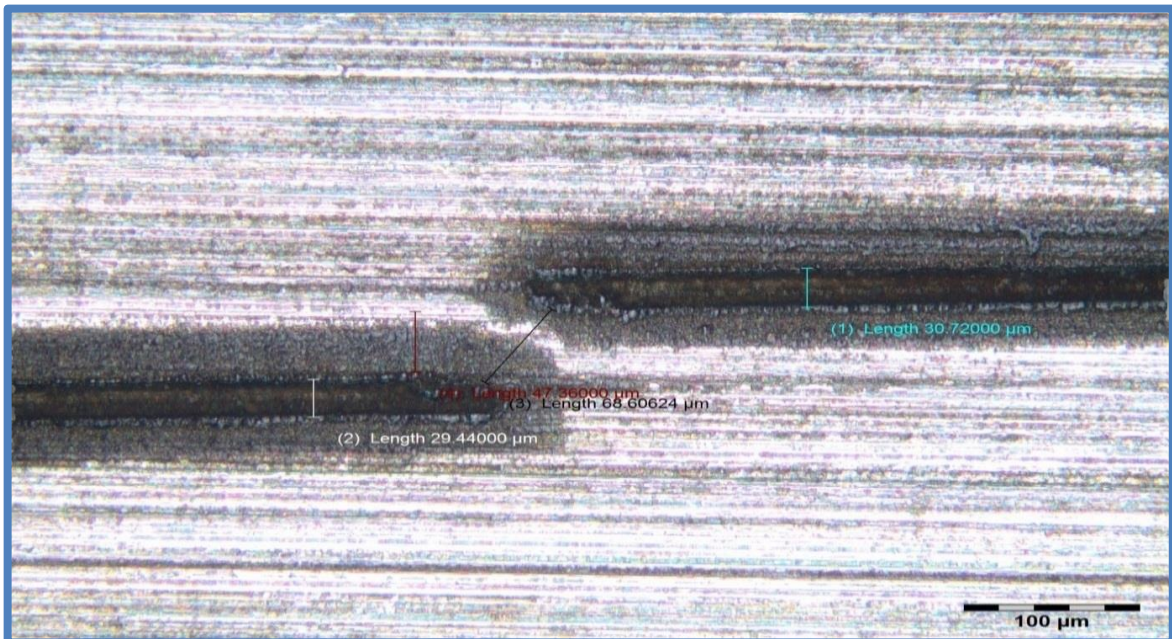


Figure 57 Test constriction cut on steel with a laser power setting of 223.7 mW.

### 2.17.4.3 LASER POWER SET AT 37 mW

In figure 58, the power is reduced to 37 mW and very little or almost no ablation occurs at this power setting. This is because at this power level although we can see some amount of ablation, the material is not completely removed. Only the surface of the steel is slightly ablated. Therefore, the ablation threshold for steel should be above 40 mW with this laser.

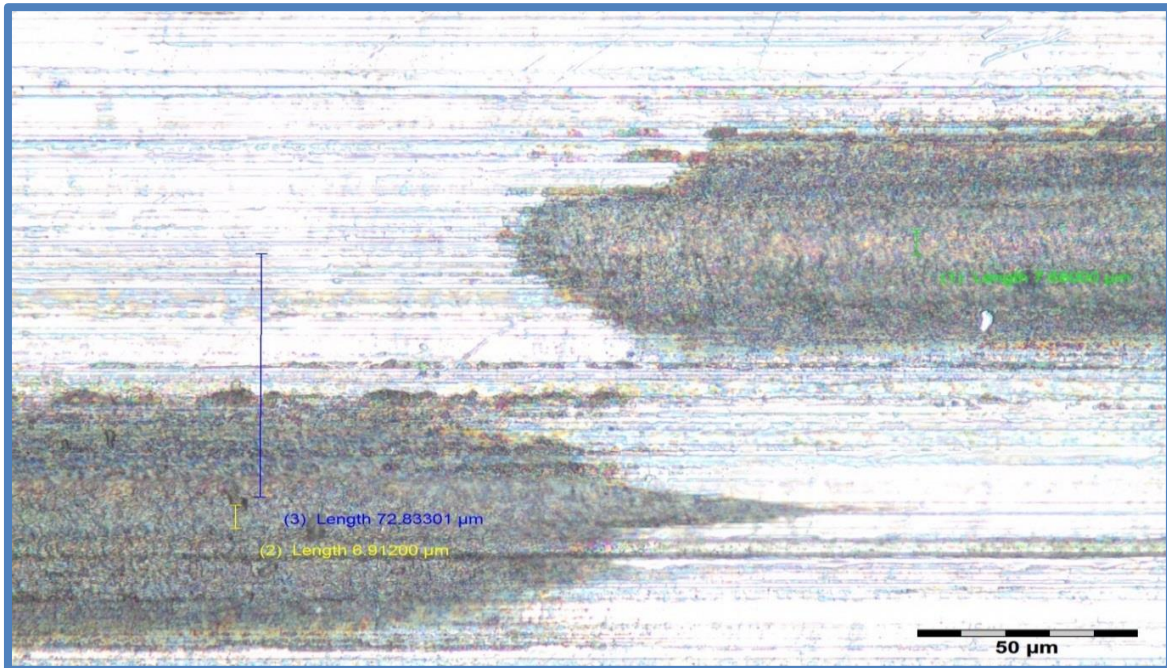


Figure 58 Test constriction cut on steel with a laser power setting of 37.5 mW.

### 2.17.5 AFM IMAGES OF CONSTRICTIONS CUT ON STEEL AFTER THE BEAM COLLIMATION PROCESS.

In the previous section the constrictions were cut on steel and then images were taken of these constrictions using the optical microscope (OM). In this section some additional constrictions were cut on steel at varying power levels and images were taken of these constrictions using the Atomic Force Microscope (AFM) instead.

#### 2.17.5.1 LASER POWER SET AT 220 mW

The cylindrical lenses of focal length -12.5 mm and 25 mm were separated by a distance of 12.75 mm in the beam collimation set up. At this spacing between lenses, the laser beam is not well focused and therefore the image of the constriction in the AFM is not very sharp but slightly blurred.

In the G-code program, the separation distance between the laser ablation spots is set at 60  $\mu\text{m}$ . The AFM image (amplitude – line fit) in figure 59 shows us that the laser ablation spot size is 30.49  $\mu\text{m}$  at this power level. The constriction width is 30.89  $\mu\text{m}$  as can be seen in figure 60 and the constriction length is 25.74  $\mu\text{m}$  shown in figure 58.

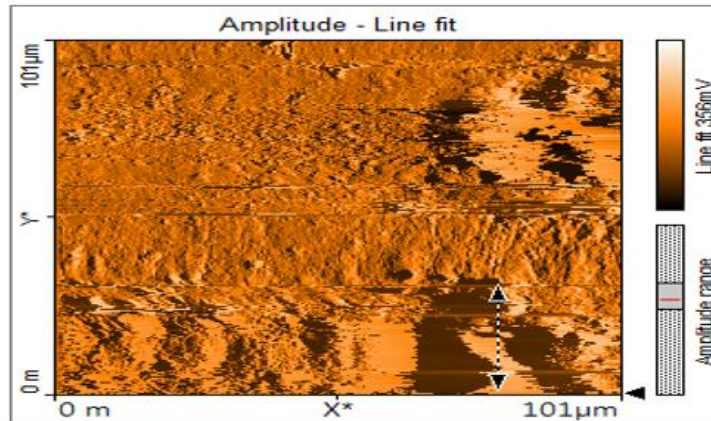


Figure 59 AFM image showing the laser ablation width is 30.49  $\mu\text{m}$  at a power setting of 220 mW.

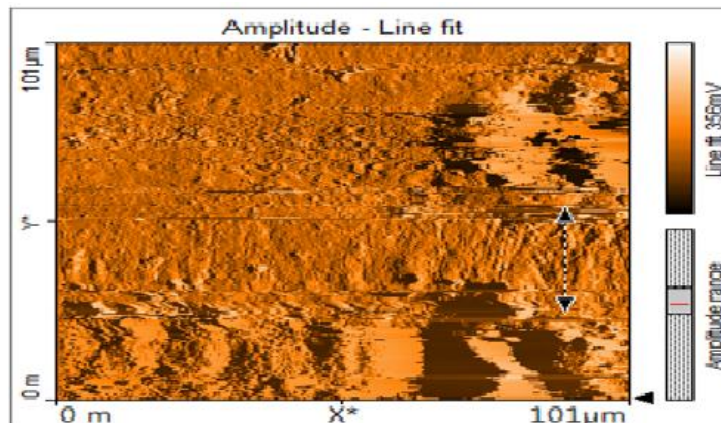


Figure 60 AFM image showing the constriction width is 30.89  $\mu\text{m}$  at a power setting of 220 mW.

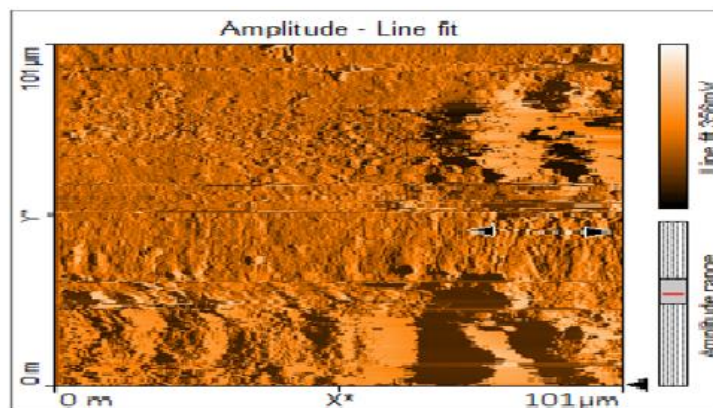


Figure 61 AFM image showing the constriction length is 25.74  $\mu\text{m}$  at a power setting of 220 mW.

From the images taken by the AFM one can see that there is an outer ablation layer around the central laser ablation spot, which represents the laser heating effects on the constriction. In addition, there is what we call interference fringes caused by the reflection of laser light between the cylindrical lenses used for beam collimation. This occurs because the lenses are not silver coated. The cylindrical lenses used for beam collimation have a small geometric dimension that is 10 X 10 mm. This is very close to the laser spot size of 9.85 mm emanating from the source. The laser beam spot is therefore very close to the edges of the cylindrical lens causing spherical aberration of the spot. Since a lens consists of many small lenses each refracting and collimating the laser beam, this produces many small laser ablation spots that overlap each other. As a result, a large diffuse spot is created not suitable for fabricating nano constrictions. However, these problems can be solved by procuring new cylindrical lenses for the beam collimation process. Ones, which are silver coated and have a geometric aperture of 25 X 25 mm which is much bigger than the laser beam waist from the laser source of 9.85 mm.

#### 2.17.5.2 LASER POWER SET AT 104 mW

Again the cylindrical lenses in the beam collimation set up of focal length -12.5 mm and 25 mm, aperture size of 10 mm X 10 mm where separated by a distance of 12.75 mm in order to cut the constrictions on steel at power setting of 104 mW.

As a result of the power setting the laser ablation spot size reduces to 25.75  $\mu\text{m}$  as can be seen in figure 62. The constriction width increases to 35.24  $\mu\text{m}$ , because the separation distance between the laser ablation spots set in the G – code program has not been changed and is still 60  $\mu\text{m}$ . The length of the constriction achieved is 15.05  $\mu\text{m}$  as seen in figure 64.

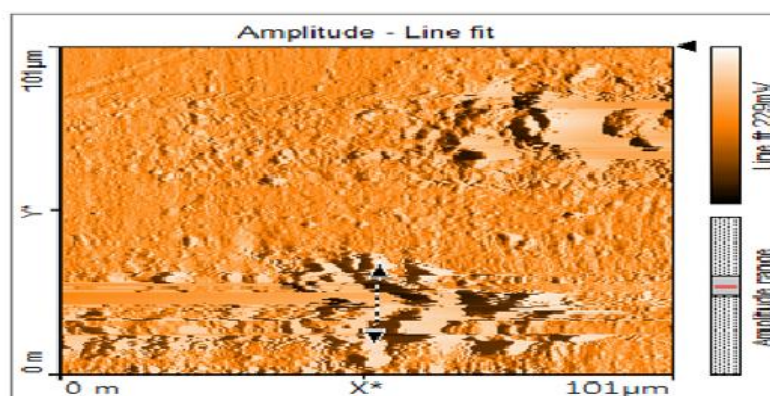


Figure 62 AFM image showing the laser ablation width is 25.75  $\mu\text{m}$  at a power setting of 104 mW.

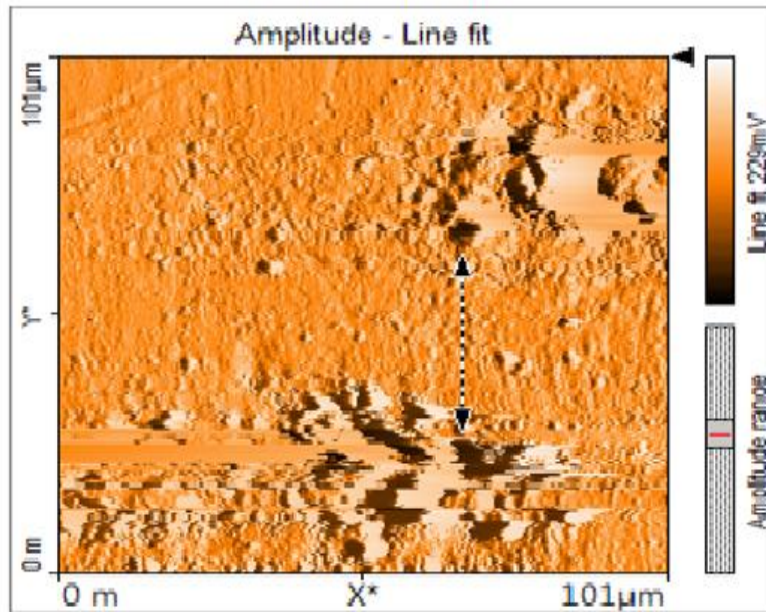


Figure 63 AFM image showing the constriction width is 35.24  $\mu\text{m}$  at a power setting of 104 mW.

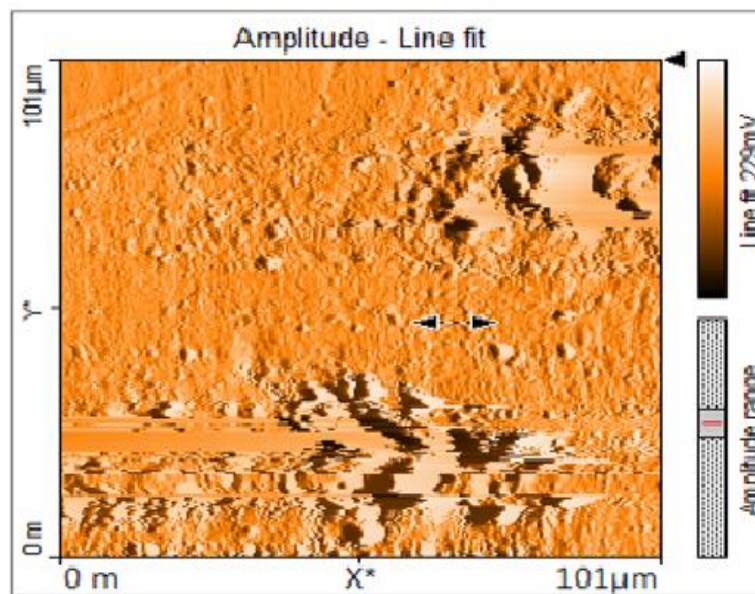


Figure 64 AFM image showing the constriction length is 15.05  $\mu\text{m}$  at a power setting of 104 mW.

#### 2.17.6 AFM IMAGES OF CONSTRICTIONS CUT ON STEEL WITH THE LASER CONTROL TIMING SETTINGS CHANGED.

The timing settings on the control console are used to achieve a phase lock between the master frequency (pumped diode laser) and the fibre oscillator frequency (Erbium doped fibre). When the timing settings on the control console are changed, then the profile distribution of the laser will change and the peak power that can be achieved by the laser changes slightly.

The timing settings are set on the time console for the laser. The timing settings can be changed by changing the values on the 3 delay switches.

In this case, the timing settings were changed from the original timing settings which were;

Delay 1      070 90

Delay 2      069 a1

Delay 3      069 6c

to the new timing settings which are;

Delay 1,     070 90

Delay 2,     069 61

Delay 3,     069 fc

As a result of changing the timing settings of the laser the profile distribution of the laser changed on the oscilloscope. This was done to see if the variation of the timing delay would have a marked change on the shape of the laser ablation spot and hence the shape of the constrictions cut. With the timing settings changed, the laser was used to cut a test constriction on a steel surface once again with the following settings;

The cylindrical lenses of focal length -12.5 mm and 25 mm where separated by a distance of 12.75 mm in the beam collimation set up. The focus point of the X and Y- axis of the laser spot was found at a relative position of 6.0 mm along the Z- direction. The laser power was set at 190 mW and the separation distance between the laser ablation spots was set at 60  $\mu\text{m}$  in the G-code program. With these settings, the following images of the constriction achieved are shown in figures 65 and 66.

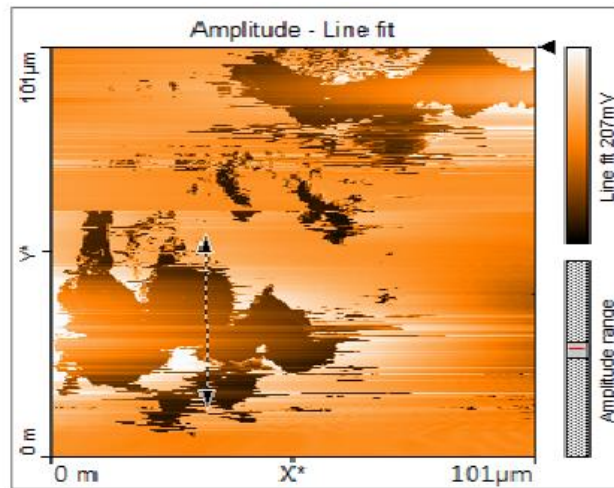


Figure 65 AFM image of the constriction achieved with the Laser ablation spot size being  $43.56 \mu\text{m}$  the laser power setting is 190 mW.

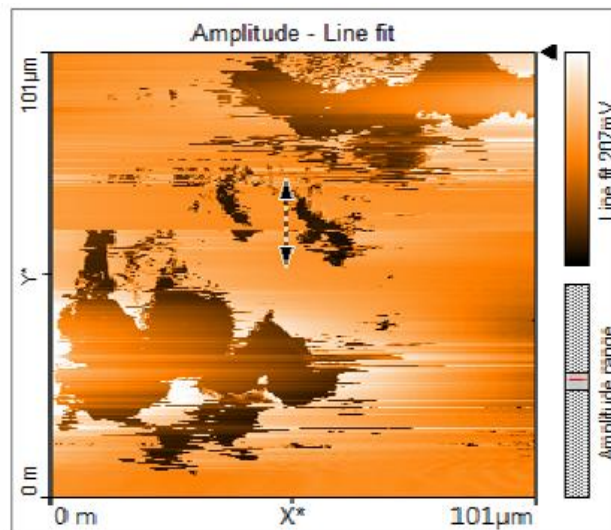


Figure 66 AFM image of the constriction achieved with a constriction width of  $20.19 \mu\text{m}$ , at a power setting of 190 mW.

For the laser settings specified above, the constrictions achieved on steel show a laser ablation spot size of  $43.56 \mu\text{m}$  and a constriction width of  $20.19 \mu\text{m}$  when the separation distance between the laser ablation spots set in code is  $60 \mu\text{m}$ . These values verify equation (7) in the previous section to some extent.

By direct substitution of values into equation (7), the width of the constriction should have been  $16.44 \mu\text{m}$ . However, the achieved width of  $20.19 \mu\text{m}$  is not far off from the calculated value. There are many factors that could have influenced this slight difference such as temperature variation in the room where machining is done, vibrations in the room, airflow, and slight imperfections in the movement of the translation stage.

## **KEYNOTE AREA:**

*By varying, the timing settings of the laser the profile distribution of the laser and its actual peak power changed as observed on the oscilloscope. The change is also observed by the fact that the laser ablation spot has become poorly shaped as can be seen in figures 65 and 66. From previous figures such as figure 59 one takes note that at a power setting of 220 mW an ablation spot size of 30.49  $\mu\text{m}$  is achieved. However, in this experiment after the change in timing settings and a slight increase in the actual peak power we achieved a much larger laser ablation spot size of 43.56  $\mu\text{m}$  at a power setting of 190 mW. In conclusion, the laser timing settings play a marked role on both the shape of the constriction obtained and the size of the laser ablation spots on the same material.*

### **2.17.7 FUTURE WORK**

#### **2.17.7.1 NEW CYLINDRICAL LENSES WITH LARGER APERTURES TO BE USED FOR THE BEAM COLLIMATION PROCESS.**

New lenses were ordered with the following specifications;

1. Diverging cylindrical lens of focal length - 50 mm, converging cylindrical lens of focal length 100 mm.
2. The aperture of the lenses was increased from 10 X 10 mm lenses to 25 X 25 mm lenses. This was done because the diameter of the laser beam waist is 9.85 mm, which is very close to the aperture of the initial cylindrical lenses of 10 mm X 10 mm. This can cause spherical aberration of the laser spot. Therefore, to improve the beam collimation process and to prevent spherical aberration cylindrical lenses of 25 mm X 25 mm aperture were used in the subsequent experiments.
3. The new cylindrical lenses were procured with a silver coating to reduce reflections between the lenses. These reflections can produce a poorly shaped laser ablation spot. In addition, interference fringes originating from the laser source can be reproduced through these reflections.

Before the new cylindrical lenses, were utilized to fabricate constrictions as part of the beam collimation set up. Their application was simulated in the Gaussian beam

software. The optical set up with the new cylindrical lenses to be used for the fabrication of further constrictions can be seen in the Gaussian beam software in figure 67. According to the Gaussian beam software in figure 67, the new cylindrical lenses of focal length - 50 mm and 100 mm should be separated by 58 mm to achieve beam collimation. However, this is incorrect. In order to achieve perfect beam collimation, the cylindrical lenses should be separated by 50 mm.

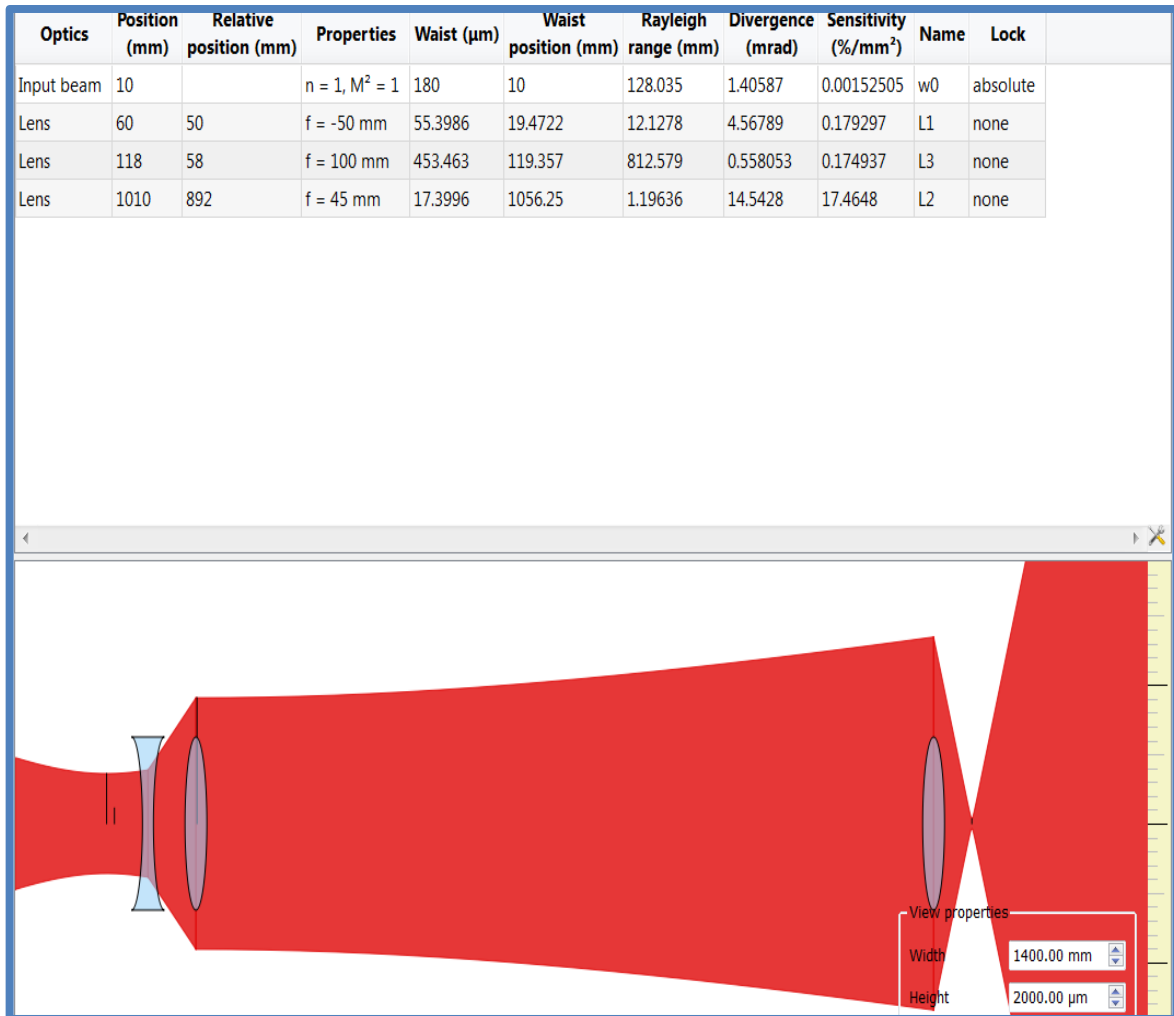


Figure 67 New cylindrical lenses for beam collimation in the Gaussian beam simulation software.

## 2.18 INITIAL CONSTRICTIONS FABRICATED ON THE YBCO THIN FILM.

The first constrictions or bridges made on the YBCO thin film were made on the YBCO thin film based on the LAO substrate. The laser ablation spots on these first constrictions were poorly shaped. The Laser ablation spots had a poor shape for two reasons:

1. When the laser is focused onto the sample its necessary to be careful in choosing the focus point of the laser along the Z-direction that is the smallest hole drilled. The focus spots of the laser have different shapes, sometimes you have two circles intertwined as can be seen in figure 68. This will give a sort of a projection on the laser ablation spot when its moved either in the forward or reverse direction.

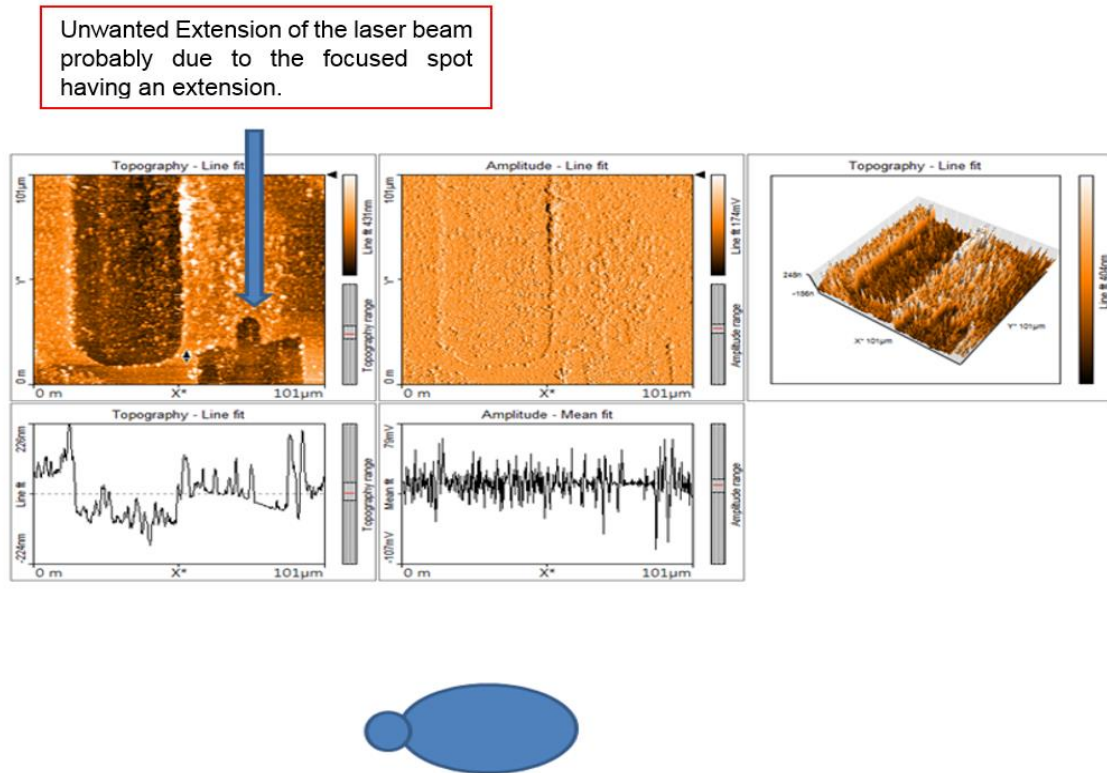


Figure 68 Unwanted extension of the laser beam. When its moved either in the forward direction or reverse direction viewed through the Atomic Force microscope (AFM).

2. The second reason is that the initial cylindrical lenses used for beam collimation are not perfect. These cylindrical lenses of aperture 10 mm X 10 mm are almost the same size as the laser beam diameter of 9.85 mm. These lenses should not be of the same diameter as the laser beam effluent from the laser source. The laser beam diameter should be smaller relative to the dimensions of the lenses. In this case, the lenses had an aperture of 10 X 10 mm and the beam waist 9.85 mm. The laser beam waist is too close to the edges of the lenses used. Since a lens is essentially a combination of many lenses this causes different sections of the lens to refract the beam and converge the beam separately producing two or more spots after focusing which makes an overall bigger spot and a poor beam shape. This is referred to as spherical aberration as can be seen in figure 68.

### **2.18.1 METHODS USED TO IMPROVE THE LASER ABLATION SPOT SHAPE.**

When the lenses used for beam collimation were replaced by larger lenses of 25 X 25 mm the shape of the laser ablation spot improved a great deal and became smaller. This improvement occurs because only the central part of the cylindrical lenses now refracts and converges the beam hence spherical aberration is reduced considerably.

Secondly, an iris diaphragm with a manually adjustable aperture made of black rubber was used to reduce the diameter of the laser beam waist that passes through to the final spherical convex lens. The diameter of the laser beam waist that passes through to the final convex lens was reduced from a diameter of 5000  $\mu\text{m}$  (5mm) to 2550  $\mu\text{m}$  (2.55 mm) to 1500  $\mu\text{m}$  (1.5 mm) by the aid of the iris (manually adjusted aperture). The iris is placed at a specific distance after the beam collimation setup and it reduces the diameter of the laser beam that goes through to the sample. The iris improves the laser ablation spot shape significantly by removing unwanted sections of the laser coming from the source. The iris removes uneven and unwanted sections of the laser beam that lie in the outer periphery of the laser beam waist. Therefore, only the central core of the laser beam waist and the central part of the laser profile with the highest light intensity are able to pass through to the convex lens. After this central core of the laser beam is focused, it can then be used to cut the constrictions and ablate the thin film. The diameter of the iris aperture is measured with digital calipers when it is being set.

### **2.18.2 AFM (ATOMIC FORCE MICROSCOPE) SCANNING OF THE CONSTRICTIONS.**

In a very simplified explanation, the Atomic Force Microscope (AFM) was used in combination with optical images from an optical microscope (OM) to determine the dimensions of samples fabricated. Images were initially taken with an optical microscope to get an idea of the laser ablation spot size, the width and length of the constrictions cut and then verified with the AFM. Subsequently with this information, settings such as the separation distance between the laser ablation spots were adjusted in the G-code program to fabricate the desired constriction widths.

Cuts of constrictions were then made and measurements were taken again with an atomic force microscope to validate the exact dimensions of the constrictions that have been fabricated.

The process of taking images with the AFM includes mounting a cantilever tip on a cantilever head. This tip moves back and forth over the scan area selected by yourself. Normally one would set a scan area in the AFM software and the cantilever tip moves over the span of that area. Before scanning the image, the sample is placed just underneath the cantilever tip, which will focus on the sample and scan over the area of interest.

Generally, there are two types of operational modes used to scan the samples. There is the contact mode and the tapping mode. In the case of constrictions fabricated on a soft YBCO material, the tapping mode is utilised. The reason for using the tapping mode is that the YBCO thin film and the constriction made are very sensitive to contact and can be easily scratched or damaged. Hence, the tapping mode will not damage the small (micron, sub-micron and nano) constrictions fabricated. The contact mode comes into full contact with the constriction and may damage the constriction. The tapping mode taps slightly and does not damage the constriction.

Figure 69 shows an image of the Atomic Force Microscope used. This AFM was manufactured by the “Nanosurf” company and is called the Nanosurf FlexAFM, modelled in 2011. The image shows the main parts of the AFM, namely; the camera, the AFM cantilever head and the iso-stage. The iso-stage is used to stabilize the image taking process and absorbs any vibrations from the surrounding environment where the measurement is being done. During the movement of the cantilever head and tip over the sample, the iso-stage also moves slightly to dampen and prevent vibrations coming from the surroundings from being transferred to the movement of the cantilever tip. This will severely affect the images taken and transmit noise to the image taken making the AFM image blurred.



Figure 69 Overall diagram of the AFM (Atomic Force Microscope) block.

Figure 70 shows the cantilever tip of the AFM directly above the S-shaped constrictions that were designed. The cantilever tip scans over the constriction area consisting of two laser ablation spots. The cantilever tip is positioned precisely above the relevant section of the constriction. This would enable us to determine the width of the constriction after the scan is completed. The sample is positioned such that the cantilever tip scans transversely or at angle of 90 degrees to the laser ablation spots, across the constriction. The image is developed such that it is possible to determine the exact width of the constriction between the laser ablation spots.

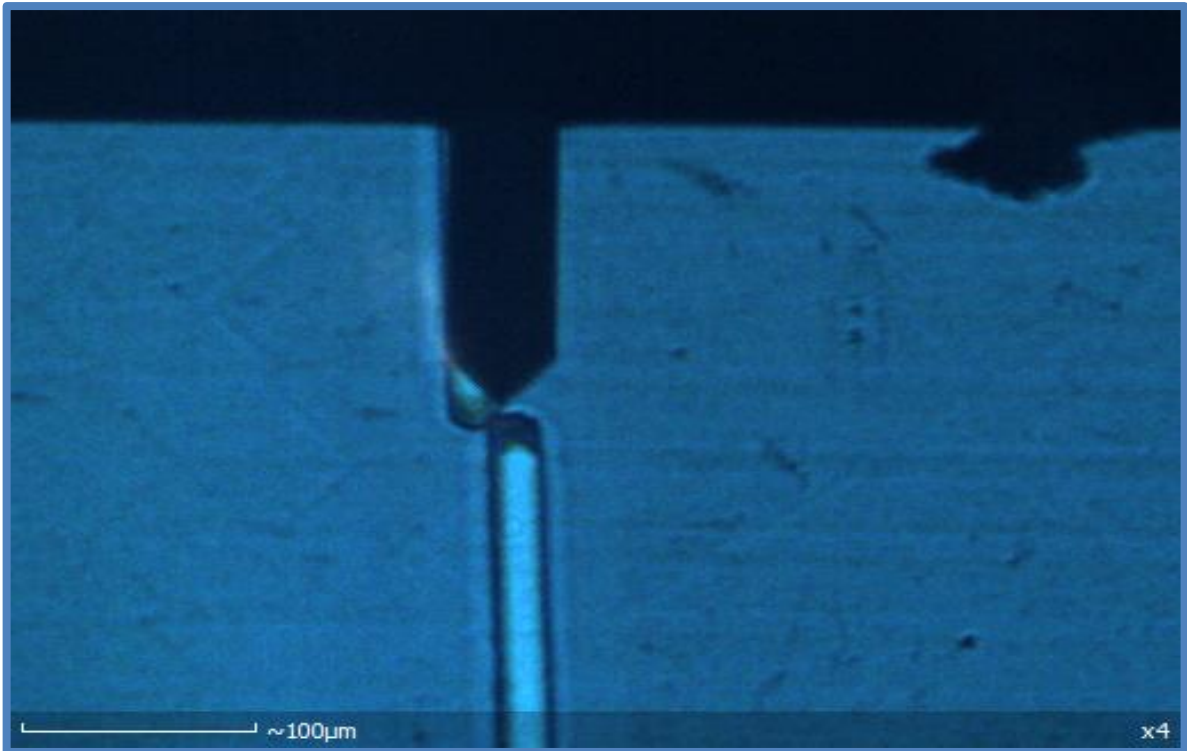


Figure 70 Atomic Force Microscope scanning process with the cantilever tip above a constriction.

### **2.18.3 AFM IMAGES OF THE INITIAL CONSTRICTIONS FABRICATED ON THE YBCO THIN FILMS WITH A POORLY SHAPED LASER ABLATION SPOT.**

This section discusses the first constrictions that were fabricated on the YBCO thin film. Upto this point all the previous constrictions had been fabricated on steel. All the tests for the design of the S-shaped constrictions had been done on a steel surface. These first constrictions were fabricated on a YBCO thin film on an LAO substrate. The thickness of the YBCO thin film is 200 nm and the thickness of the substrate is about 500  $\mu\text{m}$ . The initial constrictions fabricated had a poorly shaped laser ablation spot. However, measures were taken to improve on these.

The initial constrictions were fabricated with the laser settings listed on the following page and numbered (1-4) and AFM images were taken of the resulting constrictions. The laser power settings were varied in this manner because the ablation threshold for YBCO was not yet determined. In other words, we had not yet determined what laser power if applied to the YBCO sample would be too much and cut into the substrate, and what laser power will be too little and not ablate the material.

Therefore the following settings were applied in trial and error mode.

1. Laser power 5 mW and a laser ablation spot separation distance of 90  $\mu\text{m}$ ,
2. Laser power of 5 mW and a laser ablation spot separation distance of 60  $\mu\text{m}$ ,
3. Laser power of 22.7 mW and a laser ablation spot separation distance of 60  $\mu\text{m}$
4. Laser power of 11.65 mW and a separation distance of 25  $\mu\text{m}$ .

### 2.18.3.1 CONSTRICTION FABRICATED WITH A LASER POWER SETTING OF 5 mW AND A SEPARATION DISTANCE BETWEEN THE LASER ABLATION SPOTS OF 90 $\mu\text{m}$ .

In this constriction, the laser power was set at 5 mW and the separation distance between the laser ablation spots was set at 90  $\mu\text{m}$ . With these settings, the laser ablation spot size achieved was 31.68  $\mu\text{m}$ . The width of the constriction as a result of this was 60.19  $\mu\text{m}$ . These results can be seen in figure 71 and 72. At a power setting of 5 mW the YBCO thin film was substantially ablated as can be seen from the 3-D images in the figures without cutting into the substrate. The laser ablation spot size is measured in figure 71 in the AFM profile distribution curve between the black arrows.

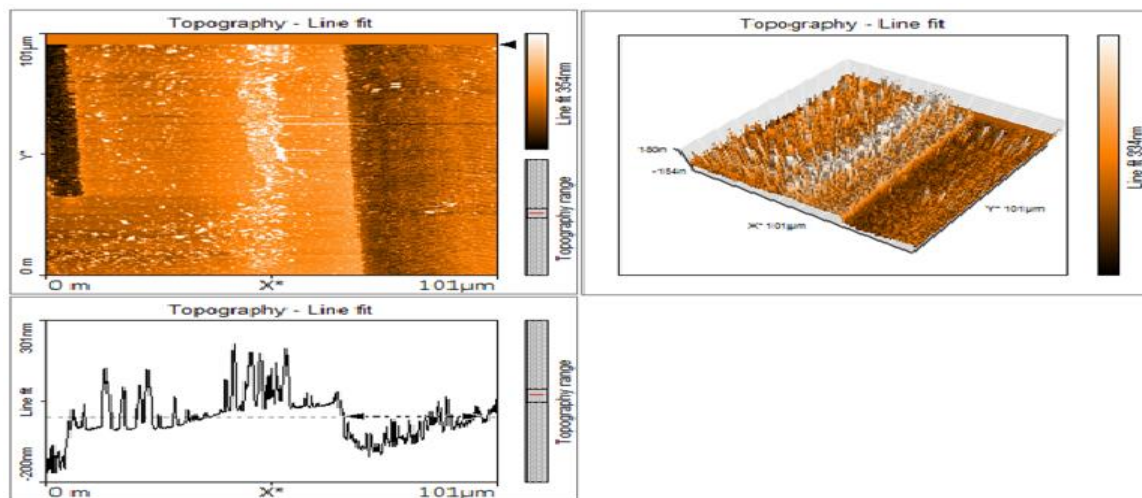


Figure 71 AFM image showing the laser ablation spot size is 31.68  $\mu\text{m}$ .

The constriction width can be observed in figure 72. The laser ablation spots are however poorly shaped with extensions making it slightly difficult to determine the constriction width. With the separation distance of 90  $\mu\text{m}$  and a laser ablation spot of 31.68  $\mu\text{m}$  the constriction width is too large, therefore, the laser ablation spots are brought closer in the next fabrication by changing the separation distance in the G-code.

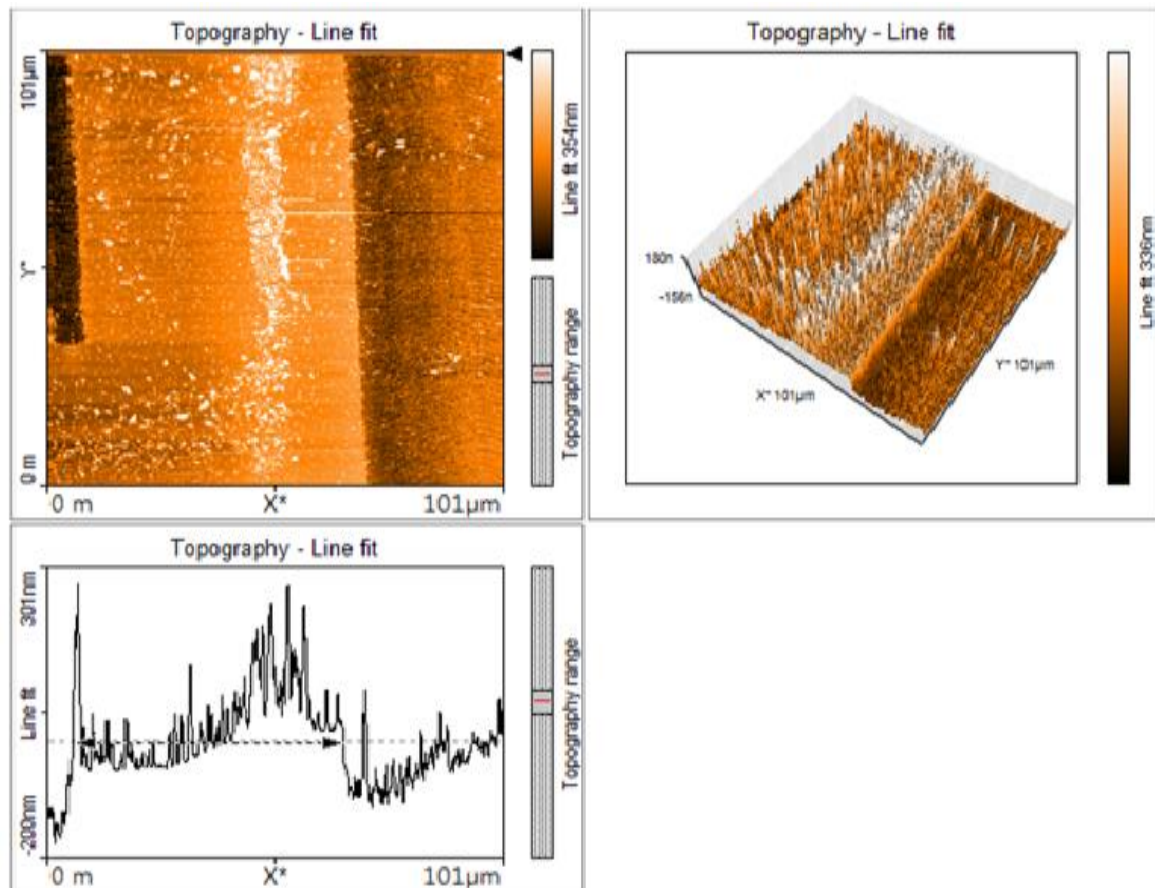


Figure 72 AFM image of the constriction showing constriction width is 60.19  $\mu\text{m}$ .

### 2.18.3.2 CONstriction FABRICATED WITH A LASER POWER SETTING OF 5 mW AND A SEPARATION DISTANCE BETWEEN THE LASER ABLATION SPOTS OF 60 $\mu\text{m}$ .

In this constriction, the separation distance between the laser ablation spots is changed from 90  $\mu\text{m}$  to 60  $\mu\text{m}$  in the G-code to bring the laser ablation spots closer together to achieve a narrower constriction and exhibit control in the program code. The constriction in this case is cut with a laser power setting of 5 mW. Therefore, the laser ablation spot size does not change by much from the constriction in the previous section and is 34.05  $\mu\text{m}$  as can be seen in figure 73. With the separation distance reduced to 60  $\mu\text{m}$  the constriction width reduces to 30.49  $\mu\text{m}$  as can be seen in figure 74.

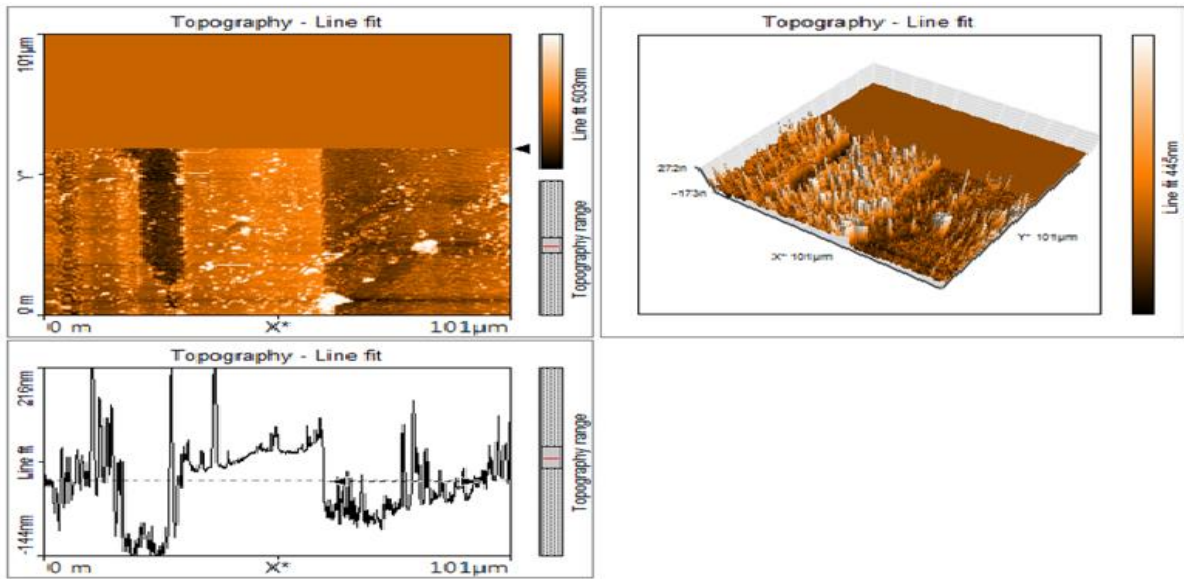


Figure 73 AFM image showing the laser ablation spot size is 34.05  $\mu\text{m}$ .

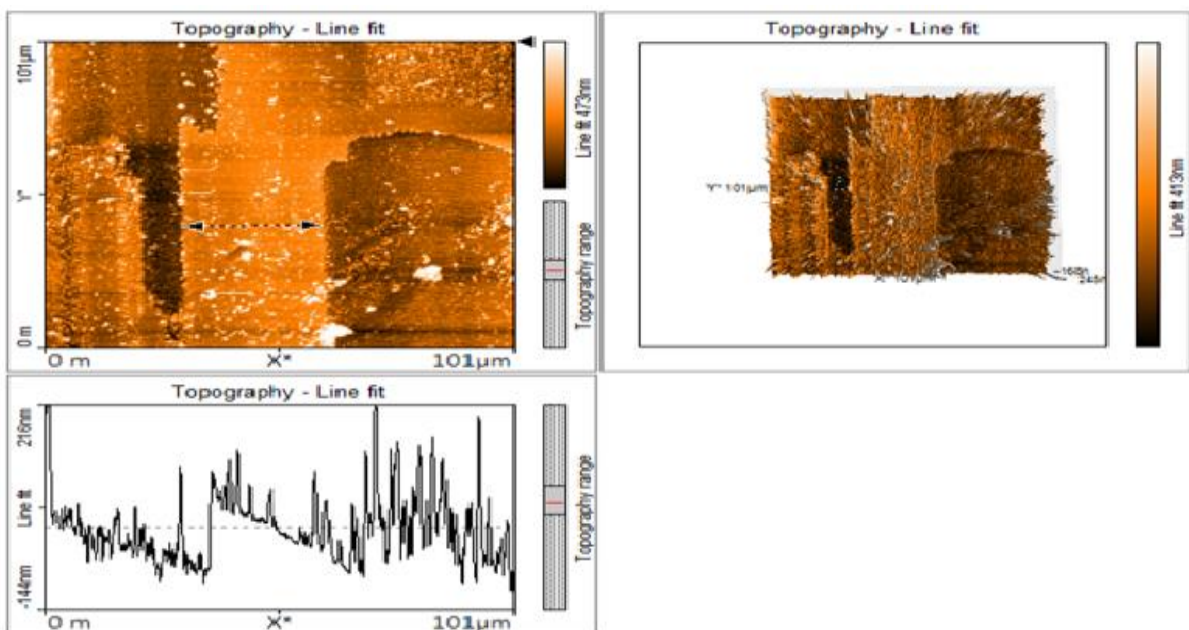


Figure 74 AFM image showing constriction width is 30.49  $\mu\text{m}$ .

The constriction length is determined to be 53.46  $\mu\text{m}$  as can be seen in figure 75. This length is extremely large and may not be correct because the shape of the ablation spot is very poor as can be seen in figure 75. The laser ablation spot does not have a good spherical shape instead: it has an extension at the tip.

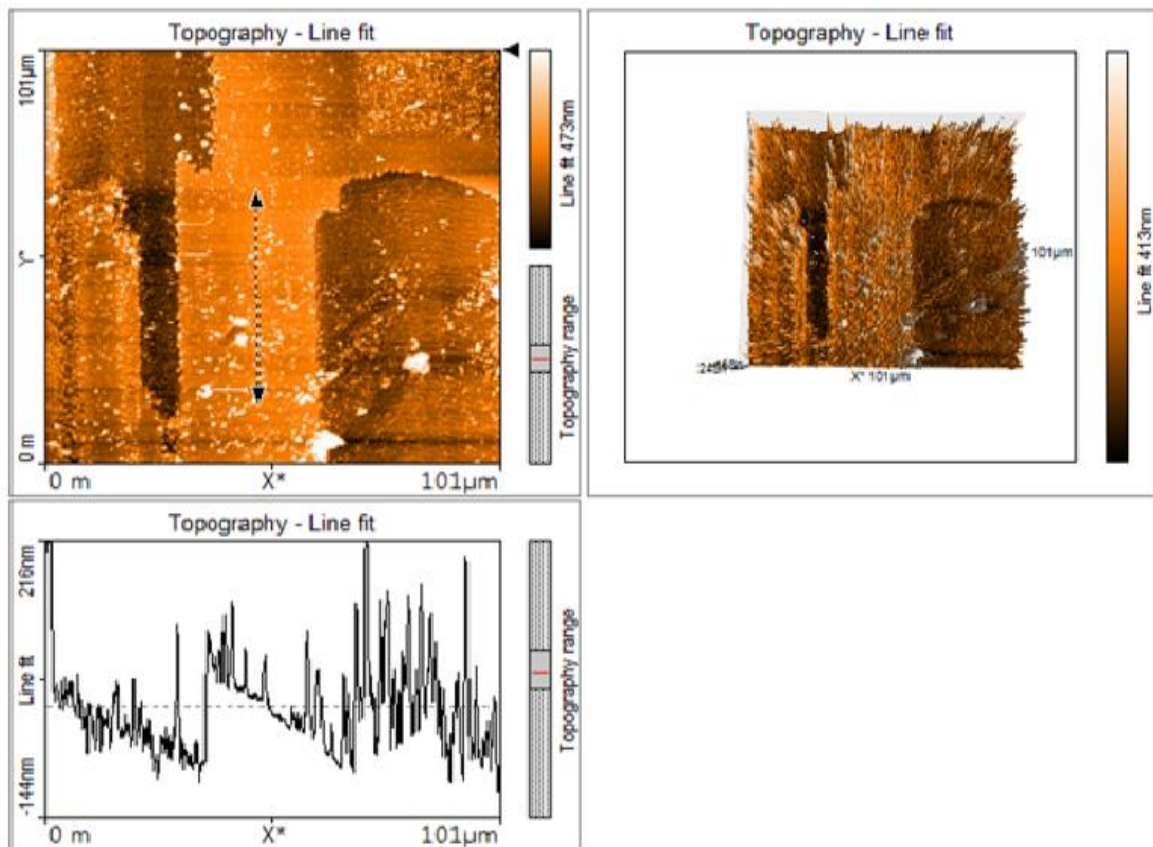


Figure 75 AFM image showing the constriction length is 53.46  $\mu\text{m}$ .

### 2.18.3.3 CONstriction FABRICATED WITH A LASER POWER SETTING OF 22.7 mW AND A SEPARATION DISTANCE BETWEEN THE LASER ABLATION SPOTS OF 60 $\mu\text{m}$ .

In this constriction, the power was set at 22.7 mW and the laser ablation spots were separated by a distance of 60  $\mu\text{m}$ . This power level exceeds the ablation threshold of YBCO thin film largely. With this power setting of 22.7 mW the laser cuts into the substrate material in this case LAO substrate. This is made evident by the fact that there are now two laser ablation fringes as can be seen in the topography line fit of figure 76. The one is a thick black central line, which represents the laser cutting into the substrate, and the outer fringe represents the section where the laser only ablates the YBCO material. Another point that can be made is that in this case the laser ablation spots were separated by a distance of 60  $\mu\text{m}$  in the G-code while the laser ablation spots at this power setting have an ablation width of about 90  $\mu\text{m}$  exceeding the separation distance. Hence, the ablation spots overlap each by a dimension of 28.51  $\mu\text{m}$  as can be seen in figure 76.

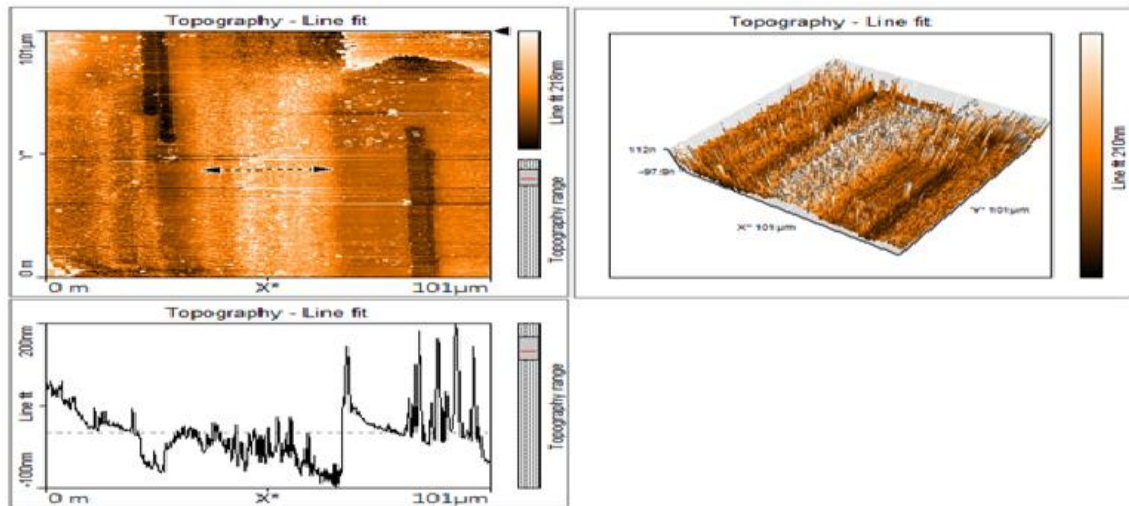


Figure 76 AFM image of a constriction showing the overlapping width to be 28.51  $\mu\text{m}$ .

#### 2.18.3.4 CONSTRICTION FABRICATED WITH A LASER POWER SETTING OF 11.65 mW AND A SEPARATION DISTANCE BETWEEN LASER ABLATION SPOTS OF 25 $\mu\text{m}$ .

For this constriction, the laser power was set at 11.65 mW and the separation distance between the laser ablation spots was set at 25  $\mu\text{m}$  in the G-code program. At this power setting the laser ablation spot size increases to 62.96  $\mu\text{m}$ . This can be seen in between the black arrows in the topography line fit of figure 77. Since the separation distance between the laser ablation spots of 25  $\mu\text{m}$  is less than the laser ablation spot size of 62.96  $\mu\text{m}$ . Then the laser ablation spots overlap each other this can be seen in figure 78. The width of the overlapping area is 38.41  $\mu\text{m}$ .

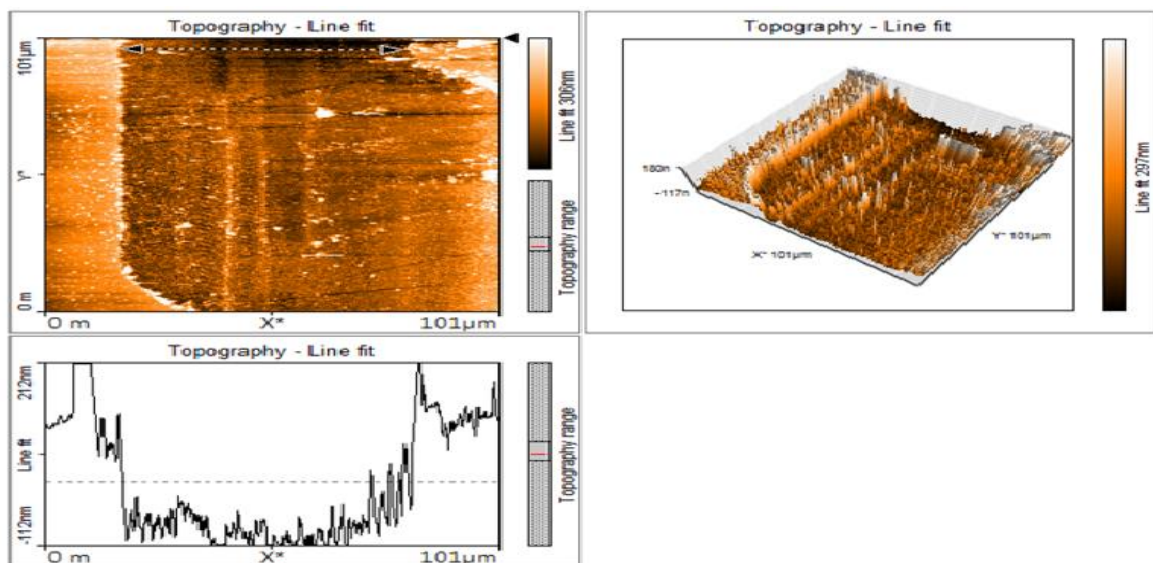


Figure 77 AFM image showing the laser ablation spot size of the constriction is 62.96  $\mu\text{m}$ .

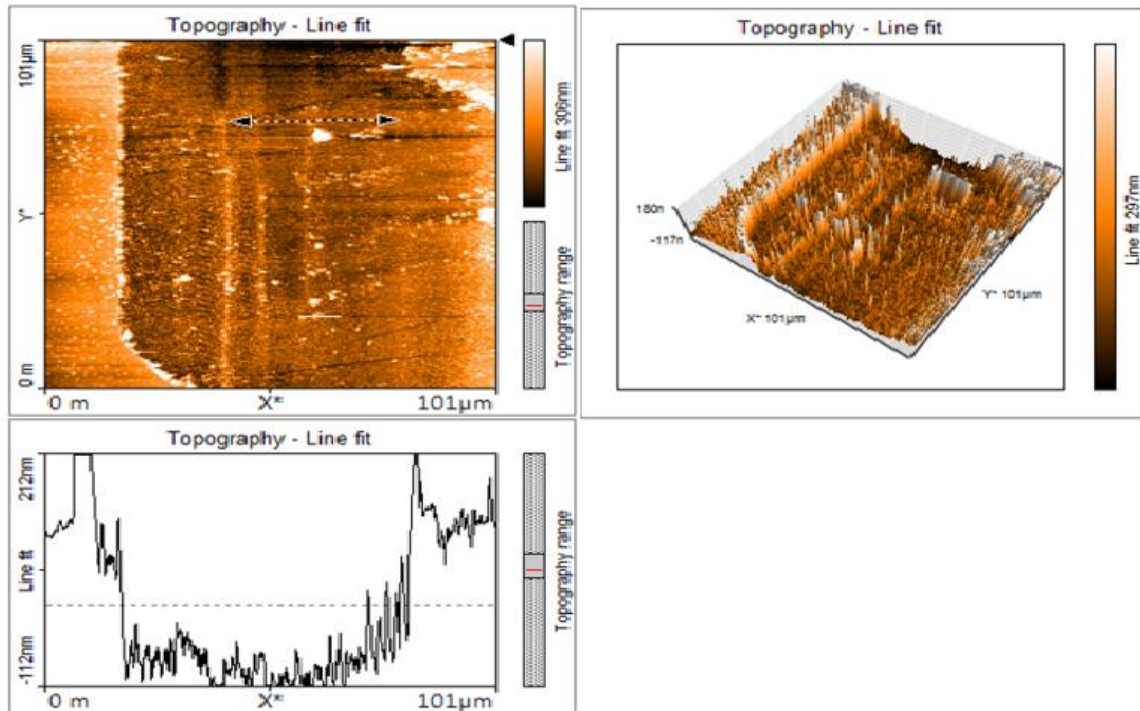


Figure 78 AFM image showing the overlapping area of the constriction to be 38.41  $\mu\text{m}$ .

#### 2.18.4 ANALYSIS OF THE RESULTS

A power setting of 22.7 mW is way above the ablation threshold of the YBCO material therefore it ablates the material, creates a large ablation spot size and cuts into the substrate. For our purposes, this power setting is too large.

A power setting of 11.65 mW is still above the required ablation threshold of the YBCO thin film and etches slightly into the substrate. This power setting also produces a very large laser ablation spot size of about 62.96  $\mu\text{m}$  and when combined with a separation distance of 25  $\mu\text{m}$  the laser ablation spots overlap each other.

The power setting of 5 mW is only slightly above the ablation threshold of the YBCO thin film. The laser ablation spot size produced by this power is 34.05  $\mu\text{m}$ . When combined with a laser spot separation distance of 60  $\mu\text{m}$  the laser ablation spots do not overlap each other and a constriction is formed. For the purposes of our experiments to fabricate constrictions this power setting can be used.

However we still have to take into consideration that as the laser beam travels to the sample for cutting it passes through optical components along its path and after each component especially the beam collimation set up there are power losses.

From the analysis of these experiments and the AFM images of the constrictions made it can be concluded that;

When the laser ablation spots overlap then:

$$\textit{The overlapping width} = \textit{laser ablation spot size} - \textit{separation distance between the laser spots set in program code} \quad (8)$$

As extracted from section 2.18.3.4;

$$62.96 \mu\text{m} - 25 \mu\text{m} = 37.96 \mu\text{m}.$$

The overlapping width achieved in figure 78 from that section is actually 38.41  $\mu\text{m}$  hence it agrees with equation (8).

In the case where there is no overlapping and a constriction is formed as in the equation below;

$$\textit{the width of the constriction} = \textit{separation distance in the code between laser spots} - \textit{laser ablation spot size}$$

As extracted from section 2.18.3.2;

$$60 \mu\text{m} - 34.05 \mu\text{m} = 25.95 \mu\text{m}$$

The width of the constriction achieved in figure 74 from that section is actually 30.49  $\mu\text{m}$ , hence it agrees with the equation.

## 2.19 REFERENCES

- [1] CPA-Series User Manual, Version 2.4, Copyright 2007, Clark-MXR, Inc.
- [2] John M. Senior, M. Yousif Jamro, "Optical Fiber Communications Principles and Practice
- [3] Korte, F., Serbin, J., Koch, J. et al. "Towards nanostructuring with femtosecond laser pulses", Appl Phys A (2003) 77: pg 229-235,(2003) doi:10.1007/s00339-003-2110-z.
- [4] A. I. Kuznetsov, J. Koch, B. N. Chichkov, "Nanostructuring of thin gold films by femtosecond lasers," vol. 94, pp. 221–230, (2009), DOI 10.1007/s00339-008-4859-6.
- [5] N. Hass, G. Deutscher, G. Desgardin, I. Monot, and M. Weger, "Sharp Gap Edge and Determination of the Fermi Velocity in YBa<sub>2</sub>Cu<sub>3</sub>O<sub>7-x</sub> by Point Contact Spectroscopy," Journal of Superconductivity, vol. 5, no. 2, pp. 191–194, 1992.

# CHAPTER 3

## LITHOGRAPHY PROCESS DEVELOPED FOR THE FABRICATION OF THE NOVEL S-SHAPED CONSTRICTIONS ON $YBa_2Cu_3O_{7-x}$ THIN FILMS.

### 3.1 INTRODUCTION

The initial constrictions fabricated had a poorly shaped laser ablation spot. With a poorly shaped laser ablation spot the main problem that can be encountered is having difficulty in determining the constriction width of a junction. The laser ablation spot having a poor shape was caused by two major reasons. The first reason was due to spherical aberration caused by the cylindrical lenses used for the beam collimation process and the second reason was due to the laser beam having imperfections originating from the laser source itself that is the laser lamp. This chapter focuses on the method used to improve the shape of the laser ablation spot and the lithography process used in the design of the S-shaped constrictions.

### 3.2 LASER OPTICAL EXPERIMENTAL SETUP USED TO IMPROVE THE LASER ABLATION SPOT SHAPE.

The block diagram of the optical experimental set up used to improve the laser ablation spot shape and to fabricate the constrictions with the femtosecond laser can be seen in figure 79. This optical experimental set up consists of the laser source (pump laser diode), the beam collimation set up already described before, reflective mirrors, iris or a manually adjustable aperture set at a diameter of 5000  $\mu\text{m}$  (5 mm), and a spherical convex lens of 45 mm focal length.

Figure 79 shows that the power released from the laser source or lamp is 4.15 mW in this specific setting but the power reaching the convex lens or the sample would be about 2.7 mW. This is because each component introduced in the optical set up contributes to a loss of power.

The power at each stage of the set up can be measured with a laser power meter (measures laser power in Watts). The wattmeter has a spherical receiving aperture on which the laser light must be incident on and the power is then measured on the power meter's digital screen. An example of a typical laser power meter can be seen in figure 80. This specific power meter is based on a thermal power sensor. It

basically has a thermal sensor which when the laser light is incident on, measures the heat generated and then converts this heat into a proportional electrical power read in Watts.

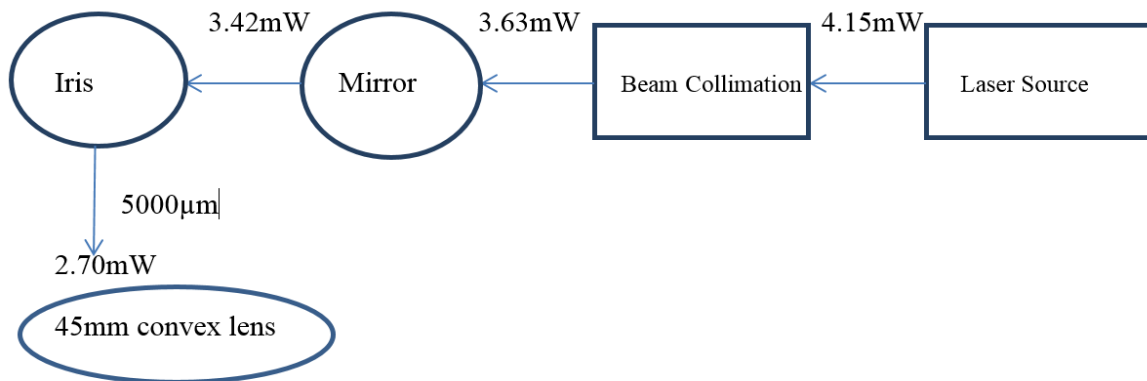


Figure 79 Block diagram of the overall laser optical experimental set up used to cut the constriction.



Figure 80 Image of a Laser optical power meter based on a thermal power sensor.

### 3.2.1 IRIS DIAPHRAGM (MANUALLY ADJUSTABLE APERTURE)

In order to improve the shape of the laser spot after the beam collimation process we need to remove certain unwanted sections of the laser specifically in the outer periphery of the laser beam spot. This means that only the central core of the laser beam spot would be allowed to pass through to the focusing optics. To achieve this, we used an iris diaphragm. The iris diaphragm consists of a manually adjustable aperture mounted on a height adjustable stand. The manually adjustable aperture can be opened or fully closed to control the amount of laser that passes through to the sample. The image of the iris diaphragm can be seen in figure 81. The manually adjustable aperture has a diameter that ranges from (0  $\mu\text{m}$  to 10000  $\mu\text{m}$ ). This aperture was opened to a diameter of 5000  $\mu\text{m}$  (5 mm) by using a digital calliper to set the diameter of the opening. With the aperture set at a diameter of 5 mm, it was utilised to reduce the waist diameter of the laser spot from 9.85 mm to 5 mm before focusing the laser beam spot with a spherical convex lens as can be seen in figure 79. The aperture of the iris diaphragm is centred and aligned to the reflective mirrors and the centre of the laser source such that it removes the outer periphery of the laser beam coming from the source. It takes only the even central core of the laser beam and eliminates any unnecessary laser fringes that can be repeated in the outermost periphery making sure that the laser ablation spot becomes better shaped. The beam collimation process blows up the beam while the iris diaphragm allows only the central core to pass through with the highest beam intensity of the laser source.

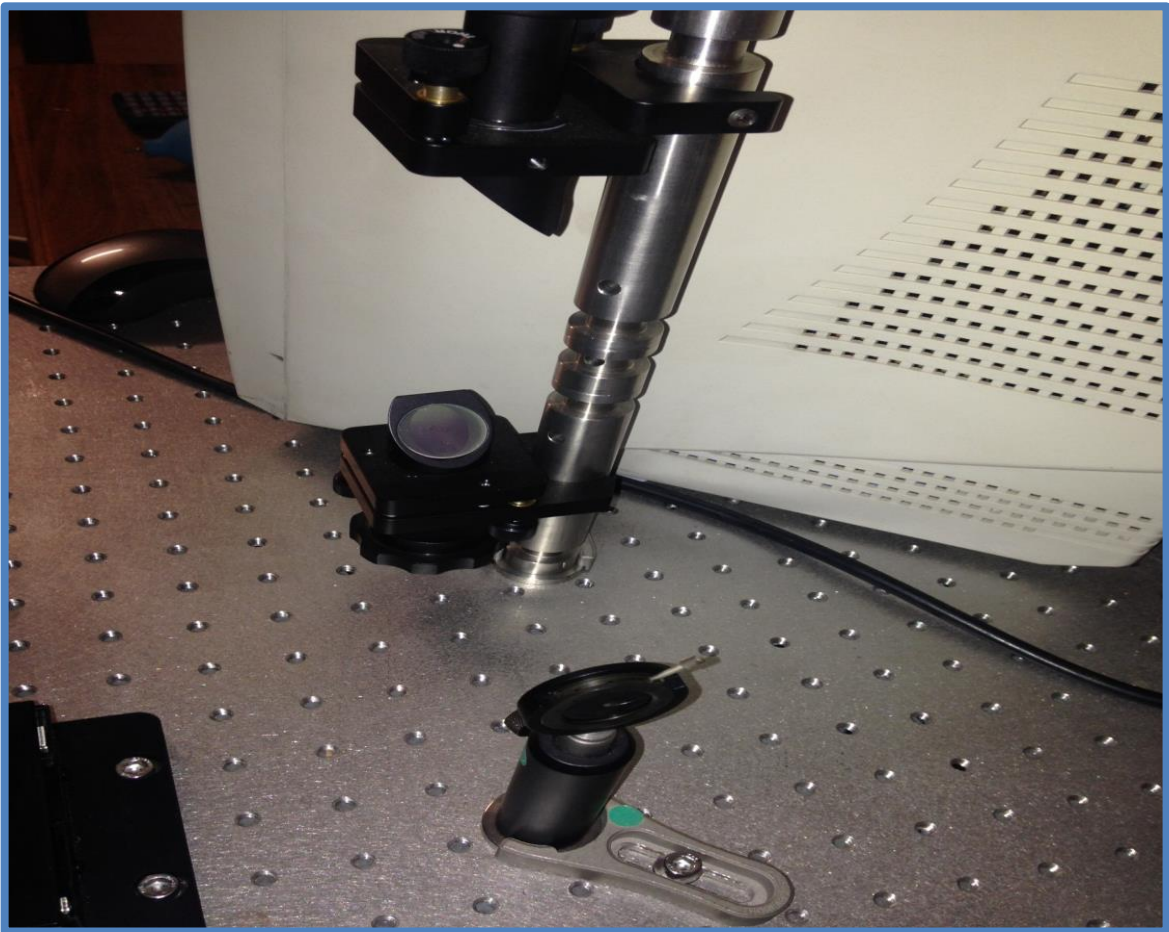


Figure 81 Iris diaphragm with a manually adjustable aperture.

### **3.3 CONSTRICTION FABRICATED ON YBCO THIN FILM WITH THE IRIS APERTURE SET AT A DIAMETER OF 5 mm.**

The laser power was set at 6.5 mW and the separation distance between the laser ablation spots was set at 41  $\mu\text{m}$  in the G-code. This constriction was fabricated on LAO substrate material. The power was set at 6.5 mW in this case to take into consideration the power losses or drops across the optical components placed for the optimisation of the laser beam. The separation distance was reduced to 41  $\mu\text{m}$  because at this point we are not sure with the iris diaphragm reducing the beam diameter what the focused ablation spot size would be. However, take into consideration that we are gradually narrowing the margin towards the perfect optimization of the laser ablation spot and the best possibly shaped constriction that can be achieved.

With the power set at 6.5 mW and the separation distance between the laser ablation spots set at 41  $\mu\text{m}$  the following AFM images show the constriction fabricated and results achieved.

The overlapping length of the constriction as can be seen in figure 82 is about 30  $\mu\text{m}$  if you include the length of the unwanted extension. This overlapping length is achieved by setting the separation distance between the laser ablation spots along the width of the sample to 3  $\mu\text{m}$  in the G-code. If the separation distance between the laser ablation spots along the width of the sample was set to 5.0  $\mu\text{m}$  in the G-code, then you would get an overlapping length of about 28  $\mu\text{m}$ . An equation for the overlapping length of the constriction will be introduced in later sections and it depends on the separation distance between the laser ablation spots along the width of the sample and the laser ablation spot size.

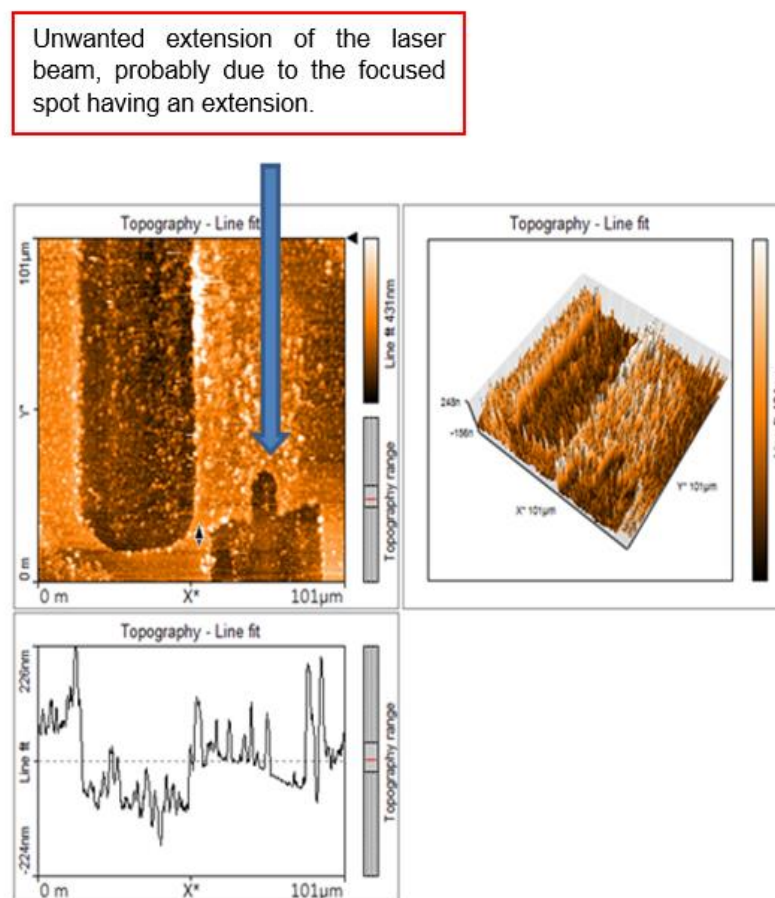


Figure 82 Overlapping length of constriction 30  $\mu\text{m}$ .

### 3.3.1 REASON FOR THE LASER SPOT HAVING AN UNWANTED EXTENSION.

*The laser ablation spot seems to have an unwanted extension as can be seen in figure 82. This is related to the laser focusing process after beam collimation and then searching for the smallest hole drilled. The cylindrical lenses used for the collimation process are not very perfect that is the dimensions of the lenses is about 10 mm X 10 mm meaning that the laser beam waist which is 9.85 mm is very close or similar to the dimension of the cylindrical lenses used. Due to this fact each little lens comprising the whole lens refracts and converges the beam and then produces several images of the laser beam spot encircling each other or what we call “spherical aberrations”. As a result of this it will be advisable to choose a well-rounded hole, not two drilled holes encircling each other such as in figure 83. If this is not done then you will have a laser spot with extensions, when the laser drills in the forward direction it may leave the odd shape but when it drills in the reverse direction the odd shape will be absent. Closing the aperture diameter of the iris diaphragm to 2550  $\mu\text{m}$  (2.55 mm) can also help to reduce the size of the unwanted projection if not eliminate it.*



Figure 83 Poorly shaped focused laser ablation spot consisting of two laser ablation spots intertwined caused by spherical aberration of the laser light.

The laser ablation spot size is measured in between the black arrows in the topography line fit as shown in figure 84 to be 33.26  $\mu\text{m}$ .

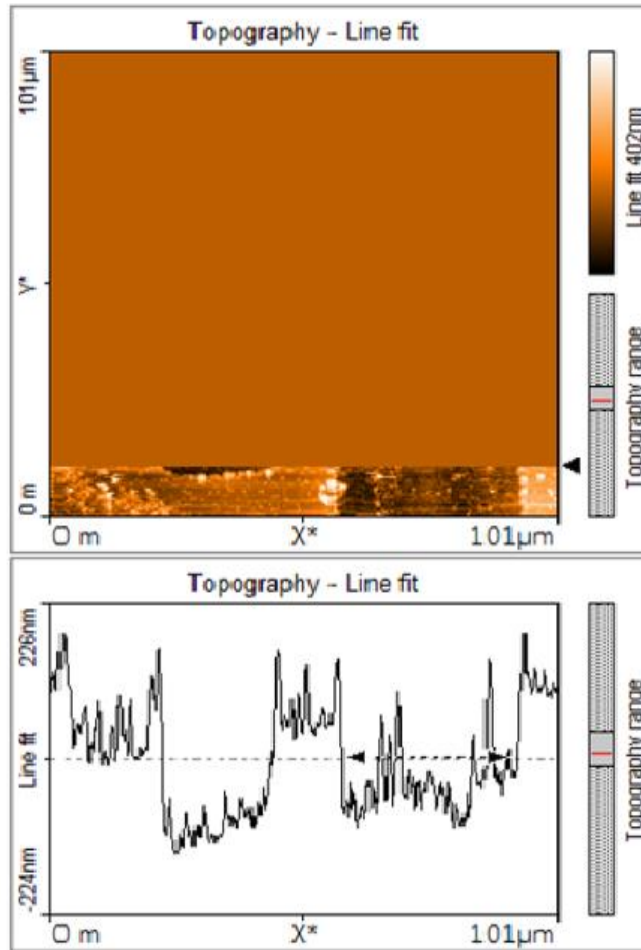


Figure 84 AFM image of the constriction showing the laser ablation spot size is 33.26  $\mu\text{m}$ .

The laser power is set at 6.5 mW and the separation distance between the laser ablation spots along the length of the sample is 41  $\mu\text{m}$ . Since the laser ablation spot size achieved is 33.26  $\mu\text{m}$  as can be seen in figure 84. The constriction width achieved in this case is 7.7  $\mu\text{m}$  as can be seen in figure 85 between the black arrows in the profile distribution curve of the topography line fit.

This confirms the theory that if you separate the laser ablation spots as in this case by 41  $\mu\text{m}$  in the G-code, when the laser ablation spot size is 33.26  $\mu\text{m}$  you will expect a constriction width of about 7.7  $\mu\text{m}$ .

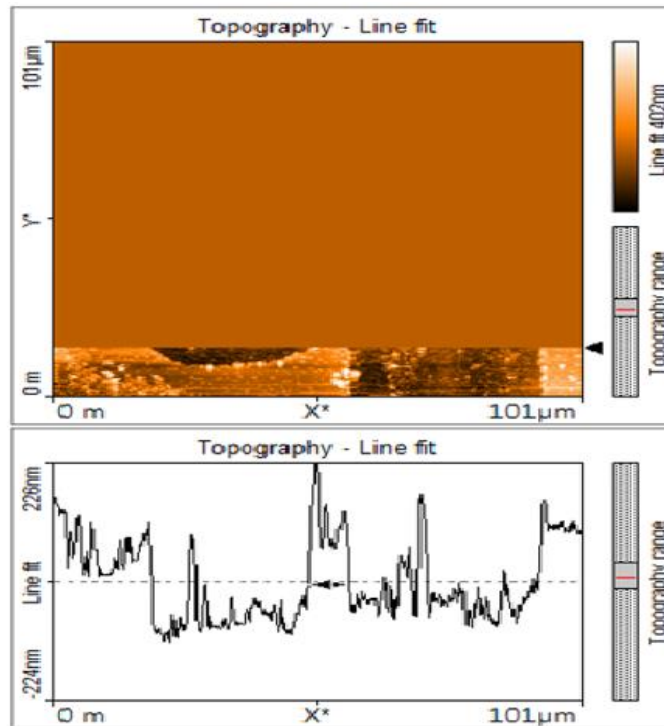


Figure 85 AFM image of the constriction showing the constriction width to be 7.7  $\mu\text{m}$ .

### 3.4 FUTURE WORK TO IMPROVE CONSTRICTION SHAPE.

To improve the shape of the constriction and completely remove the unwanted extension on the laser ablation spot, it was decided that the aperture diameter of the iris will be reduced from 5000  $\mu\text{m}$  (5 mm) to 2200  $\mu\text{m}$  (2.2 mm). This will force only the central core of the laser beam waist to pass through and eliminate all the unwanted extensions, on the laser ablation spot shape.

The power has to be increased from between 15 - 20 mW whilst using the reduced aperture diameter of 2200  $\mu\text{m}$  (2.2 mm) and then see if this power settings and aperture diameter would enable one to get a clean spot.

The reason for increasing the power emanating from the source is because when the aperture of the iris diaphragm is reduced in diameter then the laser power incident on the sample after all the optical components reduces. Hence, to maintain say a laser power of 6.5 mW incident on the sample one has to apply about 15 mW from the laser source for 6.5 mW to reach the sample. Since each optical component absorbs some, laser power and reduces the power reaching the thin film.

## **KEYNOTE:**

*The more optical components that are placed in between the sample and the laser source the smaller the power that will reach the sample.*

Secondly, power measurements will be done and the energy per pulse calculated after the iris diaphragm but before the focusing spherical convex lens. Hence based on the laser ablation spot size achieved and based on the circular area of the laser ablation spot, the energy density or the fluence of the laser incident on the sample can be calculated.

### **3.5 CONSTRICTION FABRICATED ON YBCO THIN FILM WITH THE IRIS APERTURE REDUCED TO A DIAMETER OF 2.55 mm.**

This constriction at this point in the design process was still fabricated on the LAO substrates of the YBCO thin films. The iris diaphragm as described in the previous section is used to reduce the diameter of the laser ablation spot that is used for drilling the constriction.

The lenses used for the beam collimation process are not perfect and as a result, they produce spherical aberrations of the laser ablation spot, which becomes larger and uneven.

In order to eliminate the problems associated with spherical aberration the diameter of the iris aperture was varied. Initially the iris aperture is set to a diameter of 5 mm to enable the laser beam be focused more easily. This is because it is easier to detect the focus point of the laser ablation spot when the laser ablation spot is larger in diameter, since it is more visible under the microscope. During the focusing process of the laser, the Z-position where the laser beam spot is focused is recorded. Subsequently when cutting the constriction in order to reduce the laser ablation spot size, the iris aperture is first reduced to a diameter of 2.55 mm and then to 1.5 mm. For this particular constriction being described in this section, the iris aperture was set to a diameter of 2.55 mm.

In this experimental set up there is the laser source, a beam collimation set up, reflective mirrors, the iris with a diameter set at 2.55 mm and spherical convex lens of focal length of 45 mm. The iris aperture diameter is reduced to reduce the size of

the laser ablation spot. By reducing the laser ablation spot size it would be possible to fabricate smaller constrictions.

As can be seen in figure 79 when an input power of 4.15 mW is applied from the laser source the power reaching the thin film sample is only 2.7 mW. However, at later stages it would be shown that the power level of 2.7 mW is still much higher than the ablation threshold of the YBCO thin film. Hence, 2.7 mW is still sufficient to completely remove or ablate 200 nm of the YBCO thin film from the substrate completely. In this experiment, we applied a power of 4.9 mW from the source to fabricate the constriction. The power reaching the sample in this case would be slightly more than 2.7 mW

With these settings, we fabricated a constriction with a constriction width of 1.989  $\mu\text{m}$ , a laser ablation spot size of 17  $\mu\text{m}$  and a separation distance between the laser ablation spots of 17.8  $\mu\text{m}$  as can be seen in figure 86. The laser ablation spot achieved has a good well-rounded spherical shape without any extensions. This was quite a good result for the beginning because a micron-sized constriction had been achieved.

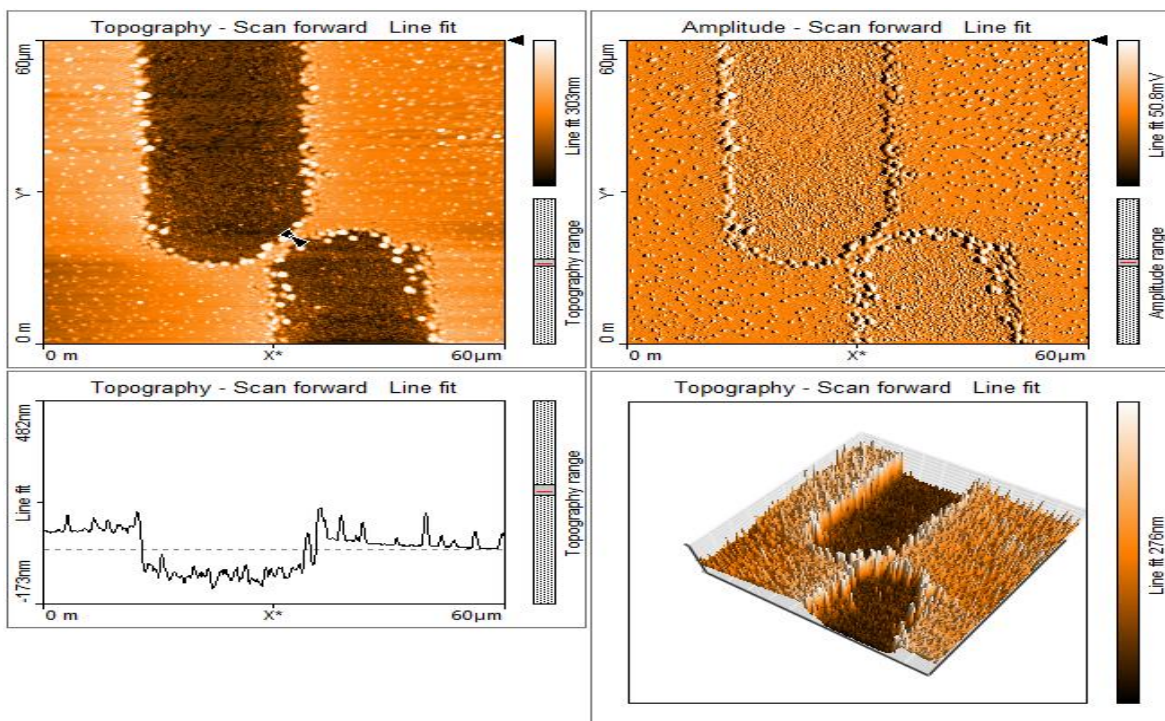


Figure 86 AFM image showing a constriction fabricated with a laser power setting of 4.9 mW, iris aperture diameter 2.55 mm, constriction width of 1.989  $\mu\text{m}$ , separation distance between the laser ablation spots of approx. 17.8  $\mu\text{m}$ .

### 3.6 LITHOGRAPHY PROCESS AND G-CODE PROGRAM USED TO CONTROL THE MOVEMENT OF THE TRANSLATION STAGE IN THE DESIGN OF THE NOVEL S-SHAPED CONSTRICTIONS.

A Simple G-code program was written to control the movement of the translation stage during the fabrication and design of the novel S-shaped constrictions. The translation stage moves in 3-dimensions holding the sample whilst the laser cuts the designed S-shaped constrictions. The S-shaped constriction just as the name implies is shaped like the letter “S” as can be seen in figure 87. In the S-shaped constriction design, we have the advantage of being able to control both the width and length of the constriction during fabrication. In the normal type of constriction seen in figure 88 only the width of the constriction can be controlled by bringing the ablation spots closer but the length of the constriction is restricted to the laser ablation spot size.

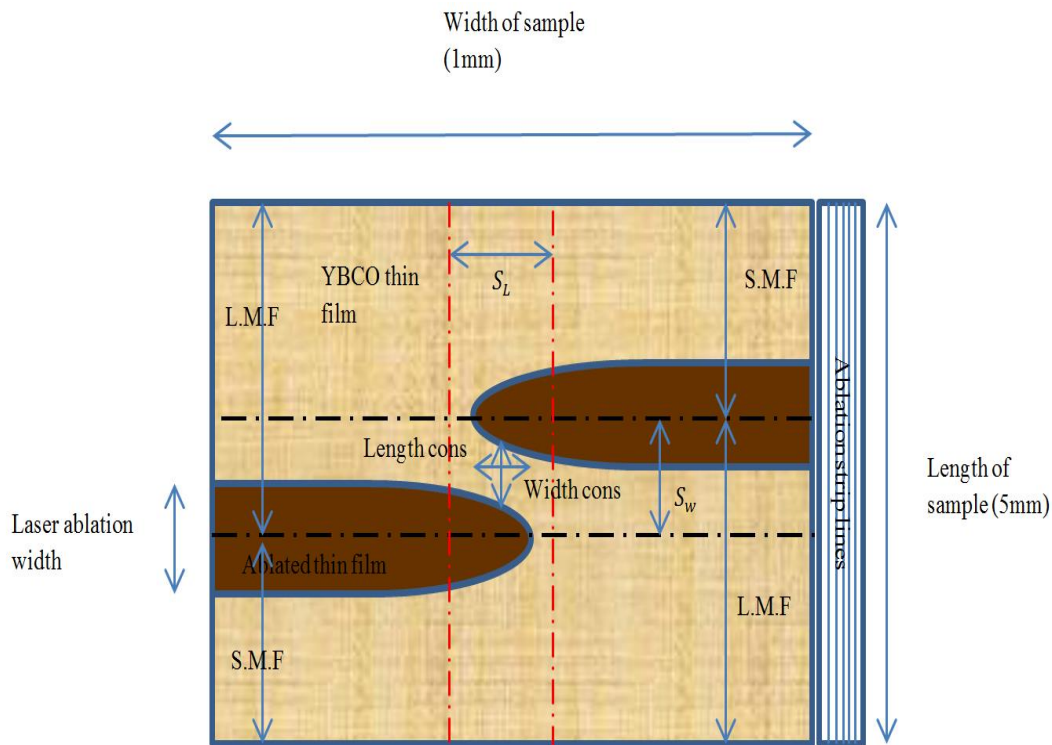


Figure 87 Design of the S-shaped constriction, Laser movement, Short movement factor (S.M.F), Long movement factor (L.M.F), Length Factor (L.F), the ablation strip lines, Length cons (constriction) and Width cons (constriction).

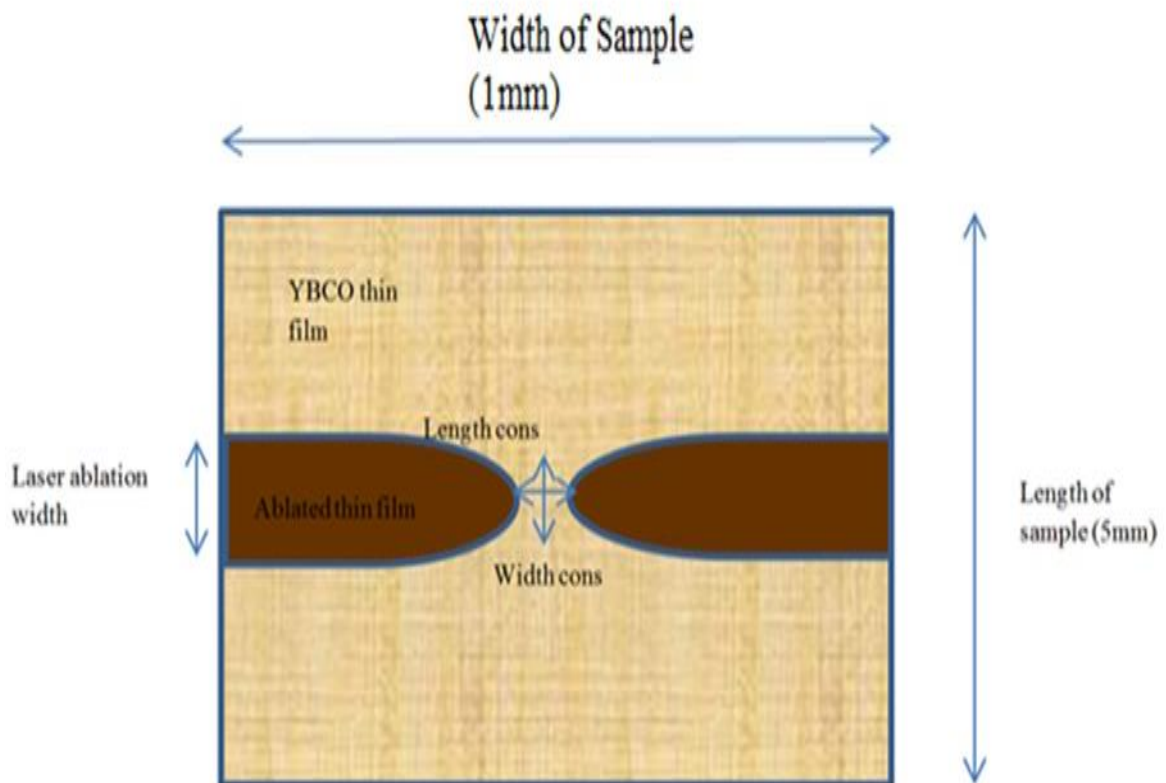


Figure 88 Normal constriction type, Length cons (constriction) and Width cons (constriction).

### 3.6.1 LITHOGRAPHY DESIGN OF THE S-SHAPED CONSTRICTION.

In the S-shape constriction, by bringing the laser ablation spots closer along the length of the sample it's possible to easily regulate the width of the bridge and by separating the laser spots along the width of the sample it's possible to regulate the overlapping length of the bridge as shown in figure 87.

The G-code program consists of a section to etch out the ablation strip lines and a second section to fabricate the S-shaped constriction. The ablation strip lines are used to separate one constriction from another electrically.

They are formed by moving the laser vertically up and down 5 mm along the length of the YBCO thin film as shown in figure 87. The horizontal spacing between the vertical lines is about 5  $\mu\text{m}$  such that an ablation strip line width of 0.5 mm is formed to separate one constriction from another. The vertical up and down movement of the laser is repeated in a loop in the G-code.

The laser is then moved vertically down the length of the sample according to the short movement factor length (SMF). Horizontally into the sample at a predetermined position along the length and then moved out again. Then it is moved down along the length of the sample according to the long movement factor length (LMF), across the width of the sample (1 mm) to the other side. Then up to a predetermined position along the length of the sample again according to the (SMF), horizontally into the sample, back out and then back to the top along the length again according to the (LMF) to begin another strip line. The ablation strip lines can be seen in figure 89 beneath the cantilever head of the AFM (atomic force microscope).

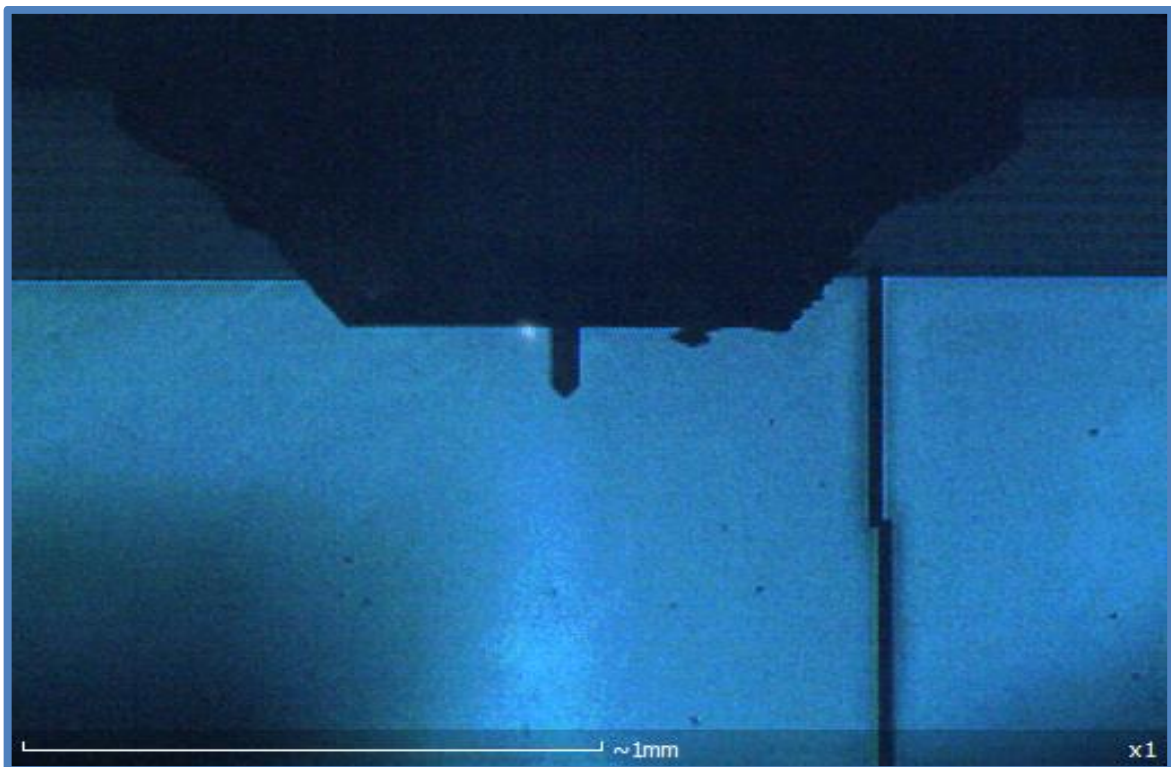


Figure 89 S-shaped constriction and ablation-strip lines captured beneath the cantilever tip of an AFM.

To determine the initial position along the length at which point the laser is moved into the sample a certain factor is calculated. Division of the length (5 mm) of the sample by this factor will produce a short movement and the factor is called SMF. Division of the length (5 mm) by the second factor will produce a long movement and the factor is called the LMF. As can be seen in figure 87 both these factors determine the separation between the laser ablation spots and hence the width of the constriction.

The formula for the short movement factor (SMF) can be seen in equation (1):

$$2 * \frac{l}{l-S_w} \quad (1)$$

Where  $l$ , is the length of the square sample (5 mm),  $S_w$  is the separation distance between the laser ablation spots along the length of the sample to determine the width of the bridge. The formula for the long movement factor (LMF) can be seen in equation (2):

$$2 * \frac{l}{l+S_w} \quad (2)$$

Finally to determine the overlapping length of the laser spots and hence the length of the bridge a factor is calculated such that division of the width of the sample by this factor enables one to know how far to move the laser into the sample.

The formula for calculating the Length factor (LF) can be seen in equation (3):

$$\frac{2w}{w-S_L} \quad (3)$$

Where  $w$  is the width of the sample (1 mm) and  $S_L$  is the separation distance between the laser ablation spots along the width of the sample to determine the length of the constriction. The short movement factor, long movement factor and the length factor can all be seen in figure 87.

Theoretically, the width of a constriction should be given by equation (4) although there are many limitations to this;

$$\text{width of constriction} = S_w - \text{laser ablation width} \quad (4)$$

The overlapping length of the constriction is given by equation (5);

$$\text{Length of constriction} = |S_L - \text{laser ablation width}| \quad (5)$$

The laser feed rate is 20 mm/min or 333  $\mu\text{ms}^{-1}$ . The feed rate is essentially the speed with which the translation stage is moved. It can also be defined as how fast the laser is moved in and out of the sample. The feed-rate can be varied depending on the need, using the interface software to control the movement of the translation stage. Generally, the slower the feed rate the higher the ablation depth.

The feed rate chosen is essentially quite fast  $333 \mu\text{ms}^{-1}$  because it enables the laser to move in and out of the sample fast. However, this feed rate speed can still be increased via software to 30 mm/min or  $500 \mu\text{ms}^{-1}$ . The reason for choosing such fast feed rates is to make it possible not to thermally alter the superconductive material during ablation by reducing the time the sample is exposed to the laser. Of course, with a fast feed rate the ablation depth will be reduced. However, this can be supplemented by increasing the incident power on the sample.

### 3.7 MOVEMENT OF THE TRANSLATION STAGE IN THE X,Y,Z CO- ORDINATES.

The X, Y, Z directions are needed to facilitate the process of writing the G-code program when moving the translation stage to cut the constriction. The reason for this is because most of the commands in the G-code are commands that give direction to the translation stage to move to a certain geometric position and by so doing cut a certain geometric pattern. Therefore, the geometric axis of the X, Y, Z co-ordinates must be very well known. The movements in the G-code for the positive and negative directions of each axis can be seen in figure 90.

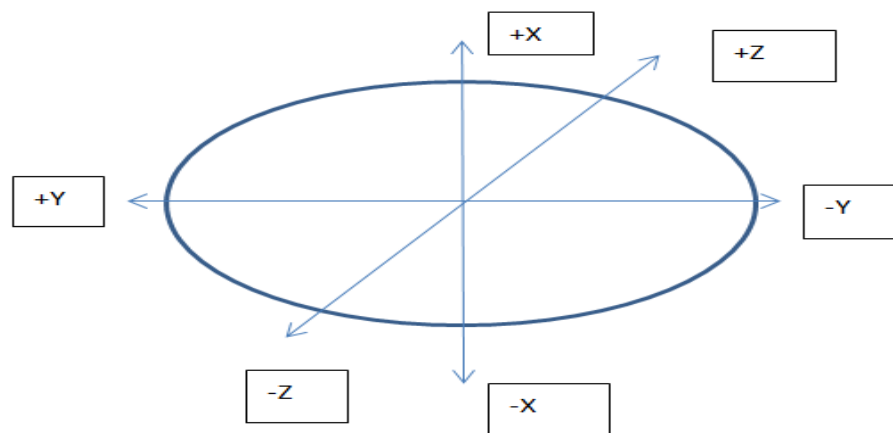


Figure 90 X, Y, Z directions for the movement of the translation stage and hence the relative movement of the laser.

If one looks at the ellipse shape above as the laser ablation spot or the directions in which the translation stage moves. Then to the right of the ellipse will be the  $-Y$  direction, to the left positive Y direction, on the XY plane moving up will be  $+X$  direction, moving down will be  $-X$  and also moving  $+Z$  will mean going up in the Z plane and moving down will  $-Z$  direction. These directions were very helpful in writing the program code in the G-code to cut (fabricate) the thin film.

### **3.8 G-CODE PROGRAMMING LANGUAGE USED TO MOVE THE TRANSLATION STAGE WHILST CUTTING THE CONSTRICTIONS**

G-code (also known as *RS-274*), which has many variants, is the common name for the most widely used numerical control (NC) programming language. It is used mainly in computer-aided manufacturing for controlling automated machine tools. G-code is sometimes called G programming language.

In fundamental terms, G-code is a language in which people tell computerized machine tools how to make something. The how is defined by instructions on where to move, how fast to move, and through what path to move. The most common situation is that, within a machine tool, a cutting tool is moved according to these instructions through a toolpath, cutting away excess material to leave only the finished work piece. The same concept also extends to noncutting tools such as forming or burnishing tools, photo plotting, additive methods, and measuring instruments.

In the case of this PhD work, the translation stage that holds the sample, operates with a control interface or was sold with a control interface that can be manually used to move the translation stage and at the same time can be used to operate the translation stage through code written in the G-programming language.

The G-programming language was used to move the translation stage during the laser cutting process of the fabrication of the constrictions. The G-code program syntax was written in NOTEPAD document and saved to be uploaded into the computer interface and then used to “RUN” the translation stage to fabricate the constrictions. Below is the G-code programming language used to cut the constrictions. The translation stage moves and the laser is held in a fixed position over the sample that is held on the moving translation stage.

#### **3.8.1 ACTUAL G-CODE PROGRAM FOR CUTTING THE S-SHAPED CONSTRICTIONS.**

The actual G-code program for cutting the S-shaped constrictions can be found in the section called: [Appendix](#)

### **3.9 EXPLAINING THE G-CODE PROGRAM USED AND THE ALGORITHM FOR THE DESIGN OF THE NOVEL S-SHAPED CONSTRICTIONS.**

- Data variables are defined such as the initial X, Y, Z co-ordinates, the Z-focus, feed rate, length of the sample film, width of the sample, the number of times the repetition loop for ablation of the strip lines is done (nrepsablation = 10), and the number of times the repetition loop for cutting the constriction is set (nrepsconstriction = 6).
- In addition, the METRIC units are set to be in mm.
- The thin film sample is 10 X 10 mm, the ablation strip line on the right side of a constriction is programmed such that it is 0.5 mm wide, 5 mm long and the constriction itself is 1 mm wide, and 5 mm long.
- The ablation strip line (0.5 mm wide) plus the constriction (1 mm wide) is repeated 6 times in a loop thus occupying a space 9 mm wide and 5 mm long and creating 6 constrictions (nrepsconstriction = 6) on the lower half of the thin film.
- The laser then moves to the top of the sample and repeats the process creating another 6 constrictions on top of the sample.
- In fabricating the ablation strip line on the right side of the constriction, the laser is moved up and down vertically 5 mm and horizontally 1 mm/200 giving 5  $\mu$ m sized horizontal movements.
- During ablation, the horizontal movements are 5  $\mu$ m wide and there are 10 such statements making 50  $\mu$ m wide horizontal movements. Then the statements are in an ablation loop that is repeated 10 times (nrepsablation) giving 500  $\mu$ m or 0.5 mm wide ablation strip line.
- The ablation loop is in another loop for creating the constriction (nrepsconstriction) and this is repeated 6 times. So overall this will create 6 constrictions with 6 ablation strips lines.
- Before moving to the top of the sample to create another 6 constrictions.
- During the creation of a constriction, there is a short movement along the length of the sample (5 mm), this short movement is obtained or calculated by dividing the length (5 mm) by the short movement factor (S.M.F);

The short movement factor is equal to  $2 * \frac{l}{l-S_w}$

Where  $l$  is the length of the sample, and  $S_w$  is the separation distance between the laser ablation spots along the length to determine the width of the bridge.

- After the short movement the laser is moved in and out of the sample along the width (1mm) and this movement amount, in and out is calculated by dividing the width of the constriction (1mm) by the Length factor (L.F.);

The length factor is equal to  $\frac{2w}{w-S_L}$

Where  $w$  is the width of the sample and equal to 1 mm and  $S_L$  is the separation distance between the laser ablation spots along the width of the sample and will determine the overlapping length of the constriction.

- Subsequently the laser is moved down along the length of the sample (5 mm) by a long movement calculated by dividing the length (5 mm) by the long movement factor (L.M.F);

The long movement factor equal to  $2 * \frac{l}{l+S_w}$ .

Where  $l$  is length of the sample (5 mm) and  $S_w$  is the separation distance between the laser ablation spots along the length of the sample that determines the width of the bridge.

- The laser is then moved across the width of the sample (1 mm).
- It is then moved up the sample by an amount equal to the short movement factor.
- Again, the laser is moved in and out of the sample by an amount equal to the length factor and then back up to the top to complete the constriction by an amount equal to the long movement factor.
- All references all definitions made in this section can be viewed in figure 87 above.

### 3.10 ENERGY DENSITY OF THE LASER AND DETERMINING THE PEAK LASER FLUENCE ABLATION THRESHOLD FOR YBCO THIN FILM.

Every material has an ablation threshold and a melting threshold. The ablation threshold is the minimum amount of power, energy density or the minimum fluence of the laser that needs to be applied to that specific material for you to just begin removing or cutting the material or taking the material away (ablating). Below that minimum laser fluence, ablation does not begin. Therefore, that minimum fluence required to begin taking the material away is called the laser fluence ablation threshold. For a specific material in this case YBCO the laser fluence ablation threshold should always be the same irrespective of the laser used. So in this particular case we are using the femtosecond laser but we want to find out the minimum amount of power or energy density of the femtosecond laser we need to apply to the YBCO to just begin cutting the material (ablation). This is done such that anyone who wants to cut or ablate YBCO with the femtosecond laser will know the minimum amount of power effluent from the femtosecond laser they would need to apply to just start ablating the sample (YBCO). First, the material melts and then it is taken away. Therefore, the melting threshold is below the ablation threshold. All the equations below show the systematic method for deriving the formula for the peak laser fluence. Having derived the formula for the peak laser fluence another method observed from the paper in [1] is used to determine the peak laser fluence ablation threshold for the YBCO thin film.

The formula for energy density is given in equation (6);

$$\text{Energy density} = \frac{\text{Energy}}{\text{Area}} = \frac{J}{\text{cm}^2} \quad (6)$$

The formula for the area of a circle is given in equation (7);

$$\text{Area of a circle} = A = \frac{(\pi)d^2}{4} \quad (7)$$

Where  $d$  is the diameter of a circle assuming that the perfect Gaussian laser ablation spot is circular in shape.

The formula for the energy per pulse of the laser is given in equation (8);

$$E_{pulse} = \frac{power}{freq} = \frac{P}{freq} \quad (8)$$

Where  $E_{pulse}$  is the energy per pulse of the laser,  $P$  is the laser power and  $freq.$  is the frequency of the laser or the pulse repetition rate, these can both be set on the laser console interface.

The energy density formula is obtained by substituting equation (7) and (8) into Equation (6). Following this you get equation (9) as can be seen below;

$$Energy\ density\ (using\ diameter\ of\ the\ ablation\ spot) = \frac{4P}{freq * (\pi) * d^2} \quad (9)$$

The diameter of a circle  $d = 2r$  is given in Equation (10);

$$d^2 = 4r^2 \quad (10)$$

Substituting equation (10) into equation (9) gives you equation (11) below which represents the average energy density formula;

The average energy density formula (using the ablation spot radius) is given by equation (11);

$$\frac{P}{freq * \pi * r^2} \quad (11)$$

The peak energy density or the peak laser fluence is then given by the formula in equation (12);

$$The\ peak\ energy\ density = peak\ laser\ fluence = \frac{2 * P}{freq * \pi * r^2} \quad (12)$$

The energy density of a laser is also referred to as the laser fluence.

### 3.10.1 FINDING THE PEAK LASER FLUENCE ABLATION THRESHOLD OF THE YBCO THIN FILM.

#### 3.10.1.1 USING THE DIAMETER OF THE LASER ABLATION SPOT METHOD.

The incident peak laser fluence in front of the sample which is the peak energy density of the laser incident on the sample is calculated by using the following formula in equation (13) [1];

$$F_0 = \frac{2P_{AVG}}{rep.rate*\pi*w_0^2} \quad (13)$$

Where  $P_{AVG}$  is the average power effluent from the laser source that eventually reaches the sample after all the optical laser beam shaping components,  $rep.rate$  is the frequency of the laser pulse or the pulse repetition rate, and  $w_0$  is the radius of the measured laser ablation spot used to cut the constriction on the YBCO thin film.

The diameter of the ablation spots as seen in figure 91 was measured by scanning using the cantilever tip of the Atomic Force Microscope (AFM). The scanning was done at 90° to the laser ablation spots, such that the transverse line fit on the topography plot gives you the diameter of the laser ablation spot, which is about 28.51  $\mu\text{m}$  ( $28.51 \times 10^{-4} \text{cm}$ ) in this case.

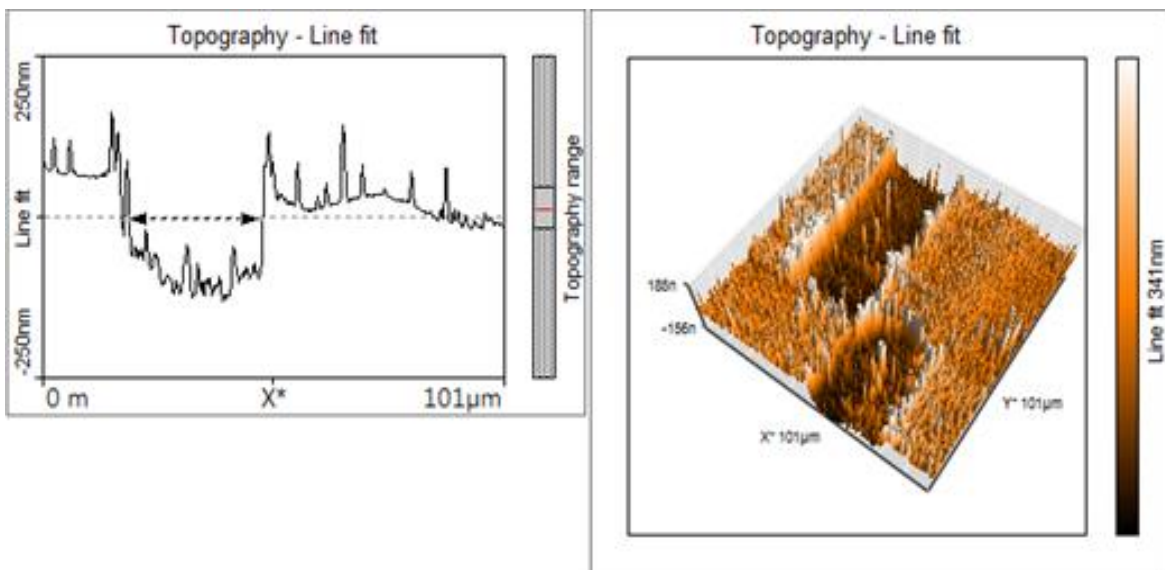


Figure 91 AFM image scan of a laser ablation tunnel created during the fabrication of a constriction, laser power 2.7 mW, and laser ablation spot diameter 28.51  $\mu\text{m}$ , constriction width 2.376  $\mu\text{m}$ , length approx. 9  $\mu\text{m}$ .

Equation (13) above was then used to calculate the peak laser fluence for each power setting applied to the sample by substituting the measured ablation beam waist radius  $w_0$  for each case tunnel in centimeters into equation (13). Table 2 was extracted by repeating the exercise for several cuts.

Table 2 Finding the Peak laser fluence ablation threshold of YBCO thin film ( $F_{th}$ , *dia*) using the laser ablation spot diameter method.

Laser power (mW)	$F_0$ peak laser fluence J/cm <sup>2</sup>	Spot size (μm)	Spot size (μm) <sup>2</sup> , (D <sup>2</sup> )
2.7	0.845	28.51	812.82
4.22	0.865	35.25	1242.56
6.88	0.932	43.36	1880.09
7.9	0.945	46.13	2127.98

Assuming a spatially gaussian shape of the laser beam profile, the peak laser fluence ablation threshold  $F_{th}$  is obtained by plotting the associated square of the laser beam ablation diameter ( $D^2$ ) versus the peak laser fluence  $F_0$  in figure 92.

In Matlab software, the curve is extrapolated to intersect the X-axis. The peak laser fluence ablation threshold  $F_{th}$  value for YBCO of 0.824J/cm<sup>2</sup> is obtained as the squared diameter of the laser ablation spot tends to zero ( $D^2 \gg 0$ )

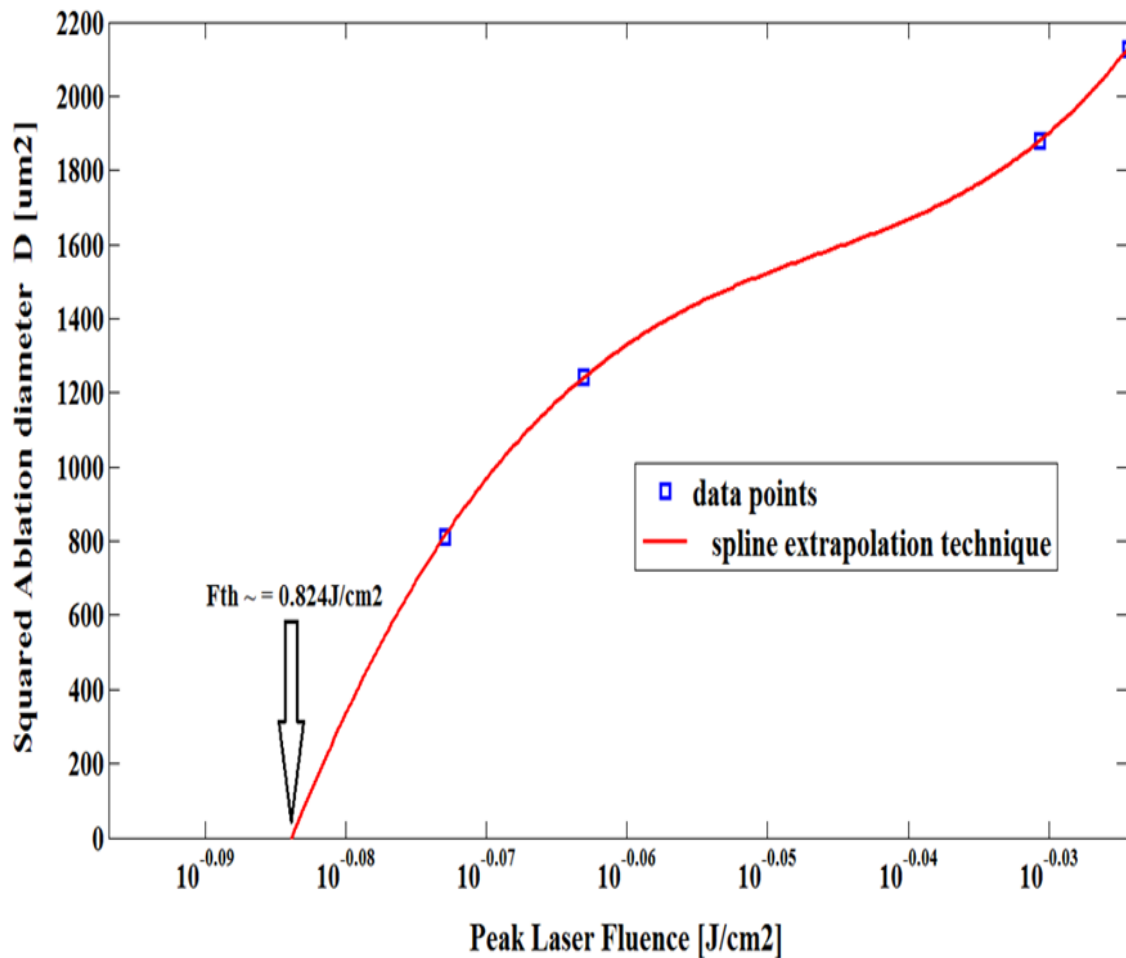


Figure 92 A semi-logarithmic plot of the squared ablation diameter  $D^2$  versus the peak laser fluence  $F_0$  for YBCO on LAO substrate (red line is for the spline interpolation technique of curve fitting and the blue squares represents data points from Table 2, the peak laser fluence ablation threshold from the graph is approximately  $0.824\text{J/cm}^2$  with ( $F_{th}$ , dia) method.

### 3.10.1.2 CRATER TOPOGRAPHY METHOD TO FIND THE PEAK LASER FLUENCE ABLATION THRESHOLD FOR VERIFICATION OF THE THRESHOLD VALUE.

To verify the results obtained above for the peak laser fluence ablation threshold of YBCO, the crater topography method is used. During ablation, a crater is formed with a certain depth profile that can be observed using the (AFM).

The topography line fit obtained with the AFM shows the maximum crater depth to be 146.2 nm in figure 93 for an incident power of 4.22 mW. This method is repeated for a series of laser cut craters with varying laser power. The AFM is used to scan the craters to determine the crater depths and extract table 3.

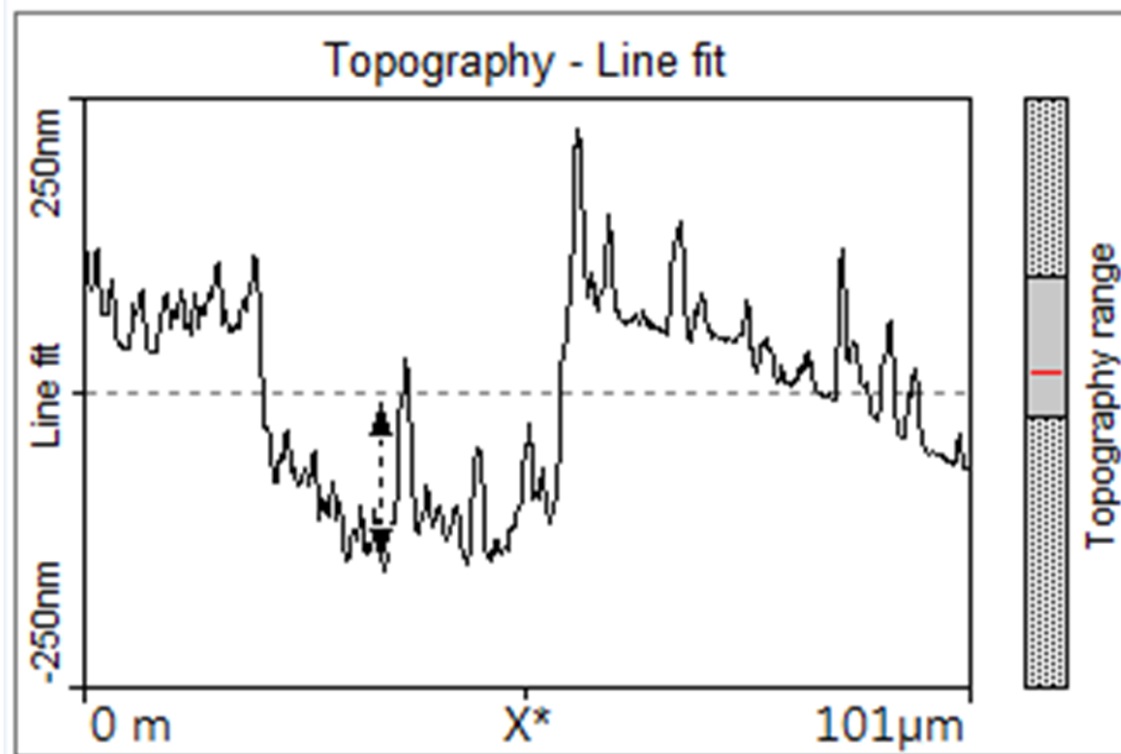


Figure 93 AFM image of a laser ablation spot tunnel created during the fabrication of a constriction, incident power 4.22 mW and maximum crater depth 146.2 nm.

Table 3 Finding the Peak laser fluence ablation threshold of YBCO thin film ( $F_{th, dia}$ ) using the laser ablation spot diameter method.

Laser power (mW)	Peak laser fluence ( $J/cm^2$ )	Max crater depth (nm)
2.7	0.845	134.5
4.22	0.865	146.2
6.88	0.932	155

The maximum laser ablation crater depth ( $d_{max}$ ) is then plotted versus the peak laser fluence as can be seen in figure 94. The curve is extrapolated in Matlab such that it intersects with the X-axis. The peak laser fluence ablation threshold for YBCO is then obtained at the point where the maximum crater depth tends to zero ( $d_{max} \gg 0$ ).

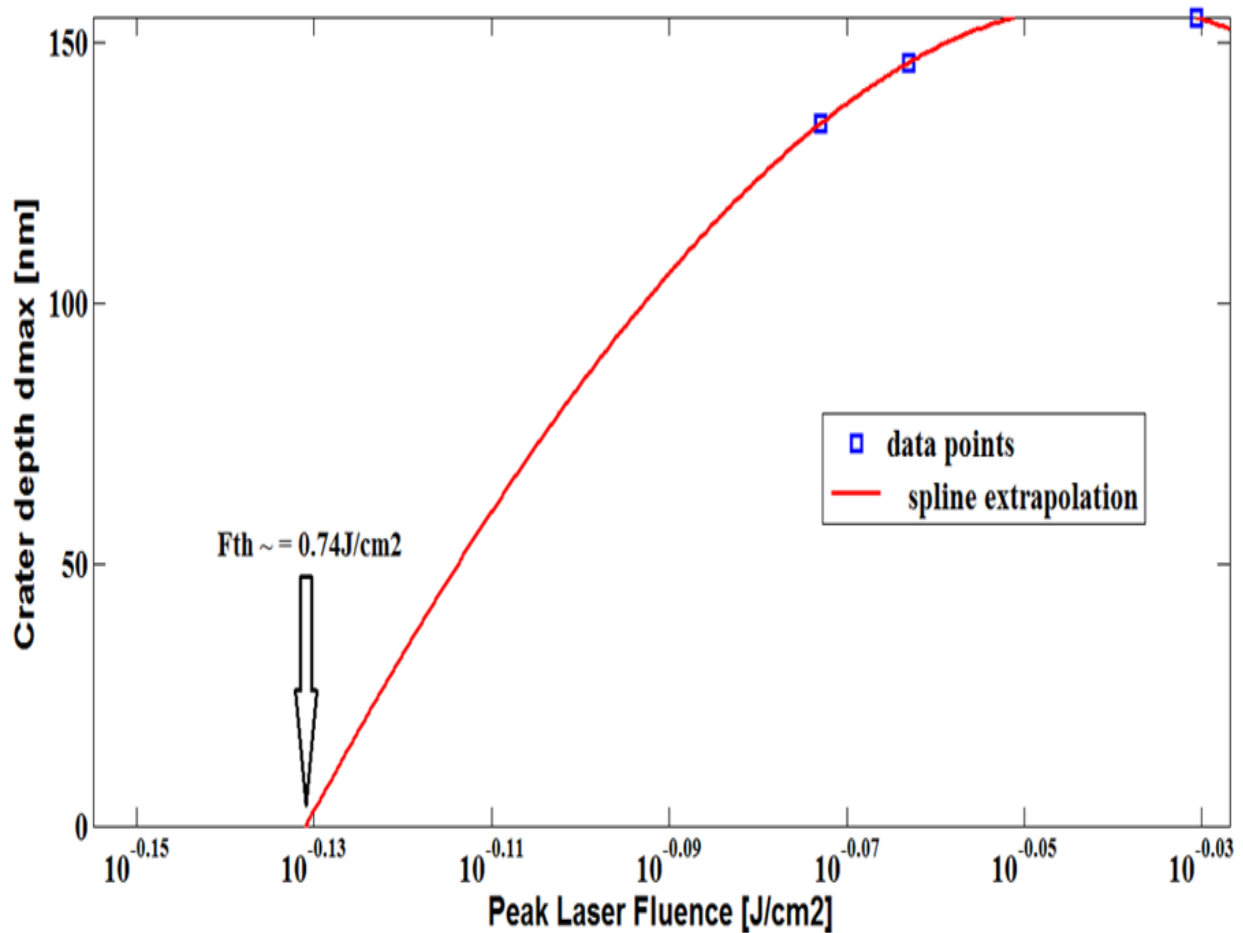


Figure 94 A semi-logarithmic plot of maximum depth of the ablation craters  $d_{max}$  versus the incident peak laser fluence  $F_0$  for YBCO (red line for the spline fit and blue squares for the values from the Table 3, peak laser ablation threshold at x-intercept approximately 0.74 J/cm<sup>2</sup> with ( $F_{th, dep}$ ) method.

The value for the peak laser fluence ablation threshold obtained from the crater depths method ( $F_{th, dep}$ ) is in close approximation with the value obtained from the diameters of the laser ablation spot method ( $F_{th, dia}$ ) namely (0.74J/cm<sup>2</sup>, 0.824J/cm<sup>2</sup>) respectively. There is however, a slight difference, which could be attributed to the fact that the number of points used for extrapolation should actually be more to get a precise measurement.

By using Table 3-1 above it is possible to plot the squared laser ablation diameter versus the incident power applied unto the sample. We then extrapolate the graph to the point where ( $D^2 \gg 0$ ). This is done by using the spline extrapolation technique in matlab. At the X-intercept on the graph, one can see that the power ablation threshold for the YBCO thin film is about 0.6 mW. This means that below this incident power (0.6 mW) there will be no ablation on YBCO thin film with the laser as can be seen in figure 95.

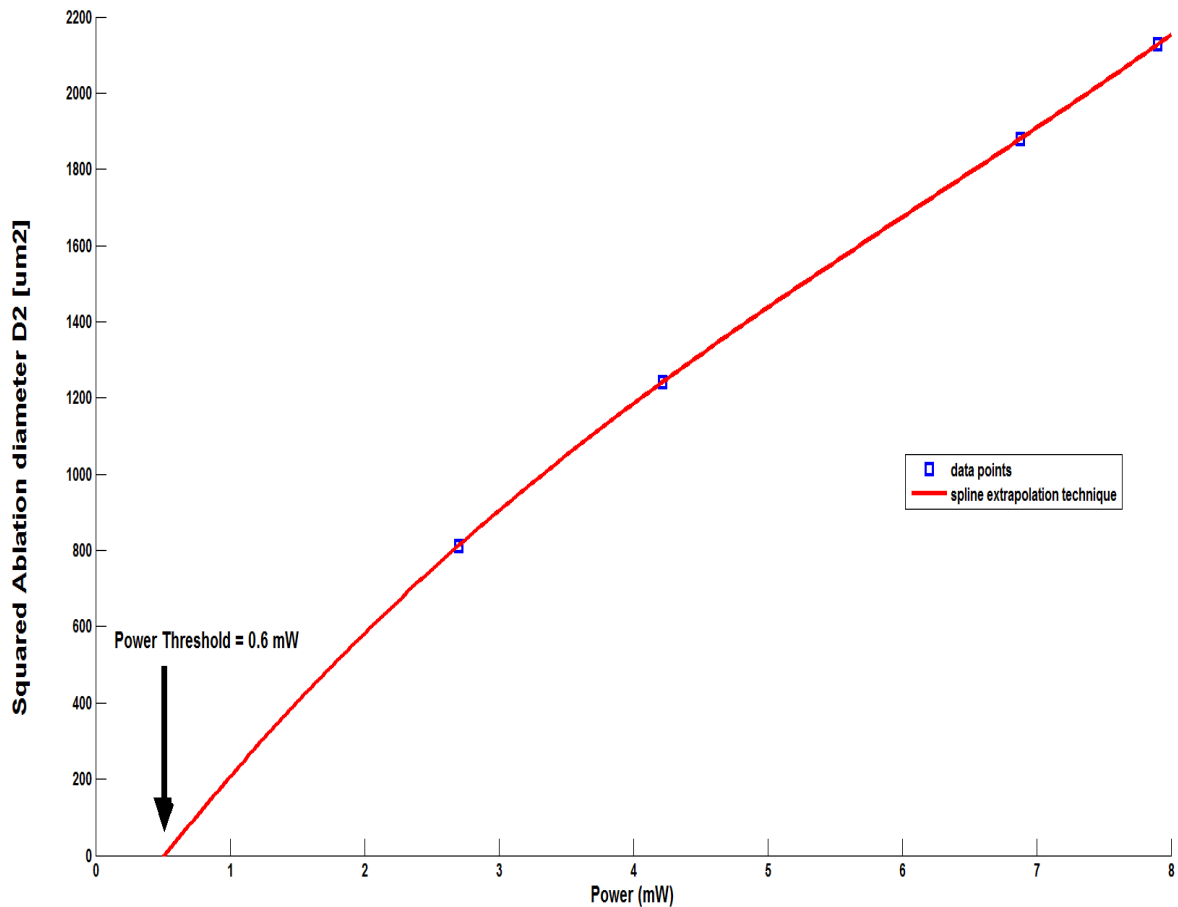


Figure 95 Squared laser ablation diameter Vs Laser power (Laser power Threshold of YBCO thin film).

## **3.11 IMPROVEMENTS IN THE OPTICAL EXPERIMENTAL SET UP AND CONSTRICTIONS MADE WITH NEW SET UP.**

### **3.11.1 THE NEW OPTICAL EXPERIMENTAL SET UP.**

A new optical experimental set up was introduced to attempt in making further reductions in the diameter of the laser ablation spot size used for drilling. The reason for the continuous need to optimize or reduce the laser ablation spot size to a minimum is because the smaller the laser ablation spot size the smaller the width and length of the constriction that can be fabricated. In order to further reduce the laser ablation spot size, the following additions were made to the optical set up;

1. The spherical convex lens of focal length 45 mm that was used at the end of the optical set up as the focusing optics was changed to an objective Plano convex lens with a numerical aperture of NA 0.25 and X 10 magnification as seen in figure 96 and table 4. The objective Plano convex lens is the same as that in a microscope. It has a much higher focusing power than a conventional spherical convex lens. Hence, it immediately reduces the laser ablation spot size even further.
2. The second major addition is that the cylindrical lenses used for beam collimation were changed from ones with an aperture diameter of (10 mm X 10 mm) and focal lengths of (-12.5 mm and 25 mm respectively) to ones with an aperture diameter of (25 mm X 25 mm) and focal lengths of (-50 mm and 100 mm respectively).

The change in the aperture diameter of the cylindrical lenses used for beam collimation helps to reduce spherical aberration and hence reduce the diameter of the laser ablation spot even further. The spherical aberration occurs because the laser beam waist is 9.85 mm. This is very close to the edges of the initial cylindrical lenses used, whose aperture diameter is 10 mm X 10 mm. Therefore, in the smaller aperture cylindrical lenses, each small lens refracts and converges the laser beam producing many small spherical spots or images of the laser spot that overlap each other, forming one big focused laser spot. On the other hand, with the larger aperture cylindrical lenses of 25 mm X 25 mm, the laser beam waist which is 9.85 mm is far off from the edges of the cylindrical lenses.

Hence it's only a few of the lenses in the central part of the overall cylindrical lens that refract and converge the laser beam, thereby, producing only a few images of the laser beam spot that overlap each other, hence forming a smaller laser ablation spot. Some minor changes made in the optical set up include;

1. The first iris diaphragm in the new set up is placed just after the beam collimation lenses. The aperture diameter is adjusted to 9.85 mm as can be seen in figure 96. This aperture diameter is close to the diameter of the laser beam waist that is immediately eminent from the laser source. This iris diaphragm removes the uneven and unwanted parts of the laser beam in the outer periphery.
2. A second iris diaphragm is introduced after a set of reflection mirrors placed after the first iris diaphragm as can be seen in figure 96. The aperture diameter of the second iris diaphragm is reduced from 2.55 mm to 1.5 mm to allow only the central core of the laser beam to pass through. This also reduces the laser ablation spot size after focusing the laser beam and totally excludes any unwanted extensions in the laser ablation spot.

At this point after all the improvements in the optical set up where completed the constrictions where now fabricated on the YBCO thin films based on the MgO substrates.

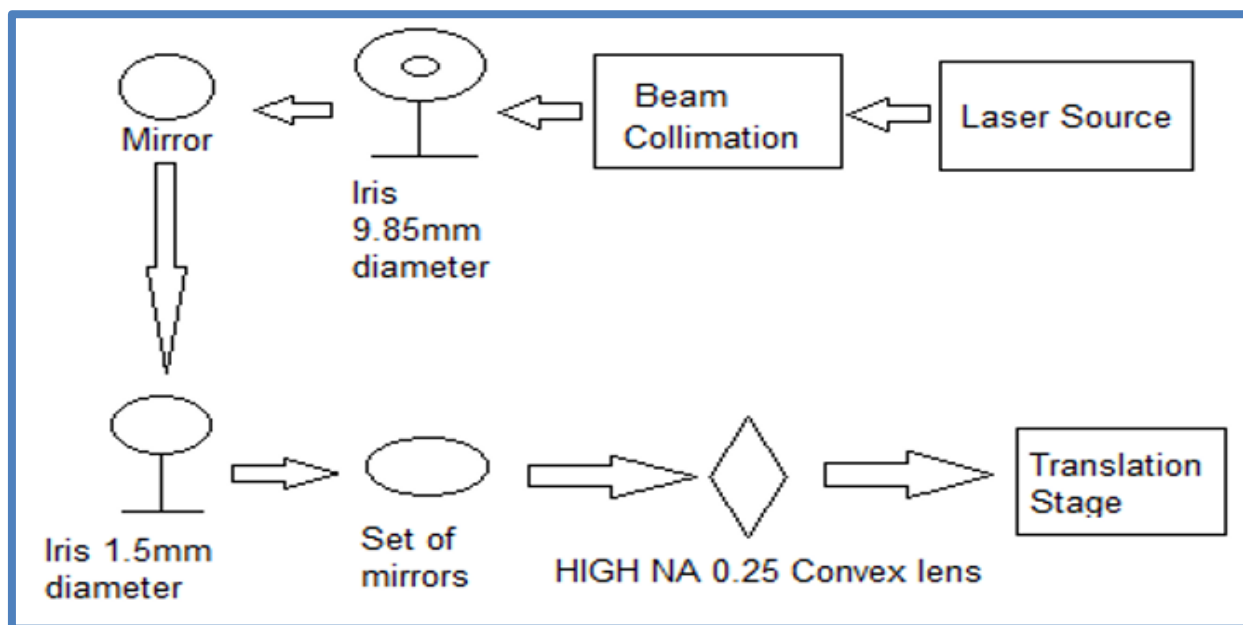


Figure 96 Overall optical experimental set up used to optimize the laser ablation spot.

Table 4 Objective Plano convex lenses with different parameters or specifications.

### Objective Numerical Apertures

Magnification	Plan Achromat (NA)	Plan Fluorite (NA)	Plan Apochromat (NA)
0.5x	0.025	n/a	n/a
1x	0.04	n/a	n/a
2x	0.06	n/a	0.10
4x	0.10	0.13	0.20
10x	0.25	0.30	0.45
20x	0.40	0.50	0.75
40x	0.65	0.75	0.95
40x (oil)	n/a	1.30	1.00
60x	0.75	0.85	0.95
60x (oil)	n/a	n/a	1.40
100x (oil)	1.25	1.30	1.40
150x	n/a	n/a	0.90

#### 3.11.2 KEYNOTE AREA:

*Because of the optical components between the laser source and the YBCO thin film being machined, power is lost as the laser beam passes through these optical components. Optical components such as the beam collimation set up, the reflective mirrors, the first iris diaphragm and the second iris diaphragm. When the second iris is set to an aperture diameter of 1.5 mm, then for the incident laser beam reaching the sample to have a power of 1.876 mW, then the power effluent from the laser source has to be set to approximately 25.27 mW. As the laser beam passes through the optical components it loses some of its power and eventually the power reaching the sample with this set up is only about 1.876 mW. This power level of 1.876 mW is just optimum to remove the top 200 nm layer of YBCO thin film in areas applied and leave behind the substrate only.*

*Again, the laser power is measured with a laser power wattmeter at each point along the optical set up. However, the laser power wattmeter is positioned just before the objective plano convex lens and after the second iris diaphragm when measuring the laser power that is incident on the sample. It cannot be placed after the focusing optical lens because the focus point can damage the laser power wattmeter because of the focusing power of the objective lens and the small size of the focused spot (AREA). In order to measure the laser power emanating from the laser source the laser power wattmeter is placed just before the beam collimation set up.*

### 3.11.3 AFM IMAGES OF THE CONSTRICTIONS FABRICATED WITH THE NEW AND IMPROVED OPTICAL SETUP.

The first constriction was fabricated using the following equipment in the optical set up namely; the objective Plano convex lens, the first iris diaphragm was set to an aperture diameter of 9.85 mm, the second iris diaphragm was set to an aperture diameter of 1.5 mm, and cylindrical lenses with an aperture diameter of 10 mm X 10 mm.

By using the objective Plano convex lens the laser ablation spot size reduced from 17.0  $\mu\text{m}$  to 10.47  $\mu\text{m}$  this can be seen in figure 97. The focus position for the objective Plano convex lens is much closer to the lens itself along the Z-axis as compared to the other conventional spherical convex lenses; this is because the objective lens has a much higher focusing power. The constriction shown in figure 97 was fabricated and imaged with the following settings; laser power level 1.728 mW, objective Plano convex lens of numerical aperture 0.25, second iris diaphragm set at an aperture diameter of 1.5 mm, separation distance between the laser ablation spots ( $S_W$ ) is 13.8  $\mu\text{m}$  and the AFM image scan area is 40  $\mu\text{m}$  X 40  $\mu\text{m}$ . The result of the fabrication is that the laser ablation diameter seen in figure 97 is 10.47  $\mu\text{m}$ , measured between the black arrows in the topography line fit.

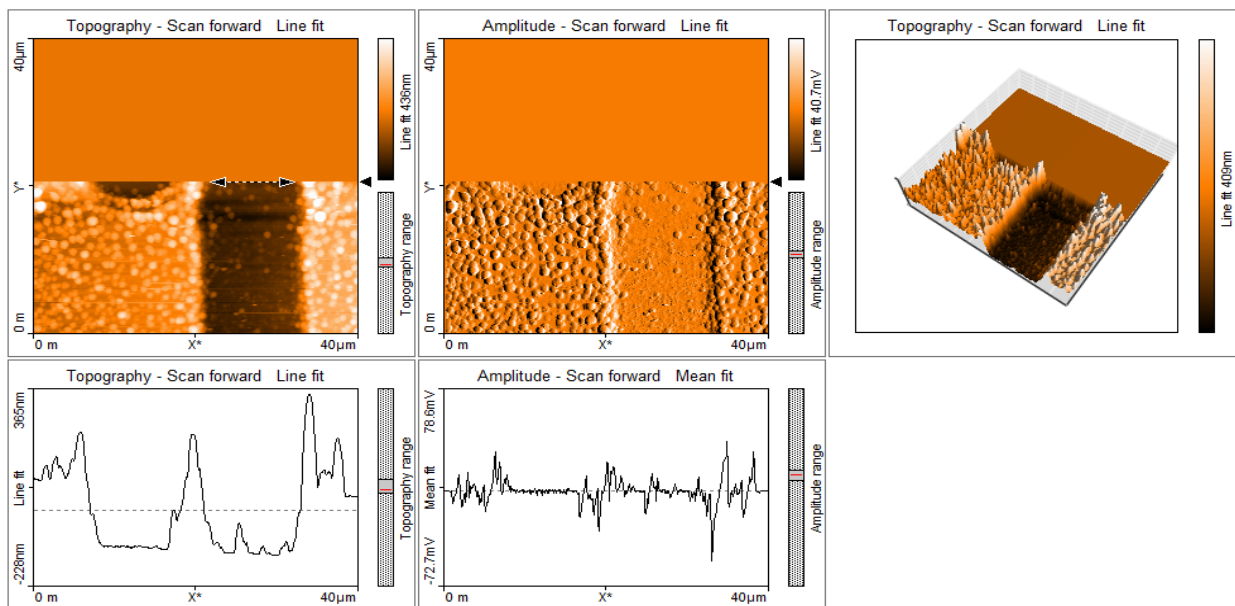


Figure 97 AFM image of constriction showing the laser ablation spot size is 10.47  $\mu\text{m}$ .

The constriction width is determined by using the amplitude line fit of the AFM image in figure 98. The constriction width measured between the black arrows in figure 98 is determined to be 2.59  $\mu\text{m}$ , which is a micron-sized constriction.

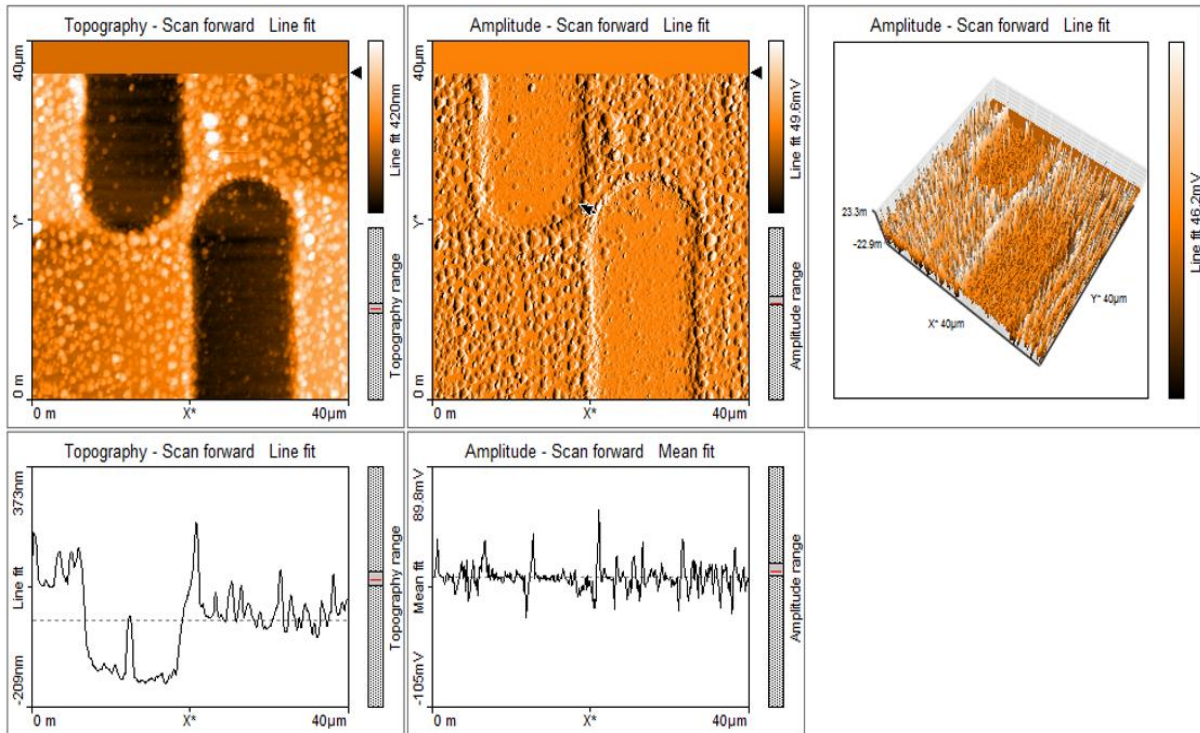


Figure 98 AFM image of the constriction made showing the constriction width achieved is 2.59  $\mu\text{m}$ .

### 3.11.3.1 PROBLEM ENCOUNTERED

*The main problem that occurred in this set up was that the objective Plano convex lens was damaged in the centre by the power of the laser beam during the process of finding the focus point of the lens before cutting. When finding the focus point of the lens the laser ablation spots have to be large enough to be easily seen during the focusing process. Therefore, you need to begin by using a laser power setting of about 150 mW. However, with this laser power setting the objective lens can be easily burnt in the centre during the focusing process. This is because of the objective lens high propensity to converge the laser beam. Therefore, one has to work with a laser power less than 150 mW during the focusing process with these lenses and later on reduce the power during fabrication to the desired level. With a power level of 150 mW the lens got burnt and subsequently “smoked” the sample during fabrication. Hence, further constrictions fabricated with these lenses would look blurred or show noise in the AFM image.*

### 3.11.3.2 CYLINDRICAL BEAM COLLIMATION LENSES CHANGED TO APERTURE DIAMETER 25 mm X 25 mm.

The constrictions fabricated from this point onwards were made by using the cylindrical lenses with an aperture diameter of 25 mm X 25 mm and focal lengths of - 50 and + 100 mm respectively. The cylindrical lenses were aligned as seen in figure 99 and 100 in order to collimate the laser beam.

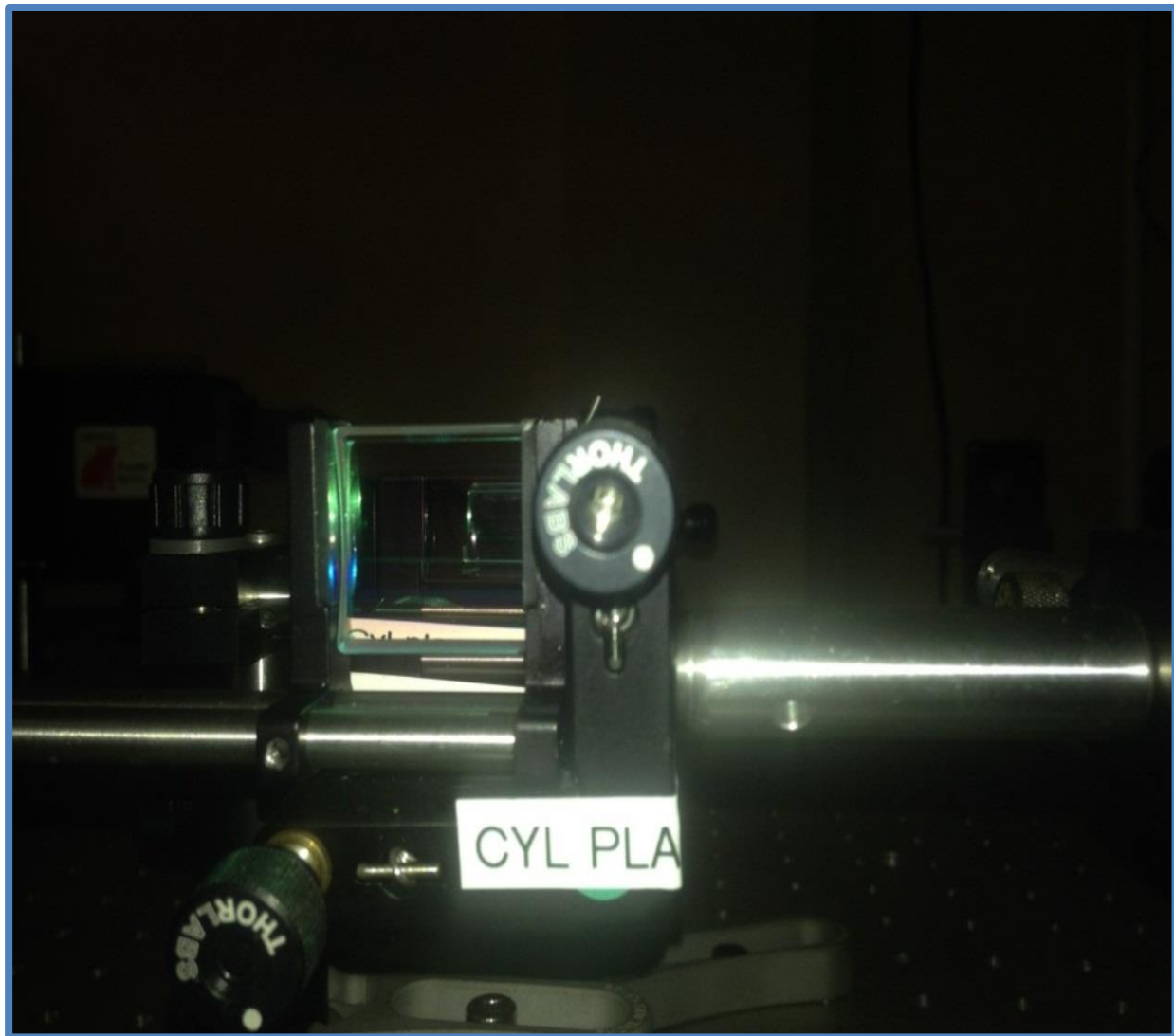


Figure 99 Cylindrical concave lenses of focal length of (-50 mm ) and Cylindrical convex lens with a focal length of (100 mm) aligned to collimate the laser beam.

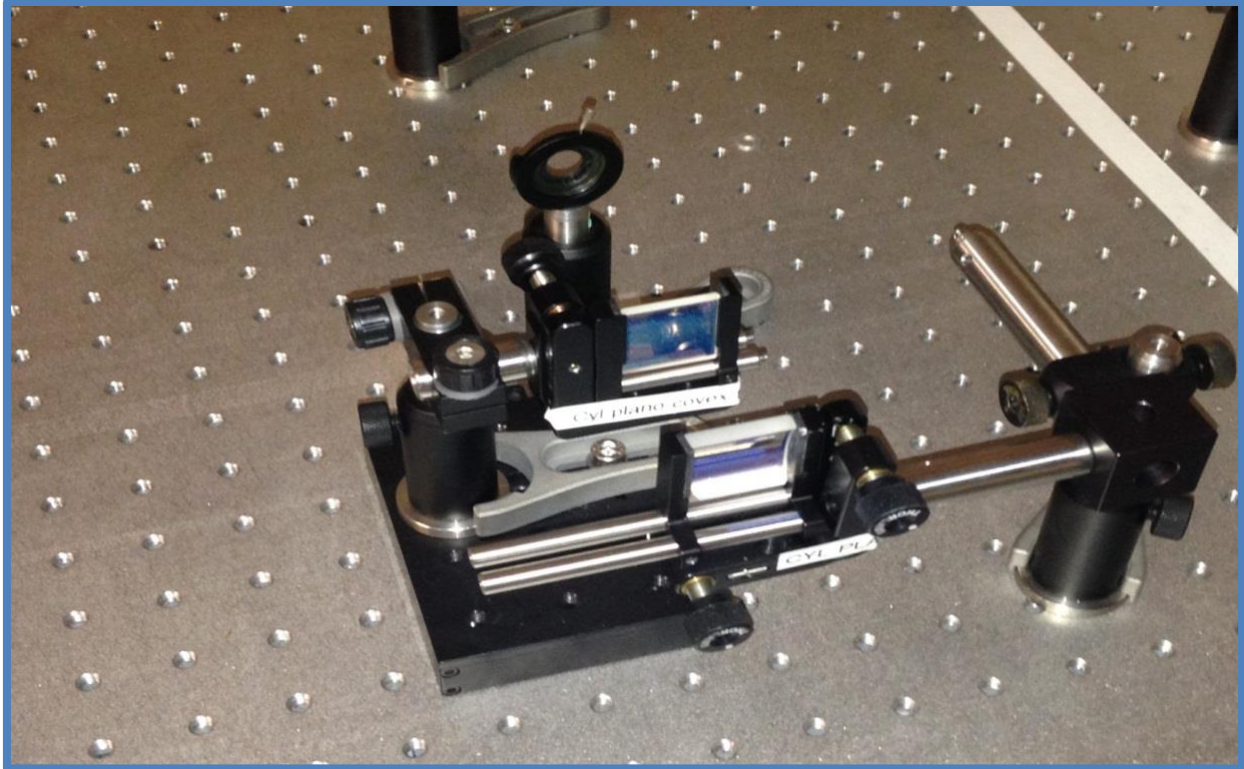


Figure 100 3-D view of the cylindrical diverging lenses of focal length (-50 mm) and the cylindrical convex lenses of focal length (100 mm).

The cylindrical convex lens of focal length 25 mm and the cylindrical concave lens of -12.5 mm were replaced by a cylindrical convex lens of 100 mm and cylindrical diverging lens of -50 mm. These lenses have a larger aperture diameter 25 mm X 25 mm, a bit slimmer and better made. The larger aperture diameter (25 mm X 25 mm) helps prevent spherical aberration and reduces the size of the laser ablation spot produced even further.

#### **3.11.4 RESULTS OF USING THE COMBINATION OF THE LARGER APERTURE DIAMETER CYLINDRICAL LENSES AND THE OBJECTIVE LENS.**

##### **3.11.4.1 AFM IMAGES OF THE CONSTRICTIONS MADE WITH THE LARGER APERTURE CYLINDRICAL LENSES.**

The constrictions fabricated with the larger aperture diameter cylindrical lenses were cut with the following laser settings. Laser power 2.104 mW, with an objective lens whose numerical aperture is 0.25, the second iris diaphragm is set to an aperture of 1.5 mm, AFM scan area 40  $\mu\text{m}$  X 40  $\mu\text{m}$  and the separation distance between the laser ablation spots is 8.0  $\mu\text{m}$ .

Increasing the apertures of the cylindrical lenses used for beam collimation and combining these lenses with the objective Plano convex lens reduced the diameter of the laser ablation spot even further. The laser ablation diameter reduced from 10.47  $\mu\text{m}$  to 7.344  $\mu\text{m}$  seen in figure 101. The measurement is taken between the black arrows in the topography line fit. Because of the reduced laser ablation spot diameter the separation distance between the laser ablation spots ( $S_W$ ) is also reduced to 8.0  $\mu\text{m}$ .

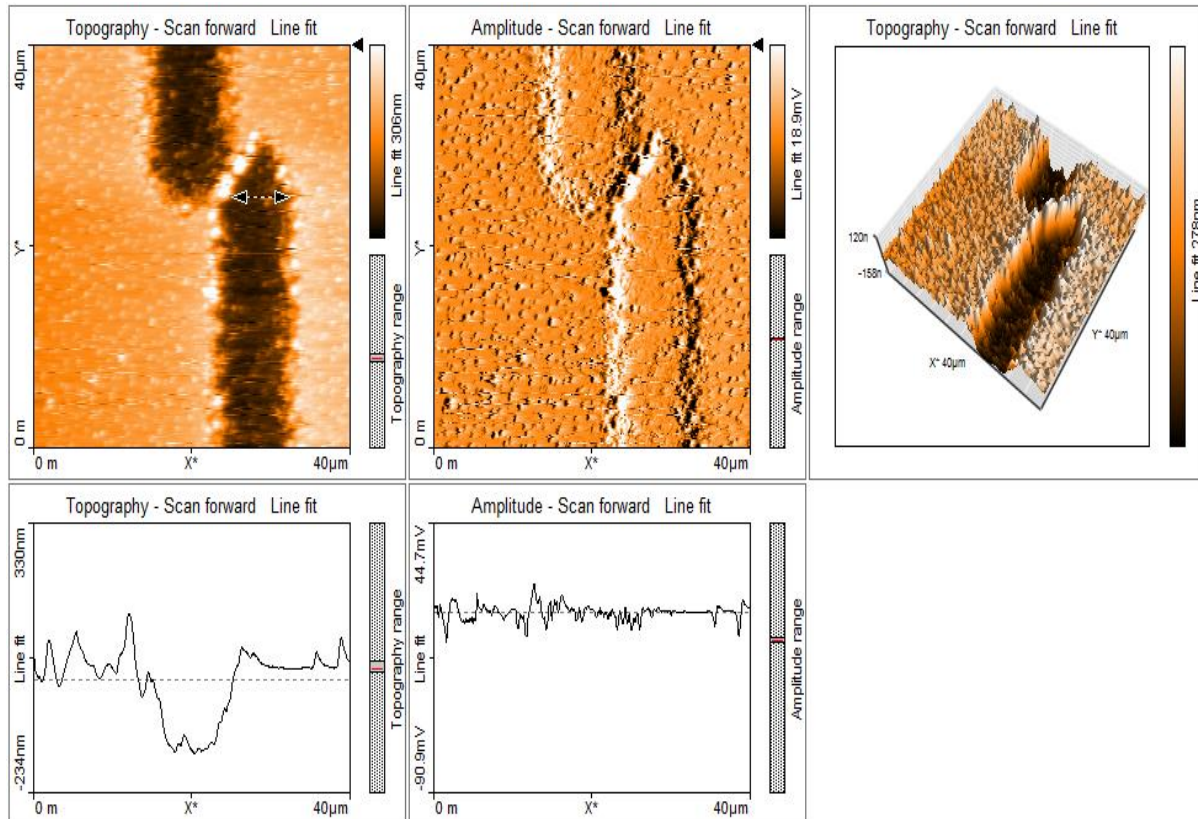


Figure 101 AFM image of the resulting constriction showing the laser ablation spot diameter of 7.344  $\mu\text{m}$ . The AFM image in figure 102 shows the width of the constriction is 1.8  $\mu\text{m}$  in the micron range. The width is measured between the black arrows in the amplitude line fit. The images look a little blurred or like they have noise in them. The reason for this is that the objective Plano convex lens used to fabricate the constriction was burnt by the laser power of (150 - 200 mW) during focusing of the laser beam. As a result, the sample is smoked during fabrication; hence, the cutting is not very clear or defined.

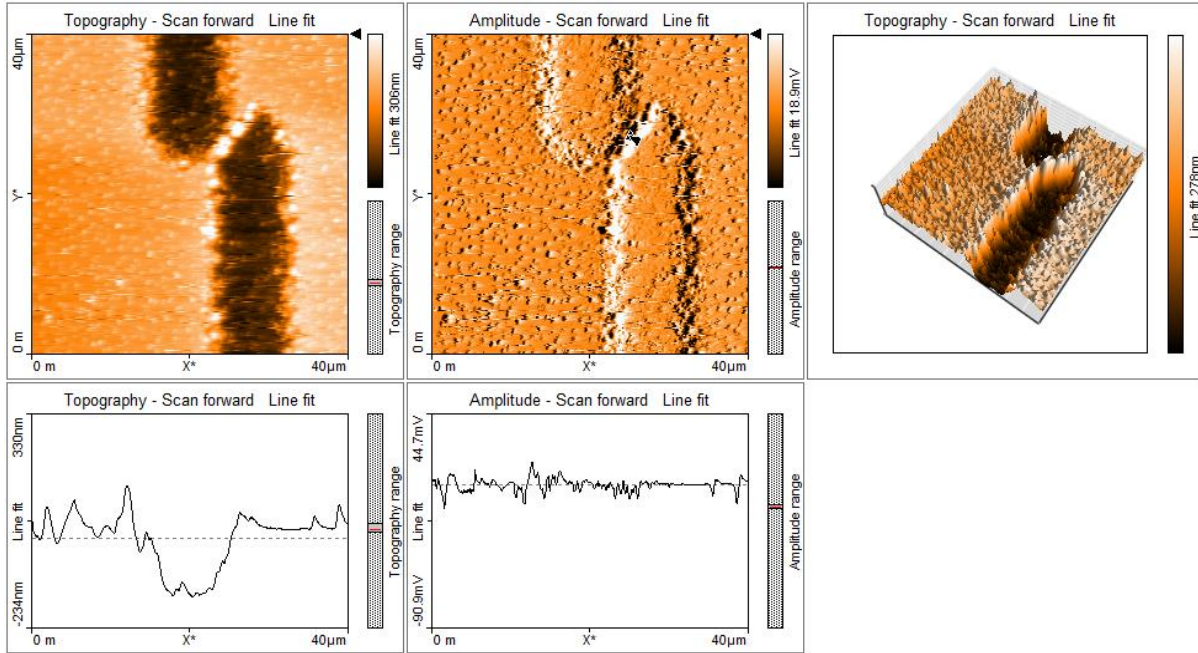


Figure 102 AFM image of the constriction showing the constriction width is 1.82  $\mu\text{m}$ .

The AFM image in figure 103 shows that the constriction length is 6.89  $\mu\text{m}$ . This was achieved by separating the laser ablation spots along the width of the sample by a separation distance of 5  $\mu\text{m}$ . Hence, just as the laser ablation diameter reduces in size with the objective Plano convex lens so also the overlapping length of the constriction reduces.

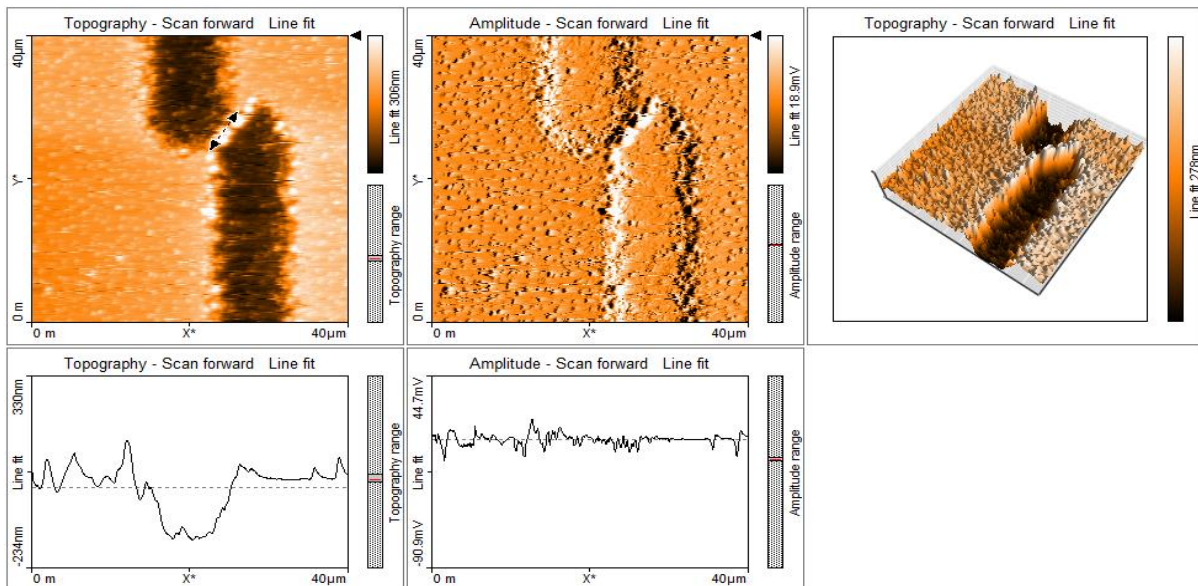


Figure 103 AFM image showing the length of the constriction is 6.89  $\mu\text{m}$ .

The laser ablation diameter of the constriction in figure 101 is 7.344  $\mu\text{m}$ . With a separation distance between the laser ablation spots ( $S_W$ ) of 8  $\mu\text{m}$  one was supposed to achieve a constriction with of about 0.7  $\mu\text{m}$  (sub-micron) but instead in practice this is not achieved and we achieved a constriction width of 1.8  $\mu\text{m}$ .

The objective Plano convex lens enabled the laser beam to be focused to a smaller laser ablation spot size of 7.344  $\mu\text{m}$ . However, the sample was “smoked” because the lens was initially burnt or damaged by a high power laser application (150 - 200 mW) and as a result, the lens could no longer be used to fabricate smaller sub-micron and Nano sized junctions.

### 3.12 REFERENCES

- [1] M. Grehn *et al.*, “Femtosecond-laser induced ablation of silicate glasses and the intrinsic dissociation energy,” vol. 4, no. 4, pp. 3030–3032, 2014.

# CHAPTER 4

## MICRON, SUB-MICRON AND NANO SIZED CONSTRICTIONS

### 4.1 INTRODUCTION

A series of constrictions were fabricated utilizing all the optical technology, optimization techniques and programming tools described in previous chapters and using all the specifications and settings described in previous chapters. In order to measure the dimensions of the constrictions fabricated the AFM (Atomic force microscope) was utilised to get the exact measurements of the dimensions of these constrictions. The AFM scans were initially done using the prototype cantilever tips on the AFM in the tapping mode. Later when better images were required and the process of imaging was established then the AFM Scans were done with a type DT-NCHR diamond cantilever tips.

### 4.2 REPLACING THE OBJECTIVE PLANO CONVEX LENS (NA 0.25) WITH A SPHERICAL CONVEX LENS OF FOCAL LENGTH (30 mm).

It became necessary to replace the objective Plano convex lens because the objective Plano convex lens of NA 0.25 was “burnt” or damaged in the centre and could no longer produce clear cut constrictions. The way in which the objective lens was damaged is described in the previous section. By changing from the objective Plano, convex lens to a spherical convex lens of focal length 30 mm the laser ablation diameter increased in size. The reason for this is that the objective lens focuses the laser beam more and produces a much smaller laser ablation spot diameter. The spherical convex lens 30 mm focal length produces a laser ablation spot size diameter smaller than that of the spherical convex lens 45mm focal length but it produces a bigger laser ablation spot size than that of the objective Plano convex lens (NA 0.25).

To be precise with an objective lens numerical aperture 0.25, X10 magnification, the laser ablation spot size diameter achieved with a power of 2.1 mW was about 7.3  $\mu\text{m}$ . The spherical convex lens of focal length 45 mm with a power setting of 4.9 mW produced a laser ablation diameter of about 17  $\mu\text{m}$ . Finally, with the spherical convex lens of 30 mm

focal length and a power setting of 2.1 mW, a laser ablation spot size diameter of about 15.8  $\mu\text{m}$  was achieved. Of course, the smaller the laser ablation spot achieved the easier it would be to fabricate a NANO sized constriction as indicated in the objectives of the thesis.

### 4.3 MICRON-SIZED CONSTRICTION ACHIEVED ON YBCO THIN FILM

#### 4.3.1 SEPARATION DISTANCE BETWEEN LASER ABLATION SPOTS ( $S_W$ ) OF 18 $\mu\text{m}$ in G-CODE.

As described earlier in chapter 3 the G-code instructs the movement of the translation stage such that 6 constrictions are cut on the bottom lower side of the rectangular thin film and 6 constrictions are cut on the top end of the thin film. The micron-sized constriction being discussed in this section is the 1<sup>st</sup> constriction on the lower side of the thin film for the separation distance between the laser ablation spots of 18  $\mu\text{m}$  set in G-code. To fabricate this constriction the laser power was set at 2.035 mW incident on the sample, a spherical convex lens of 30 mm focal length was used, and an AFM scan area of 75  $\mu\text{m}$  X 75  $\mu\text{m}$  was set in the AFM software.

Figure 104 shows the AFM image of the micron-sized constriction fabricated. In the topography line fit of the AFM image the width of the constriction was determined to be 1.6  $\mu\text{m}$  in between the black arrows seen in the image.

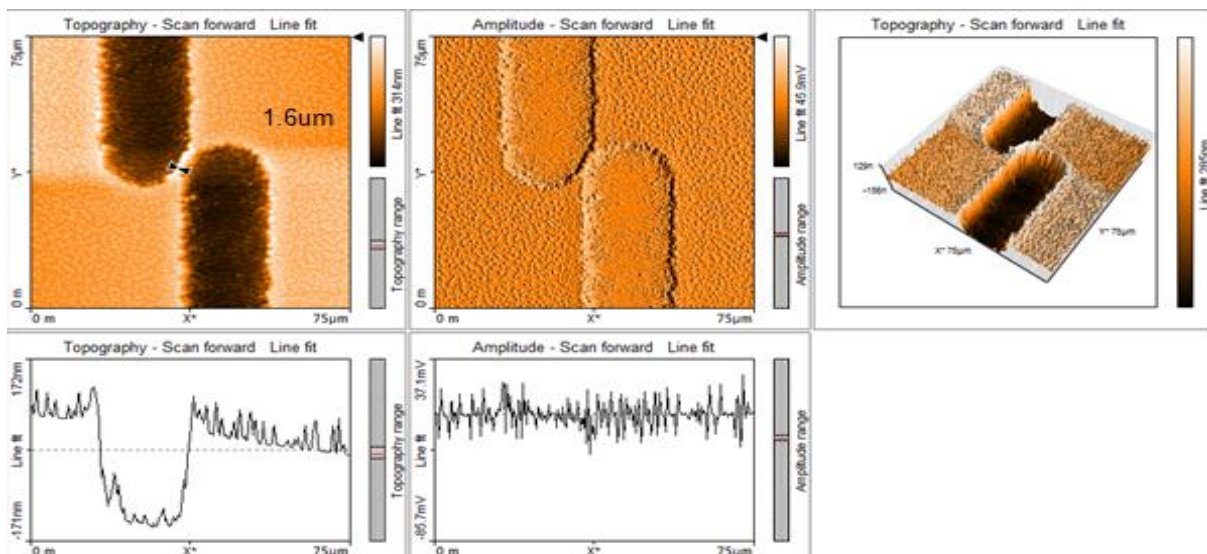


Figure 104 AFM image of micron-sized constriction with ( $S_W = 18 \mu\text{m}$ ) and an AFM scan area of 75  $\mu\text{m}$  X 75  $\mu\text{m}$ , showing a constriction width of 1.6  $\mu\text{m}$ .

From the topography line fit of the AFM image in figure 105 the width of the same constriction as above was determined to be  $1.76 \mu\text{m}$ . The constriction in figure 105 is the same as that in figure 104 however the determined widths are not exactly the same although they are close. In figure 105, a slightly different method is used to measure the width of the constriction. This is done by capturing an image at each point as the cantilever tip scans transversely at 90 degrees perpendicularly to the laser ablation spot. Several images are taken during this process one of which is shown on the topography line fit in figure 105. The image shows the scan right at the narrowest point on the constriction. By using the topography line fit the width of the constriction is represented as an amplitude above the zero axis. The width of this amplitude above the zero axis in between the black arrows is the width of the constriction. There are troughs on both sides of the width representing the laser ablation spots themselves. Although it is the same constriction, the widths are not the same but they are close, the reason for this is that in determining such small dimensions using the free hand slight errors can occur. The second reason is that the constrictions fabricated have a variable width along the length of the constriction so it is possible that the point at which the width is measured in figure 104 is not exactly the same point at which the width is measured in figure 105.

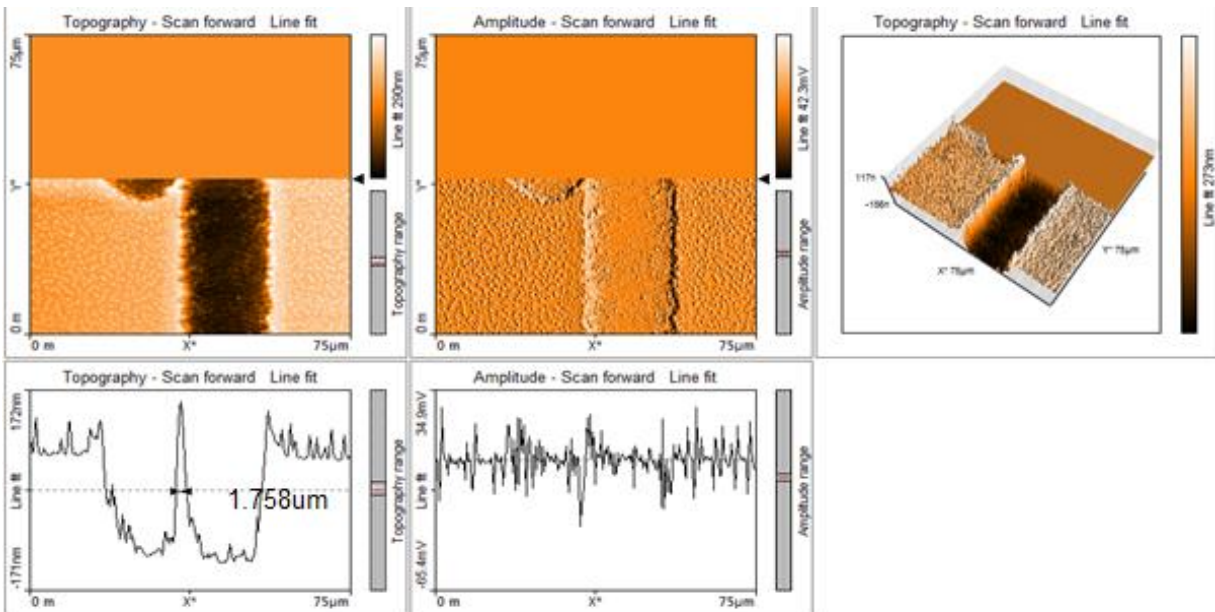


Figure 105 AFM image of micron-sized constriction with ( $S_w = 18 \mu\text{m}$ ) and an AFM scan area of  $75 \mu\text{m} \times 75 \mu\text{m}$ , showing a constriction width of  $1.76 \mu\text{m}$ .

In figure 106, we focus on a very small scan area on the sample that is 20.5  $\mu\text{m}$  X 20.5  $\mu\text{m}$  and by doing so we zoom in on the sample. It should now be easier to measure a more precise value for the constriction width by zooming in. In this case, the constriction width is determined to be 1.68  $\mu\text{m}$  in between the black arrows. The constriction is still the same as in the previous section but we are getting a more precise measurement of it.

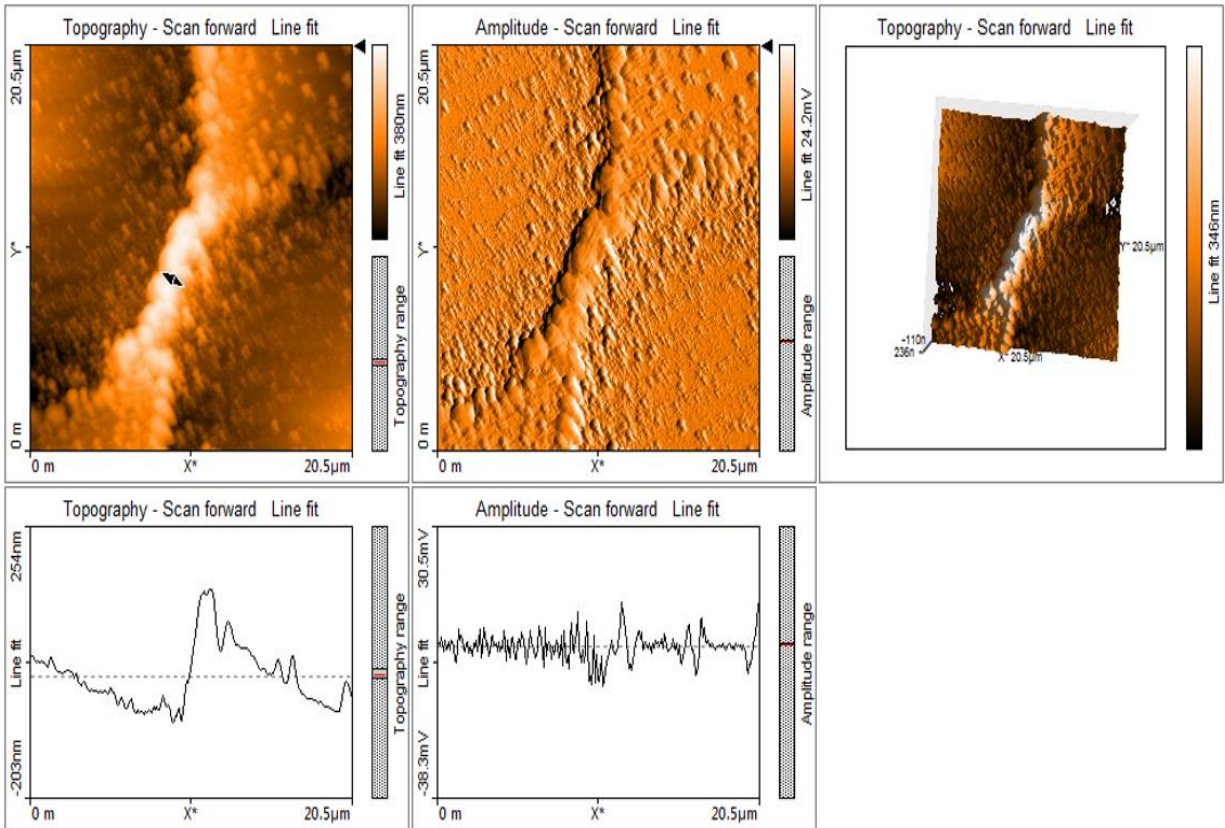


Figure 106 AFM image of the micron-sized constriction with ( $S_W = 18 \mu\text{m}$ ) and AFM scan area of 20.5  $\mu\text{m}$  X 20.5  $\mu\text{m}$ , showing a constriction width of 1.68  $\mu\text{m}$ .

By using the same scan, area of 20.5  $\mu\text{m}$  X 20.5  $\mu\text{m}$  the constriction length is determined to be 12.79  $\mu\text{m}$ . This can be seen in the topography line fit image in figure 107. The measurement is done in between the black arrows in the image.

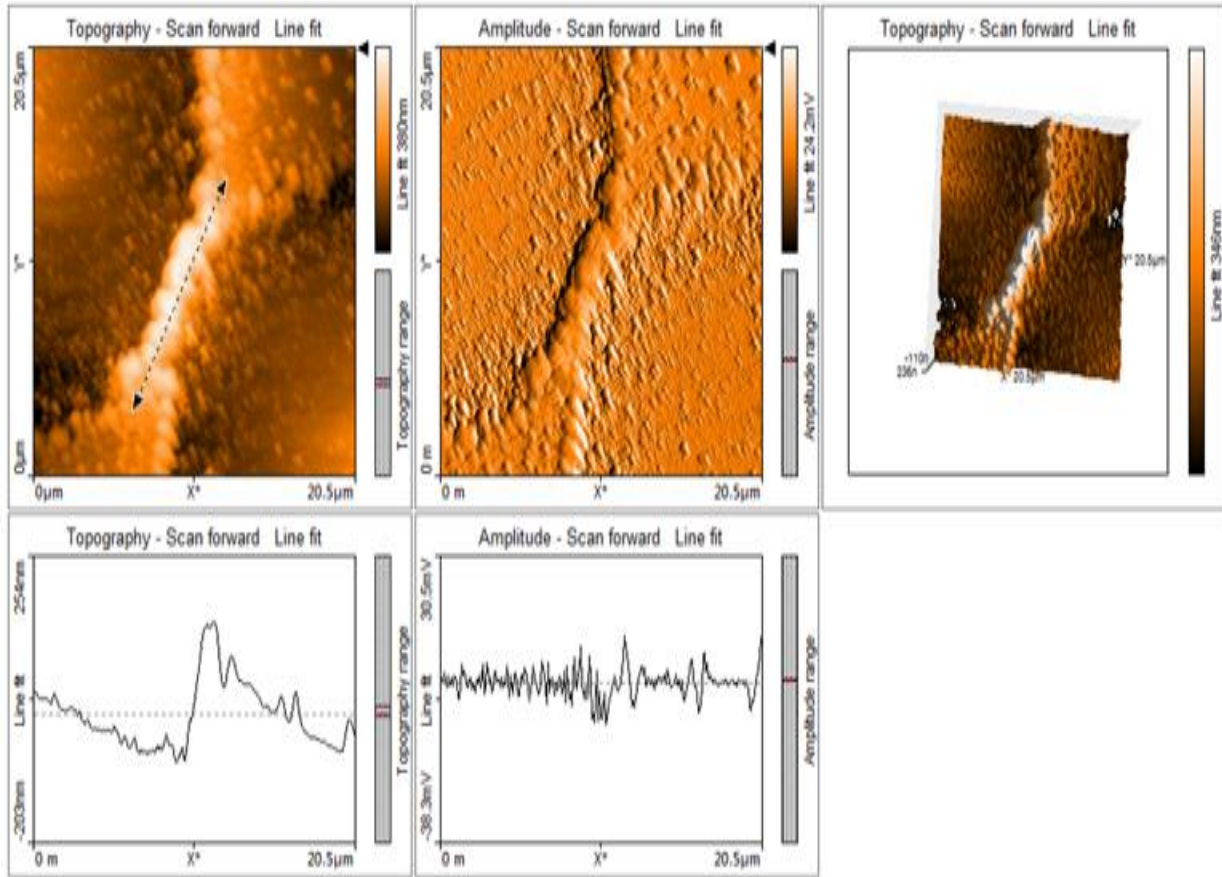


Figure 107 AFM image of the micron-sized constriction with ( $S_W = 18 \mu\text{m}$ ) and AFM scan area of  $20.5 \mu\text{m} \times 20.5 \mu\text{m}$ , showing the constriction length is  $12.79 \mu\text{m}$ .

#### 4.4 MICRON-SIZED CONSTRICTION ACHIEVED ON THE YBCO THIN FILM.

##### 4.4.1 SEPARATION DISTANCE BETWEEN THE LASER ABLATION SPOTS ( $S_W$ ) OF $17.5 \mu\text{m}$ IN G-CODE.

As in the previous section, this is the 1<sup>st</sup> constriction on the sample. In this case the separation distance between the laser ablation spots ( $S_W$ ) is reduced to  $17.5 \mu\text{m}$  and a new constriction is fabricated. The resulting AFM images can be seen in figures below. The constriction in figure 108 was fabricated and imaged with the following laser and AFM settings. The laser power was set at  $2.035 \text{ mW}$ , the AFM scan area is  $75 \mu\text{m} \times 75 \mu\text{m}$ , spherical convex lens of  $30 \text{ mm}$  focal length was used and the constriction width achieved is  $1.58 \mu\text{m}$  as seen in the topography line fit between the black arrows.

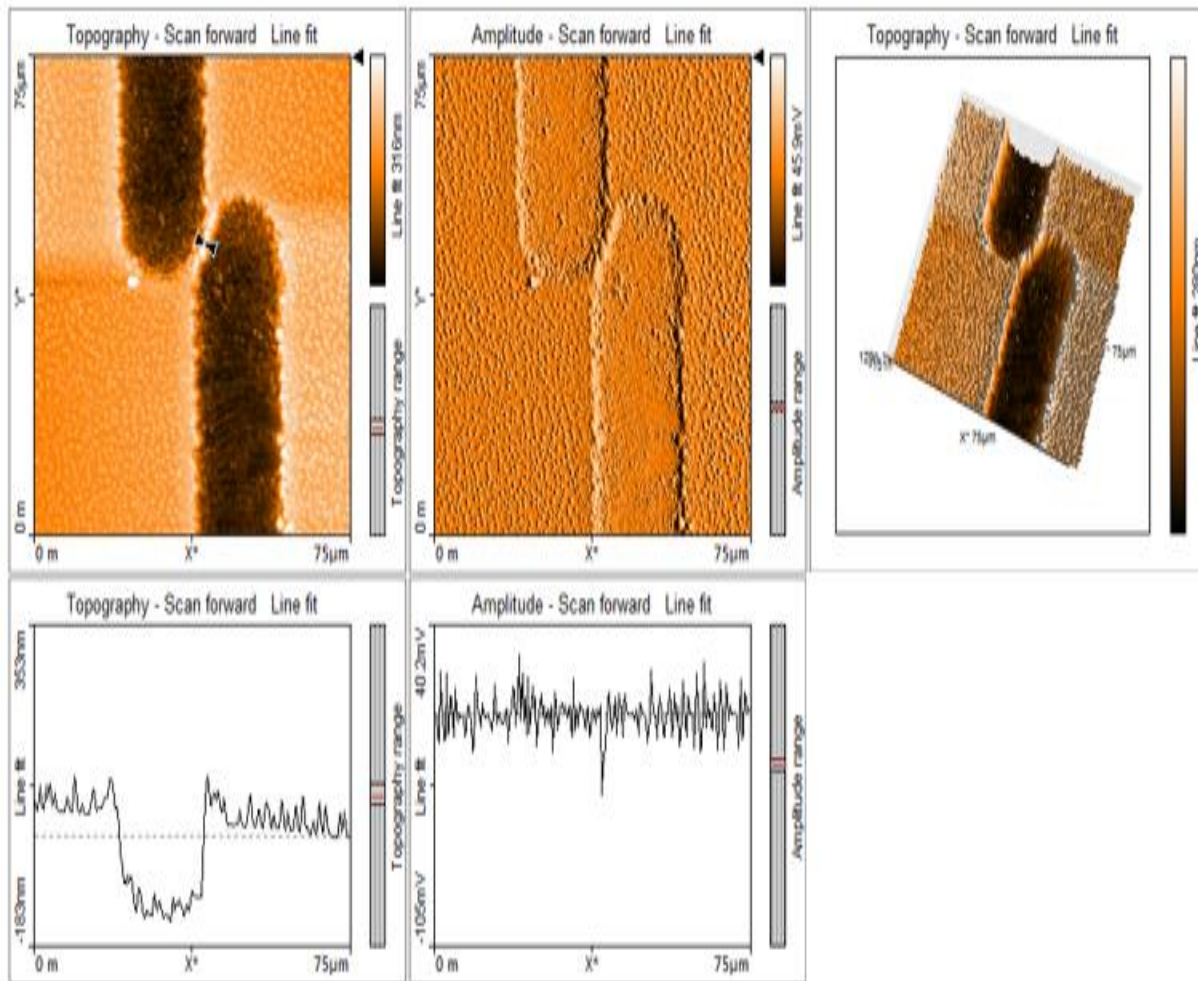


Figure 108 AFM image of the micron-sized constriction fabricated with ( $S_w = 17.5 \mu m$ ) and AFM scan area of  $75 \mu m \times 75 \mu m$  showing a constriction width of  $1.58 \mu m$ .

Figure 109 shows the same constriction with a laser separation distance of  $17.5 \mu m$ . A snap shot is taken in the AFM software at a specific point on the cross section as can be seen on the topography line fit image. On the profile distribution image below it, an amplitude of the constriction rises above the zero axis and a line is drawn across the amplitude to determine the width of the constriction as  $1.47 \mu m$ .

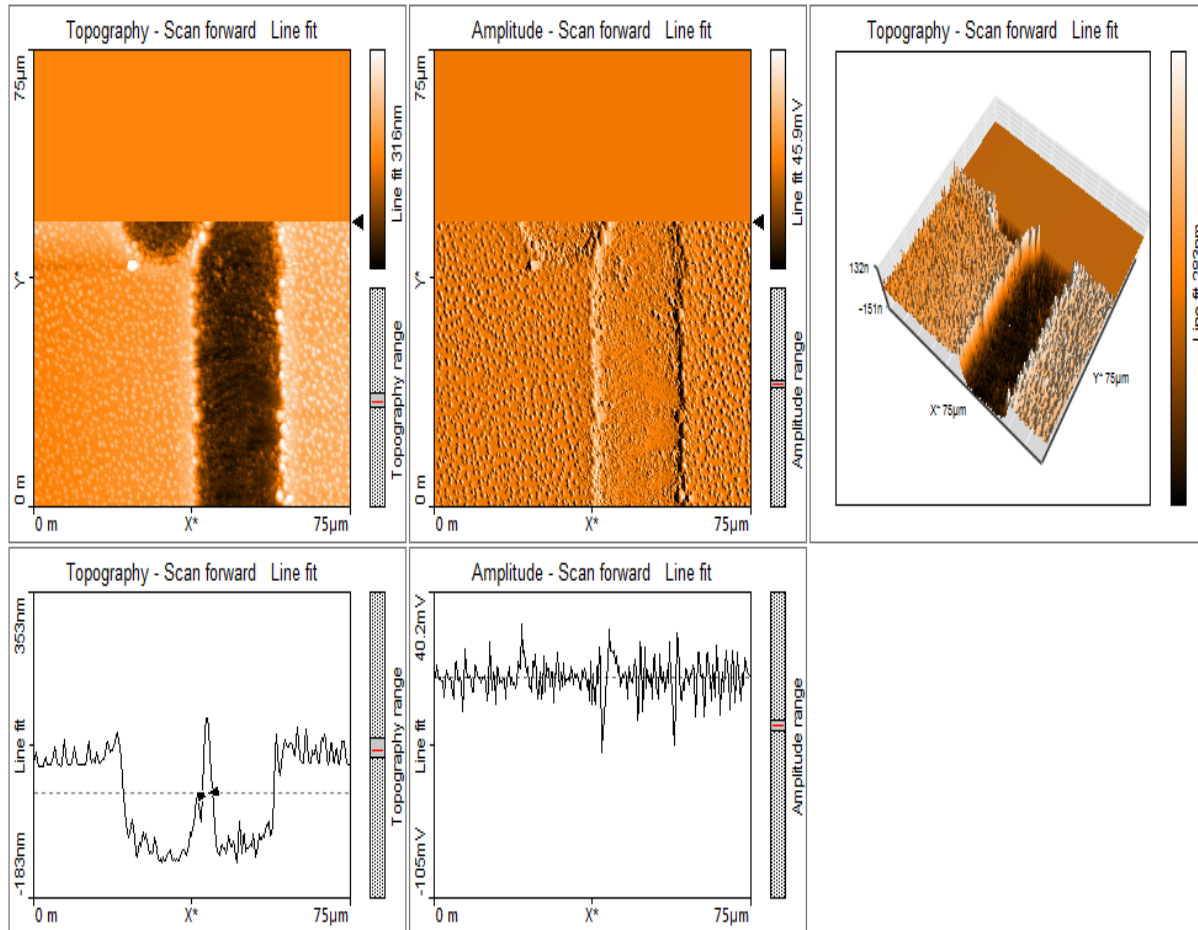


Figure 109 AFM image of the micron-sized constriction fabricated with ( $S_w = 17.5 \mu m$ ) and AFM scan area of  $75 \mu m \times 75 \mu m$  showing a constriction width of  $1.47 \mu m$ .

The constriction depicted in figures 108 and 109 is the same constriction. However the constriction widths are different. This is because although aiming for the narrowest point on the constriction the two measurements are taken at slightly different points along the width. The approximate narrowest width of the constriction is determined to be in the range ( $1.47 \mu m - 1.58 \mu m$ ).

When the scan area is reduced to  $20.5 \mu m \times 20.5 \mu m$  in the AFM software, then the image in figure 110 is achieved. With these reduced scan area it's easier to find the narrowest point on the constriction and then determine the more precise width of the constriction as  $1.39 \mu m$ .

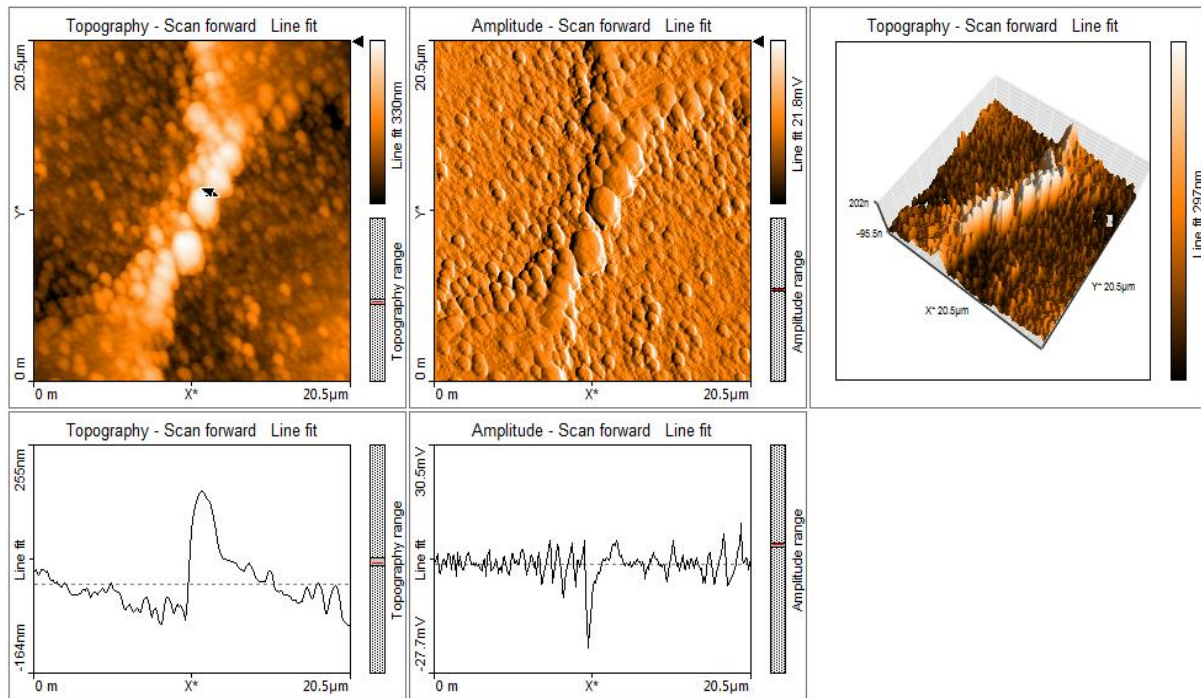


Figure 110 AFM image of the micron-sized constriction fabricated with ( $S_W = 17.5 \mu m$ ) and AFM scan area of  $20.5 \mu m \times 20.5 \mu m$  showing a constriction width of  $1.39 \mu m$ .

The length of this constriction can be seen in figure 111 and is approximately  $12.26 \mu m$ .

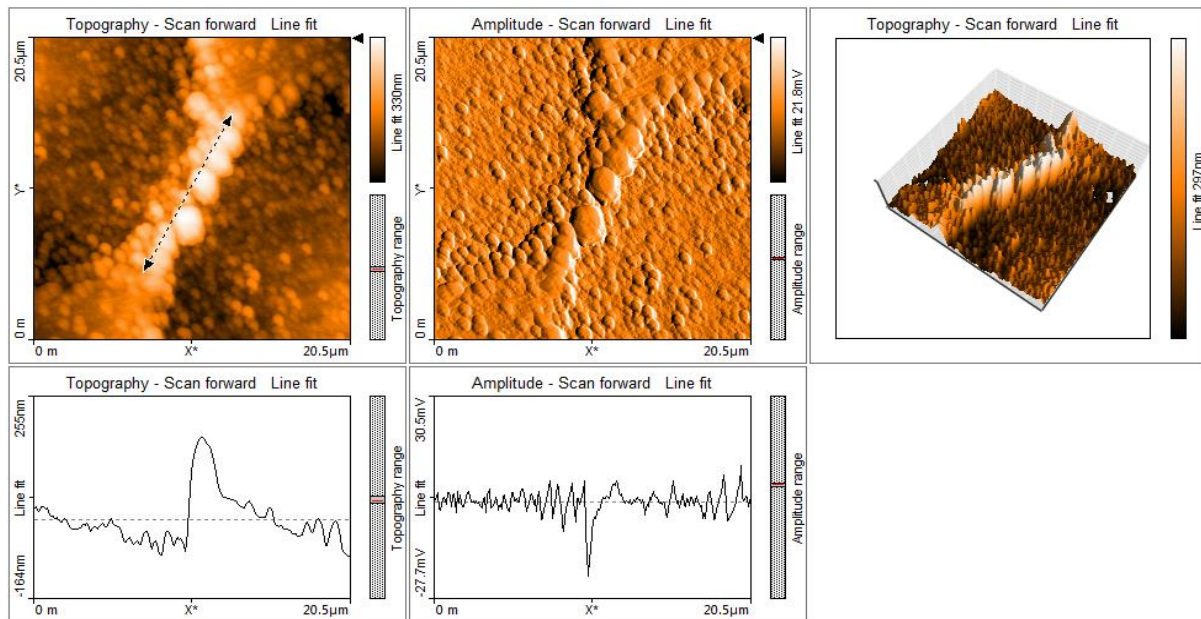


Figure 111 AFM image of the micron-sized constriction fabricated with ( $S_W = 17.5 \mu m$ ) and AFM scan area of  $20.5 \mu m \times 20.5 \mu m$  showing a constriction length of  $12.26 \mu m$ .

A cross section was cut across the narrowest point on the constriction by zooming into a scan area of  $20.5 \mu\text{m} \times 20.5 \mu\text{m}$ . This is done to get a more precise measurement of the constriction and to validate that the constriction width is indeed  $1.39 \mu\text{m}$  as can be seen in figure 112.

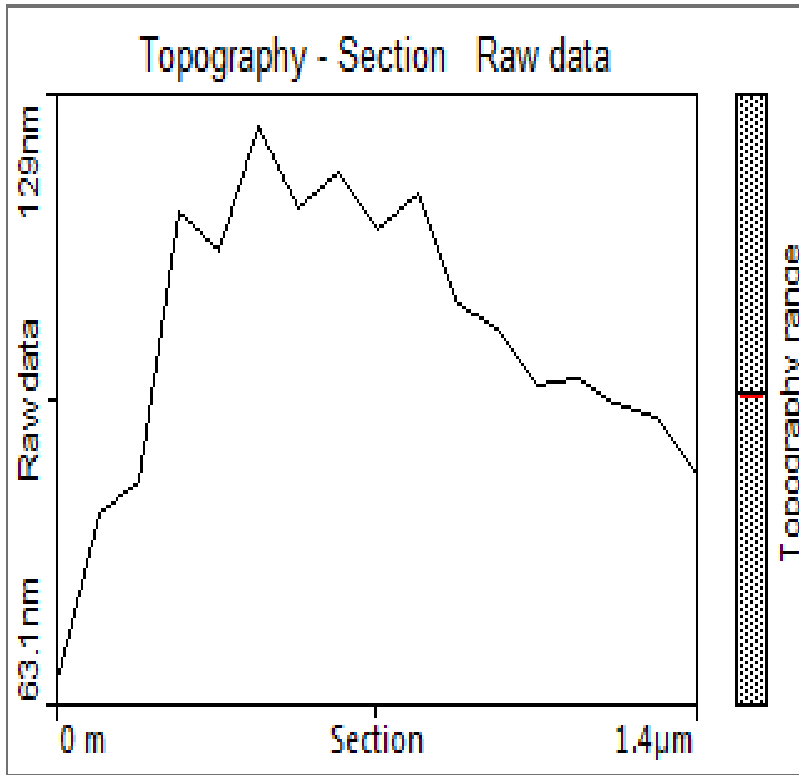


Figure 112 Cross section taken of the constriction showing a constriction width of  $1.39 \mu\text{m}$ .

## 4.5 MICRON-SIZED CONSTRICTION ACHIEVED ON YBCO THIN FILM

### 4.5.1 SEPARATION DISTANCE BETWEEN THE LASER ABLATION SPOTS ( $S_w$ ) OF $17 \mu\text{m}$ IN G-CODE.

In this case, this is the 2<sup>nd</sup> constriction or qubit on the thin film. The separation distance between the laser ablation spots ( $S_w$ ) is reduced to  $17 \mu\text{m}$  in the G-code. This constriction was fabricated and imaged with the following settings. The laser power is set to 2.035 mW, the AFM scan area is set to  $20.8 \mu\text{m} \times 20.8 \mu\text{m}$  and a spherical convex lens of 30 mm focal length is used. The width of the constriction fabricated is  $1.63 \mu\text{m}$  as seen in figure 113.

As stated in previous chapters according to equation (1) the;

$$\text{Width of the constriction} = \text{separation distance between the laser ablation spots } (S_W) - \text{laser ablation diameter} \quad (1)$$

By gradually reducing ( $S_W$ ), we should be achieving smaller widths for the constrictions fabricated if the laser ablation spot remains the same. Initially the constriction widths fabricated reduced in size then in this last scenario slightly increased in size. However, this is a temporary setback.

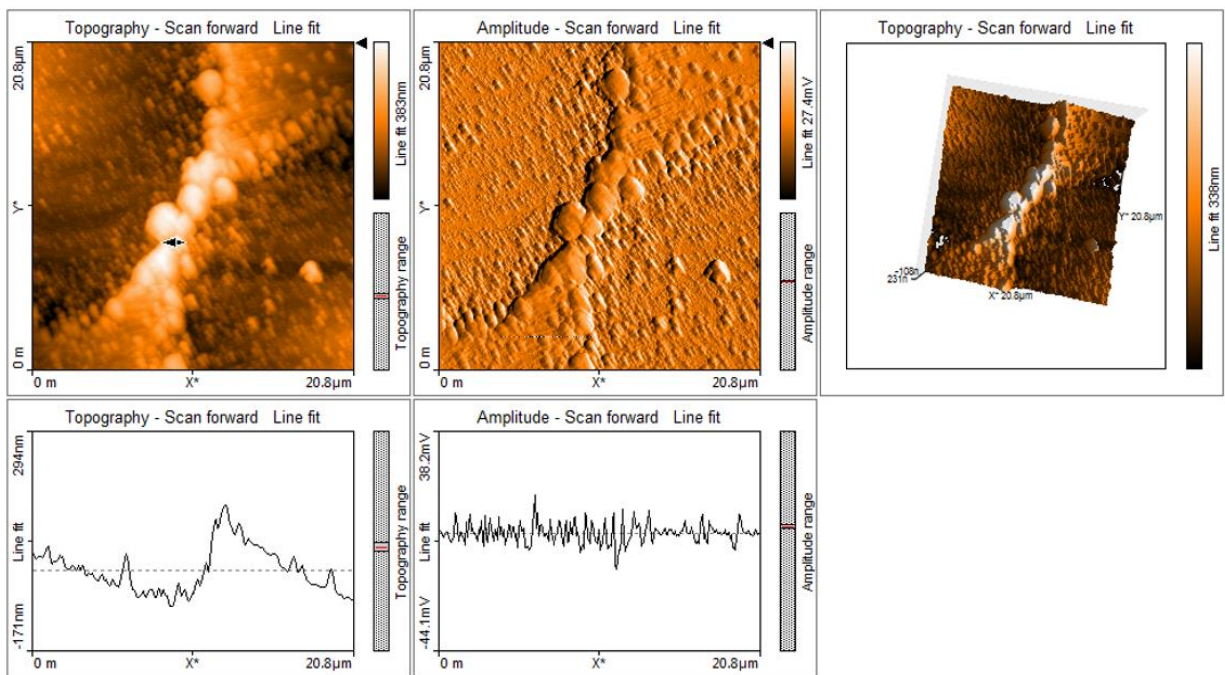


Figure 113 AFM image of the micron-sized constriction fabricated with ( $S_W = 17 \mu m$ ) and AFM scan area of  $20.8 \mu m \times 20.8 \mu m$  showing the constriction width is  $1.63 \mu m$ .

## 4.6 SUB-MICRON - SIZED CONSTRICTION ACHIEVED ON YBCO THIN FILM.

### 4.6.1 SEPARATION DISTANCE BETWEEN THE LASER ABLATION SPOTS ( $S_W$ ) OF $16.5 \mu m$ .

This is the 2<sup>nd</sup> constriction on the sample. The separation distance between the laser ablation spots ( $S_W$ ) was reduced to  $16.5 \mu m$ .

The constriction was fabricated with a laser power setting of 2.035 mW, using spherical convex lenses of 30 mm focal length, and an AFM scan area of 75  $\mu\text{m}$  X 75  $\mu\text{m}$ . The complete diagram of the resulting constriction can be seen in figure 114. The constriction width from the figure is 1.06  $\mu\text{m}$ .

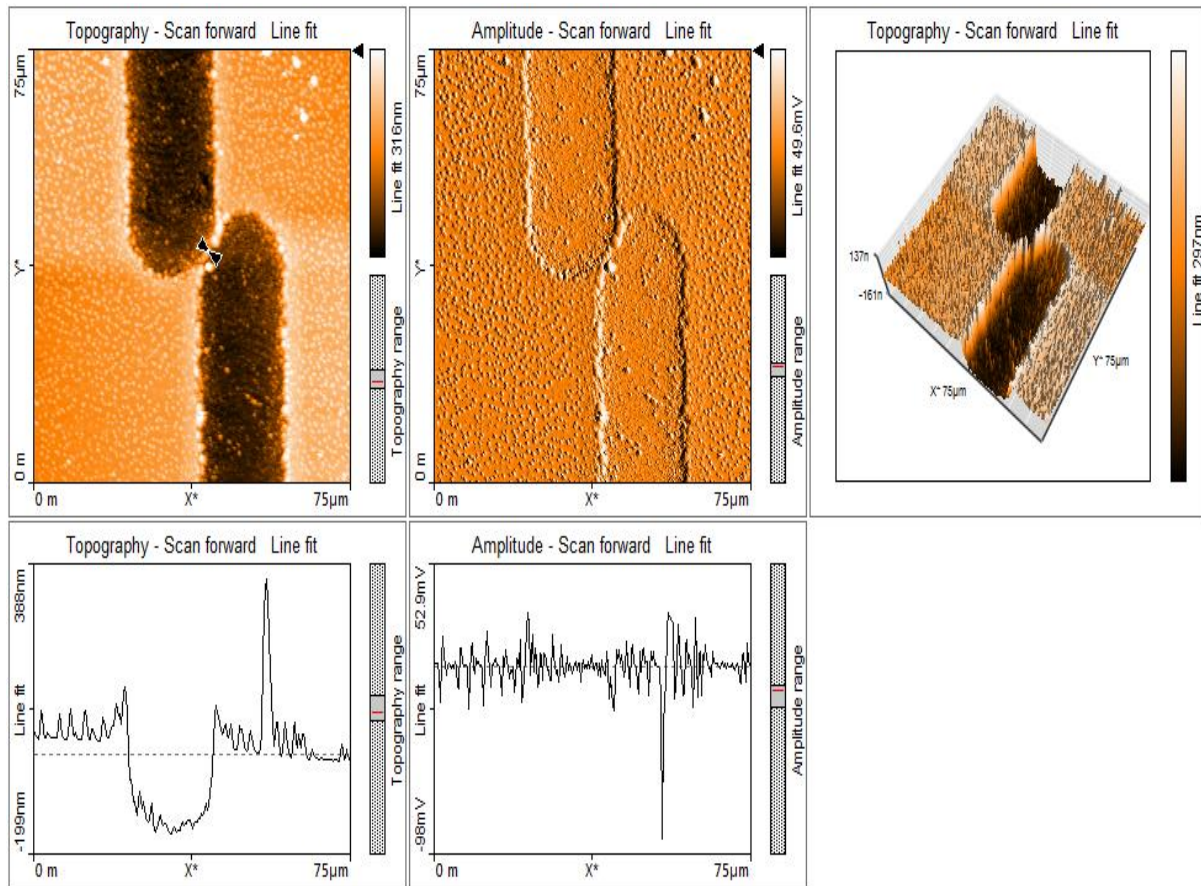


Figure 114 AFM image of the sub micron-sized constriction fabricated with ( $S_W = 16.5 \mu\text{m}$ ) and AFM scan area of 75  $\mu\text{m}$  X 75  $\mu\text{m}$  showing the constriction width is 1.06  $\mu\text{m}$ .

To make a precise measurement of the width of the constriction on the sample, the scan area is reduced to 14.6  $\mu\text{m}$  X 14.6  $\mu\text{m}$  as can be seen in figure 115. With this scan area, a line is drawn across the narrowest point on the topography line fit and the width of the constriction is determined to be 895.6 nm. This is a sub-micron sized constriction.

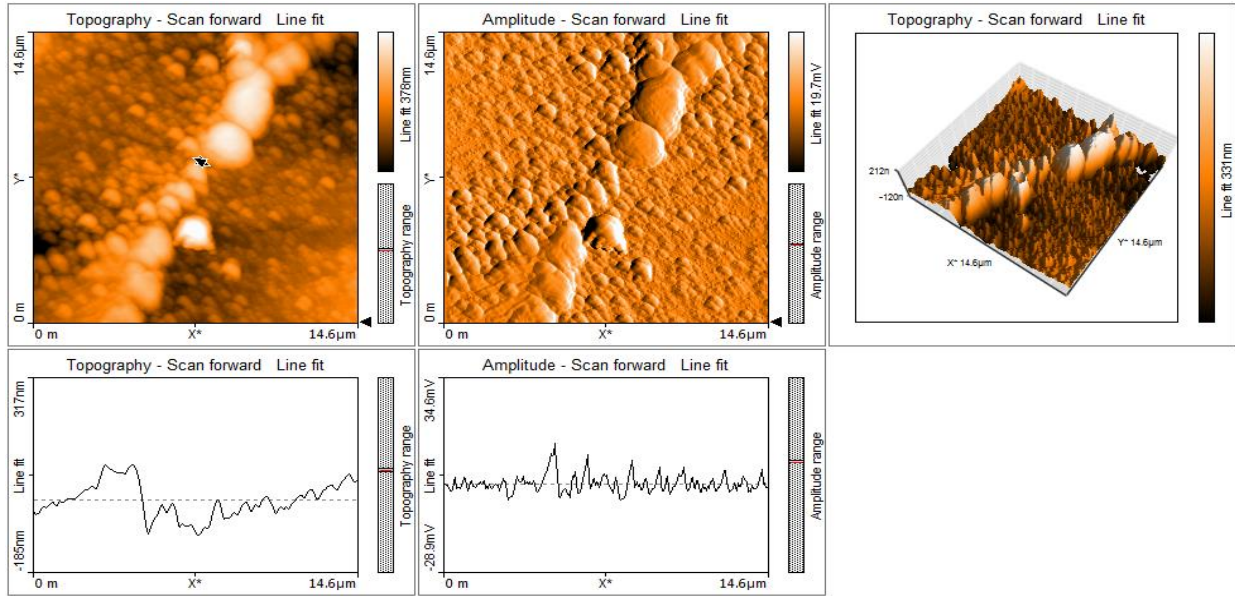


Figure 115 AFM image of the sub micron-sized constriction fabricated with ( $S_W = 16.5 \mu m$ ) and AFM scan area of  $14.6 \mu m \times 14.6 \mu m$  showing the constriction width is 895.6 nm

Figure 116 in which the width is determined to be 858.3 nm shows the same sample as figure 115; the only difference is that this time a snap shot is taken at the point when the AFM is scanning perpendicularly to the laser ablation spots at the narrowest point on the constriction. The profile of the constriction can be seen in the topography line fit. The width of the constriction is determined to be 858.3 nm in between the black arrows from the topography line plot.

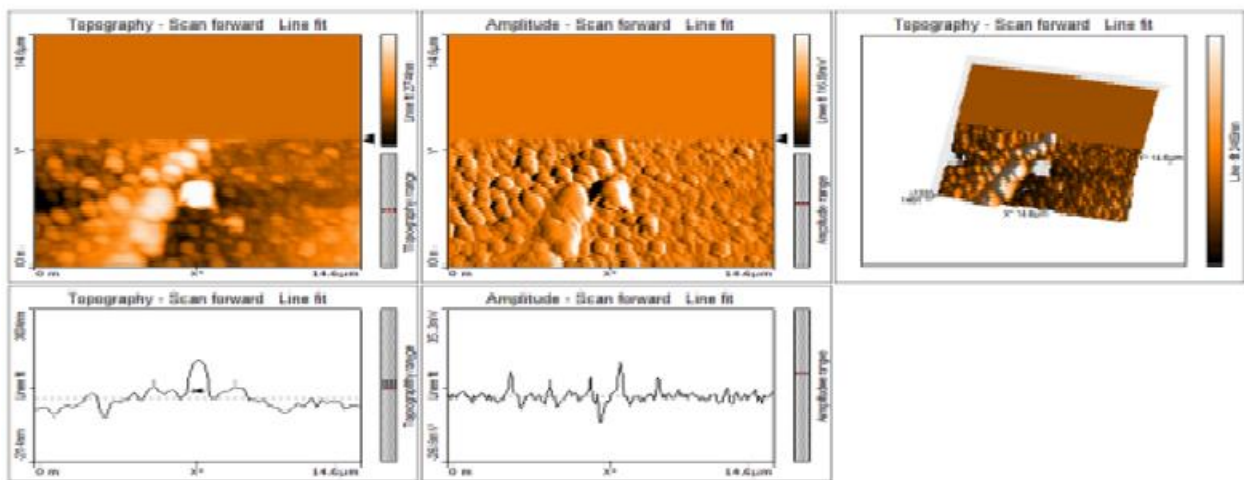


Figure 116 AFM image of the sub micron-sized constriction fabricated with ( $S_W = 16.5 \mu m$ ) and AFM scan area of  $14.6 \mu m \times 14.6 \mu m$  showing the constriction width is 858.3 nm.

Finally figure 117 shows the length of the constriction to be 9.66  $\mu\text{m}$ .

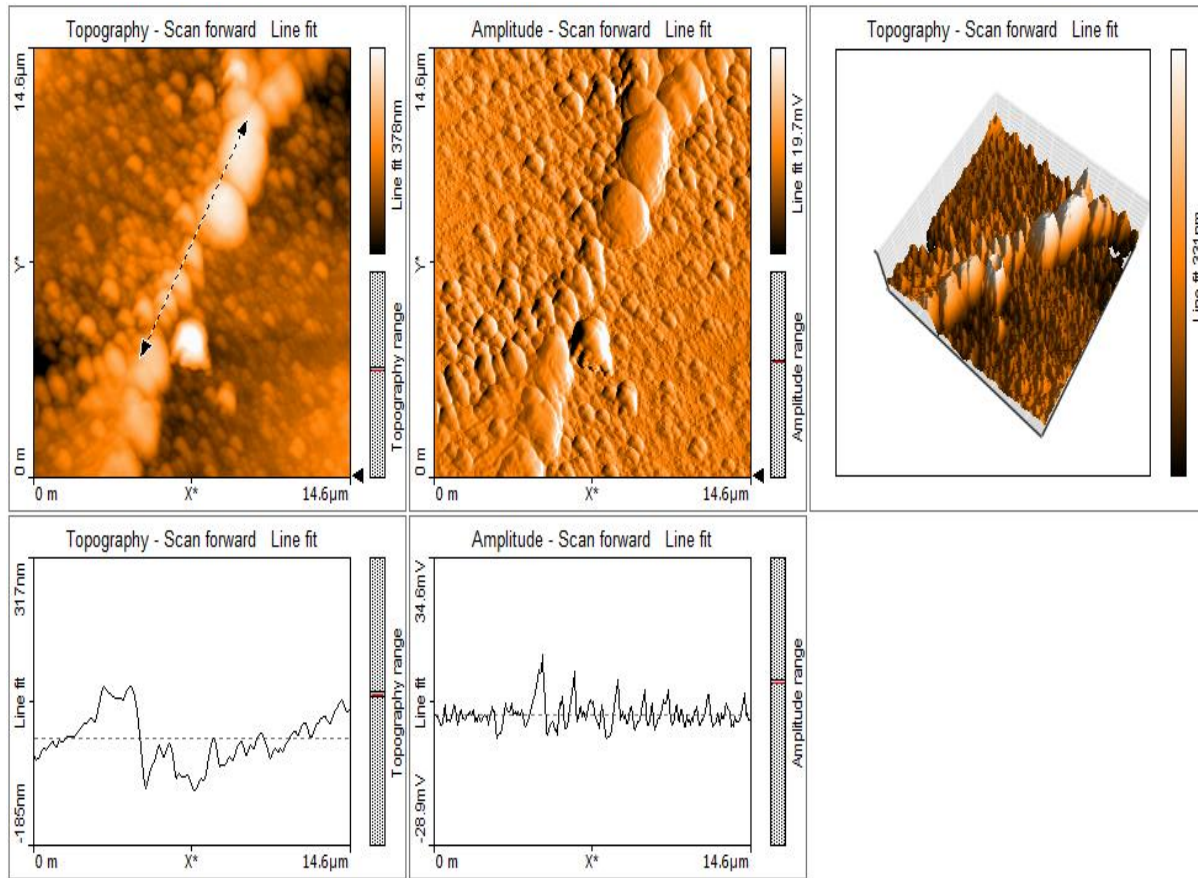


Figure 117 AFM image of the sub micron-sized constriction fabricated with ( $S_W = 16.5 \mu\text{m}$ ) and AFM scan area of  $14.6 \mu\text{m} \times 14.6 \mu\text{m}$  showing the constriction length is  $9.66 \mu\text{m}$ .

## 4.7 MICRON-SIZED CONSTRICTION FABRICATED ON YBCO THIN FILM.

### 4.7.1 SEPARATION DISTANCE BETWEEN THE LASER ABLATION SPOTS ( $S_W$ ) OF $16.5 \mu\text{m}$ .

This is the 5<sup>th</sup> constriction on the sample. In this constriction, the laser ablation spot size is  $15.82 \mu\text{m}$  as seen in figure 118. Since, the separation distance between the laser ablation spots ( $S_W$ ) is  $16.5 \mu\text{m}$  then the constriction width should be  $700 \text{ nm}$  but this is not the case in figure 119.

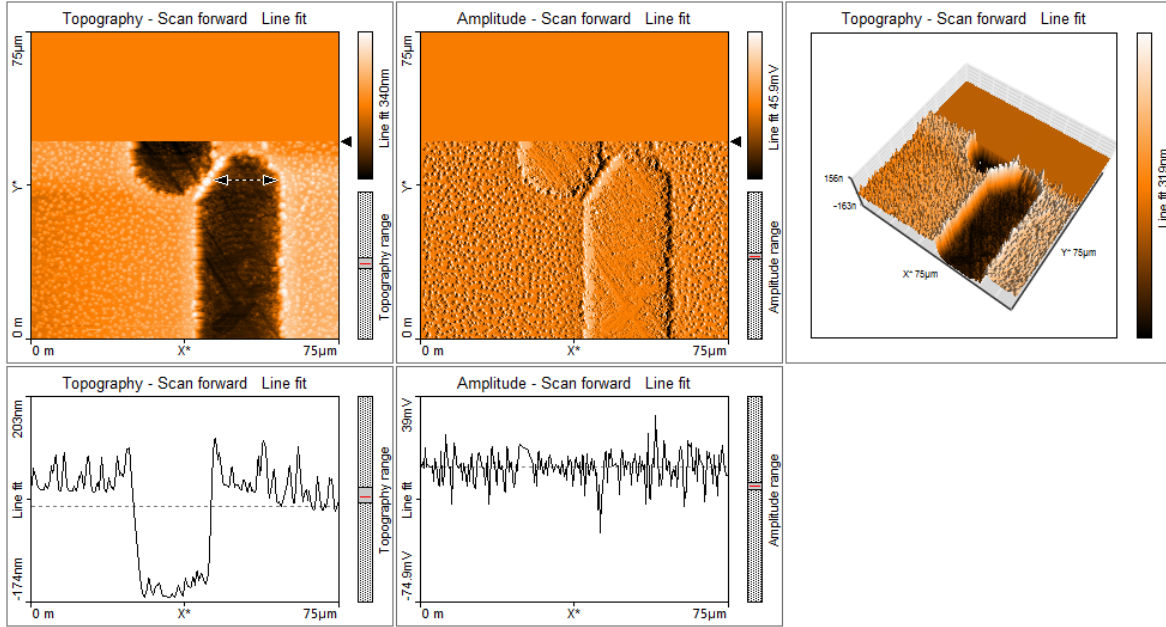


Figure 118 AFM image of the sub micron-sized constriction fabricated with ( $S_W = 16.5 \mu\text{m}$ ) and AFM scan area of  $75 \mu\text{m} \times 75 \mu\text{m}$  showing the laser ablation spot size is  $15.82 \mu\text{m}$ .

In order to determine the exact constriction width of this sample the scan area was reduced to  $16.7 \mu\text{m} \times 16.7 \mu\text{m}$  in the AFM software. Using this scan area the constriction width was determined to be  $1.231 \mu\text{m}$  as seen in figure 119.

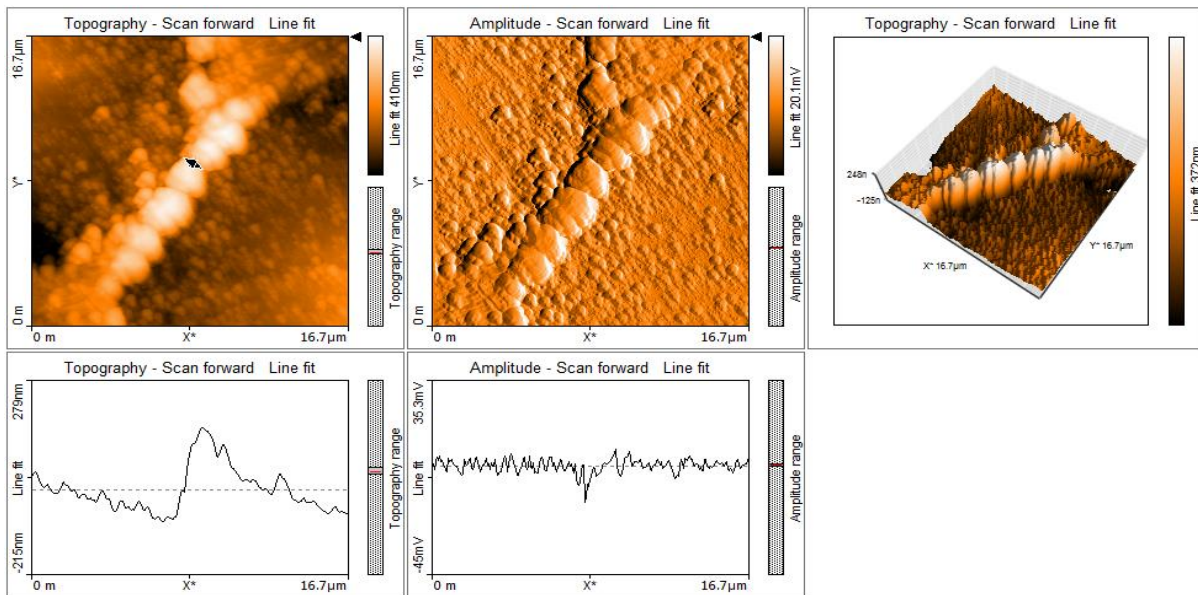


Figure 119 AFM image of the sub micron-sized constriction fabricated with ( $S_W = 16.5 \mu\text{m}$ ) and AFM scan area of  $16.7 \mu\text{m} \times 16.7 \mu\text{m}$  showing the constriction width is  $1.231 \mu\text{m}$ .

## 4.8 SUB-MICRON - SIZED CONSTRICTION FABRICATED ON YBCO THIN FILM

### 4.8.1 SEPARATION DISTANCE BETWEEN THE LASER ABLATION SPOTS ( $S_W$ ) OF 16 $\mu\text{m}$ .

This is the 2<sup>nd</sup> constriction on the sample. The separation distance between the laser ablation spots was reduced to ( $S_W$ ) of 16  $\mu\text{m}$  and as a result a constriction width of 576.7 nm was achieved. This is a sub-micron sized constriction. The image in figure 120 is the overall image of the constriction.

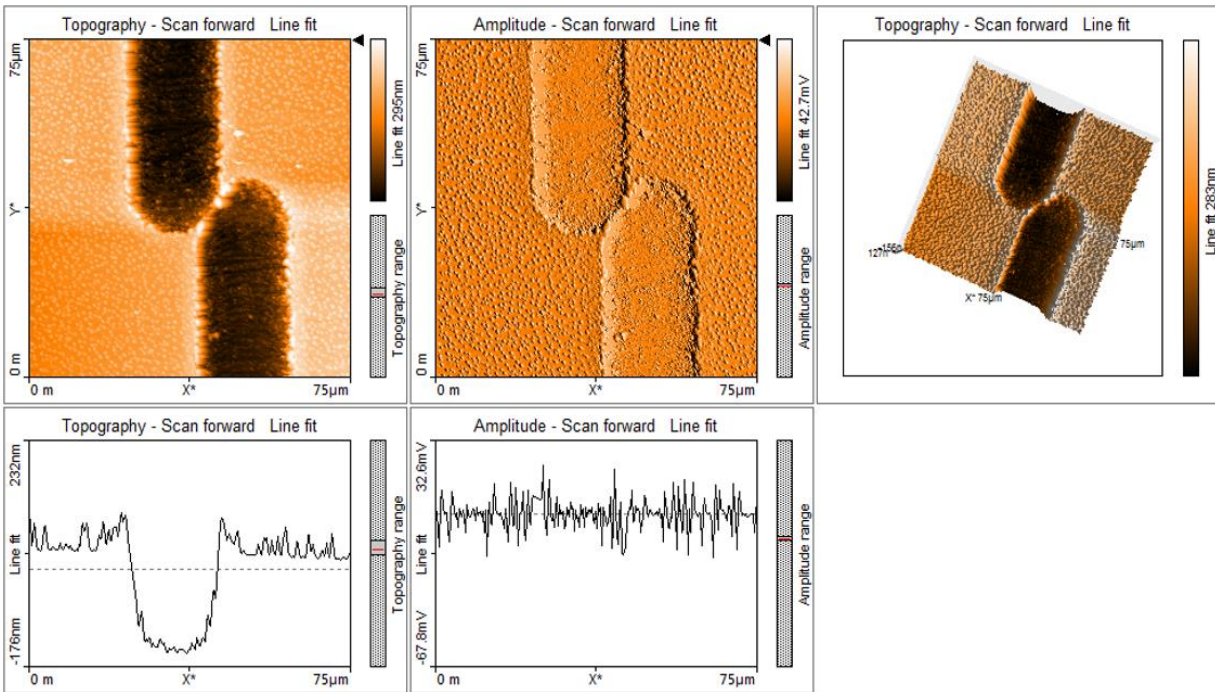


Figure 120 AFM image of the sub micron-sized constriction fabricated with ( $S_W = 16 \mu\text{m}$ ) and AFM scan area of 75  $\mu\text{m}$  X 75  $\mu\text{m}$  showing the overall constriction shape.

Figure 121 shows a snap shot image taken of the sub-micron sample, the image is captured at the narrowest point on the constriction. Using the profile distribution of the constriction shown in the topography line fit and stretching the scan area to 49.2  $\mu\text{m}$  X 49.2  $\mu\text{m}$  the width was determined by drawing a line across the amplitude above the zero axis and is determined to be indeed 576.7 nm.

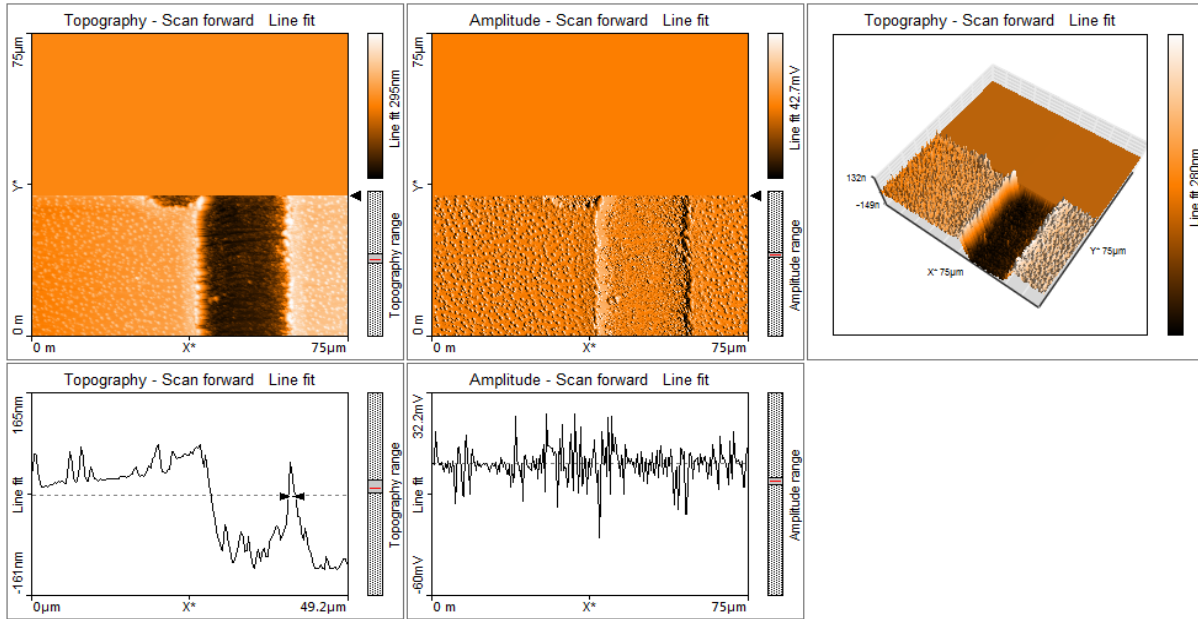


Figure 121 AFM image of the sub micron-sized constriction fabricated with ( $S_W = 16.5 \mu\text{m}$ ) and AFM scan area of  $16.7 \mu\text{m} \times 16.7 \mu\text{m}$  showing the constriction width is  $576.7 \text{ nm}$ .

In order to determine the exact width of the constriction, the scan area was reduced in the AFM software to  $18.8 \mu\text{m} \times 18.8 \mu\text{m}$ . The precise constriction width achieved is  $732.4 \text{ nm}$  as seen in figure 121.

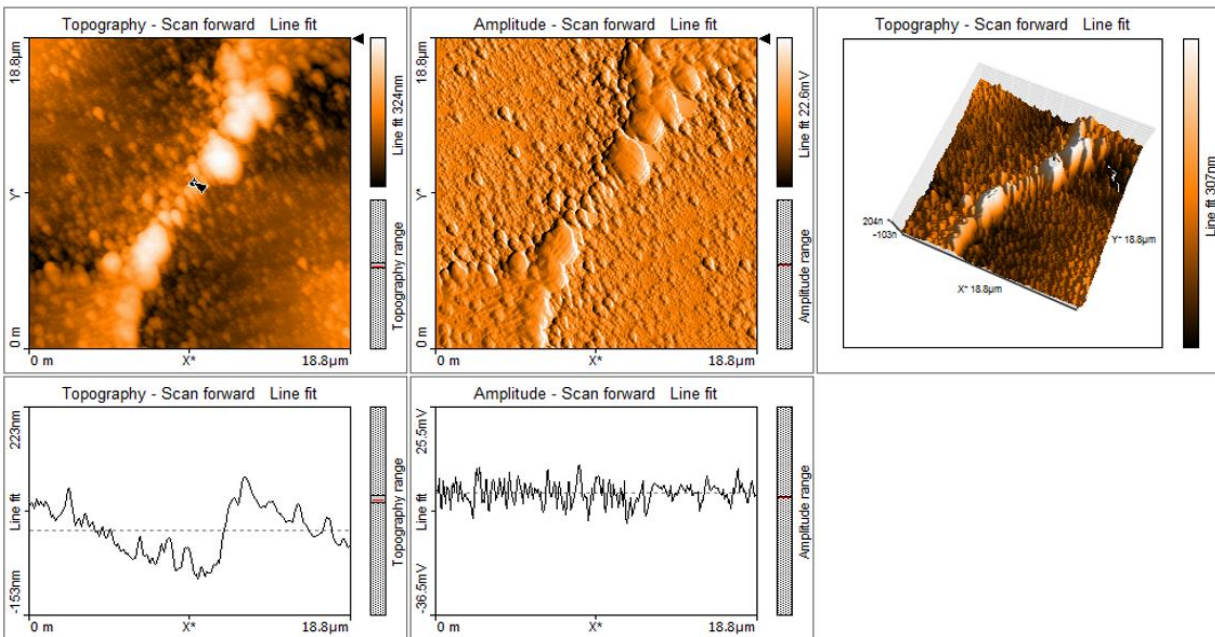


Figure 122 AFM image of the sub-micron-sized constriction fabricated with ( $S_W = 16 \mu\text{m}$ ) and AFM scan area of  $18.8 \mu\text{m} \times 18.8 \mu\text{m}$  showing the constriction width is  $732.4 \text{ nm}$ .

#### 4.9 SUMMARY OF CONSTRICTIONS FABRICATED, SCANNED USING AFM AND LABELLED ON THE YBCO THIN FILM.

Table 5 Summarizing the constrictions fabricated so far, their widths measured in AFM, position on the thin films sample and the separation distances between the laser ablation spots ( $S_w$ ) is given in the table.

Number	Size of Constriction	Separation distance ( $S_w$ ) between laser ablation spots	Qubit number on the YBCO thin film	Constriction Width	Laser ablation spot diameter.
1	MICRON	18 $\mu\text{m}$	1 <sup>st</sup> Constriction	1.68 $\mu\text{m}$	15.8 $\mu\text{m}$
2	MICRON	17.5 $\mu\text{m}$	1 <sup>st</sup> Constriction	1.39 $\mu\text{m}$	15.8 $\mu\text{m}$
3	MICRON	17 $\mu\text{m}$	2 <sup>nd</sup> Constriction	1.63 $\mu\text{m}$	15.8 $\mu\text{m}$
4	SUB-MICRON	16.5 $\mu\text{m}$	2 <sup>nd</sup> Constriction	858.3 nm	15.8 $\mu\text{m}$
5	MICRON	16.5 $\mu\text{m}$	5 <sup>TH</sup> Constriction	1.231 $\mu\text{m}$	15.8 $\mu\text{m}$
6	SUB-MICRON	16 $\mu\text{m}$	2 <sup>nd</sup> Constriction	732.4 nm	15.8 $\mu\text{m}$

#### 4.10 METHOD USED FOR CLEANING THE THIN FILM SAMPLES AFTER LASER FABRICATION.

After the laser cutting process is complete, the thin film samples normally have the ablated material piling up onto the surface of the bridge or the constriction making the dimensions of the constriction, namely the width incorrect.

To clean the extra pile up, this can be done by using a chemical liquid such as acetone or ethanol.

In this case, the thin film measuring 10 mm X 10 mm was dipped in the acetone placed in a plastic holder or test tube and subsequently placed in equipment called the sonicator. The model used is power sonic 405. The sonicator is filled with water. This is a micro process controlled bench ultrasonic cleaner.

The sonicator works by sending out ultrasonic waves through the water surrounding the sample in a plastic container. The ultrasonic waves vibrate the sample and at the same time produce a magnetic field that pulls the loose ablated particles away. The magnetic field is able to attract the ablated particles because they have metallic properties. Figure 123 shows the sample placed in a sonicator during the cleaning process. After the cleaning process, it becomes much easier to scan the sample in AFM, determine the width of the constriction and get a clean image.



Figure 123 Thin film being cleaned in a sonicator

As can be seen in figure 123, the thin film is placed in acetone in a beaker, which is placed in the sonicator containing water. There is a ripple effect produced by the ultrasonic waves and the magnetic field pulls the loose particles off. Figure 124 shows the resulting cleaned thin film samples placed back into the packaging and labelled according to the separation distance between the laser ablation spots ( $S_W$ ), that is 16.0  $\mu\text{m}$ , 17.0  $\mu\text{m}$ , 17.5  $\mu\text{m}$  etc.



Figure 124 Cleaned thin films in packaging

## 4.11 AFM IMAGES OF OTHER USEFUL CONSTRICTIONS FABRICATED.

### 1. SUB-MICRON CONSTRICTION

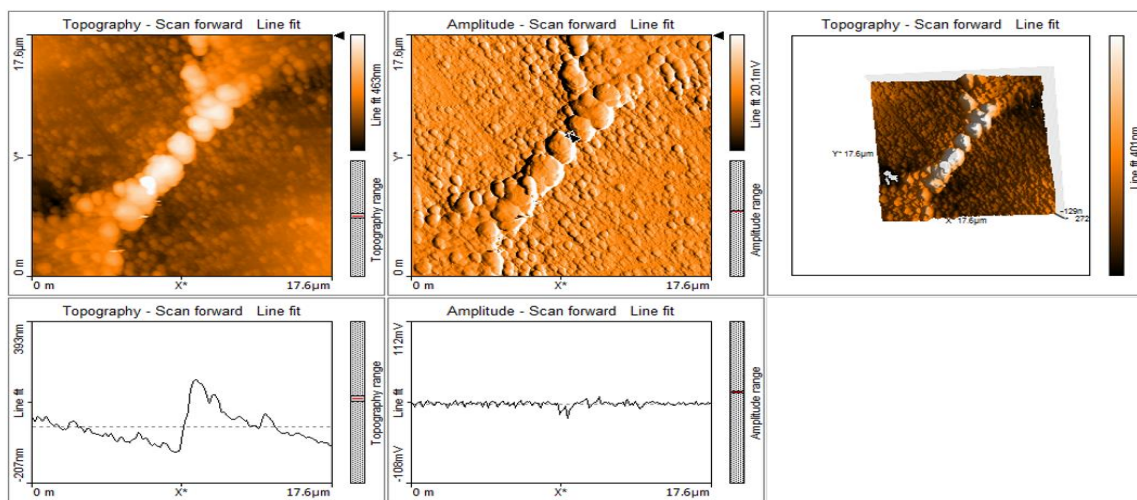


Figure 125 AFM image of a sub-micron constriction of width 879.3 nm fabricated with laser power 2.035 mW, spherical convex lens (30mm focal length), scan area  $17.6 \mu\text{m} \times 17.6 \mu\text{m}$ , separation distance between laser ablation spots ( $S_W$ )  $16.5 \mu\text{m}$ , 5<sup>th</sup> constriction on sample.

## 2. SUB-MICRON CONSTRICTION

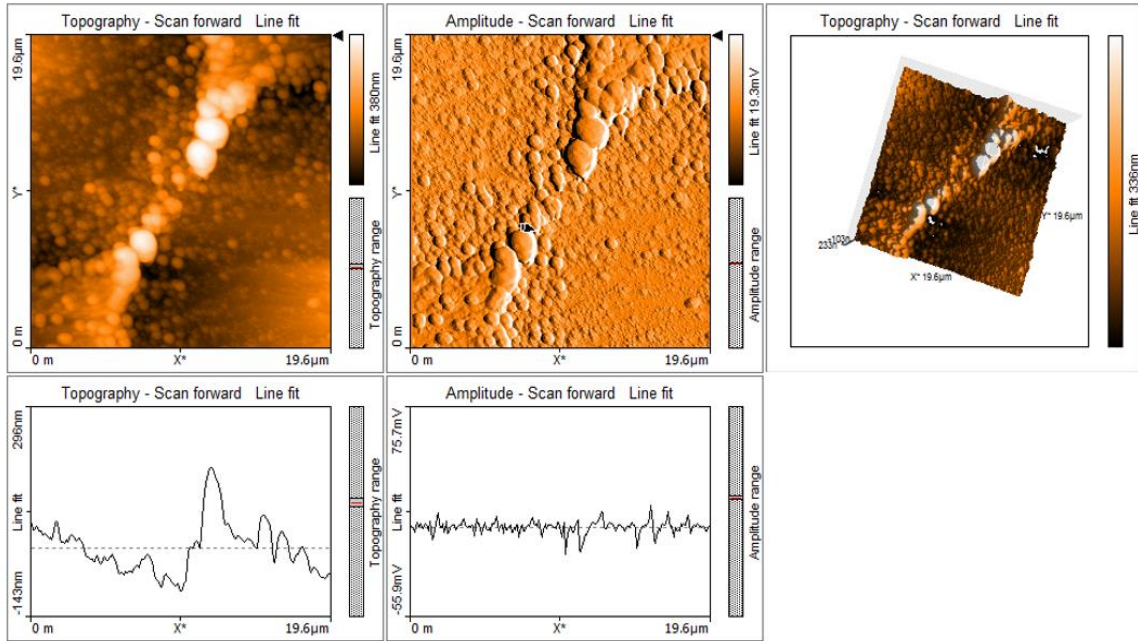


Figure 126 AFM image of a sub-micron constriction of width 874.2 nm fabricated with laser power 2.035 mW, spherical convex lens (30mm focal length), scan area 19.6 µm X 19.6 µm, separation distance between laser ablation spots ( $S_W$ ) 16.5 µm, 3<sup>rd</sup> constriction on sample.

## 3. SUB-MICRON CONSTRICTION

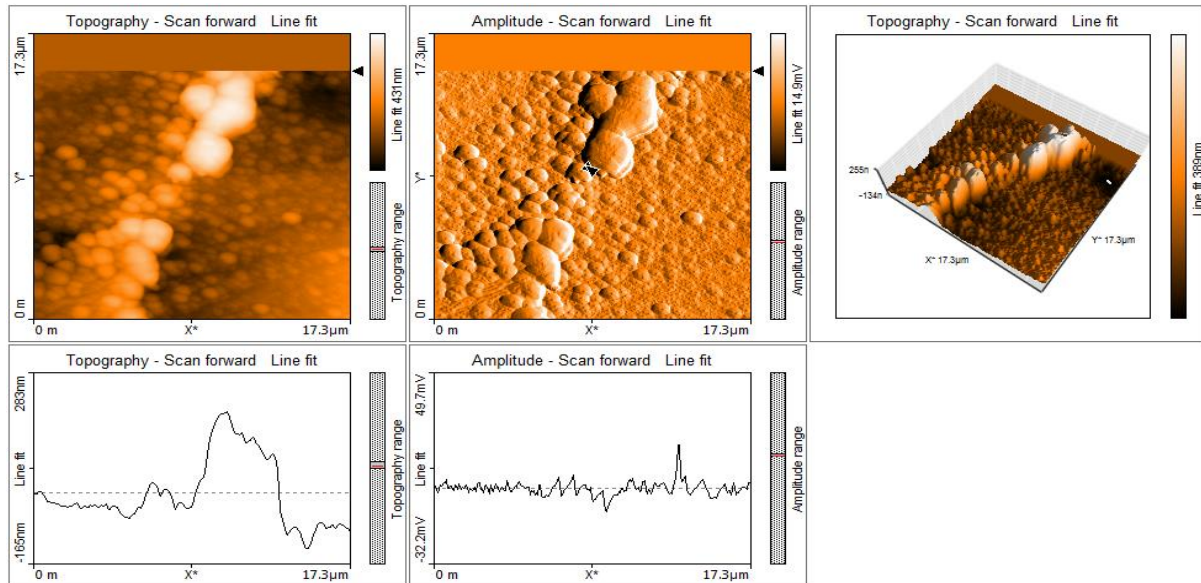


Figure 127 AFM image of a sub-micron constriction of width 813.1 nm fabricated with laser power 2.035 mW, spherical convex lens (30mm focal length), scan area 17.3 µm X 17.3 µm, separation distance between laser ablation spots ( $S_W$ ) 16.5 µm, 4<sup>th</sup> constriction on sample.

#### 4. MICRON CONSTRICTION

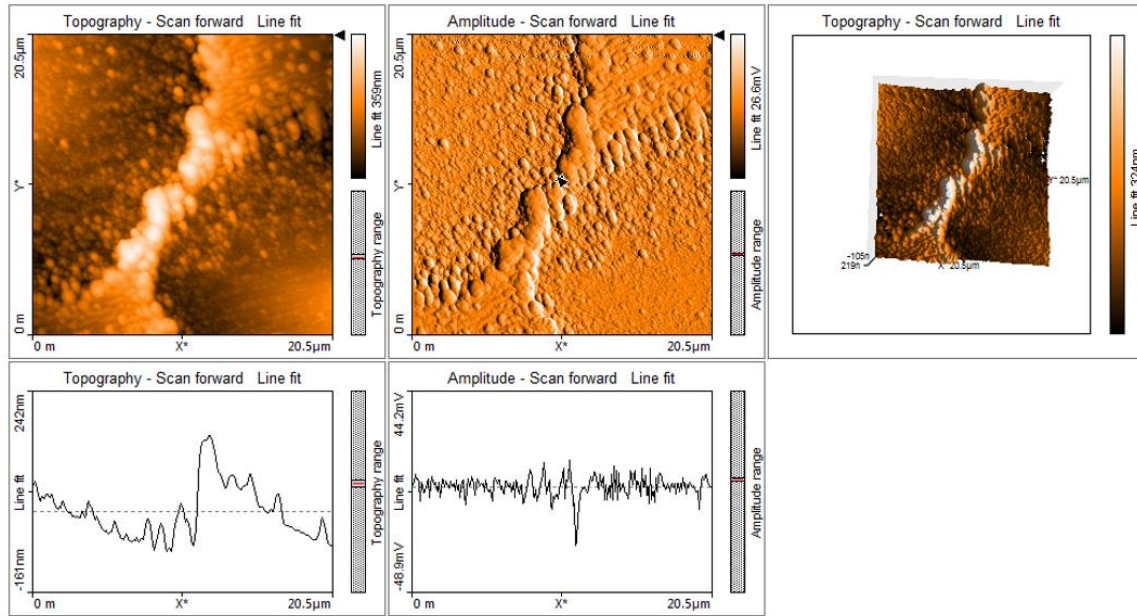


Figure 128 AFM image of a micron constriction of width 1.191  $\mu\text{m}$  fabricated with laser power 2.035 mW, spherical convex lens (30mm focal length), scan area 20.5  $\mu\text{m}$  X 20.5  $\mu\text{m}$ , separation distance between laser ablation spots ( $S_W$ ) 17  $\mu\text{m}$ , 5<sup>th</sup> constriction on sample.

#### 5. MICRON CONSTRICTION

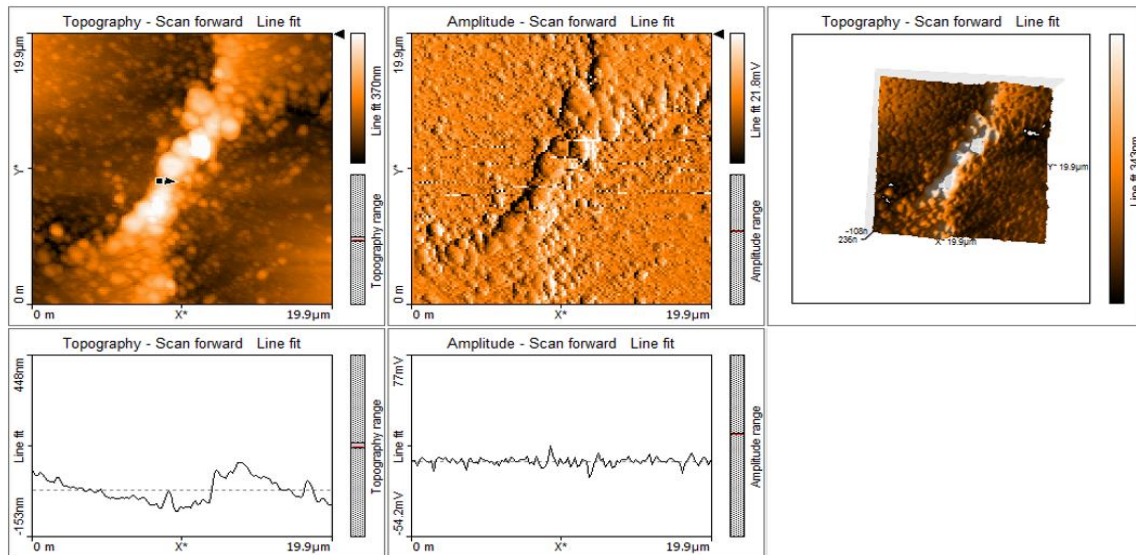


Figure 129 AFM image of a micron constriction of width 1.248  $\mu\text{m}$  fabricated with laser power 2.035 mW, spherical convex lens (30mm focal length), scan area 19.9  $\mu\text{m}$  X 19.9  $\mu\text{m}$ , separation distance between laser ablation spots ( $S_W$ ) 17  $\mu\text{m}$ , 4<sup>th</sup> constriction on sample.

## 6. MICRON CONSTRICTION

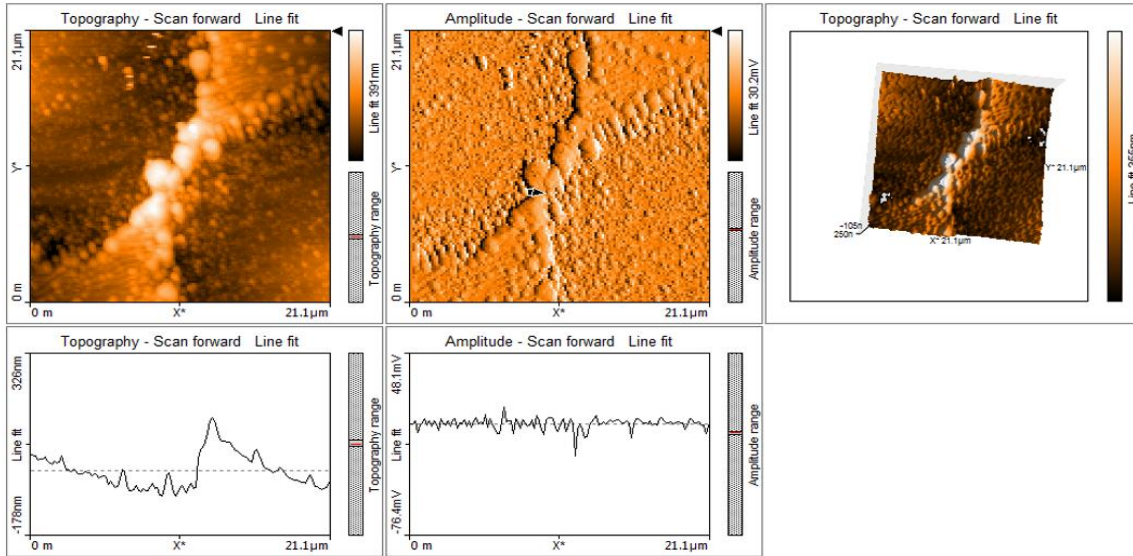


Figure 130 AFM image of a micron constriction of width  $1.074 \mu\text{m}$  fabricated with laser power  $2.035 \text{ mW}$ , spherical convex lens ( $30\text{mm}$  focal length), scan area  $21.1 \mu\text{m} \times 21.1 \mu\text{m}$ , separation distance between laser ablation spots ( $S_W$ )  $17 \mu\text{m}$ , 2<sup>nd</sup> constriction on sample.

## 7. SUB-MICRON CONSTRICTION

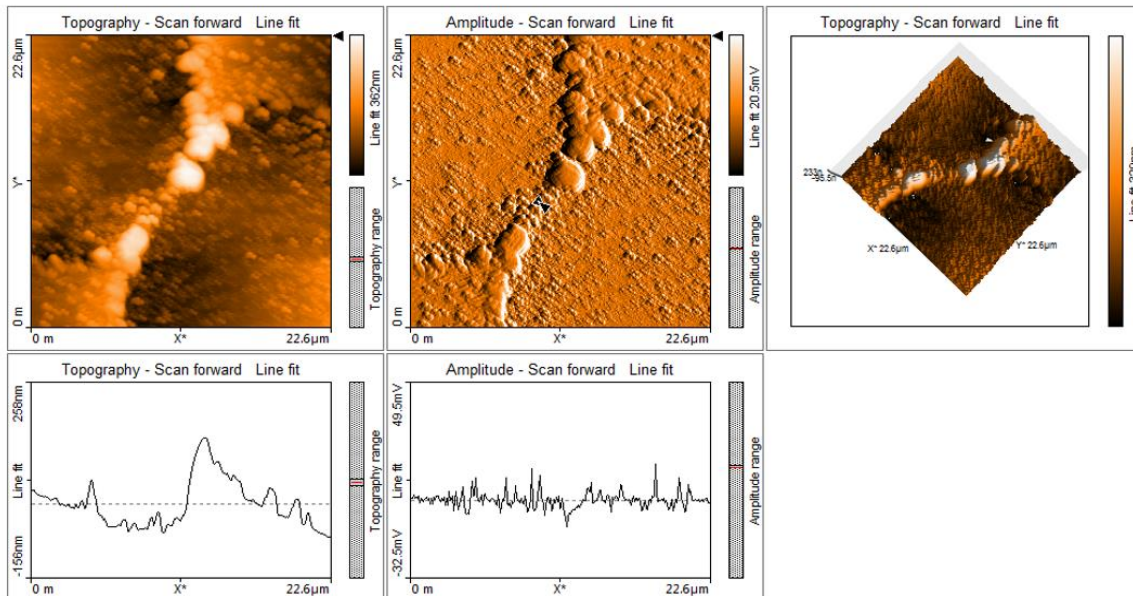


Figure 131 AFM image of a sub-micron constriction of width  $812.4 \text{ nm}$  fabricated with laser power  $2.035 \text{ mW}$ , spherical convex lens ( $30\text{mm}$  focal length), scan area  $22.4 \mu\text{m} \times 22.4 \mu\text{m}$ , separation distance between laser ablation spots ( $S_W$ )  $16 \mu\text{m}$ , 3<sup>rd</sup> constriction on sample.

## 4.12 SUMMARY OF THE ABOVE CONSTRICTIONS SCANNED IN AFM AND LABELLED ON THE THIN FILM

Table 6 Summarizing other useful constrictions fabricated, scanned in AFM showing the widths, position on the thin film, and the separation distance between the laser ablation spots ( $S_W$ ).

Number	Separation distance ( $S_W$ ) between the laser ablation spots	Qubit number on the YBCO thin film sample	Constriction width achieved	Laser ablation spot diameter used
1	16.5 $\mu\text{m}$	5 <sup>th</sup> qubit	879.3 nm	15.8 $\mu\text{m}$
2	16.5 $\mu\text{m}$	3 <sup>rd</sup> qubit	874.2 nm	15.8 $\mu\text{m}$
3	16.5 $\mu\text{m}$	4 <sup>th</sup> qubit	813.1 nm	15.8 $\mu\text{m}$
4	17 $\mu\text{m}$	5 <sup>th</sup> qubit	1.191 $\mu\text{m}$	15.8 $\mu\text{m}$
5	17 $\mu\text{m}$	4 <sup>th</sup> qubit	1.248 $\mu\text{m}$	15.8 $\mu\text{m}$
6	17 $\mu\text{m}$	2 <sup>nd</sup> qubit	1.074 $\mu\text{m}$	15.8 $\mu\text{m}$
7	16 $\mu\text{m}$	3 <sup>rd</sup> qubit	812.4 nm	15.8 $\mu\text{m}$

## 4.13 GEOMETRIC ANALYSIS OF CONSTRICTIONS FABRICATION.

### 4.13.1 SPECIFICATIONS OF CONSTRICTIONS FABRICATED

There are a series of constrictions fabricated with widths in the micron, sub-micron and Nano range as described in the preceding sections and the in the sections that follow. The thickness of these constrictions ranged from about 160 nm -190 nm as defined by the depth profile on the 3-D AFM images. The length of these constrictions ranged from about 7.2  $\mu\text{m}$  to 8.2  $\mu\text{m}$ . The length of these constrictions depends on the laser ablation spots size used for cutting and the separation distance between the laser ablation spots along the width ( $S_L$ ) of the sample.

### 4.13.2 EXPERIMENTAL DETAILS

The femtosecond laser used has a wavelength of 775 nm and a pulse duration time of 130 fs. The laser ablation width achieved using a spherical convex lens of 30 mm focal length was on average 15.53  $\mu\text{m}$ . When the separation distance between the laser ablation spots ( $S_W$ ) is 16.5  $\mu\text{m}$  this setting produced the sub-micron-sized constrictions. With a separation distance between the laser ablation spots ( $S_W$ ) of 16.0  $\mu\text{m}$  we achieved the nano-sized constriction. Lastly, with a separation distance of 17.0  $\mu\text{m}$  we achieve micron-sized constrictions, this theory can be derived from equation (1) in section 4.5.

The constrictions fabricated were shaped like the letter “S”. With this shape, it is possible to regulate both the width and the length of the constriction, as described elsewhere [1]. The width is controlled by bringing the laser ablation spots closer along the length of the thin film sample. While the length can be controlled by separating the laser ablation spots along the width of the thin film sample. As the laser ablation spots are brought closer together along the length of the sample the constriction width tends to become smaller, until in some instances the constrictions fabricated would collapse.

### 4.13.3 FACTORS THAT LIMIT THE FABRICATION OF NANO CONSTRICTIONS.

When Nano-structuring a material using the femtosecond laser, the width of the constriction or the diameter of the smallest structure that can be fabricated is determined by equation (2);

$$d = k\lambda/NAq^{1/2} \quad (2)$$

Where  $d$ , the diameter of the constriction made or the width,  $\lambda$  is the wavelength of the femtosecond laser,  $NA$  the numerical aperture of an objective lens or the focusing optics,  $q$  the energy band gap of the material sample being used for nano structuring. This equation is obtained from [2].

The main factors that limit the fabrication of Nano bridges is discussed as follows;

1. One of the main limiting factors for the fabrication of nano bridges is in the specification of the lens being used for optimizing the size of the laser ablation spot during focusing the laser spot. The laser ablation spot has to be as small as possible before cutting the sample, the conventional spherical convex lenses such as those with a relative focal length place a limit on the size of the laser ablation spot they can produce because of their focusing power. The smaller the laser ablation spot size then the smaller the constriction that can be fabricated. This is because if a constriction of Nano range has to be made then the spot size has to be in the 1  $\mu\text{m}$  – 5  $\mu\text{m}$  range, so that the laser ablation spots can be approached to one another without clipping the constriction bridge. The objective Plano convex lenses with a high numerical aperture such as NA (0.25, 0.40, 0.65) are more suitable to produce smaller laser ablation spot size and hence smaller constrictions because they are able to converge the laser beam much more and achieve smaller ablations spots.
2. The Energy band gap of the material being used for Nano-structuring in this case the YBCO thin film also plays a role. The materials with a higher energy band gap tend to have the possibility of producing smaller constriction sizes, for example, YBCO thin film has an energy band gap of as low as 5 meV [3], which allows it to produce Nano structures somewhere in the limit of 400 nm. Therefore, when the constriction of Nano size (394.8 nm) was produced, the walls of the constriction had a tendency to collapse after fabrication. Other factors that can contribute to the collapsing of the constriction walls include how close the laser ablation spots are brought to each other, vibration and the temperature in the clean room while cutting.
3. The last limiting factor is the radiation wavelength of the laser used. The femtosecond laser used for this experiment has a radiation wavelength  $\lambda$  of 775 nm. Essentially this places a diffraction limit on the light that is incident on the sample from the laser when cutting. This limit could also reduce the chances of

constrictions fabricated whose diameter is less than 775 nm without the walls of the constriction collapsing.

#### 4.13.4 CONstrictions FABRICATED

##### 4.13.4.1 SUB-MICRON SIZED CONstriction (500 – 1000 nm)

To fabricate this constriction the following laser settings were applied, laser power 2.035 mW, separation distance between the laser ablation spots ( $S_W$ ) 16  $\mu\text{m}$ . This was the 2<sup>nd</sup> constriction on the sample. The scan area is 75  $\mu\text{m}$  X 75  $\mu\text{m}$  set using the AFM software [4]. The laser ablation diameter seen in figure 132 is 15.82  $\mu\text{m}$ .

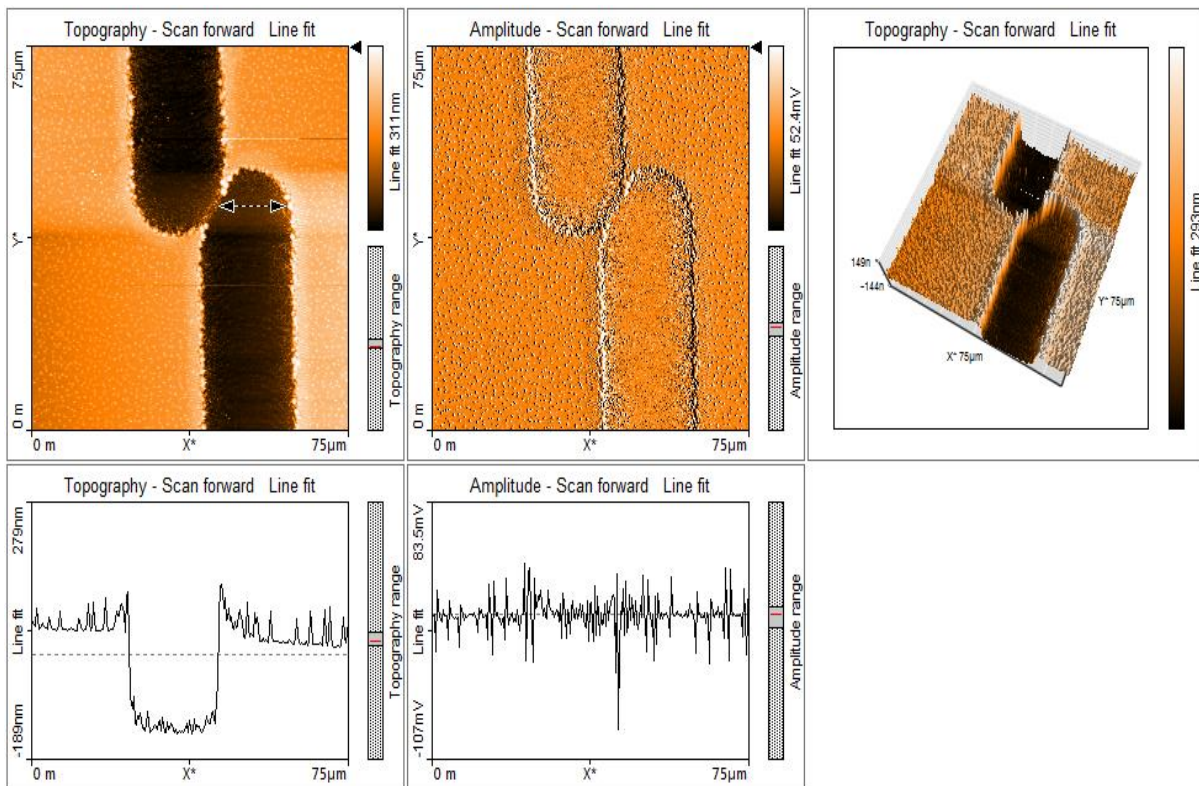


Figure 132 AFM image of a sub-micron constriction with a laser ablation spot diameter of 15.82  $\mu\text{m}$ , fabricated with laser power 2.035 mW, spherical convex lens (30mm focal length), scan area 75  $\mu\text{m}$  X 75  $\mu\text{m}$ , separation distance between laser ablation spots ( $S_W$ ) 16  $\mu\text{m}$ .

The AFM scan area is reduced to 23.4  $\mu\text{m}$  X 23.4  $\mu\text{m}$  in figure 133. We then measure a point on the constriction to determine the width of the constriction as 549.3 nm.

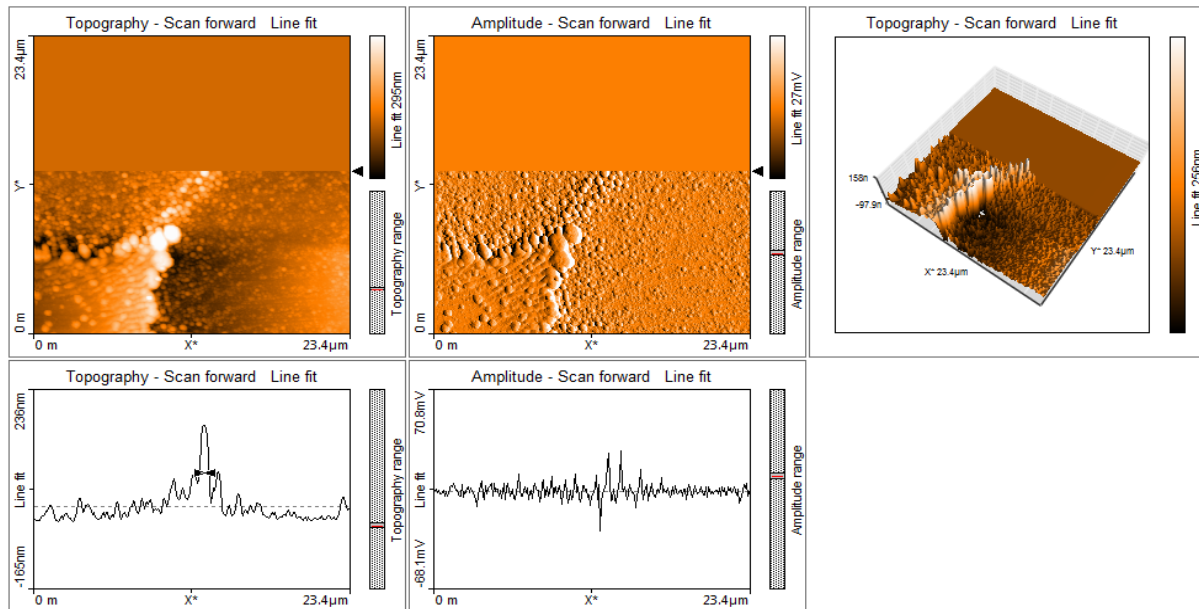


Figure 133 AFM image of a sub-micron constriction with a constriction width of 549.3 nm, fabricated with laser power of 2.035 mW, spherical convex lens (30mm focal length), scan area 23.4  $\mu\text{m}$  X 23.4  $\mu\text{m}$ , separation distance between laser ablation spots ( $S_W$ ) 16  $\mu\text{m}$ .

From figure 134, the length is determined to be 8.17  $\mu\text{m}$ . It seems as though the constriction is clipped. However to confirm this, other tests such as I-V characterization needs to be done. In an (I-V' c) test, a high resistance would indicate a clipped constriction or an open constriction.

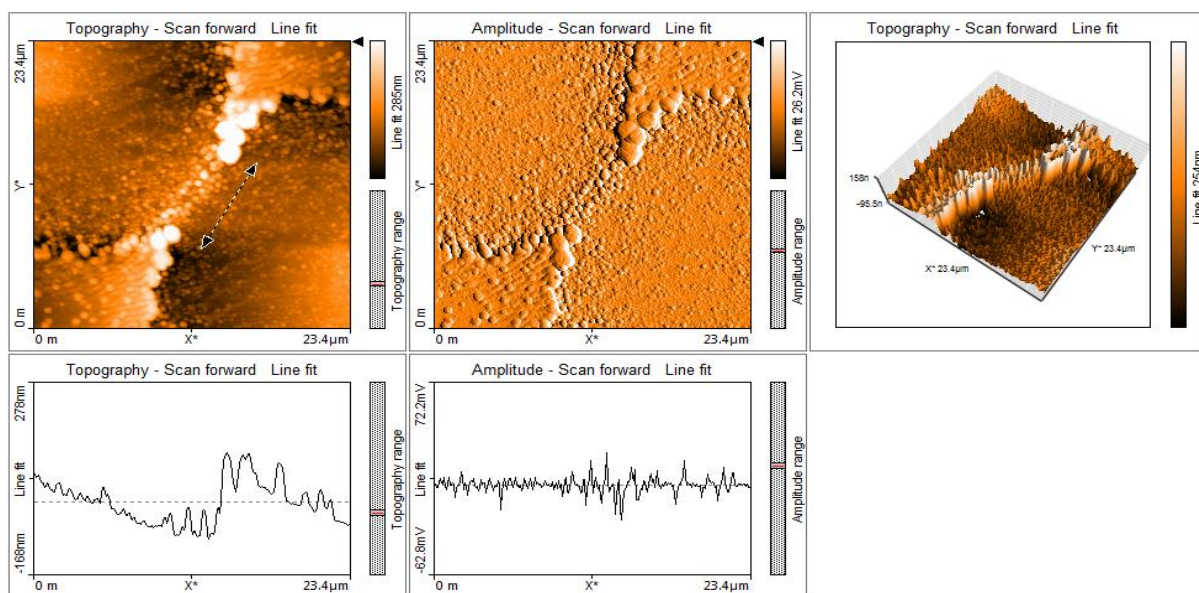


Figure 134 AFM image of a sub-micron constriction with a constriction length of 8.17  $\mu\text{m}$ , fabricated with laser power of 2.035 mW, spherical convex lens (30mm focal length), scan area 23.4  $\mu\text{m}$  X 23.4  $\mu\text{m}$ , separation distance between laser ablation spots ( $S_W$ ) 16  $\mu\text{m}$ .

#### 4.13.4.2 NANO CONSTRICTION (0 – 500 nm)

The Laser settings applied for the fabrication of this constriction in figure 135 include; separation distance between the laser ablation spots ( $S_W$ ) is 16  $\mu\text{m}$ , this is the 3<sup>rd</sup> qubit on the sample, laser power is 2.035 mW, a spherical convex lens of 30 mm focal length was used and the AFM scan area was 75  $\mu\text{m}$  X 75  $\mu\text{m}$ .

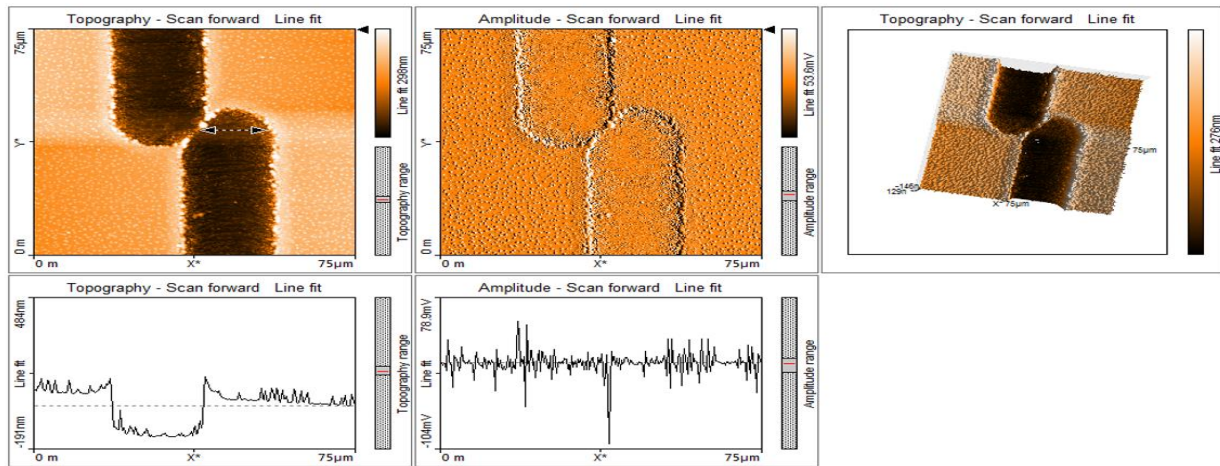


Figure 135 AFM image of a nano constriction with a laser ablation spot size is 15.53  $\mu\text{m}$ , fabricated with laser power of 2.035 mW, spherical convex lens (30mm focal length), scan area 75  $\mu\text{m}$  X 75  $\mu\text{m}$ , separation distance between the laser ablation spots ( $S_W$ ) 16  $\mu\text{m}$ .

We reduce the scan area in the AFM software to 20.2  $\mu\text{m}$  X 20.2  $\mu\text{m}$  in figure 136. We then measure a more precise width of the constriction at a point and determine the width to be 394.8 nm.

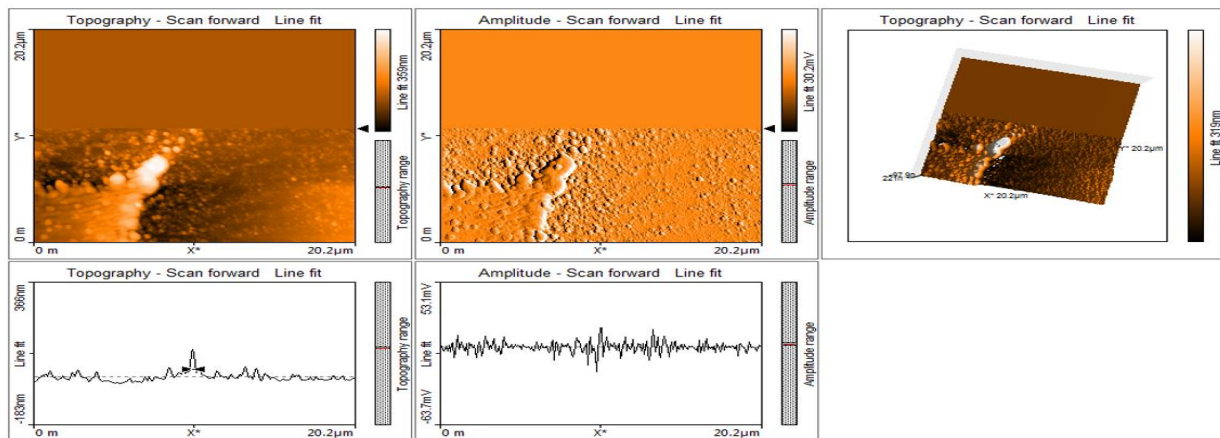


Figure 136 AFM image of a nano constriction with a constriction width of 394.8 nm, fabricated with laser power of 2.035 mW, spherical convex lens (30mm focal length), scan area 20.2  $\mu\text{m}$  X 20.2  $\mu\text{m}$ , separation distance between the laser ablation spots ( $S_W$ ) 16  $\mu\text{m}$ , 3<sup>rd</sup> qubit.

The length of the constriction is determined to be 7.53  $\mu\text{m}$ , this can be seen in figure 137.

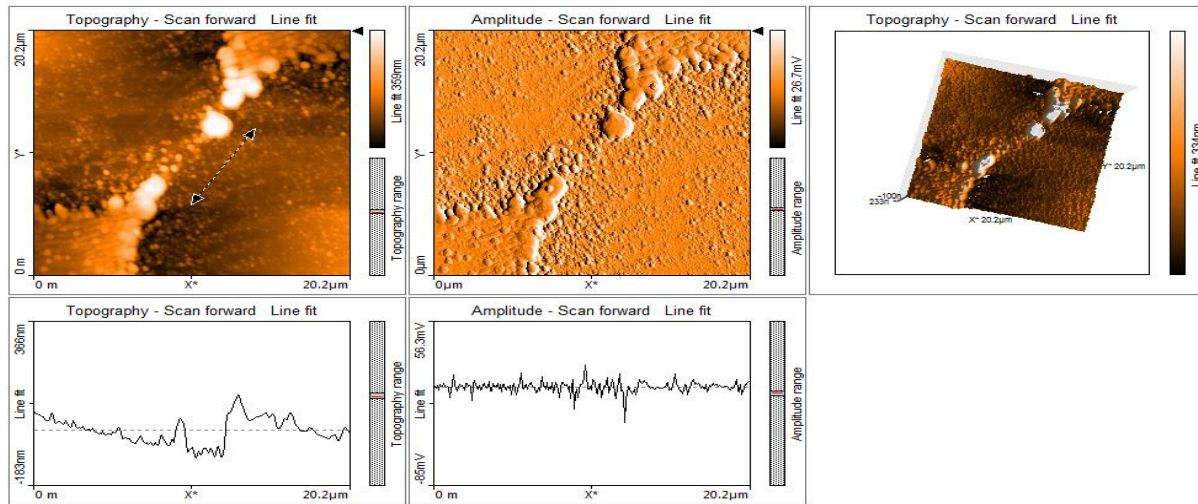


Figure 137 AFM image of a nano constriction with a constriction length of 7.53  $\mu\text{m}$ , fabricated with laser power of 2.035 mW, spherical convex lens (30mm focal length), scan area 20.2  $\mu\text{m}$  X 20.2  $\mu\text{m}$ , separation distance between the laser ablation spots ( $S_W$ ) 16  $\mu\text{m}$ , 3<sup>rd</sup> qubit.

#### 4.13.4.3 SUB-MICRON SIZED CONSTRICTION (500 – 1000 nm)

The laser settings include; separation distance between laser ablation spots ( $S_W$ ) is 16.5  $\mu\text{m}$ . This is the 2<sup>nd</sup> constriction on sample. The laser power settings 2.035 mW. The laser ablation spot for this constriction is 15.82  $\mu\text{m}$  as can be seen in figure 138 while the separation distance is ( $S_W$ ) is 16.5  $\mu\text{m}$ .

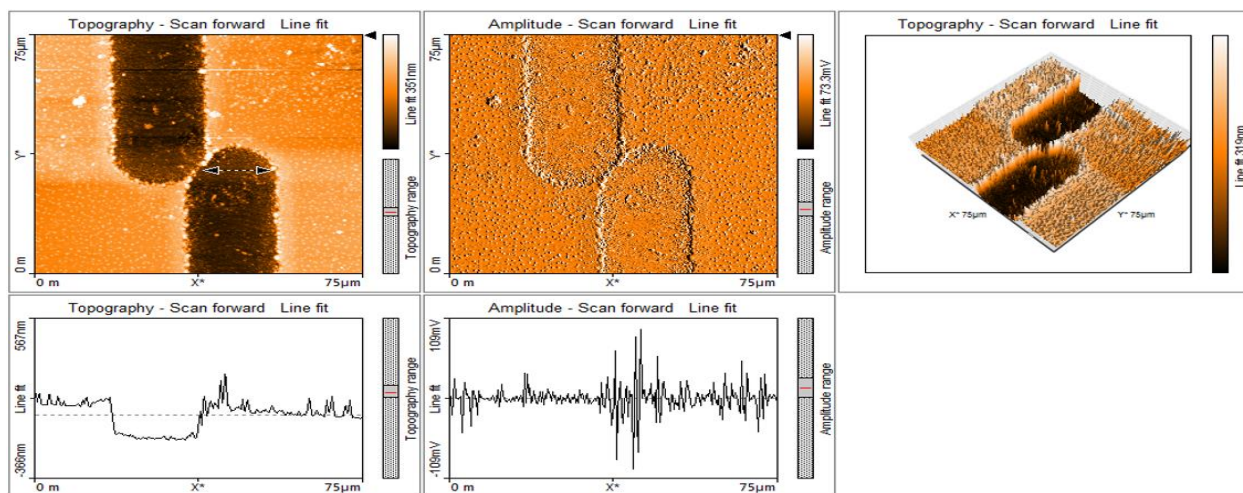


Figure 138 AFM image of a sub-micron constriction with a laser ablation spot size of 15.82  $\mu\text{m}$ , fabricated with laser power of 2.035 mW, spherical convex lens (30mm focal length), scan area 75  $\mu\text{m}$  X 75  $\mu\text{m}$ , separation distance between the laser ablation spots ( $S_W$ ) 16.5  $\mu\text{m}$ , 2<sup>nd</sup> qubit.

The scan area was reduced to 20.5  $\mu\text{m}$  X 20.5  $\mu\text{m}$  as can be seen in figure 139. Hence, the constriction width was precisely determined to be 881.2 nm.

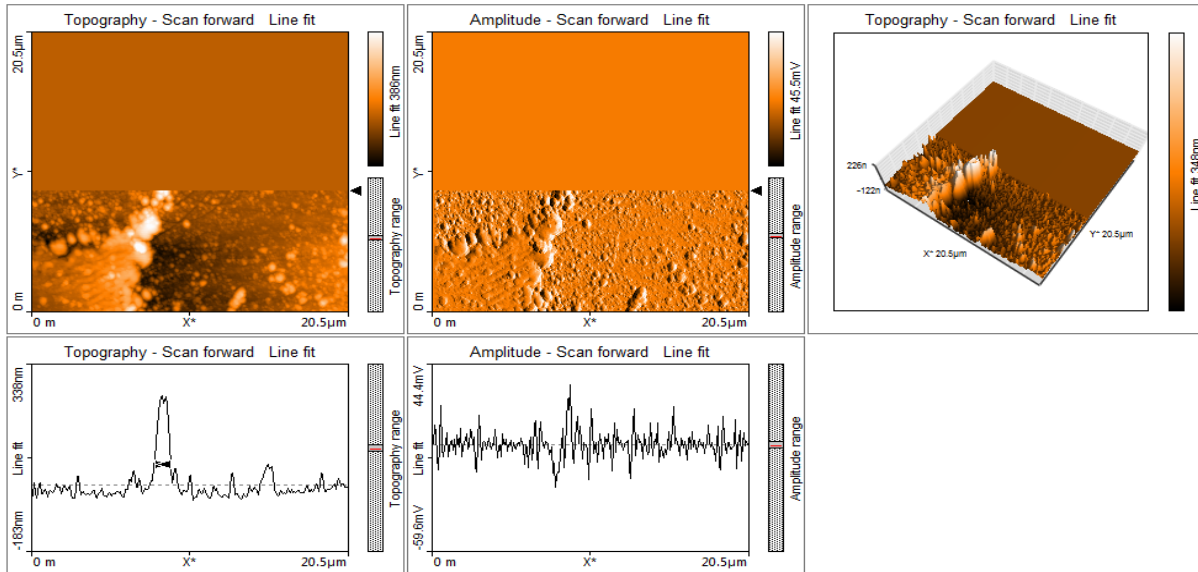


Figure 139 AFM image of a sub-micron constriction with a constriction width of 881.2 nm, fabricated with laser power of 2.035 mW, spherical convex lens (30mm focal length), scan area 20.5  $\mu\text{m}$  X 20.5  $\mu\text{m}$ , separation distance between the laser ablation spots ( $S_W$ ) 16.5  $\mu\text{m}$ , 2<sup>nd</sup> qubit.

The constriction length is 7.24  $\mu\text{m}$  as can be seen in figure 140.

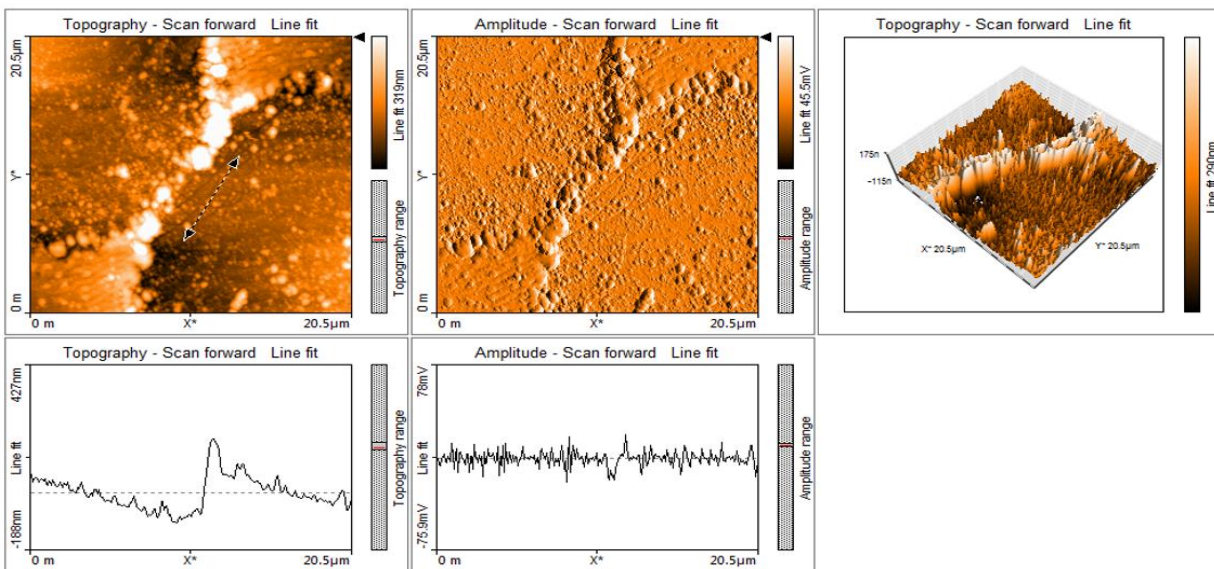


Figure 140 AFM image of a sub-micron constriction with a constriction length of 7.24  $\mu\text{m}$ , fabricated with laser power of 2.035 mW, spherical convex lens (30mm focal length), scan area 20.5  $\mu\text{m}$  X 20.5  $\mu\text{m}$ , separation distance between the laser ablation spots ( $S_W$ ) 16.5  $\mu\text{m}$ , 2<sup>nd</sup> qubit.

#### 4.13.4.4 MICRON-SIZED CONSTRICTION (ABOVE 1000 nm)

In this case, we fabricated a micron-sized constriction with the following laser settings, separation distance between the laser ablation spots ( $S_W$ ) is 17  $\mu\text{m}$ , this is the 4<sup>th</sup> constriction on the sample. The laser power settings is 2.035 mW. The laser ablation spot is 15.23  $\mu\text{m}$  as seen in figure 141.

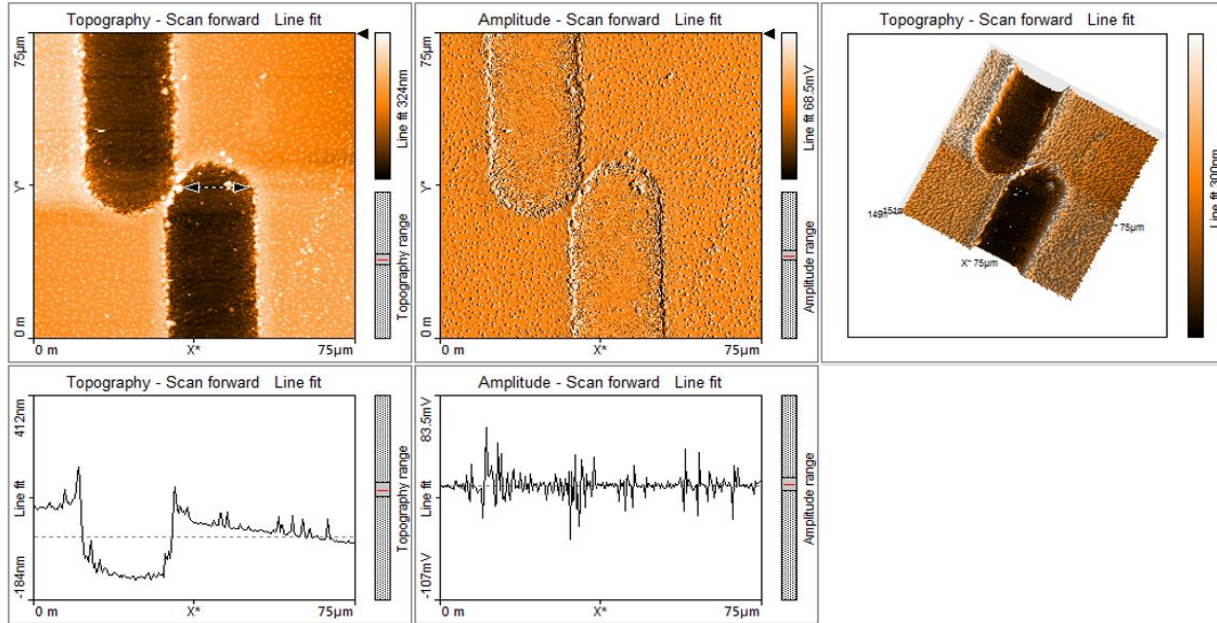


Figure 141 AFM image of a micron constriction with a laser ablation spot size of 15.23  $\mu\text{m}$ , fabricated with laser power of 2.035 mW, spherical convex lens (30mm focal length), scan area 75  $\mu\text{m}$  X 75  $\mu\text{m}$ , separation distance between the laser ablation spots ( $S_W$ ) 17  $\mu\text{m}$ , 4<sup>th</sup> qubit.

Due to the fact that the laser ablation spot is slightly smaller in this constriction (15.23  $\mu\text{m}$ ) than in the previous constriction while the separation distance between the laser ablation spots ( $S_W$ ) is increased to 17.0  $\mu\text{m}$ , hence the constriction width increases to micron size in figure 142.

By reducing the scan area to 21.4  $\mu\text{m}$  X 21.4  $\mu\text{m}$  as can be seen in figure 142 we obtain a precise measurement of the width of the constriction which is 1.086  $\mu\text{m}$ .

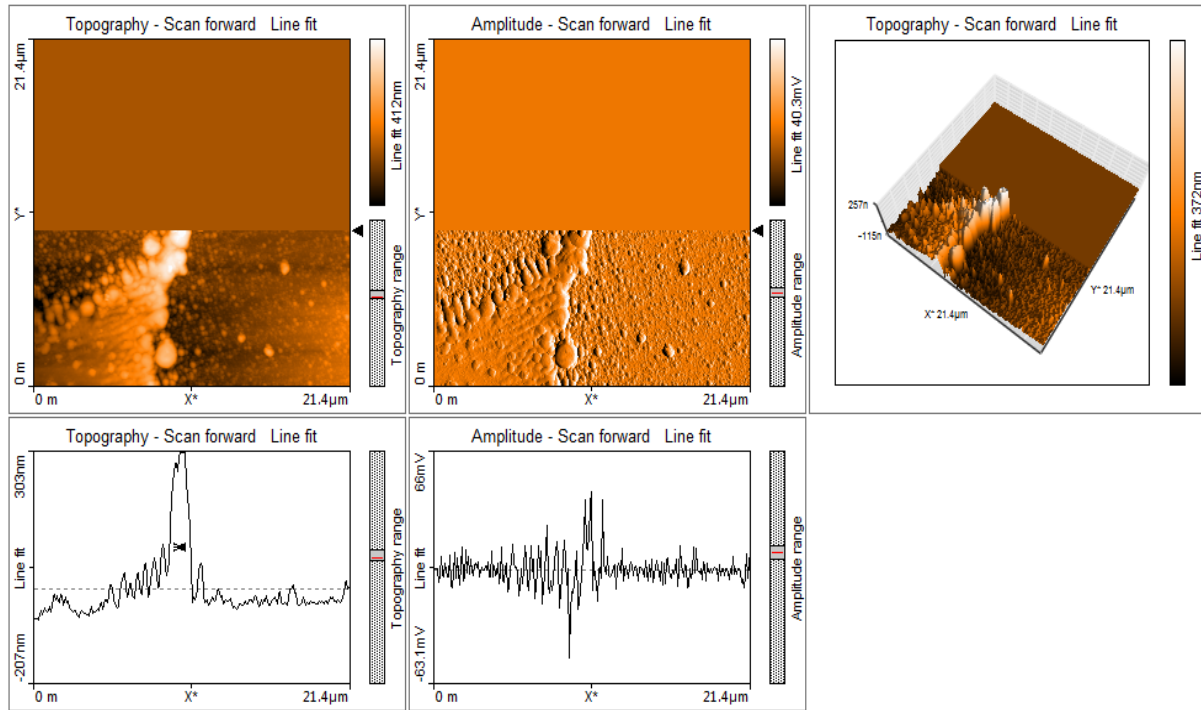


Figure 142 AFM image of a micron constriction with a constriction width of  $1.086 \mu\text{m}$ , fabricated with laser power of  $2.035 \text{ mW}$ , spherical convex lens ( $30\text{mm}$  focal length), scan area  $21.4 \mu\text{m} \times 21.4 \mu\text{m}$ , separation distance between the laser ablation spots ( $S_w$ )  $17 \mu\text{m}$ , 4th qubit.

The length of the constriction is  $7.21 \mu\text{m}$ , which can be seen in figure 143.

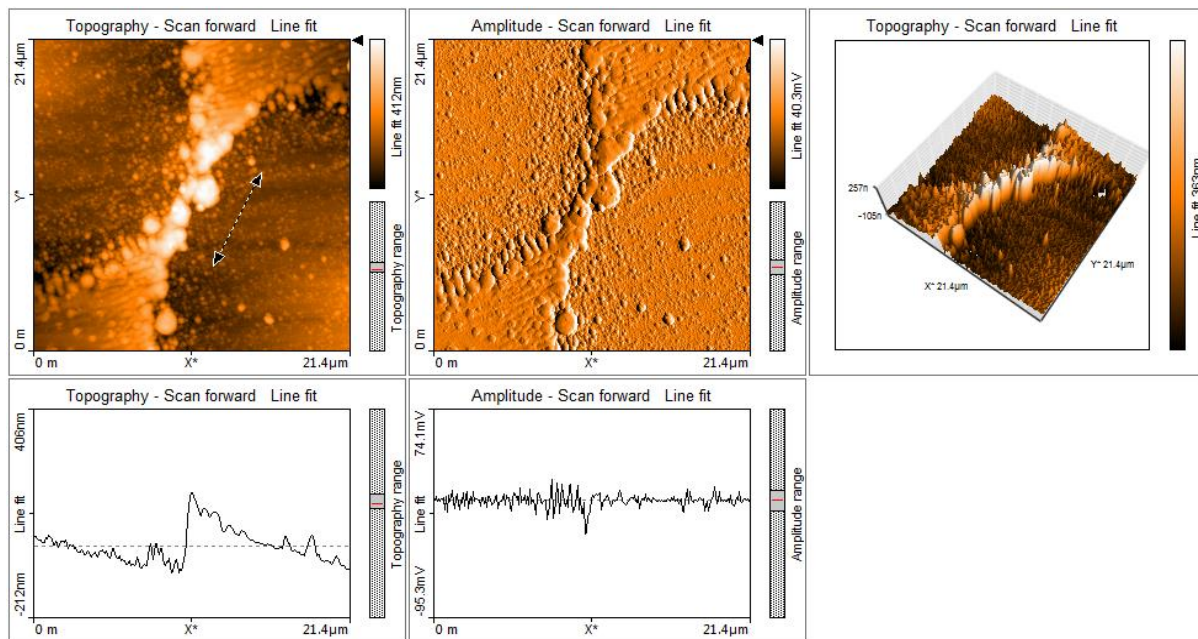


Figure 143 AFM image of a micron constriction with a constriction length of  $7.211 \mu\text{m}$ , fabricated with laser power of  $2.035 \text{ mW}$ , spherical convex lens ( $30\text{mm}$  focal length), scan area  $21.4 \mu\text{m} \times 21.4 \mu\text{m}$ , separation distance between the laser ablation spots ( $S_w$ )  $17 \mu\text{m}$ , 4th qubit.

#### 4.13.5 SUMMARY OF THE CONSTRICTIONS FABRICATED.

Table 7 Summary of constrictions fabricated in this sub-section with all specifications.

Number	Constriction type	Separation distance ( $S_W$ ) between laser ablation spots.	Qubit number on YBCO thin film.	Constriction width	Laser ablation spot diameter
1	SUB-MICRON	16 $\mu\text{m}$	2 <sup>nd</sup>	549.3 nm	15.82 $\mu\text{m}$
2	NANO	16 $\mu\text{m}$	3 <sup>rd</sup>	394.8 nm	15.53 $\mu\text{m}$
3	SUB-MICRON	16.5 $\mu\text{m}$	2 <sup>nd</sup>	881.2 nm	15.82 $\mu\text{m}$
4	MICRON	17 $\mu\text{m}$	4 <sup>th</sup>	1.09 $\mu\text{m}$	15.23 $\mu\text{m}$

#### 4.14 REFERENCES

- [1] Patrice Umenne and V.V. Srinivasu, “Femtosecond-laser fabrication of micron and sub-micron sized S-shaped constrictions on high  $T_c$  superconducting YBCO thin films: ablation and lithography issues”, Journal of Materials Science: Materials in Electronics, April 2017, Volume 28, Issue 8, pp 5817 – 5826.
- [2] F. Korte, J. Serbin, J. Koch, A. Egbert, C. Fallnich, A. Ostendorf, B.N. Chichkov, “Towards nanostructuring with femtosecond laser pulses”, Appl. Phys. A, vol.77, no.2, pp.229–235, (2003).
- [3] N. Hass, G. Deutscher, G. Desgardin, I. Monot, and M. Weger, “Sharp Gap Edge and Determination of the Fermi Velocity in YBa<sub>2</sub>Cu<sub>3</sub>O<sub>7-x</sub> by Point Contact Spectroscopy,” Journal of Superconductivity, vol. 5, no. 2, pp. 191–194, 1992.
- [4] Nanosurf FlexAFM, “Operating Instructions Version 3”, November 2011, NANOSURF.

# CHAPTER 5

## OBSERVATION OF THE JOSEPHSON-LIKE EFFECT IN THE VERY LONG SUPERCONDUCTING CONSTRICTIONS ON YBCO THIN FILMS

All the experiments in this chapter and subsequent chapters were conducted at CSIRO, Lindfield, Australia. In this technique, a 775 nm wavelength femtosecond laser was used together with a programmable 3-D movement translation stage to laser-machine and fabricate micron sized and sub-micron sized constrictions that show the Josephson-like effect on  $\text{YBa}_2\text{Cu}_3\text{O}_{7-x}$  thin films successfully. A simple program using G-code programming language was written to control the movement of the translation stage in etching what is called S-shaped constrictions, which show the Josephson-like Effect. Two constrictions, which showed the Josephson-like effect were successfully fabricated and isolated from the rest of the samples, discussed in previous chapters. Their widths were measured at the narrowest point along the constrictions using both the atomic force microscope (AFM) and the scanning electron microscope (SEM). One constriction had a micron-sized width of 2.1  $\mu\text{m}$  and the second had a sub-micron sized width of 816 nm. These widths were measured after cleaning the samples in acetone and wire bonding. To prove that the Josephson-like effect is observed,  $I$ - $V$  characteristics and Shapiro steps are shown and analysed for the two constrictions. The wide micron-size constriction shows a linear relationship for the measured critical current dependence on temperature, which is consistent with the behaviour of the constriction type junction. In the case of the sub-micron, sized constriction the measured critical current dependence on temperature shows an exponential decay function, which is consistent with the behaviour of the S-N-S type junction. The wide micron-sized constriction, experiences partial heating from the laser forming an S-s'-S type constriction. While in the case of the sub-micron sized constriction most of the constriction width is heated and changes from the superconductive phase to a normal one forming an S-N-S type constriction.

## 5.1 JOSEPHSON JUNCTION APPLICATIONS AND USING THE FEMTOSECOND LASER TO FABRICATE THE JOSEPHSON JUNCTIONS.

Josephson junctions (JJs) can be used in many fields of application such as superconducting electronics, magnetic sensors, mining and metrology. Many methods have been used in the past for the fabrication of Josephson junctions such as focused ion beam [1-4], e-beam lithography [5-8], off-axis epitaxial fabrication [9-10], laser-etching methods [11], and atomic force microscopy scribing [12]. These methods work towards the miniaturization of JJs to the micron, sub-micron and Nano scale for application in qubit technology and SQUIDS [13-19]. The femtosecond laser technique was used to attempt in making sub-micron and nano sized Josephson junctions and to introduce a new method that could possibly reduce the effects of thermal heating. Although micron and sub-micron sized Josephson junctions were successfully made the thermal heating of the constriction was not eliminated with this method and remains present even with the low pulse duration of 130 fs for the femtosecond laser. This can be seen in figure 144 in the optical microscope (OM) image where there is an outer fringe surrounding the laser ablation spot representing the local heating.

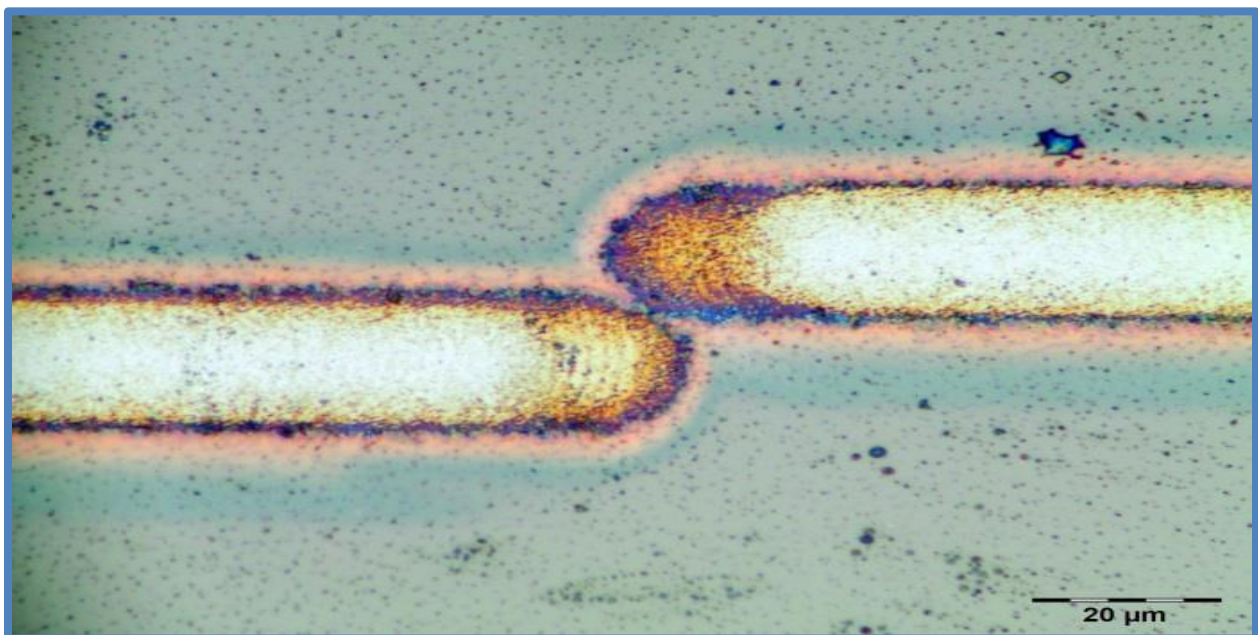


Figure 144 Optical microscope (OM) image of a constriction made showing the heating fringe.

In this method, the laser beam was processed before being used to etch the constrictions as has been described in the previous chapters.

## **5.2 EXPERIMENTAL DETAILS**

The  $\text{YBa}_2\text{Cu}_3\text{O}_7$  thin films were commercially purchased from ceraco ceramic coating company in Germany (GmbH). The thin films were 9 x 9 mm YBCO film, single sided 200 nm thick, on 10 x 10 x 0.5 mm MgO and LAO substrates. The  $T_C$  temperature is 87 K. The surface roughness is the S-type smooth matrix.

The fabricated constrictions on the YBCO thin film were washed in an ultrasonic bath of acetone, deposited 4-point Gold (Au) contacts and wire bonded to the nitrogen immersion probe in a clean room as will be described in detail in the following sections. The gold contacts are used to facilitate *I-V* characterization.

### **5.2.1 PHOTOLITHOGRAPHY PROCESS AND PLACING GOLD (AU) CONTACT PADS ON THE YBCO TRACKS TO FACILITATE I-V MEASUREMENTS.**

After all the previously listed constrictions were fabricated at the National laser centre (NLC) at the CSIR, Pretoria using the femtosecond laser. A photograph combined with a sketch of the dimensions of the YBCO tracks as can be seen in figure 145 was sent to a research facility CSIRO in Lindfield Australia. The sketch of the dimensions was used to produce a soft mask of the YBCO tracks at CSIRO Australia. The soft mask shown in figure 146 is used to produce a hard mask. The hard mask is then used to facilitate the photolithography process to place gold (Au) contact pads on the superconductive YBCO thin film. The gold (Au) contact pads on the YBCO tracks enable the measurement of current – voltage (*I-V*) characteristics of the constrictions fabricated. The soft mask shows a 4-point probe measuring system. There are two gold contacts above the constriction and two below the constriction. Two of these gold contacts are used for passing current through the constriction with a d.c current source and the other two gold contacts are used to measure the resulting voltage across the constriction using a d.c voltmeter. The resulting d.c current and d.c voltage are plotted against each other to produce an *I-V* curve with the “SQUID” national instruments software.

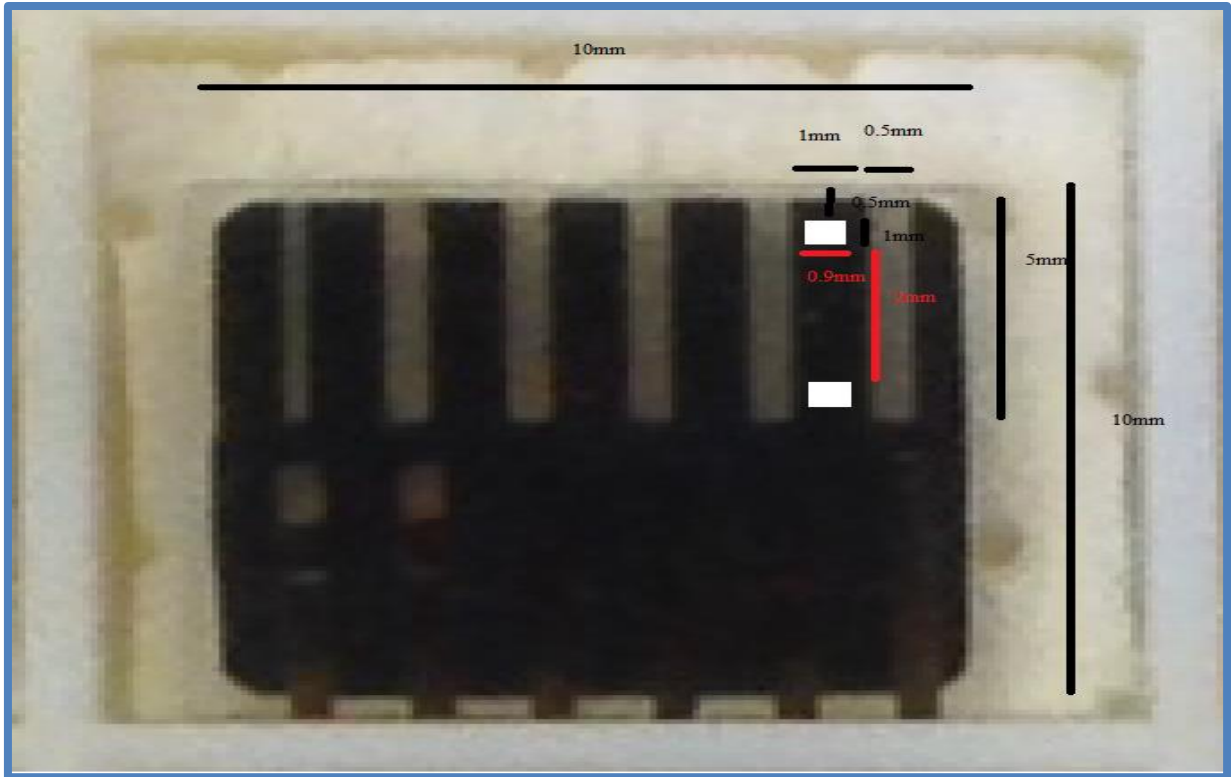


Figure 145 A sketch of the dimensions of the YBCO tracks containing the constrictions etched in the middle with the ablation strip lines on the sides. The dimensions where done to create a soft mask to facilitate the photolithography process to place Gold (Au) contact pads on the YBCO tracks.

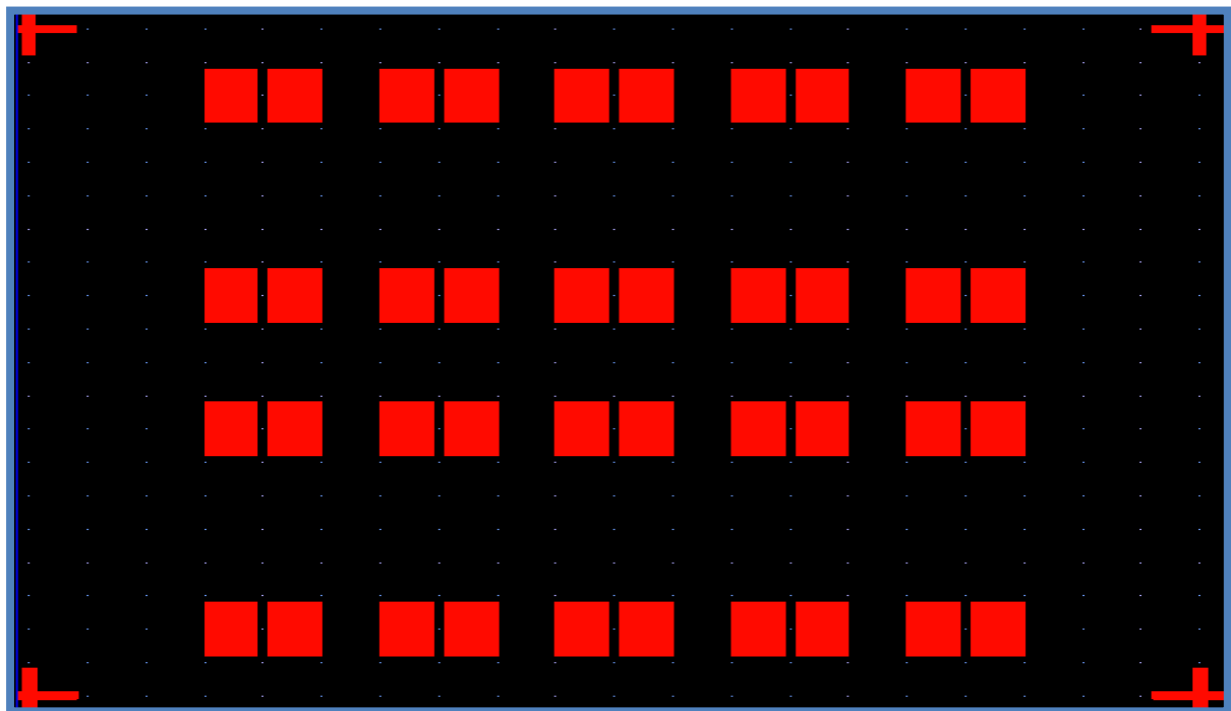


Figure 146 Soft mask: gold (Au) contact pads, one grid is 0.5 mm

In order to place the gold contacts onto the thin film a number of photolithography steps were followed. I will outline the steps followed to place the gold contacts onto the YBCO tracks in the following sub-sections.

#### 5.2.1.1 CLEANING THE SAMPLES.

The sample is cleaned in a beaker containing acetone, which is placed in an ultrasonic bath containing water. Subsequently the sample is blown with a dryer. This process can be seen in the previous figure of a sonicator.

#### 5.2.1.2 APPLYING PHOTORESISTOR

A layer of photo resist material is applied on the surface of the YBCO thin film as seen in figure 147. The photoresist liquid is applied by using a pipette to place a drop on the thin film. It is then spun at 30 revolutions per minute (RPM) on the spinner for 60 secs, which deposits a thin film of photoresist evenly on the surface. Then it is baked at 105 degrees Celsius for 60 secs timed with a stopwatch. All the equipment used can be seen in figure 147 that is the spinner, pipette, photoresist liquid and the baker.



Figure 147 photoresistor application.

The result of the application of the photoresistor can be seen in a 2-D profile sketch in figure 148. There is the first layer of the YBCO thin film and a second layer of photoresistor liquid on top.



Figure 148 2-D profile showing the YBCO thin film and the photoresistor layer.

### 5.2.1.3 MASK ALIGNMENT

The soft mask is used to produce a hard metallic mask shown in figure 149, which is used in the photo-aligning tool or in the mask aligner shown in the next figure in 150. The mask alignment tool is used to align the hard mask with the YBCO superconductive tracks. The hard mask has holes or material translucent to the (UV) rays in the sections where the gold (au) pads are going to be deposited. The holes enable the photoresistor to be exposed to the ultraviolet (UV) rays.

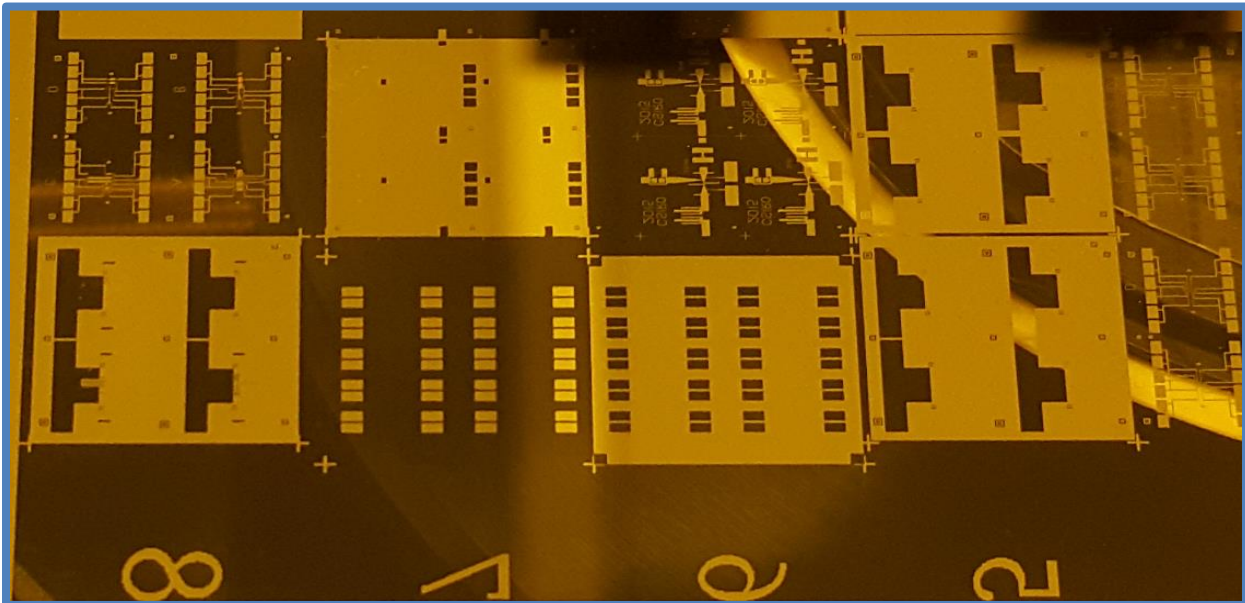


Figure 149 Hard mask used in the mask aligner tool.

The hard mask prevents the UV light from the mask alignment tool from coming in contact with the photo resist material except in places where there are holes in the hard mask. The mask aligner can be seen in figure 150.

According to the hard mask the UV light will fall on the photo resist material and the thin film only in the place where the gold contacts must be placed.



Figure 150 Mask alignment tool.

Once the photo resist is exposed in these places, the next step is to wash the YBCO thin film in the photo developer liquid. This liquid will essentially take out the photo resist material that has been exposed to UV light leaving behind only the photo resist material that has not been exposed by the hard mask in the mask aligner. The following 2-D images show the process and how the resulting photo resist and YBCO material look like after the mask alignment and washing process.

Figure 151 shows the UV light being applied to the photo resist materials in the section where the gold (au) pads are to be placed.

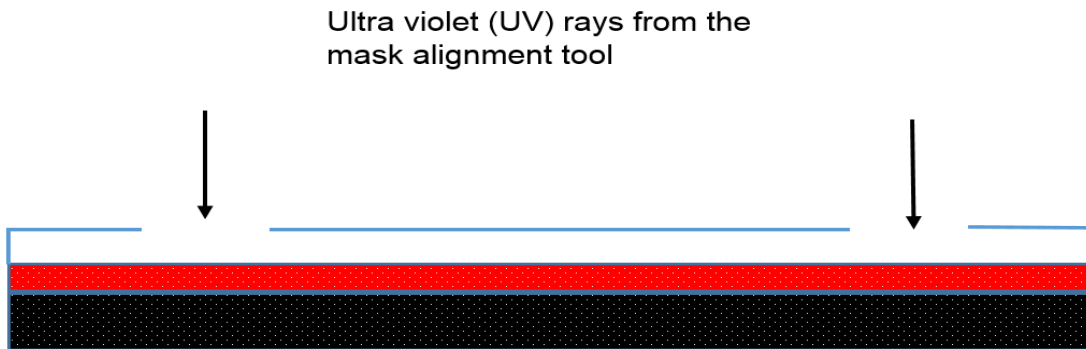


Figure 151 UV rays applied from the mask alignment tool after alignment with the hard mask

After the YBCO thin film is washed in the developer liquid and the UV exposed photo resistor material is dissolved away. The 2-D profile image in figure 152 shows what the structure looks like.



Figure 152 The photo resist material removed in the sections where the gold (Au) pads will be applied.

#### 5.2.1.4 OXYGEN PLASMA

The oxygen plasma system shown in figure 153 is used to clean the sections on the YBCO tracks where the photo resistor material has been taken out. The oxygen plasma is pumped onto the sample and it digs slightly into the YBCO thin film itself in the sections, which are exposed of photo resistor material. The cleaning of the sections where the gold contacts are to be placed is done to make sure that the gold contacts stick properly to the YBCO surface in these sections once deposited. It is an abrasive action that makes the contact point between the YBCO tracks and the gold contacts strong.



Figure 153 Oxygen plasma

The oxygen plasma system is used mainly to clean the section where the photoresist has been taken out where the gold contacts will be placed to make sure the gold contacts stick to the YBCO surface.

It works by first pumping out the nitrogen gas through the taps shown in figure 153 and then filling up the space with the oxygen plasma around the sample. The oxygen gas cleans the sample in the grooves where the gold will be deposited.

After the application of the oxygen plasma unto the surface of the YBCO thin film, the 2-D profile image of the photo resistor and the YBCO tracks looks like that in figure 154.

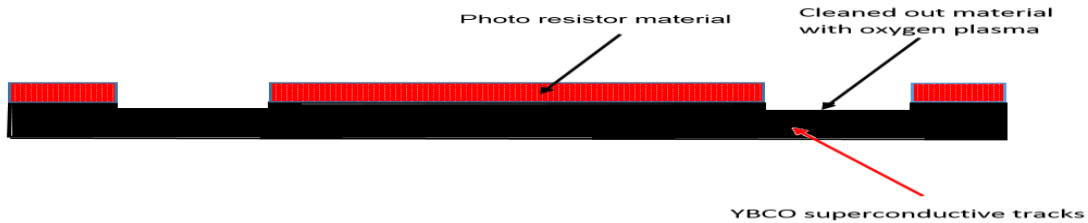


Figure 154 Oxygen plasma applied to clean the grooves where the gold (Au) contact pads are to be placed.

### 5.2.1.5 GOLD DEPOSITION

The gold (Au) is deposited onto the thin film using the pump system shown in figure 155. There is a small chamber where the thin film is placed just next to the black rotator handle in figure 155. The handle is used to close the chamber before gold deposition begins.



Figure 155 Ion beam and gold deposition chamber.

The gold deposition equipment has a control system shown in figure 156 that is used to control the deposition of gold onto the YBCO surface.



Figure 156 Control system for Gold deposition

The surface where the gold contacts are to be deposited is bombarded with an ion beam in order to slightly etch the YBCO thin film to make for good gold contact pads. This is done for about 60 s such that a depth is created of about 10 nm below the YBCO thin films thickness of 200 nm. Then the sample is rotated under the gold deposition beam and bombarded with gold. The gold deposition takes about 30 min to complete. After the gold deposition process is completed, the 2-D profile image of the YBCO thin film can be seen in figure 157.

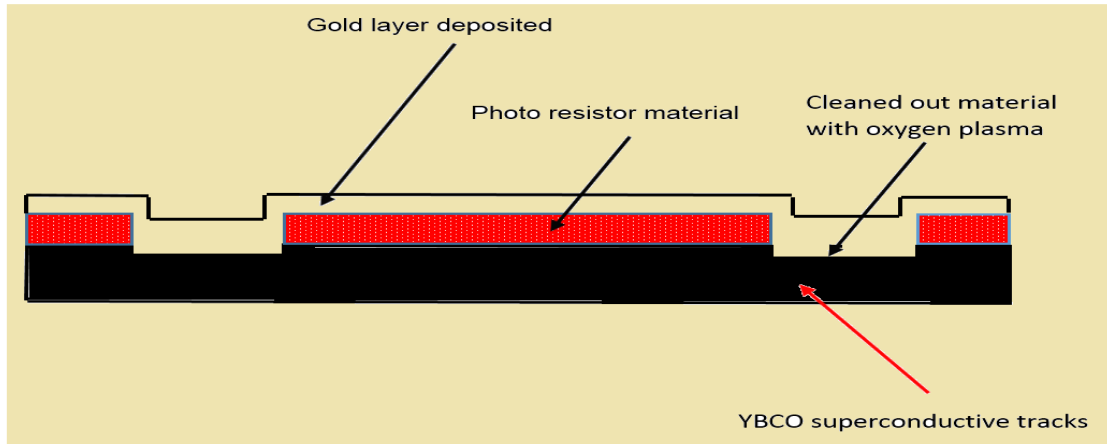


Figure 157 2-D profile image after the gold deposition process.

The sample is taken out of the gold deposition chamber and cleaned again in acetone in the ultrasonic cleaner. What happens then is that the photo resistor sections are dissolved in the acetone and as a result, all the gold deposits above the photo resistor are displaced or taken away together with the photo resistor. Leaving behind only the gold contacts as seen in figure 158.

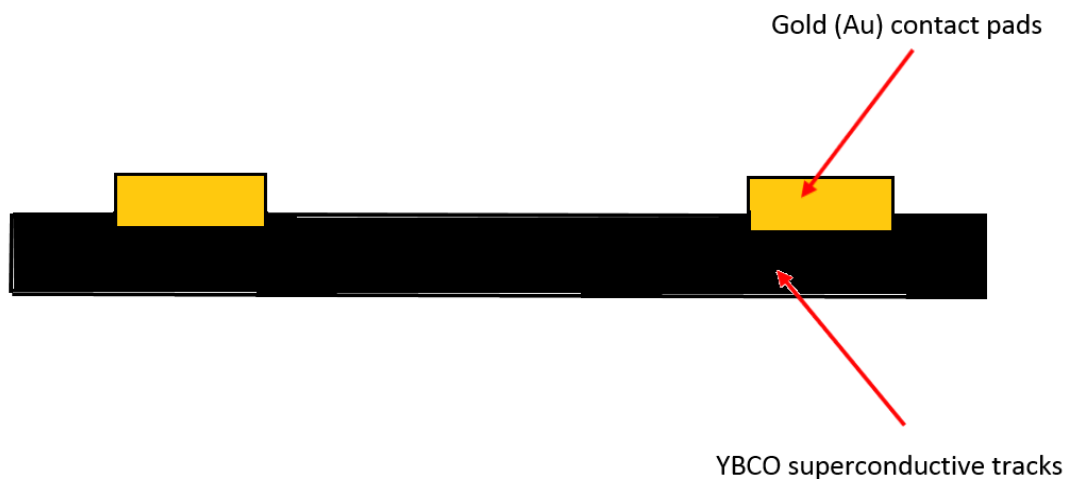


Figure 158 Photo resistor removed after cleaning in acetone leaving behind only the Gold (Au) contacts. After the gold deposition is complete, the sample looks as the one in figure 159 in the test tube showing the 4-point gold contacts.



Figure 159 The sample after gold deposition with a separation distance between the laser ablation spots ( $S_w$ ) 18.7  $\mu\text{m}$  – 18.3  $\mu\text{m}$  sample with 4-point gold contacts deposited.

#### 5.2.1.6 WIRE BONDING TO THE PCB HOLDER

The YBCO thin film with gold contacts is placed in a suitable PCB holder, which can be seen in figure 160. The PCB holder has a square holding place and two arrays of contact points going around spherically but connected underneath the PCB holder to each other.

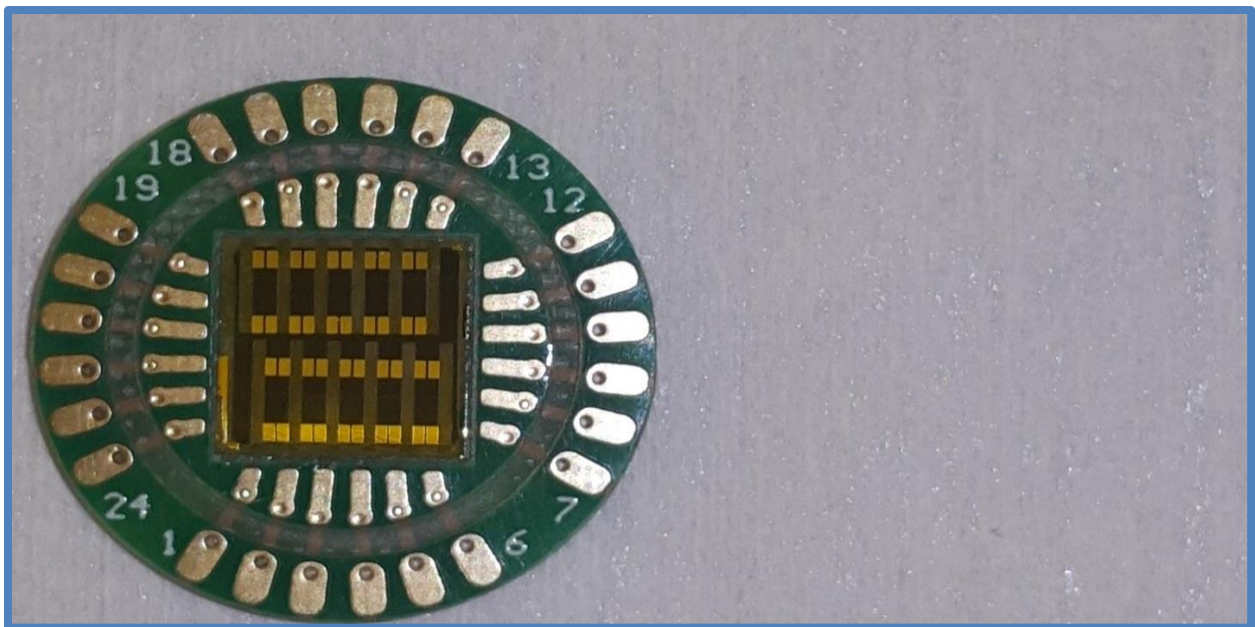


Figure 160 PCB holder with the YBCO thin film sample having gold contact points.

The gold contact points on the YBCO thin film are wire bonded to the gold contacts on the PCB holder. The wire bonding is done using the wire-bonding machine, which can be seen in figure 161. During the wire-bonding process, each gold contact on the YBCO thin film is wire bonded “twice” to each gold contact on the PCB holder. The reason for doing this is to make sure that if one wire cuts the second wire will hold the contact, this can be seen on the YBCO thin film sample in figure 162 (a). In addition, the PCB holder has gold contacts arranged spherically around the PCB and these contacts are labelled 1-24 anti-clockwise. Therefore, during the wire bonding process a “NOTE” is taken of the connections made with the gold contacts (pin numbers) on the PCB holder to the 4-probes on the thin film. That is for each constriction the 4 connections made to the gold contacts on the PCB holder are recorded in a log-book with the pin numbers for the connections.

The wire-bonding machine works in a sort of drag-and drop motion. That is a contact is made on the gold pad on the thin film and then the contact is dragged in the form of a wire to a gold contact on the PCB holder and the process repeated.



Figure 161 Wire bonding machine

### 5.2.1.7 SOLDERING THE PCB WITH THE SAMPLE TO THE NITROGEN IMMERSION PROBE AND I-V CHARACTERIZATION.

The nitrogen immersion probe has connections on both sides. On the top side of the nitrogen immersion probe the red ( $X_1$ ) connection is wired to the yellow wire (to be immersed) which is soldered onto a gold contact pin number on the PCB holder according to the wire bonding specifications. On the top side again of the nitrogen immersion probe the black ( $X_1$ ) connection is wired to the blue wire (to be immersed) which is soldered onto a gold contact on the PCB holder again according to the wire bonding specifications. The wire bonding, soldering process and the nitrogen immersion probe can be seen in figure 162 (a) and 162 (b) respectively.

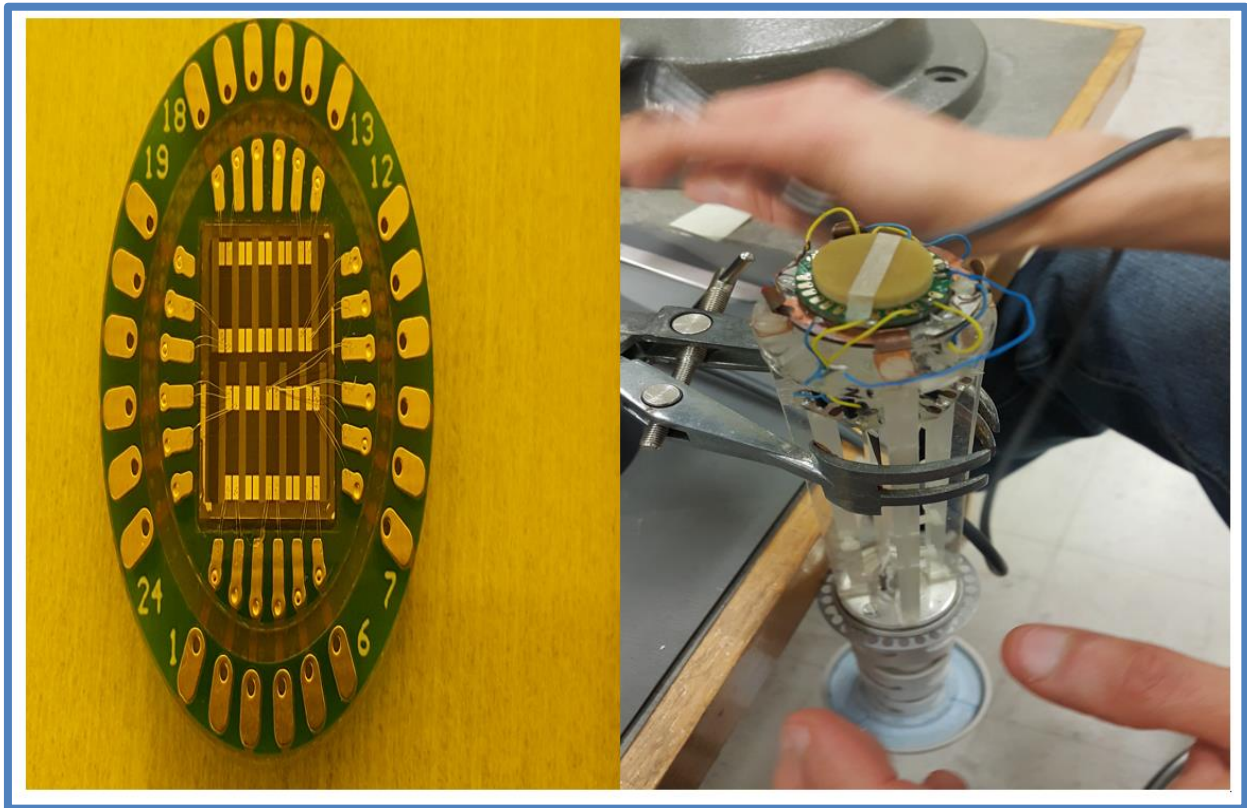


Figure 162 (a) YBCO sample with 4-point gold contacts, wire bonded to the PCB holder, 162 (b) PCB holder mounted onto a nitrogen immersion probe.

Finally, the nitrogen immersion probe is lowered with the PCB end, first into a cylinder containing liquid nitrogen to take the sample to a cryogenic temperature of 77 K. At this temperature I-V characteristic measurements can be done.

The current is passed into the sample between probes red ( $X_1$ ) and black ( $X_1$ ) as can be seen in figure 163 (a) using the d.c field current source in figure 163 (b). Then the resulting voltage is measured between probes red ( $Y_1$ ) and black ( $Y_1$ ) as can be seen in figure 163 (a) using the d.c voltmeter in figure 163 (b). The resulting current – voltage characteristics are plotted against each other using the “SQUID” software from national instruments seen in figure 164.



Figure 163 (a) The probe with sample immersed in liquid nitrogen, 163 (b) DC current source and DC voltmeter.

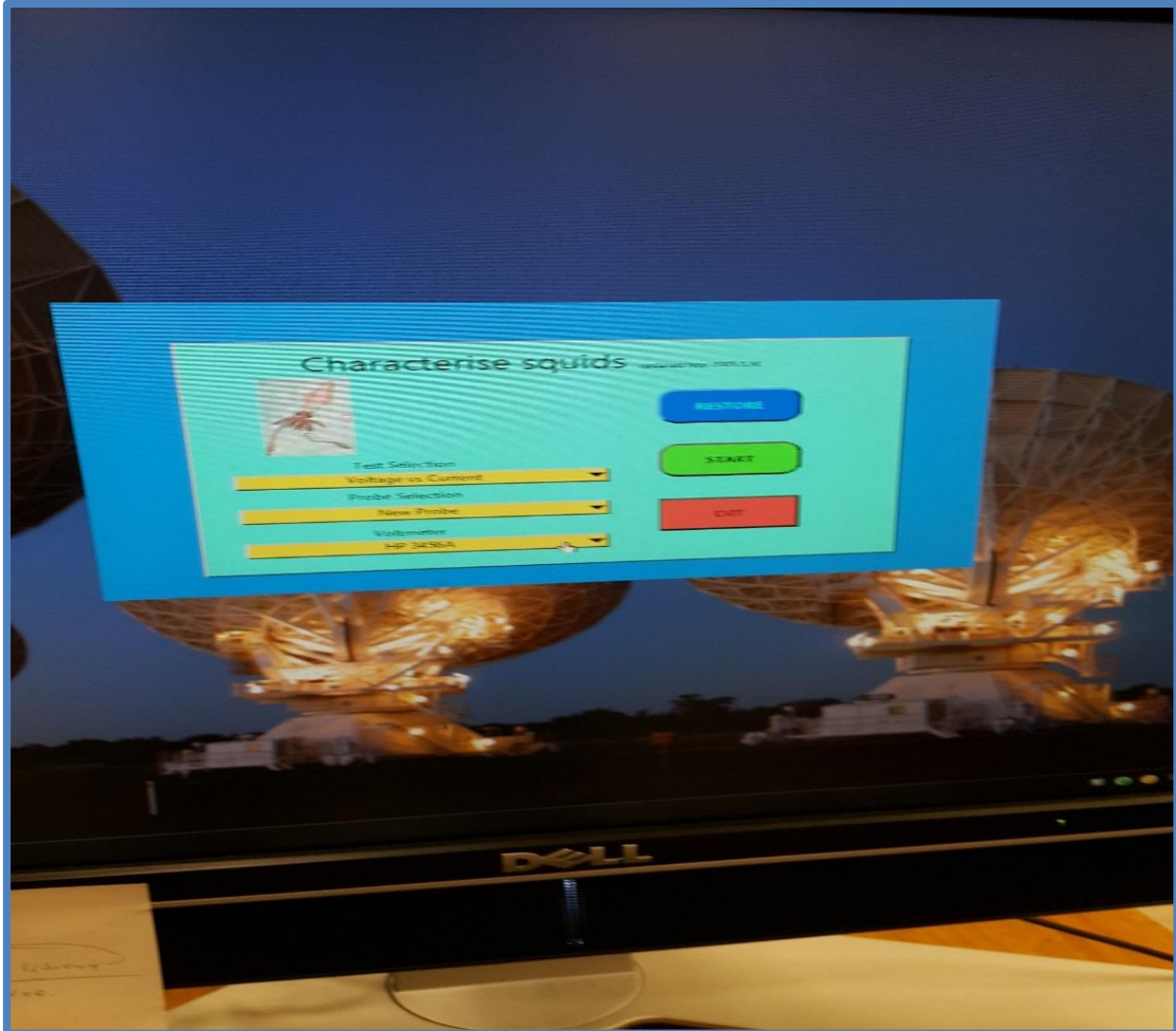


Figure 164 “SQUID” software from national instruments for plotting I-V characteristics of a constriction. In order to make a quick test on the constriction to see if at all it is still superconductive. The d.c voltmeter probes are connected between the red ( $X_1$ ) connection and the black ( $X_1$ ) connection. In the same way the d.c current source probes are connected between the red ( $Y_1$ ) connection and the black ( $Y_1$ ) connection. Then the “SQUID” software for measurement is initialized. A small current is passed across the constriction and the resulting voltage is measured. If the circuit shorts at 77 K then the device is still operational (superconductive). Which you will know by a shorting “beeping” sound you hear. However if no sound comes and a huge voltage is observed the device is highly resistive or “open” or “clipped”. An example of these pin connections made on the constriction sample can be observed in figure 165.

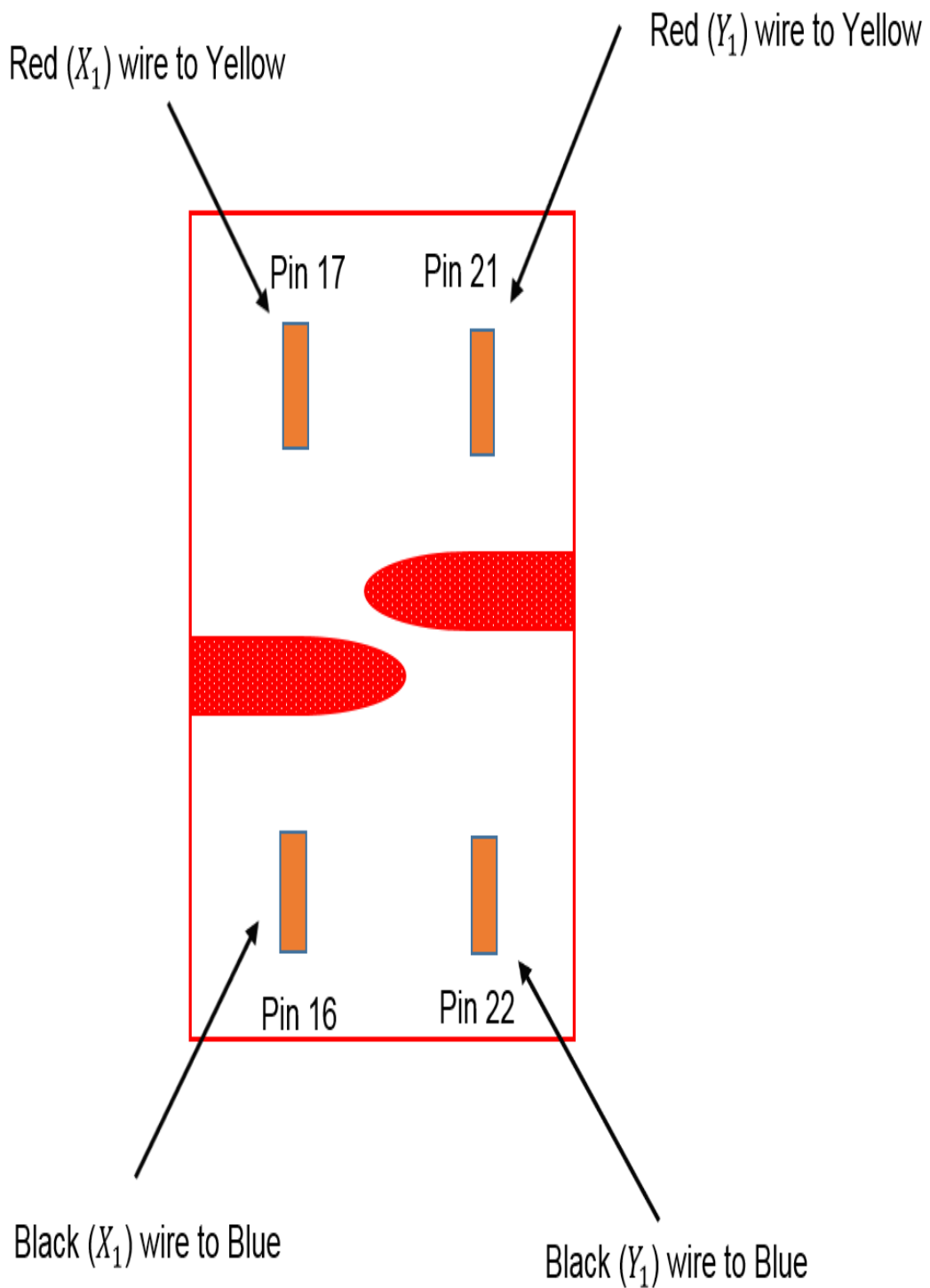


Figure 165 Image showing how each constriction is wire bonded to the PCB holder and then soldered to the nitrogen immersion probe. (Wire connections).

### 5.2.2 LASER CUTTING SETTINGS AND SPECIFICATIONS OF THE JUNCTIONS THAT SHOWED THE JOSEPHSON EFFECT.

The cleaned junction's widths were measured with an AFM and validated with an SEM. As specified earlier in the introduction to this chapter, there are two constrictions that showed the Josephson-like effect. The laser cutting settings and specifications for the sub-micron sized constriction are as follows; the separation distance between the laser ablation spots is 18.7  $\mu\text{m}$ , laser power 4.9 mW, peak laser fluence ablation threshold 0.824  $\text{J cm}^{-2}$ , the laser ablation spot size is 18.05  $\mu\text{m}$ , laser pulse repetition frequency 1 kHz and the laser beam feed rate 333  $\mu\text{m s}^{-1}$ . For the second micron-sized constriction, the separation distance between the laser ablation spots is set at 19.1  $\mu\text{m}$ , laser power 4.6 mW, peak laser fluence ablation threshold 0.824  $\text{J cm}^{-2}$ , laser ablation spot size 17.8  $\mu\text{m}$ , laser pulse repetition rate 1 kHz and the laser beam feed rate 333  $\mu\text{m s}^{-1}$ . These settings are summarized in table 8. Both samples that showed the Josephson Effect consisted of the superconductive YBCO thin film that was based on an LAO substrate.

Table 8 Constrictions that showed the Josephson-like effect – dimensions, and their laser etching parameters.

Constriction	Sub-micron junction (Sample A)	Micron junction (Sample B)
Width of constriction (Width cons)	816 nm	2.1 $\mu\text{m}$
Length of constriction (Length cons)	10 $\mu\text{m}$	9.5 $\mu\text{m}$
Thickness	200 nm	200 nm
Separation distance between the laser ablation spots along the length of the sample to determine the width of the constriction ( $S_W$ ).	18.7 $\mu\text{m}$	19.1 $\mu\text{m}$
Laser ablation spot size	18.05 $\mu\text{m}$	17.8 $\mu\text{m}$
Laser power setting from the laser source	4.9 mW	4.6 mW

### 5.2.3 RF CONNECTIONS FOR MEASUREMENT OF SHAPIRO STEPS

I-V characteristics and the Shapiro steps are measured on each constriction, using the experimental set-up shown in figure 166. The RF signal is coupled to the junction onto one of the 4-point gold contacts. It shares the contact with either the current or the voltage connection as seen practically in figure 167.

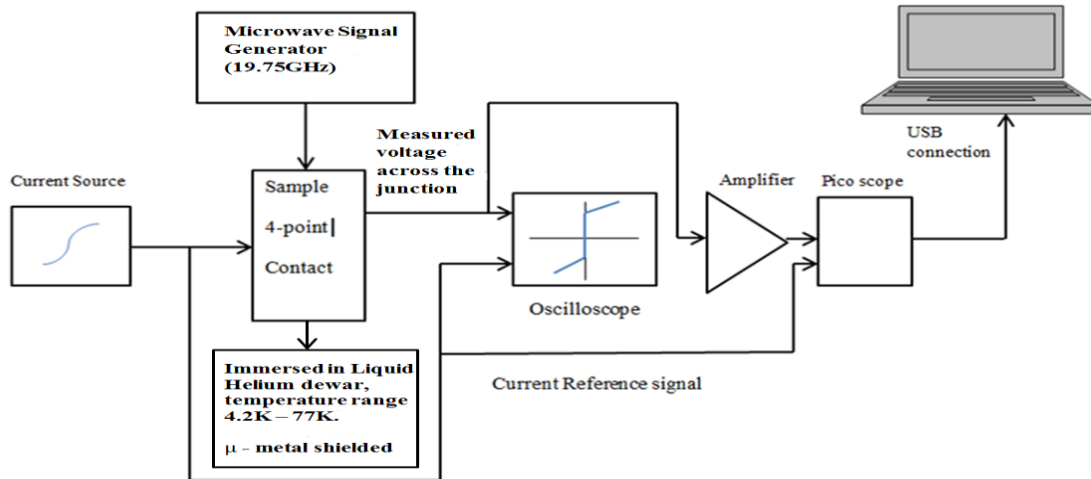


Figure 166 Schematic of the sample I-V and RF measurement set-up. The sample is a YBCO thin film containing the laser etched constrictions.

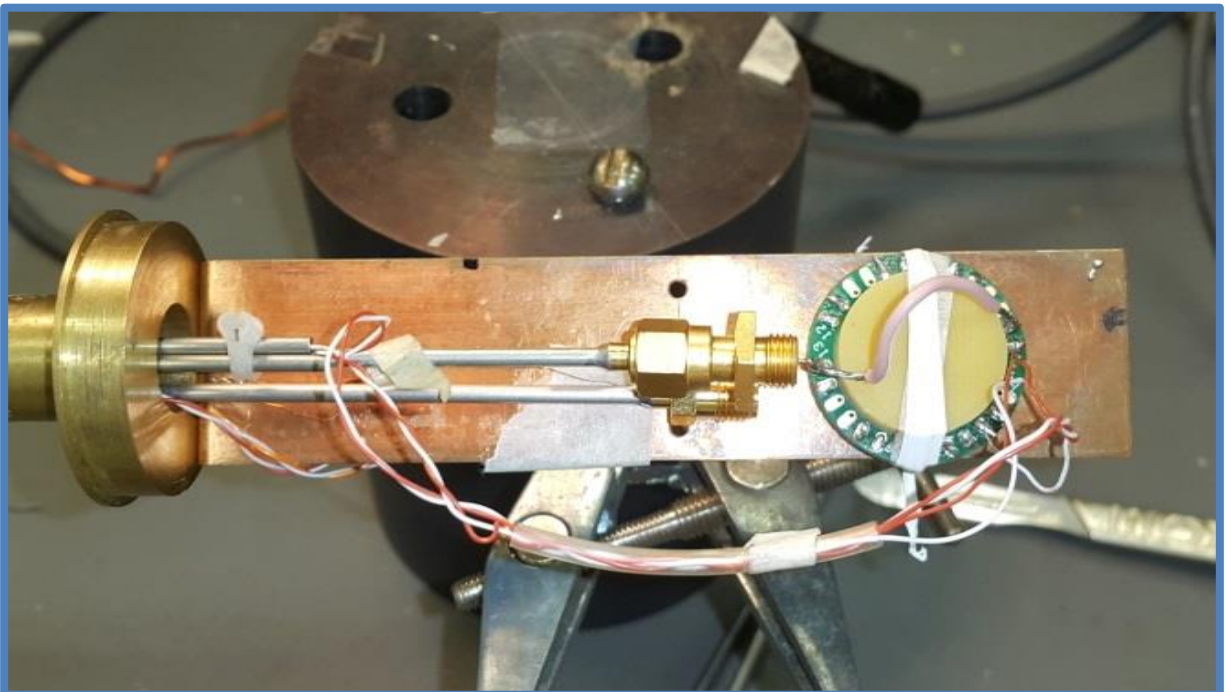


Figure 167 RF connection coupled onto the one of the 4-point gold probes on the sample.

## 5.3 DISCUSSION

### 5.3.1 DIMENSIONS OF THE FABRICATED JUNCTIONS THAT SHOWED THE JOSEPHSON-LIKE EFFECT.

Figures 168 (a), 168 (b) and 169 show the AFM images of the sub-micron sized constriction created using the femtosecond laser. Figure 168 (a) is the AFM topography line plot of the sub-micron constriction, which shows the width of the sub-micron constriction as 816 nm. Figure 168 (b) is the AFM 3-D image and figure 169 is the profile distribution of the sub-micron constriction which confirms the width of the sub-micron constriction as 816 nm.

The length of the constriction is approximately  $10\ \mu\text{m}$ , the thickness is  $200\ \text{nm}$  derived from the 3-D AFM image and the width is approximately  $816\ \text{nm}$  measured between the black arrows from the profile distribution in figure 169.

Figure 170 shows the SEM image of the sub-micron constriction taken after cleaning and wire bonding the sample. It shows the width of the constriction to be  $816\ \text{nm}$  validating the AFM determined width of the constriction.

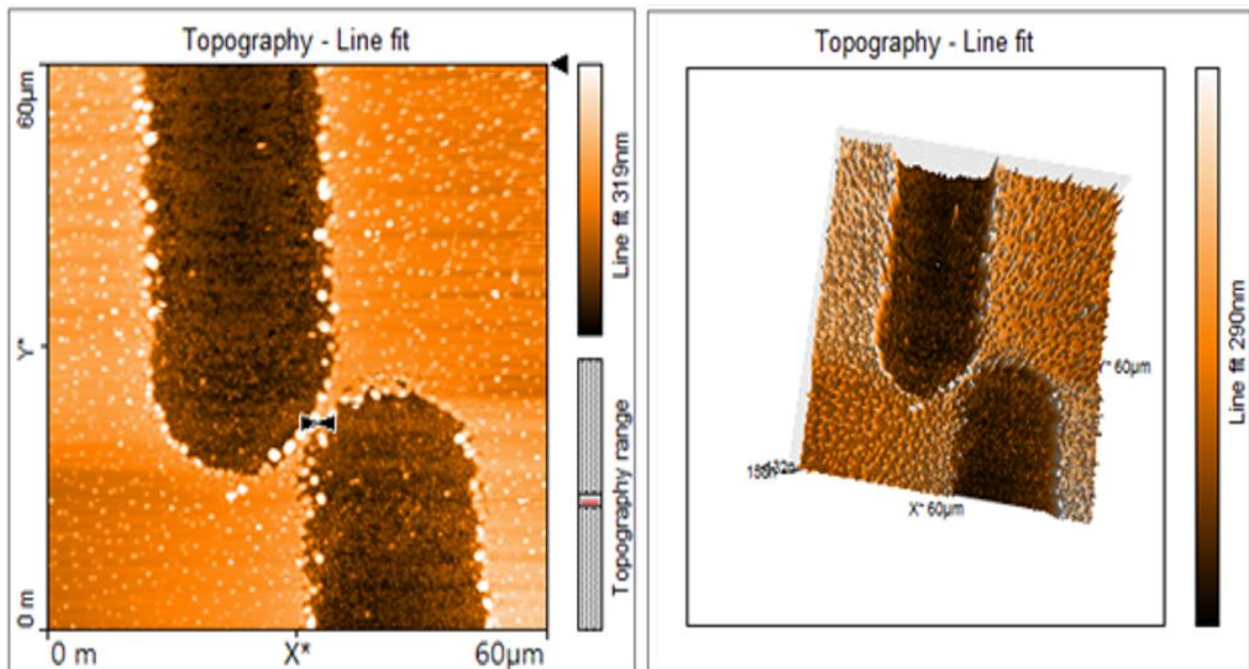


Figure 168(a) AFM image of the sub-micron constriction whose width is defined between the (black) arrows as  $816\ \text{nm}$ . 168(b) 3-D AFM image of the sub-micron constriction.

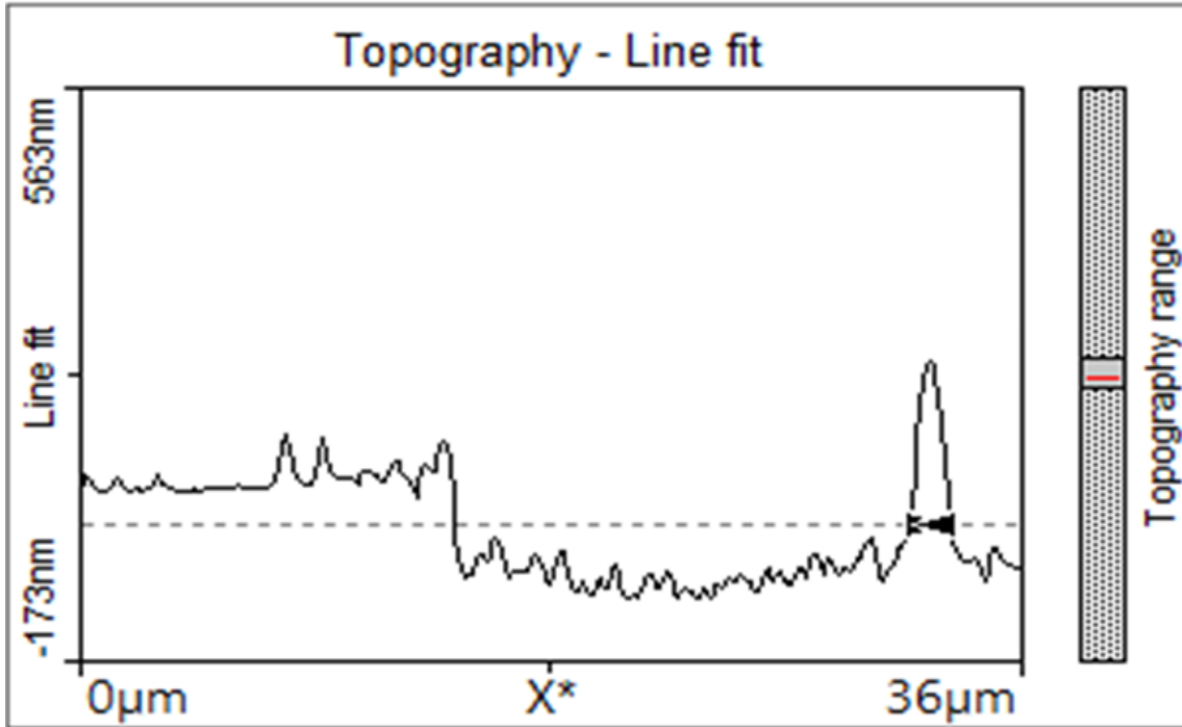


Figure 169 AFM Profile distribution of the sub-micron constriction, the width can be measured between the (black) arrows, and is 816 nm.

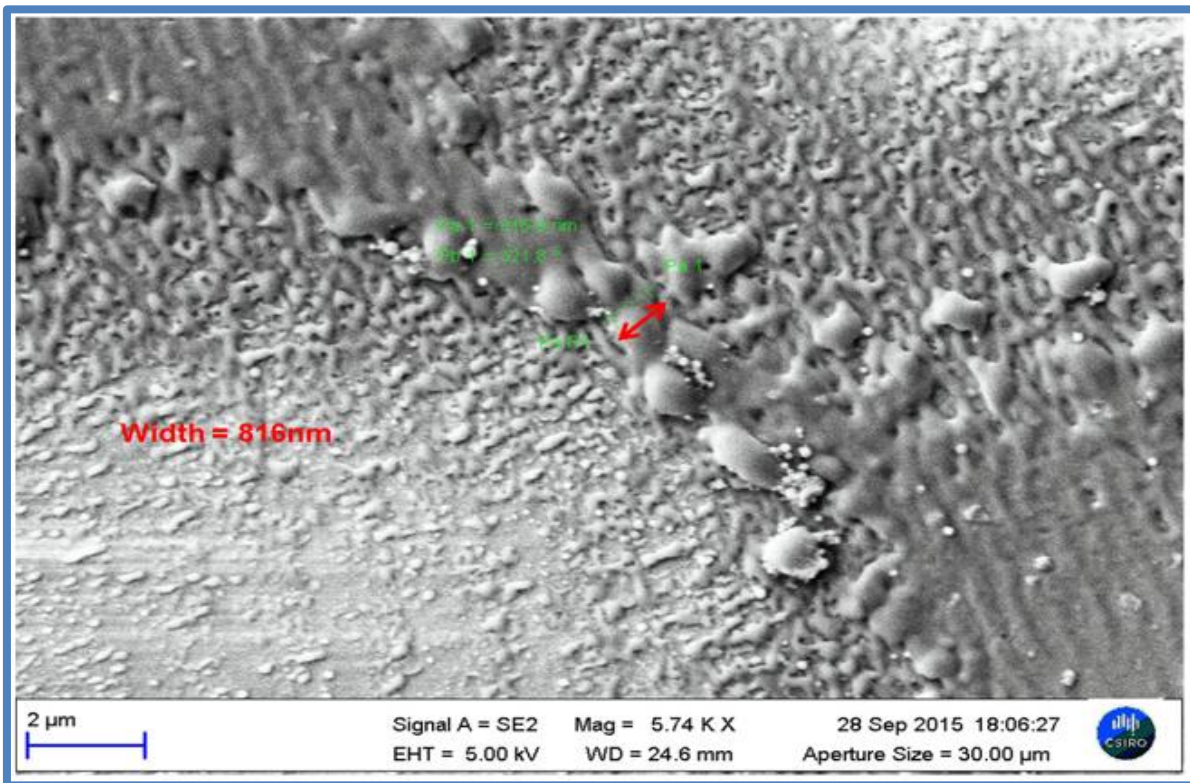


Figure 170 SEM image of the sub-micron constriction shows the width to be 816 nm between the red cursors, courtesy of CSIRO Australia Laboratory.

Figures 171 (a), 171 (b) and 172 show the AFM images of the micron-sized constriction fabricated using the femtosecond laser. Figure 171 (a) is the AFM topography line plot of the constriction that shows the width of the micron-sized constriction as 2.1  $\mu\text{m}$ . Figure 171 (b) is the AFM 3-D image and figure 172 is the profile distribution of the constriction, which confirms the width of the micron-sized constriction as 2.1  $\mu\text{m}$ . The length of the constriction is approximately 9.5  $\mu\text{m}$ ; the thickness derived from the 3-D plot is 200 nm and the width is approximately 2.1  $\mu\text{m}$ .

Figure 172 shows the SEM image of the micron-sized constriction, which again validates the width to be 2.1  $\mu\text{m}$ .

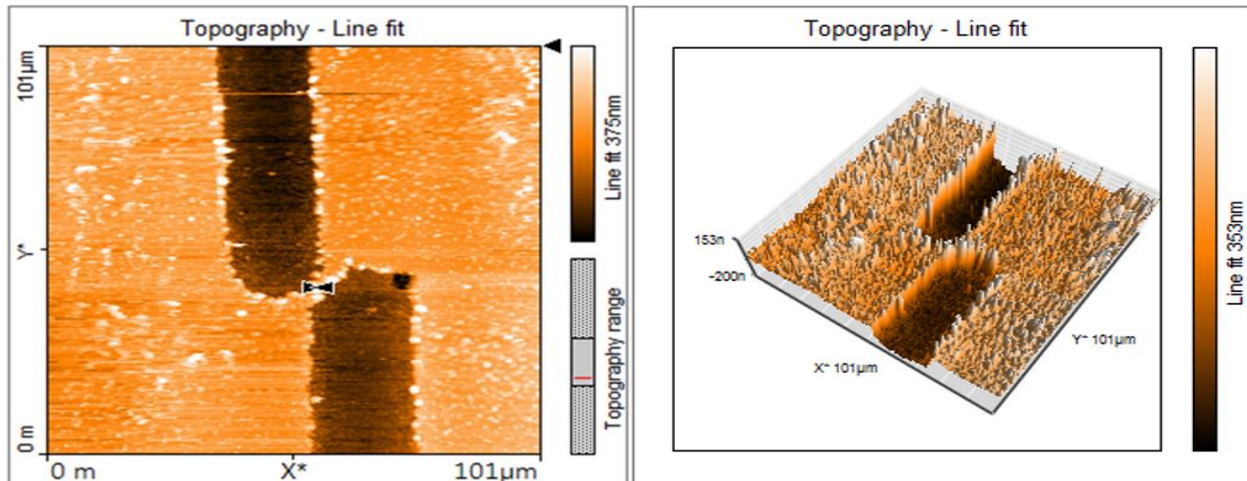


Figure 171 (a) AFM image of the micron constriction whose width is measured between the black arrows is 2.1  $\mu\text{m}$

171 (b) 3-D AFM image of the micron constriction

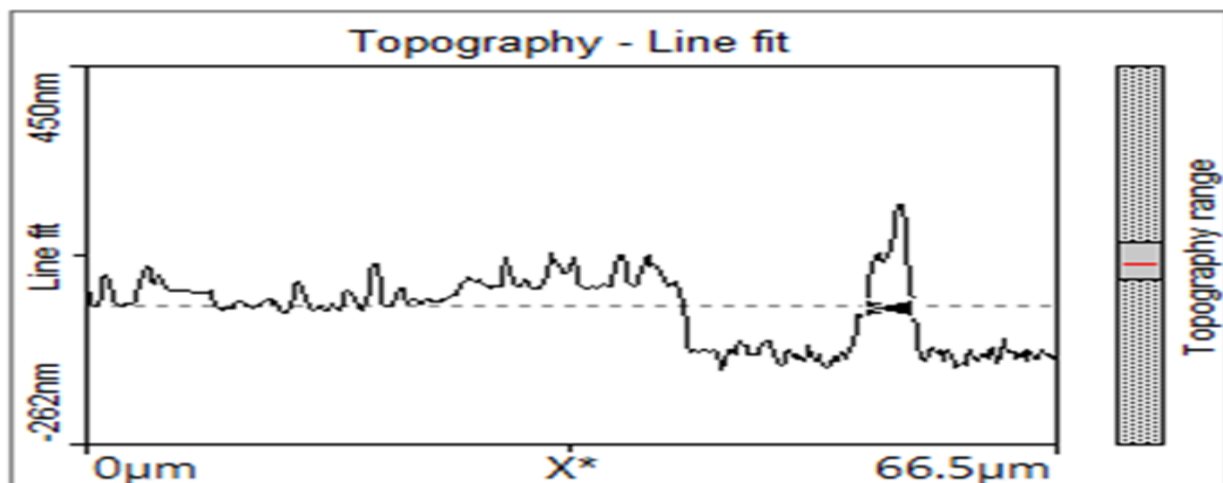


Figure 172 AFM profile distribution of the micron constriction, the width measured between the (black) arrows, is 2.1  $\mu\text{m}$ .

During the measurement of Shapiro steps on the micron-sized constriction. The d.c current source was passed through the sample without a slight a.c frequency signal (8-10 Hz) being added. Hence, the shapiro step measurement was done with an RF frequency signal of 19.5 GHz directly coupled to the sample without a slight a.c component (8-10 Hz) being added to the d.c current source. This led to the RF signal applying electronic friction to the sample and hence the sample melts from the frictional heat as can be seen in figure 173. Although the junction melted, all the necessary data had already been extracted from the sample, before this occurred.

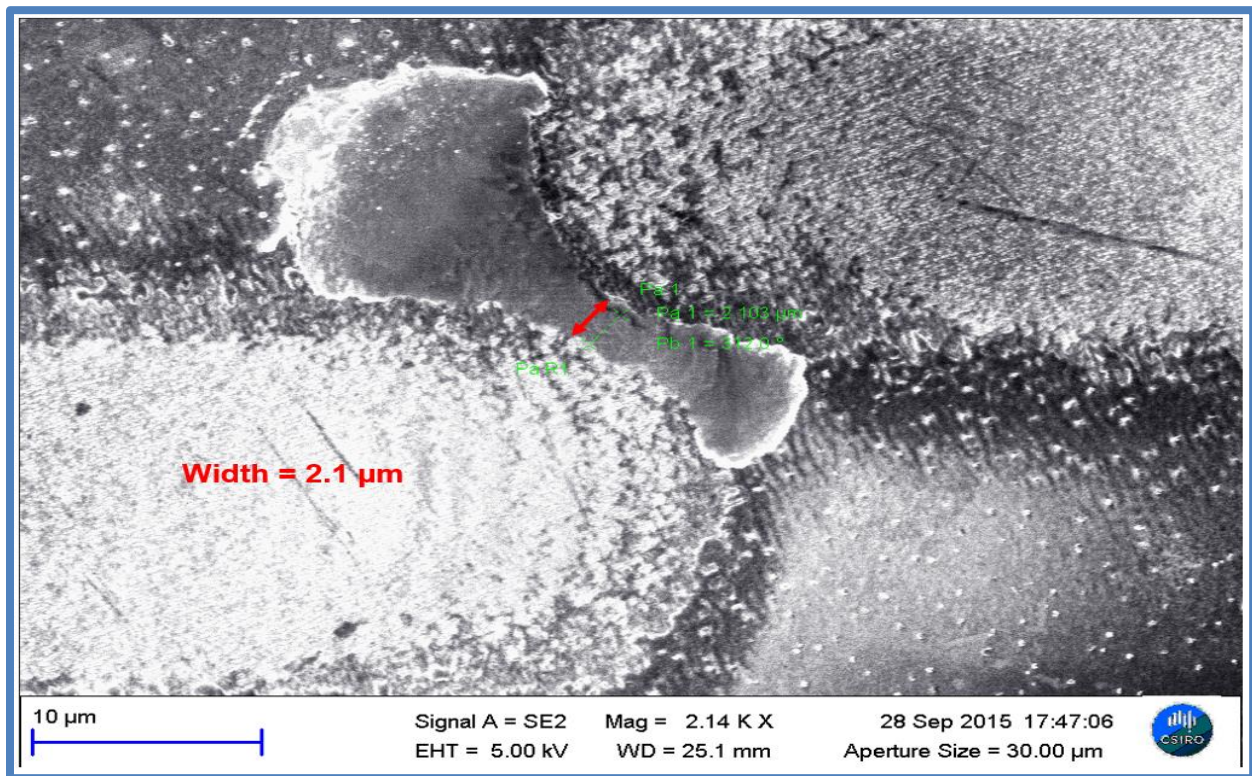


Figure 173 SEM image of micron-sized constriction showing the width to be 2.1  $\mu\text{m}$ .

### 5.3.2 CURRENT – VOLTAGE CHARACTERISTICS (IVC's) OF THE CONSTRICTIONS

The  $I$ - $V$  characteristic for the sub-micron sized junction is shown in figure 174. The  $I$ - $V$  characteristic for this junction was measured at a temperature of 8.5 K. The reason for using this low cryogenic temperature is that these constrictions showed a very small ( $I_C$ ) critical current at 77 K. They thus needed to be cooled down to low cryogenic

temperatures with helium gas to show a significant critical current. For example for the sub-micron constriction, the critical current at 8.5 K is 102  $\mu\text{A}$ .

The  $I$ - $V$  Characteristic shows a bit of bending at the knee of the graph [11]. This is in contrast to the sharp edge at the knees, which is observed in step-edge junctions [20]. The bending at the knees can be attributed to the localized heating of the constriction by the femtosecond laser, which changes the constriction from the superconductive phase to a normal phase producing an S-N-S type junction. The critical current was measured at a voltage offset of about 40  $\mu\text{V}$  on the X-axis.

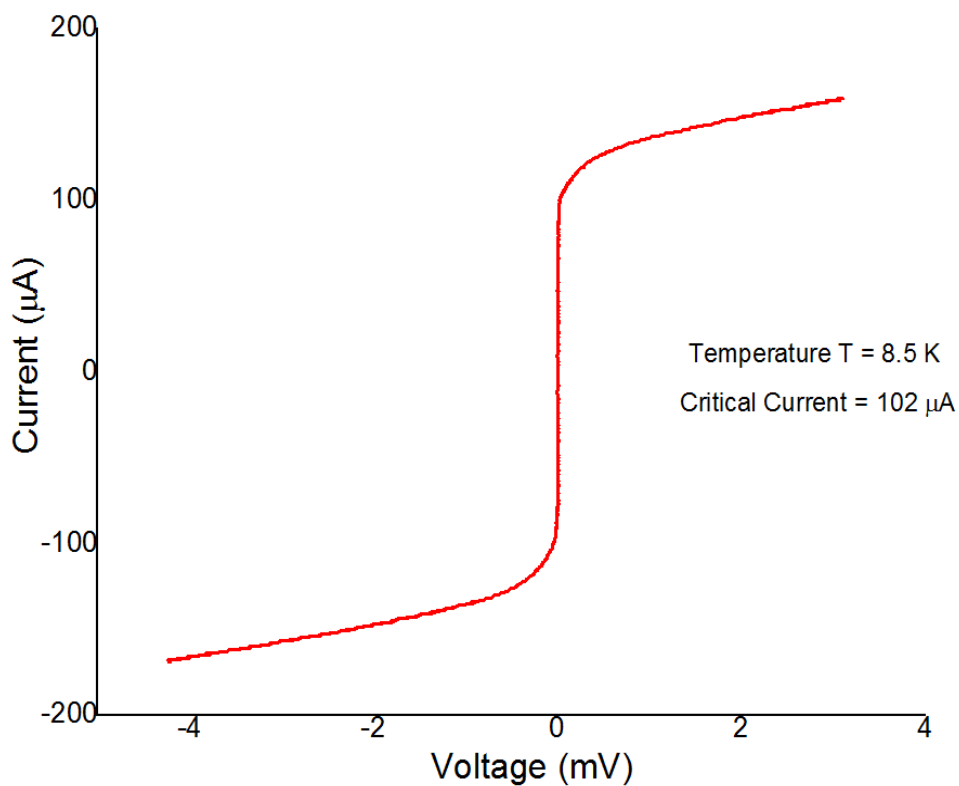


Figure 174  $I$ - $V$  characteristic for the sub-micron constriction measured at  $T = 8.5 \text{ K}$

The  $I$ - $V$  characteristic for the micron-sized constriction is shown in figure 175. The  $I$ - $V$  characteristic shown for this sample was measured at a temperature of 10 K. The  $I_C$  critical current for this sample at 10 K is about 720  $\mu\text{A}$ . This is  $\sim 7$  times the value of the critical current for the sub-micron junction, which is not consistent to the difference of the sample width if assuming the critical current density is uniform across the width of the constriction. The reason could be attributed to the fact that the micron constriction is

considerably wider than the sub-micron constriction and hence the heating fringe from the laser does not normalize the whole superconductive phase of the constriction width in this case. The micron sized constriction is therefore, more of an S-**s**'-S type junction. The “**s**” in the material stands for a superconductive phase whose geometric size is reduced by the local heating from the laser and whose critical temperature is lower than the value of “S”. The critical current was measured at a voltage offset of 20  $\mu\text{V}$  in this case on the X-axis.

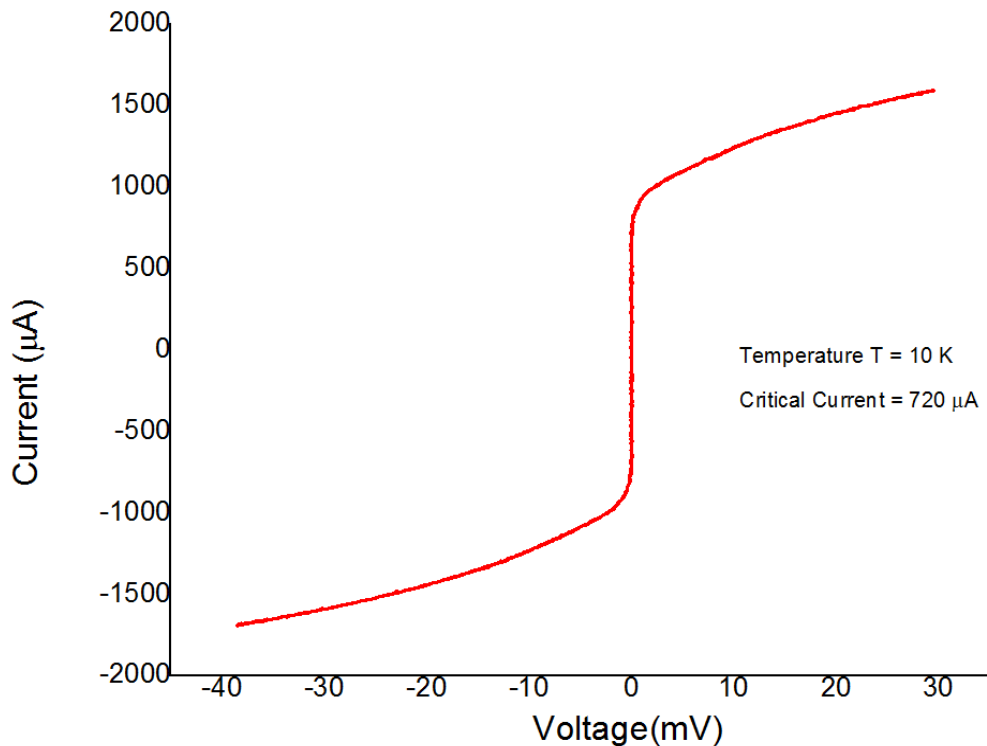


Figure 175 *I-V* characteristic for the micron size constriction measured at Temperature  $T=10$  K.

As can be seen in figure 175 there is still rounding or bending on the knee of the curve representing the localized heating from the femtosecond laser on the constriction.

### 5.3.3 SHAPIRO STEPS

For the sub-micron sized constriction, we applied an RF signal with a power of -30 dBm (0.001 mW) and a frequency of 19.5 GHz via a coaxial cable terminated on one of the 4-point contacts at a temperature of 8.5 K. At this RF signal settings Shapiro-like steps were observed as can be seen in figure 176. The fact that the constriction responded to microwave radiations proves the presence of the Josephson-like effect on the sample.

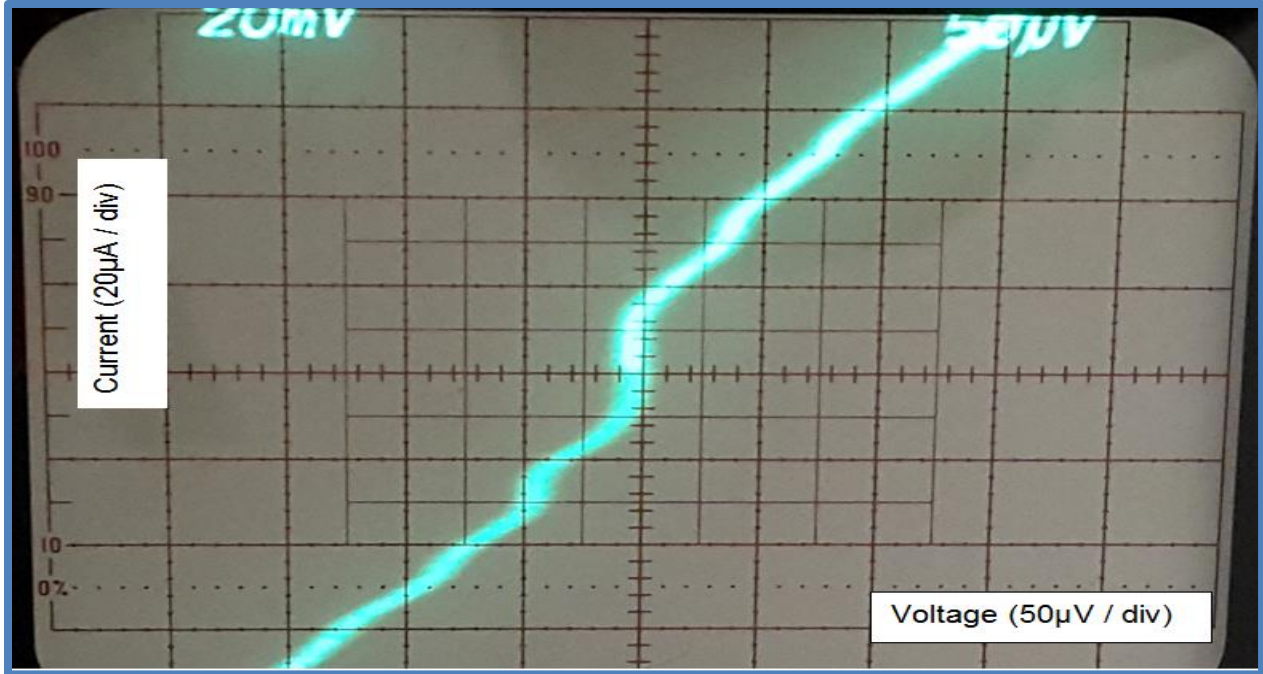


Figure 176 Shapiro-like steps for the sub-micron sized constriction, which was exposed to an RF signal of frequency of 19.5 GHz, power strength -30 dBm and sample temperature of 8.5 K.

Further measurements were done using the picoscope data logging system on the shapiro steps for the sub-micron sized constriction. The step voltage was determined to be approximately 42.6  $\mu\text{V}$  while the step current was measured to be 23.1  $\mu\text{A}$ . According to theory the Josephson step voltage [21] is given by the formula in equation (1);

$$V_0 = n \left( \frac{\Phi_0}{2\pi} \right) \omega_s \quad (1)$$

Which is equivalent to equation (2):

$$V_0 = n \left( \frac{h\omega_s}{4\pi e} \right) = n \left( \frac{hf_s}{2e} \right) \quad (2)$$

Where  $\Phi_0 = h/2e$ , in equation (1),  $n$  is the Shapiro step number taken to be 1 for the first step seen in figure 176,  $h$  is Planck's constant,  $f_s$  is the signal frequency and  $e$  the electron charge in equation (2). When we substitute the signal frequency used in this experiment of 19.5 GHz into equation (2) we get a step voltage of 40.3  $\mu\text{V}$  according to theory. This is in very close approximation to the measured value of 42.6  $\mu\text{V}$  taken from the graph derived with the picoscope software thus confirming the Josephson-like effect in the sample.

For the micron sized constriction an RF source of frequency 19.6 GHz was applied to the sample with a signal power of -12 dBm (0.0631 mW) at a temperature of 25 K. At these settings, Shapiro-like steps are achieved. The Shapiro-like steps can be seen in figure 177 for the micron-sized constriction. The fact that the sample responded to microwave radiation proves the presence of the Josephson-like effect.

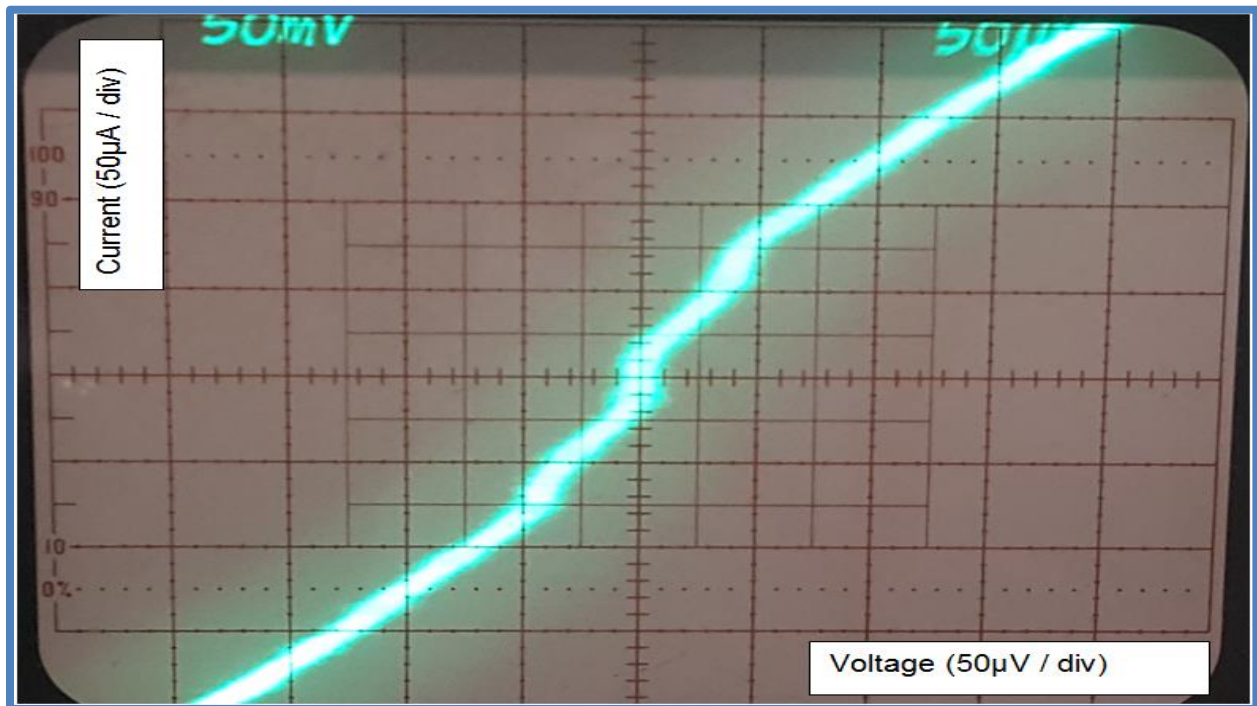


Figure 177 Shapiro-like steps of the micron-size constriction exposed to an RF frequency of 19.573GHz, signal power -12dBm and sample temperature of 25K.

Theoretically using equation (2) for the step voltage and substituting the frequency of 19.6 GHz we get a calculated theoretical value of 40.46  $\mu\text{V}$  for the step voltage. From measurements taken from the Pico scope readings of the Shapiro-like steps for the sample, we get a step voltage value of 39.9  $\mu\text{V}$ . This is very close to the theoretical value for the sample proving once again the presence of the Josephson-like effect in the constriction. For the micron sized constriction the critical step current is measured to be 58.9  $\mu\text{A}$ . This is higher than that for the sub-micron constriction. This is because the micron junction is wider and for a similar current density, the step current should be higher. When we compare the Shapiro-like steps for the two junctions, we see that the micron constriction shows less bending or rounding of the knees on the graph with sharper steps indicating less damage to the constriction due to localized heating from the

laser. Thus the micron constriction behaves like an S-s'-S type junction and the sub-micron constriction behaves like an S-N-S type junction.

### 5.3.4 THE DEPENDENCE OF $I_C$ ON RF POWER

As specified earlier the sub-micron constriction responds positively to the presence of a microwave signal again proving the Josephson-like effect. The microwave signal power is gradually increased from -40 dBm to -14 dBm at a fixed temperature of 8.5 K while the critical current  $I_C$  gets suppressed in a way similar to that in [22] from a value of 102  $\mu\text{A}$  to 4.79  $\mu\text{A}$ . This can be seen in figure 178, which shows the  $I$ - $V$  curves at 8.5 K for different levels of the RF signal power. Shapiro like steps are resolved at an RF signal power of -30 dBm but are not visible on this graph due to the high d.c sweep voltage (from -2 mV to 2 mV). The Shapiro step voltage is only 40  $\mu\text{V}$  hence cannot be seen in this sweep. Normally to see the Shapiro steps, the sweep voltage has to be reduced (say from -200  $\mu\text{V}$  to 200  $\mu\text{V}$ ) and focus on the smaller Shapiro step voltage in this case of only about 40  $\mu\text{V}$ .

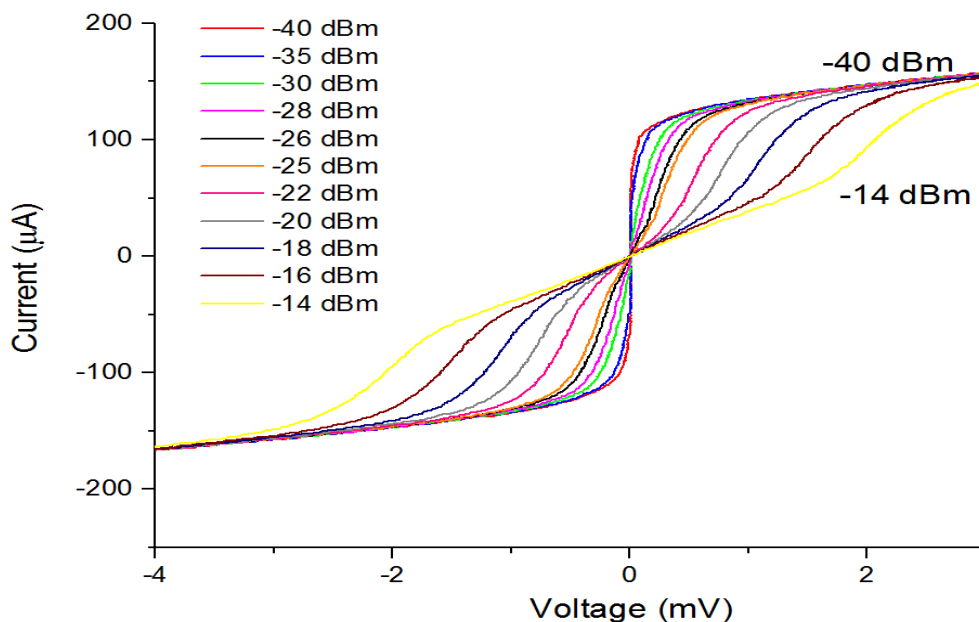


Figure 178 I-V curves at different levels of RF signal power at a temperature of 8.5 K and a frequency of 19.5 GHz for the sub-micron constriction.

The  $I$ - $V$  curves at different levels of RF (radio frequency) power for the micron-sized constriction can be observed in figure 179. A similar result is achieved for the micron-sized constriction with a very similar graph as compared to the sub-micron constriction. The only difference is that the RF signal power is increased from -40 dBm to +5 dBm at a fixed temperature of 6 K in this case. The critical current then suppresses from 720  $\mu$ A to 19  $\mu$ A. For the micron-sized constriction, the RF signal power is increased to a higher power level of +5 dBm as compared to -14 dBm for the sub-micron constriction. The reason being that the micron constriction has a higher d.c critical current (720  $\mu$ A) to suppress than for the sub-micron constriction (102  $\mu$ A) at these cryogenic temperatures (6 K - 8.5 K). No Shapiro-like steps are observed in this range of signal power and at this temperature of 6 K due to the high critical current at this temperature, which requires more critical current suppression. Again, the voltage step produced according to equation (2) is too small to observe Shapiro-like steps in this voltage sweep.

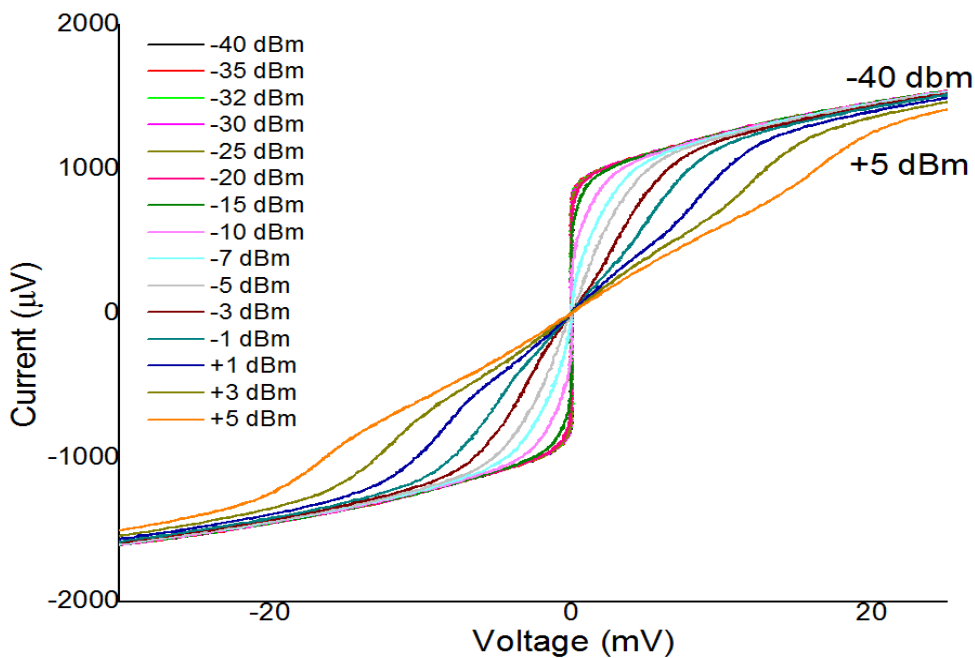


Figure 179  $I$ - $V$  curves at varying levels of RF signal power, temperature of 6 K, RF signal frequency of 19.5 GHz for the micron sized constriction.

### 5.3.5 CURRENT – VOLTAGE CHARACTERISTICS (IVC's) AT VARYING TEMPERATURES AND THE CRITICAL CURRENT - TEMPERATURE DEPENDENCE CURVES.

Figure 180 shows the I-V curves for the sub-micron constriction at different temperatures with the RF power not applied in this case. As the temperature increases the critical current for each (I-V) curve decreases.

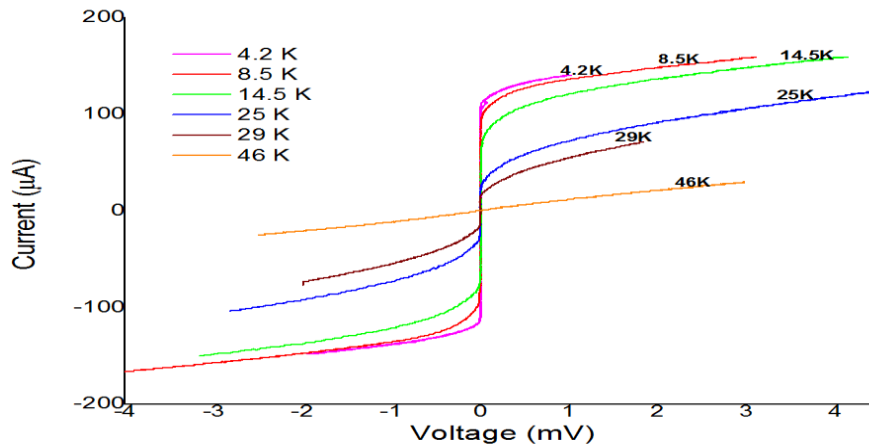


Figure 180 I-V curves for the sub-micron sized constriction at different temperatures.

For the micron sized junction there is a very similar trend as the temperature increases the  $I_c$  decreases. This can be seen in figure 181. The  $I_c$  of the micron constriction is approximately  $\sim 7$  times the  $I_c$  of the sub-micron sized constriction at similar temperatures. For the submicron constriction, the critical current is  $114 \mu\text{A}$  at  $4.2 \text{ K}$  and drops to  $1.5 \mu\text{A}$  at  $46 \text{ K}$  while for the micron constriction the critical current is  $752 \mu\text{A}$  at  $6 \text{ K}$  and drops to  $3.7 \mu\text{A}$  at  $56 \text{ K}$ . The critical current is measured on each I-V curve by using a voltage criterion of using a minimal voltage offset of approximately  $40 \mu\text{V}$ .

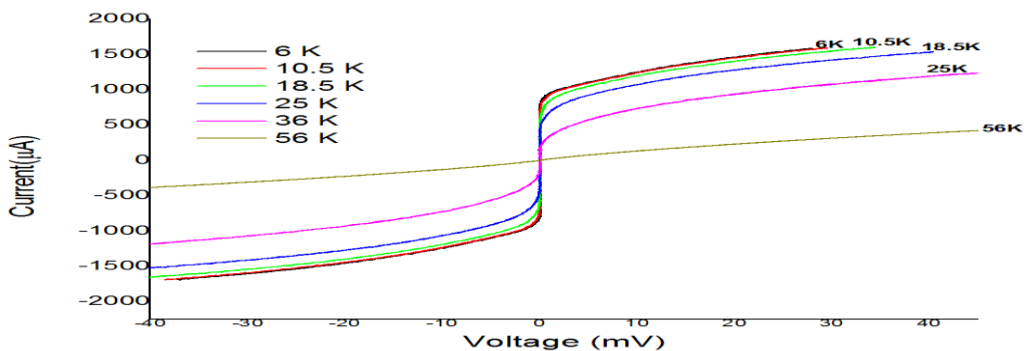


Figure 181 I-V curves for micron sized constriction at different temperatures.

In the plot of  $I_C$  versus  $T/T_{CN}$  for the sub-micron sized constriction shown in figure 182 we get an exponential decay function. This is expected, for a constriction of smaller width. Here  $T_{CN}$  stands for the critical temperature of the YBCO thin film = 87 K which is used to normalize the temperature  $T$  in the plot of the curve. The femtosecond laser ablation tends to heat the constriction, which then changes from the superconductive phase to a normal phase producing the S-N-S type junction, and hence you get an exponential decay fit on the graph. The smaller width junctions tend to show the convex shape on the  $I_C$  versus  $T/T_{CN}$  graph. In the long junction limit the temperature dependence of the critical current is:

$$I_C \propto T^{\frac{3}{2}} \exp\left(-\frac{L}{L_T}\right) \quad (3)$$

As expressed in [11] and within a limited temperature range, this expression is numerically similar to:

$$I_C \propto \exp\left(-\frac{L}{L_T}\right) \quad (4)$$

With  $L_T \propto 1/T$ , where  $T$  is the temperature of the thin film sample and  $L_T$  the junction length, which is expected in the ballistic limit [23, 24]. This leads to an exponential decay function of the type:

$$I_C \propto \exp\left(-\frac{T}{T_0}\right). \quad (5)$$

Where  $T_0$  is a decay constant. Hence the  $I_C$  versus  $T/T_{CN}$  graph in figure 182 for the 816 nm wide sub-micron constriction is an exponential decay function. This function corresponds well with the exponential decay function expected for the S-N-S type junctions [11] in the long ballistic limit. Since this  $I_C$  versus  $T/T_{CN}$  curve is numerically close to an exponential decay fit then we can say the junction is possibly a diffusive S-N-S type junction in the long junction regime.

A junction is defined as long when  $L \gg 10\xi$  [11] where  $\xi$  is the superconducting coherence length (2 nm) for YBCO and small when  $L \ll \xi$ . Because the length of the sub-micron junction is  $10 \mu\text{m}$ , the constriction shows concavity and an exponential decay in the plot of  $I_C$  versus  $T/T_{CN}$ . Therefore the junction can be said to be in the long junction ballistic limit.

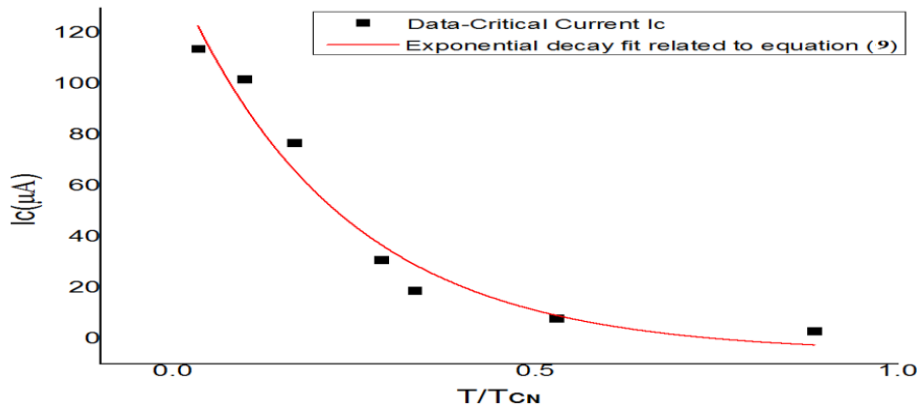


Figure 182  $I_C$  versus  $T/T_{CN}$  plot for the sub-micron constriction. The solid red line is an exponential decay fit to the experimental data (solid squares) obtained for the 816 nm constriction.

For the micron sized constriction the  $I_C$  versus  $T/T_{CN}$  plot in figure 183 shows a linear fit that is consistent with the behaviour of the constriction type junction [11, 25, 26]. This constriction is  $2.1 \mu\text{m}$  wide and not all of the superconductive phase is heated and changed to a normal phase. Some of it remains in the superconductive phase forming more of an S-s'-S type junction.

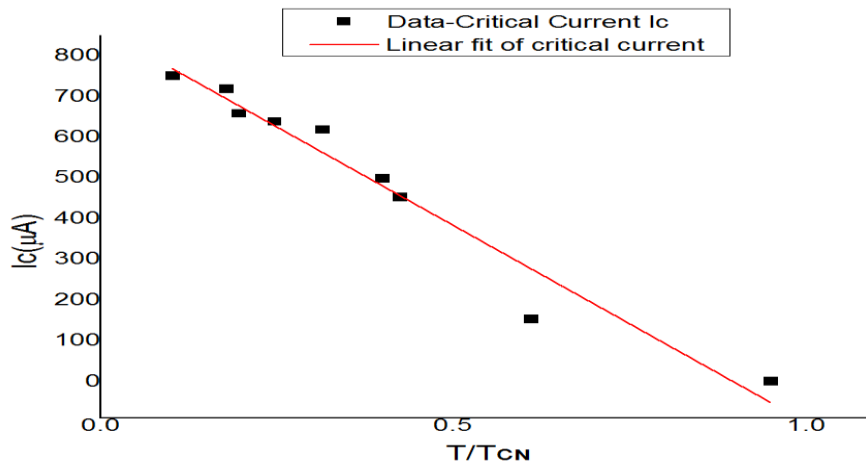


Figure 183  $I_C$  versus  $T/T_{CN}$  plot for the micron sized constriction, the solid line is a linear fit to the experimental data (solid squares) obtained for the  $2.1 \mu\text{m}$  constriction.

### 5.3.6 NORMAL RESISTANCE ( $R_N$ ) Vs TEMPERATURE FOR THE JOSEPHSON JUNCTIONS.

Some results were obtained for the normal resistance of each sample. For the sub-micron, sized constriction the normal resistance shows a more metallic-like resistive behaviour as seen in [21]. The normal resistance increasing exponentially from the lower temperatures to the higher temperatures. At low temperatures its  $7 \Omega$  at  $4.2 \text{ K}$  and then increases to  $42 \Omega$  at higher temperatures ( $77 \text{ K}$ ). At this point, the critical current is very low. This points to the fact that, as the material suffers from local heating it normalizes and becomes more resistive forming an S-N-S type constriction. An exponential fit is used to fit the normal resistance to temperature as can be seen in figure 184. The  $I_C R_N$  product for this junction is  $1.98 \text{ mV}$  at  $8.5 \text{ K}$ .

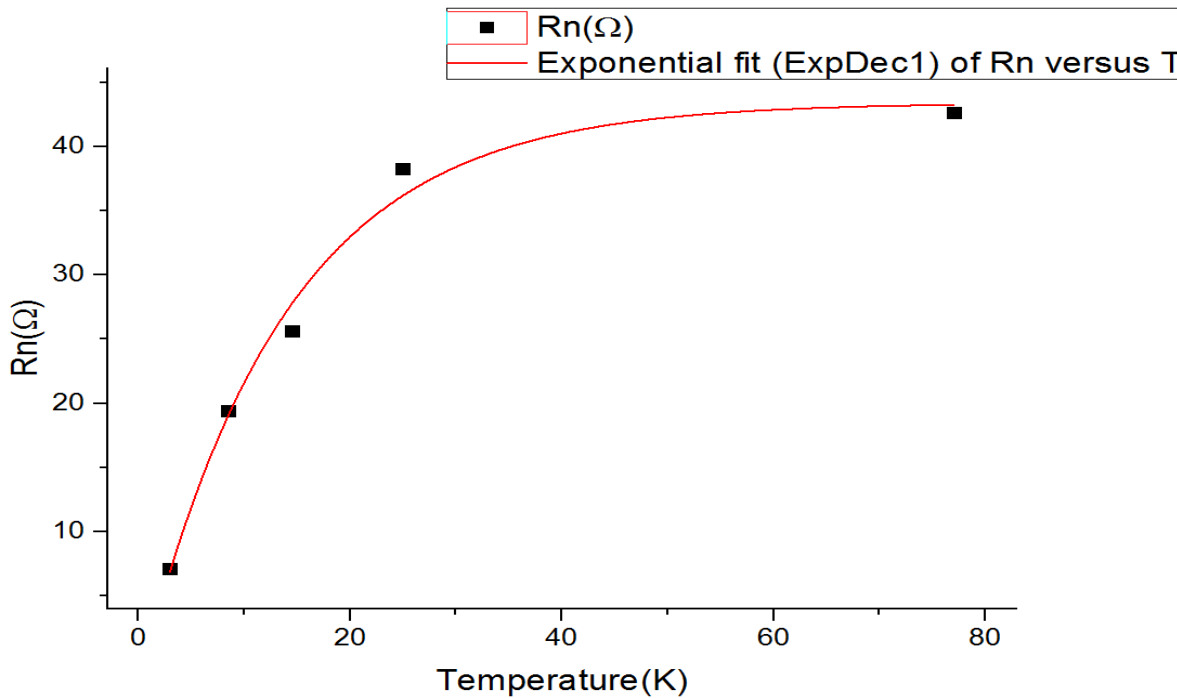


Figure 184 Normal Resistance  $R_n$  Versus temperature for the sub-micron 816 nm constriction.

The micron size constriction shows a slightly different result. Here the normal resistance remains the same with a value of  $17 \Omega$  at the lower temperature range from  $6 \text{ K}$  to  $36 \text{ K}$  and then increases exponentially at a higher temperature. This is similar to what is observed in [20], which is a step-edge junction. The micron sized constriction behaves like an S-s'-S type constriction because the resistance remains constant in the lower temperature range and then increases exponentially at a higher temperature. The graph

in figure 185 shows close similarity to the data sheet curve of a superconductive material, hence the S-s'-S nature. The  $I_C R_N$  product for the micron junction is 13.1 mV at a temperature of 6 K.

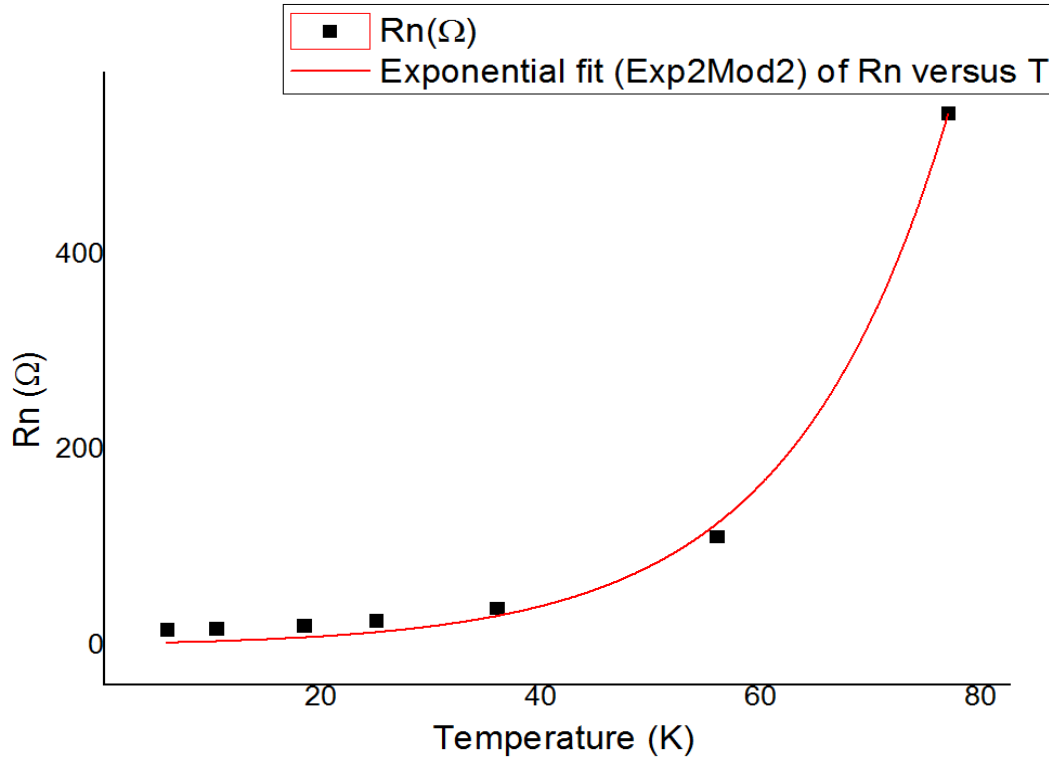


Figure 185 Normal Resistance  $R_n$  Versus Temperature for the micron 2.1  $\mu\text{m}$  constriction.

### 5.3.7 $I_C R_N$ PRODUCT VS TEMPERATURE FOR THE JOSEPHSON JUNCTIONS.

Having considered the Normal resistance  $R_N$  Vs temperature for each Josephson junction it becomes necessary to look at the  $I_C R_N$  product trend against temperature for each junction. For the micron sized junction 2.1  $\mu\text{m}$  the  $I_C R_N$  product starts at 13.1 mV at a temperature of 6 K and then drops to as low as 0.22 mV at a temperature of 56 K. The reason for this is that even though the normal resistance for the junction increases from low to high temperature, the critical current  $I_C$  is decreasing very fast linearly. Therefore, the  $I_C R_N$  product decreases following the trajectory of the critical current. This trend can be observed in figure 186.

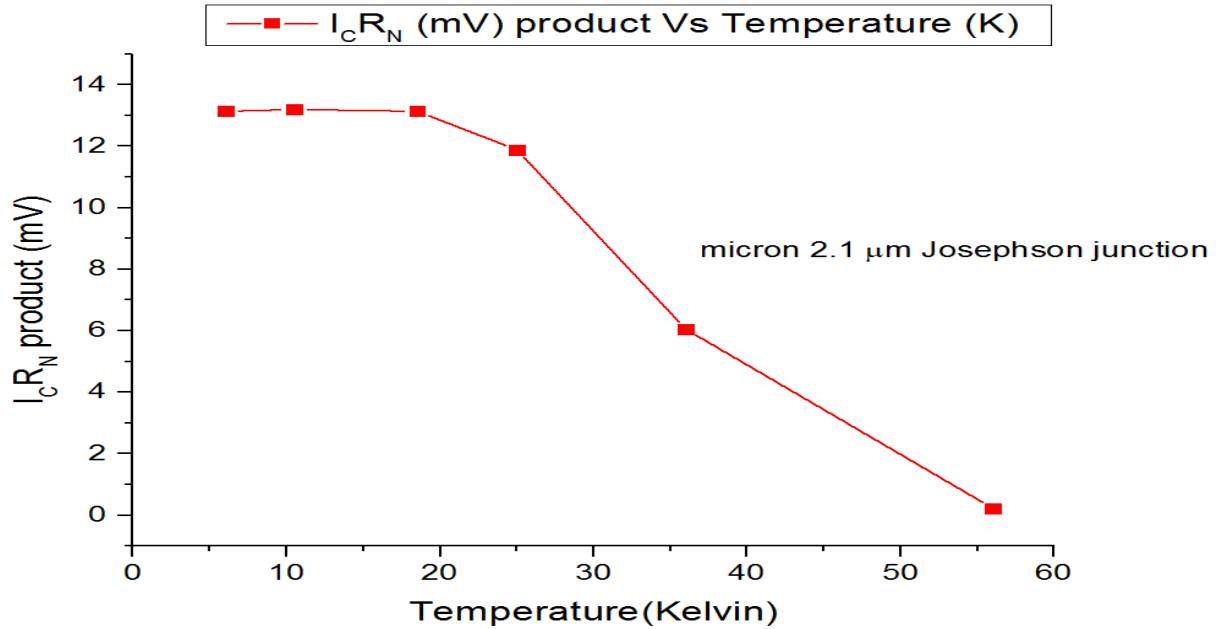


Figure 186 The  $I_C R_N$  product curve for the micron  $2.1 \mu\text{m}$  Josephson junction.

For the sub-micron sized junction  $816 \text{ nm}$  the  $I_C R_N$  product begins at  $1.983 \text{ mV}$  at a temperature of  $8.5 \text{ K}$  and drops to  $0.128 \text{ mV}$  at a temperature of  $77 \text{ K}$ . Again, although the normal resistance  $R_N$  for the sub-micron junction increases exponentially as in the previous section, the critical current  $I_C$  decreases exponentially. Hence, the  $I_C R_N$  product decreases with temperature following the trend of the critical current  $I_C$ . This can be observed in figure 187.

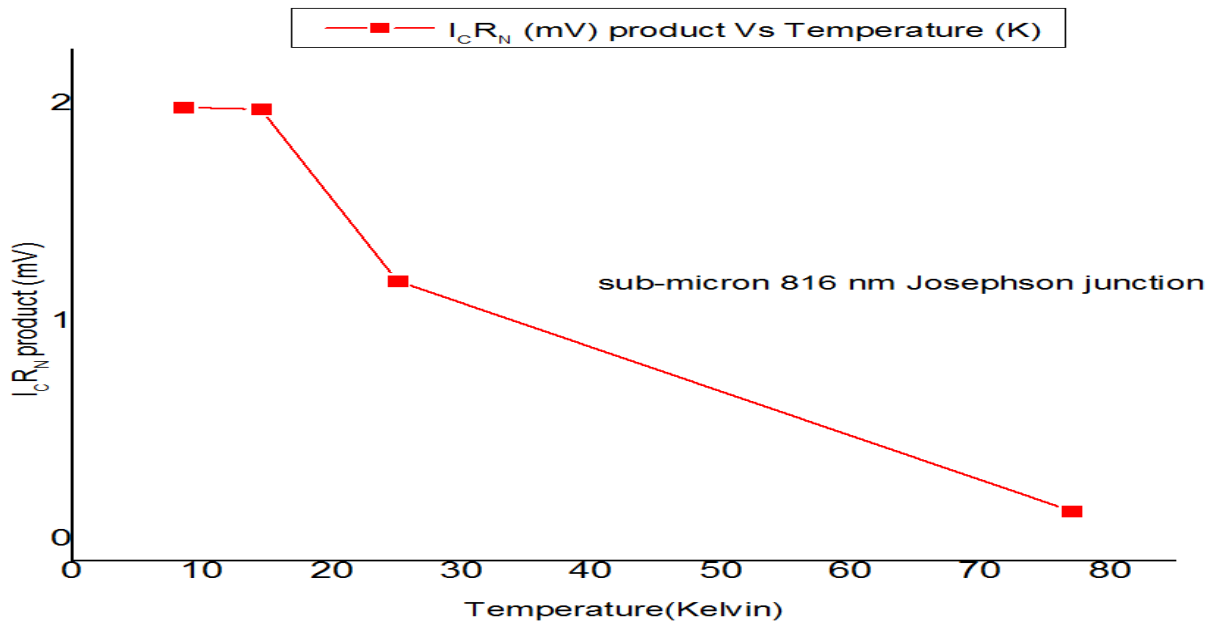


Figure 187  $I_C R_N$  product curve for the micron  $2.1 \mu\text{m}$  Josephson junction.

## 5.4 CONCLUSION

We fabricated sub-micron and micron sized constrictions that show a Josephson-like effect on YBCO thin films by using the femtosecond laser etching technique. The constriction widths were determined by using the AFM and then verified with the SEM microscope. The fabricated constrictions were tested for the Josephson-like Effect by showing the d.c ( $I$ - $V$ ) characteristics and the a.c Shapiro-like steps. The Shapiro-like steps observed confirmed the presence of the Josephson-like effect in these samples. The critical current dependence on temperature for the two samples was quite different. The micron-sized constriction showed a linear dependence of critical current versus temperature which points to the constriction type junction. The sub-micron sized constriction shows an exponential decay type behaviour which points to localized heating from the laser which changes the material from the superconductive phase to a normal phase producing the S-N-S type constriction in the long junction ballistic limit as seen in [23, 24]. The normal resistance versus temperature characteristic was shown for both samples and some similarities were observed. For both the sub-micron and micron sized constrictions the normal resistance is low at low temperatures and then increases at higher temperatures. This is because of the damage to the material from local laser heating. This makes the materials more resistive at higher temperatures and reduces the critical current at higher temperatures close to the critical temperature. However, for the micron-sized constriction at lower temperatures the normal resistance remains constant for a certain temperature range proving S-s'-S type behaviour while the sub-micron sized constriction shows a sharp exponential increase in the normal resistance from low temperature to high temperature proving metallic normalized material behaviour (S-N-S). Finally, the  $I_C R_N$  product trend against temperature is shown for both the micron and sub-micron sized junctions.

## 5.5 REFERENCES

1. L. Hao, D. C. Cox, and J. C. Gallop, "Characteristics of focused ion beam Nano scale Josephson's devices", *Supercond. Sci. Technol.*, **22**, 064011, (2009), doi:10.1088/0953-2048/22/6/064011.
2. H.-Y. Zhai, Q. Y. Chem, X. W. Xu, M. Strikovski, J. Miller, and W. K. Chu, "Planar SNS Josephson junctions using FIB processing of c-oriented YBCO thin films", *Physica C*, **341–348**(part 3), 1587-1588, (2000), doi:10.1016/S0921-4534(00)01434-9.
3. H. W. Seo, Q. Y. Chen, C. Wang, W. K. Chu, T. M. Chang, S. F. Lee, and Y. Liou, "Planar Josephson Junctions fabricated by focused-ion beam", *Int. J. Mod. Phys. B*, **15**(24 & 25), 3359-3360, (2001).
4. S.-G. Lee, S.-H. Oh, C. S. Kang, and S.-J. Kim, "Superconducting Nano bridge made from YBCO film by using focused ion beam", *Physica C: Superconductivity*, **460–462**(Part 2), 1468-1469, (2007), doi:10.1016/j.physc.2007.04.155.
5. J. Schneider, H. Kohlstedt, and R. Wordenweber, "Nano bridges of optimized YBCO thin films for superconducting flux-flow type devices", *Appl. Phys. Lett.*, **63**, 2426 (1993), <http://dx.doi.org/10.1063/1.110496>.
6. G. Papari, F. Carillo, D. Born, L. Bartoloni, E. Gambale, D. Stornaiuolo, P. Pinguet, F. Beltram, and F. Tafuri, "YBCO Nano bridges: Simplified Fabrication Process by Using a Ti Hard Mask", *IEEE Trans. Appl. Supercond.*, **19**(3), 183-186, (2009), doi:10.1109/TASC.2009.2019023.
7. K. Kajino, T. Kimura, Y. Horii, M. Watanabe, M. Inoue, and A. Fujimaki, "Preparation of Narrowed YBCO Nano bridges Down to 30nm with Reduced Degradation", *IEEE Trans. Appl. Supercond.*, **19**(3), 178-182, (2009), doi:10.1109/TASC.2009.2018189.
8. J. R. Wendt, J. S. Marteins, C. I. H. Ashby, T. A. Plut, V. M. Hietala, C. P. Tigges, and D. S. Ginley, "YBCO Nano bridges fabricated by direct-write electron beam lithography", *Appl. Phys. Lett.*, **61**, 1597, (1992), <http://dx.doi.org/10.1063/1.107508>.
9. D. Stornaiuolo, K. Cedergren, G. Rotoli, D. Born, T. Bauch, A. Barone, F. Lombardi, and F. Tafuri, "Fabrication and properties of sub-micrometric YBCO biepitaxial

- junctions”, *Phys.: Conf. Ser.*, **150**, 052246, (2009), doi:1088/1742-6596/150/5/052246.
10. D. Stornaiuolo, K. Cedergren, G. Rotoli, D. Born, T. Bauch, A. Barone, F. Lombardi, and F. Tafuri, “Sub-Micron YBCO Biepitaxial Junctions”, *IEEE Trans. Appl. Supercond.*, **19**(3), 174-177, (2009), doi:101109/TAC.2009.2018546.
  11. U Buttner, G L Hardie, R Rossouw, V V Srinivasu and W J Perold, “Fabrication of submicron YBCO Josephson junctions by sample mosaic navigation assisted laser etching process”, *Superconductor Science and Technology*, **20**, S426-S429, (2007), doi:10.1088/0953-2048/20/11/S24.
  12. A. A. O Elkaseh, W.J Perold, and V.V Srinivasu, “Josephson nanoconstrictions made by AFM plowing of  $\text{YBa}_2\text{Cu}_3\text{O}_{7-x}$  films”, *Journal of Applied Physics*, 108,053914, (2010), <http://dx.doi.org/10.1063/1/3481425>.
  13. V. Bouchiat, “Detection of magnetic moments using a Nano-SQUID: limits of resolution and sensitivity in near-field SQUID magnetometry”, *Supercond. Sci. Technol.*, **22**, 064002 (2009), doi:10.1088/0953-2048/22/064002.
  14. M. A. Nielsen and I. L. Chuang, *Quantum Computation and Quantum Information*, 10<sup>th</sup> Anniversary Edition, Cambridge University Press, Cambridge, (2000).
  15. S. Corlevi, *Quantum effects in nanoscale Josephson junction circuits*, Ph.D. thesis, AlbaNova Universitet, (2006).
  16. F. K. Wilhelm and K. Semba, *Physical Realization of Quantum Computing: “Are the DiVincenzo criteria fulfilled”*, edited by N. Bajagaram, S. Kanemitsu, Mikio Nakahara, May 2004.
  17. C. P. Foley and H. Hilgenkamp, “Why Nano Squids are important: an introduction to the focus issue”, *Supercond. Sci. Technol.*, **22**, 064001, (2009), doi:10.1088/0022-3727/43/47/474004.
  18. D. L. Tilbrook, “Nano SQUID sensitivity for isolated dipoles and small spin populations”, *Supercond. Sci. Technol.*, **22**, 064003, (2009), doi: 10:1088/0953-2048/22/6/064003.
  19. W. Wernsdorfer, “From micro- to nano-SQUIDs: applications to Nano magnetism”, *Supercond. Sci. Technol.*, **22**, 064013, (2009), doi:10.1088/0953-2048/22/6/064013.

20. WF van Staden, U Buttner, V V Srinivasu and WJ Perold, "A novel buffered high- $T_C$  superconducting step-edge Josephson junction", *Supercond. Sci. Technol.*, 20, (2007), S419-S425.
21. V V Srinivasu, W J perold, "Observation of Shapiro-Steps in AFM-Plough micron-Size YBCO Planar Constrictions", *IEEE Transactions on Applied Superconductivity*, 20, No. 3, 2009.
22. J. Du, T. Zhang, Y.J. Guo, and X.W Sun, "A high-temperature superconducting monolithic microwave integrated Josephson down-converter with high conversion efficiency", *Applied Physics letters*, 102, (2013), 212602.
23. Heida J P 1998 Josephson currents in two dimensional mesoscopic ballistic conductors PhD Thesis University of Groningen, Groningen, The Netherlands.
24. Wilhelm F K, Zaikin A D and Schon G, "Supercurrent in a mesoscopic proximity wire", 1997, *J. Low Temp. Phys.* 106, 305.
25. Sobolewski R, Xiong W, Kula W and Gavaler J R 1994 *Appl. Phys. Lett.* **64** 643.
26. Irmer B, Blick R H, Simmel F, Godel W, Lorenz H and Kotthaus J P 1998 *Appl. Phys. Lett.* **73** 2051.

# CHAPTER 6

## THE EFFECT OF RF RADIATION ON THE CRITICAL CURRENT OF CONstrictIONS FABRICATED USING THE FEMTOSECOND LASER TECHNIQUE.

In this chapter we discuss the influence of an RF signal of frequency 19.5 GHz on the critical current of a micron sized Josephson junction of width 2.1  $\mu\text{m}$  and a sub-micron sized Josephson junction of width 816 nm. Both junctions showed the presence of Shapiro-like steps as observed in the previous chapter and critical current suppression due to an increase in the RF Power. The micron sized junction showed Shapiro steps at the following specifications, RF frequency 19.5 GHz, RF power level at -12 dBm and temperature at 25 K. The sub-micron sized junction showed Shapiro steps with the RF frequency at 19.5 GHz, the RF power level at -30 dBm and temperature at 8.5 K. When the critical current  $I_c$  is plotted versus RF power then the critical current shows a gradual decrease as the RF power is increased following the Bessel function behaviour, which proves the a.c Josephson effect in these samples. Critical current suppression occurs due to the varying magnetic field produced by the RF signal power. This varying magnetic field couples with the junction inducing an a.c current into it and reducing the value of the d.c critical current flowing through it, which causes critical current suppression [1]. In my case, for the micron sized junction the unsuppressed critical current when the RF power is off is 779.85  $\mu\text{A}$  at a temperature of 6 K, while for the sub-micron sized junction the unsuppressed critical current when the RF power is off is 102.1  $\mu\text{A}$  at a temperature of 8.5 K. In the power dependence plot of the normalized critical current  $I_{cN}$  ( $I_c/I_{c_{off}}$ ) at the first Shapiro step  $n = 0$ , the narrower sub-micron junction reaches the first minima before the wider micron junction validating the Josephson Effect [2]. Finally, the narrow junction shows sharp cusps in the first minima proving the presence of the diffusive S-N-S type Josephson junction as stated in [3] while the wide junction shows smooth minima which proves the presence of the S-s'-S or constriction type Josephson junction.

## 6.1 EXPERIMENTAL

The Josephson junctions on which the RF tests were done were fabricated using the femtosecond laser technique. The femtosecond laser was used as a lithography tool to cut “S”-shaped constrictions on the YBCO superconducting thin films based on LAO or MgO substrates. The resulting constrictions were patterned with 4-point gold contacts to facilitate  $I$ - $V$  measurements. This has all been described in previous chapters. The RF power signal of frequency of 19.5 GHz was introduced on one of the 4-point gold contacts as previously shown in figure 166 from chapter 5. For  $I$ - $V$  measurements, d.c current is passed through the sample across two of the gold point contacts, with a slight frequency of 8–10 Hz added to the signal (that is an almost d.c signal with a slight a.c signal superimposed). Then the resulting d.c voltage is measured across the sample from the other two of the gold point contacts as shown in figure 166. This is done at same time as the RF signal is superimposed on the sample. The result being a plot of the  $I$ - $V$  curve with the RF power superimposed on the sample at the same time. The reason for superimposing a low frequency signal of (8-10 Hz) on the d.c current passed through the sample is because, this low frequency signal facilitates the RF signal of high frequency to pass through the sample without melting the sample. The sample could melt due to the electronic friction imposed by the high frequency (19.5 GHz) RF signal.

## 6.2 RESULTS

### 6.2.1 THE CRITICAL CURRENT VS RF POWER CURVE FOR THE MICRON SIZED JOSEPHSON JUNCTION.

For the micron sized Josephson junction,  $I$ - $V$ C's curves where plotted at different RF power levels as previously shown in figure 179 from chapter 5. The RF power level was varied on the  $I$ - $V$ C's at a fixed temperature of 6 K. The RF power was increased from -40 dBm (0.0001 mW) to +5 dBm (3.16 mW) while the critical current reduced from 774.2  $\mu$ A to 2.26  $\mu$ A. The critical current is measured at a voltage offset of 70.7  $\mu$ V for each  $I$ - $V$ C's

curve. This graph proves that a Josephson junction was produced because the critical current responds to the presence of an RF signal by getting suppressed [1].

At each specific power, level of the RF signal the critical current was measured then normalized. The normalized critical current  $I_{CN}$  is obtained by dividing the critical current  $I_C$  at a specific RF power level by the critical current  $I_{C(off)}$ , that is the critical current value when the RF power is switched (off) or when the critical current is unsuppressed. The value of  $I_{C(off)}$  in this case is 779.9  $\mu\text{A}$ . Subsequently a plot of the normalized critical current  $I_{CN}$  Vs the RF power was derived as shown in figure 188. For the sake of the completion of the plot in figure 188, it is estimated that the RF power is switched (off) when the power setting is about -50 dBm or more. The graph shows that when the power level of the RF signal is increased the critical current measured decreases at a specific temperature.

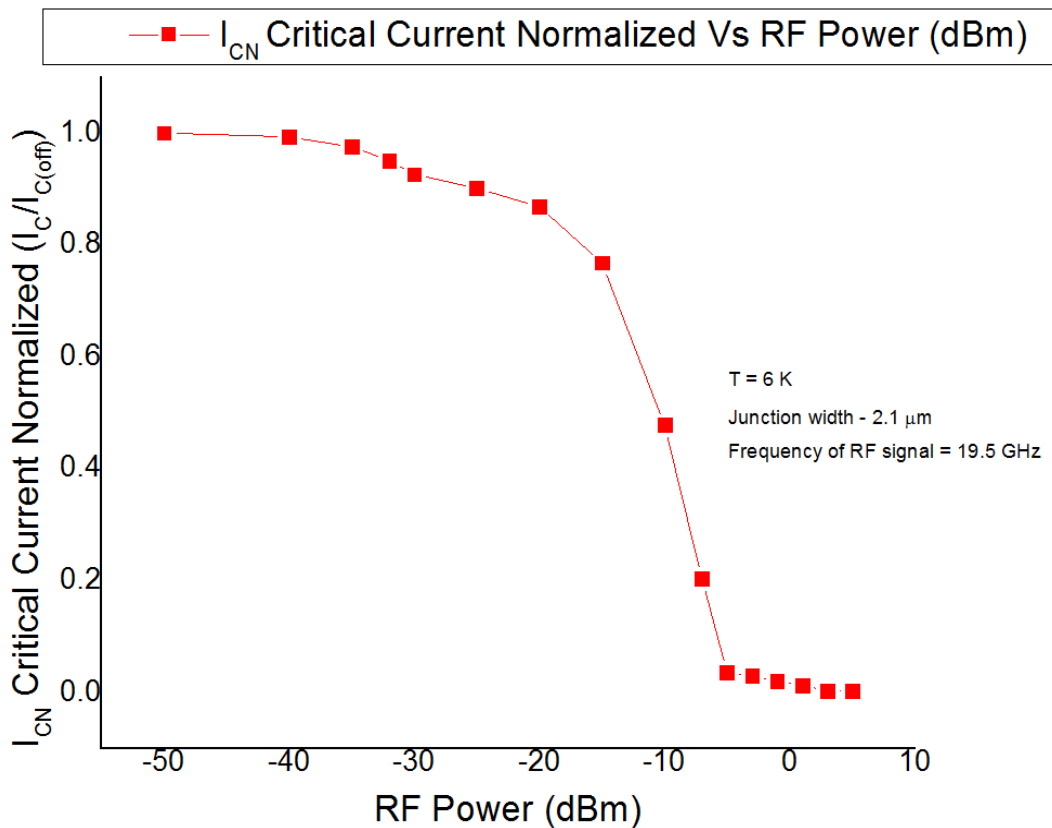


Figure 188 Power dependence of the normalized critical current  $I_{CN}$  at the first shapiro step  $n=0$ , for the Josephson junction 2.1  $\mu\text{m}$  wide, temperature 6 K and signal frequency 19.5 GHz.

## 6.2.2 THE CRITICAL CURRENT VS RF POWER CURVE FOR THE SUB-MICRON SIZED JOSEPHSON JUNCTION.

The sub-micron sized Josephson junction showed the  $I$ - $V$ C's curves seen in figure 178 from chapter 5 when the RF signal was applied to the sample with varying RF power levels. The RF power was varied on the  $I$ - $V$ C's of the sub-micron junction at a fixed temperature of 8.5 K. The RF power was increased from -40 dBm (0.0001 mW) to -14 dBm (0.0398 mW) while the critical current suppressed from 86.96  $\mu$ A to 2.26  $\mu$ A. The critical current was measured at a voltage offset of 54.2  $\mu$ V for each  $I$ - $V$ C's curve in figure 178. The fact that the sample responds to the presence of an RF signal, with the critical current being suppressed [1], when the RF power is increased proves that a Josephson junction is formed.

For the sub-micron junction at each specific power level of the RF signal the critical current is measured then normalized. The normalized critical current is referred to as  $I_{CN}$  and is obtained by dividing the critical current  $I_C$  at a specific RF power level by the critical current  $I_{C(off)}$ . This is the critical current value when the RF power is switched (off) or when the critical current is unsuppressed. The value of  $I_{C(off)}$  in this case is 102.1  $\mu$ A. A plot of the normalized critical current  $I_{CN}$  Vs the RF power is obtained for the sub-micron junction as seen in figure 189. For the sake of the completion of the plot in figure 189, it is estimated that the RF power is switched (off) when the power setting is about -50 dBm or more. The graph shows that when the power level of the RF signal is increased the critical current measured decreases at a specific temperature.

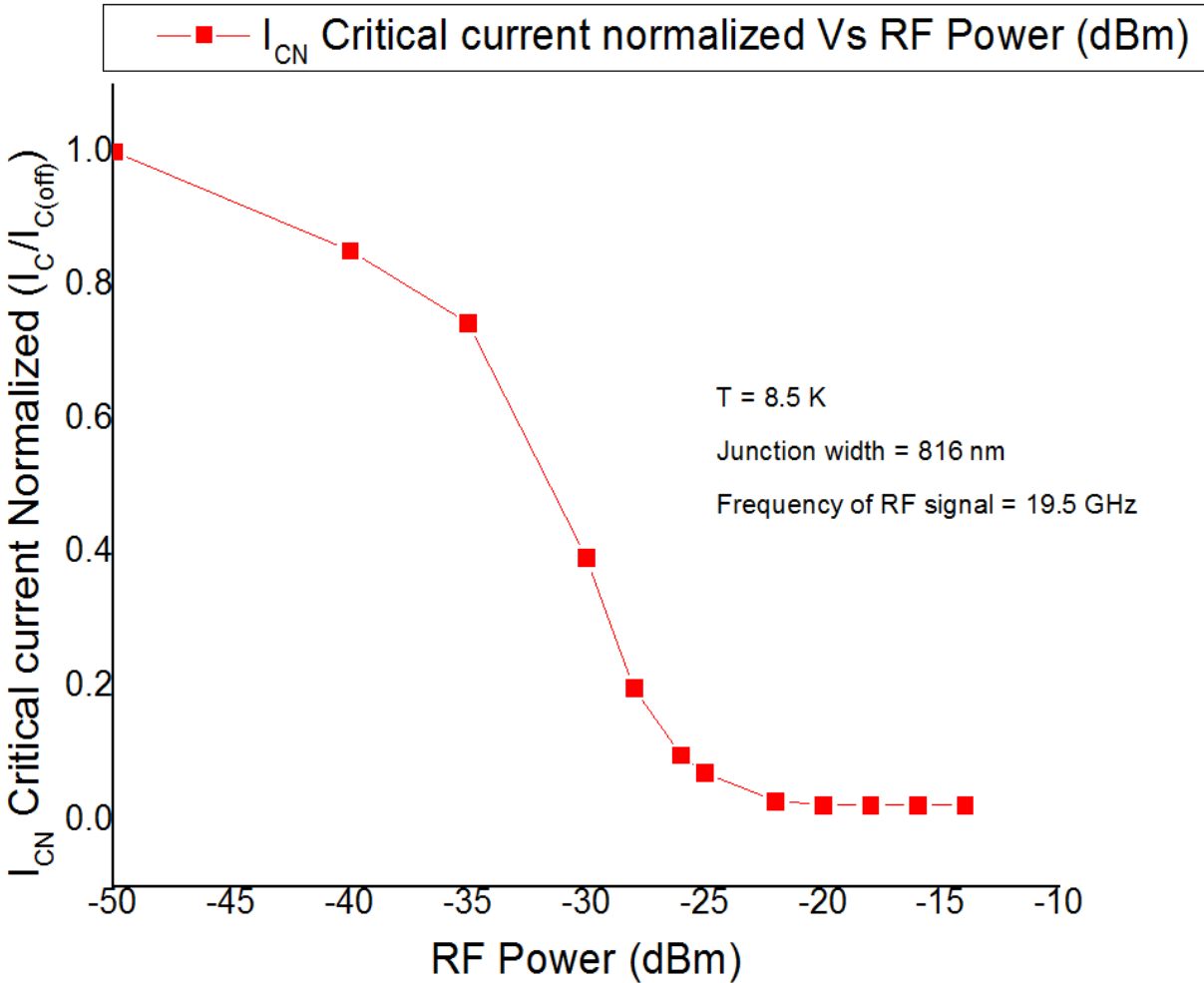


Figure 189 RF power dependence of the normalized critical current  $I_{CN}$  at the first shapiro step  $n=0$ , for the Josephson junction 816 nm wide, temperature 8.5 K and signal frequency 19.5 GHz.

### 6.2.3 PROOF OF THE A.C JOSEPHSON EFFECT IN THESE SAMPLES USING THE RF RADIATION.

The RF power dependence of the normalized critical current  $I_{CN}$  for the two samples are plotted in Fig.190. The normalized critical current  $I_{CN}$  is obtained by dividing the critical  $I_C$  at a specific RF power level by the critical current value when the RF power is switched off at a specific temperature  $I_{C(off)}$ . The critical current  $I_C$  is measured from the  $I - VC$ 's (Current – Voltage characteristic curves) at each specific RF power level at a voltage offset of approximately 50  $\mu$ V. Subsequently the normalized critical current is plotted against the RF power levels, and this process is repeated for the two junctions. The RF

power dependence curve in contrast to the fraunhofer pattern follows the Bessel function behaviour [2, 4]. Normalized critical current along with Bessel function fits are shown in figure 190 for the 816 nm and 2.1  $\mu\text{m}$  wide constrictions. According to [2,4] when the RF power dependence curves for the two junctions are superimposed on the same graph then the narrower junction, in this case the submicron sized junction which is 816 nm wide will reach its first minimum before the wider micron 2.1  $\mu\text{m}$  sized junction as can be seen in figure 190. This is an alternate proof of the Josephson Effect. The effect of microwaves on Josephson Currents in Superconducting Tunneling has been well described by Shapiro et al [4] in terms of Bessel function,  $J_n\left(\frac{2ev}{hf}\right)$  where  $v$  is the amplitude of RF voltage generated across the tunnelling sample. However  $v$  now depends on the junction dimensions length and width. For a smaller width junction, the decay of the supercurrent is more faster as expected.

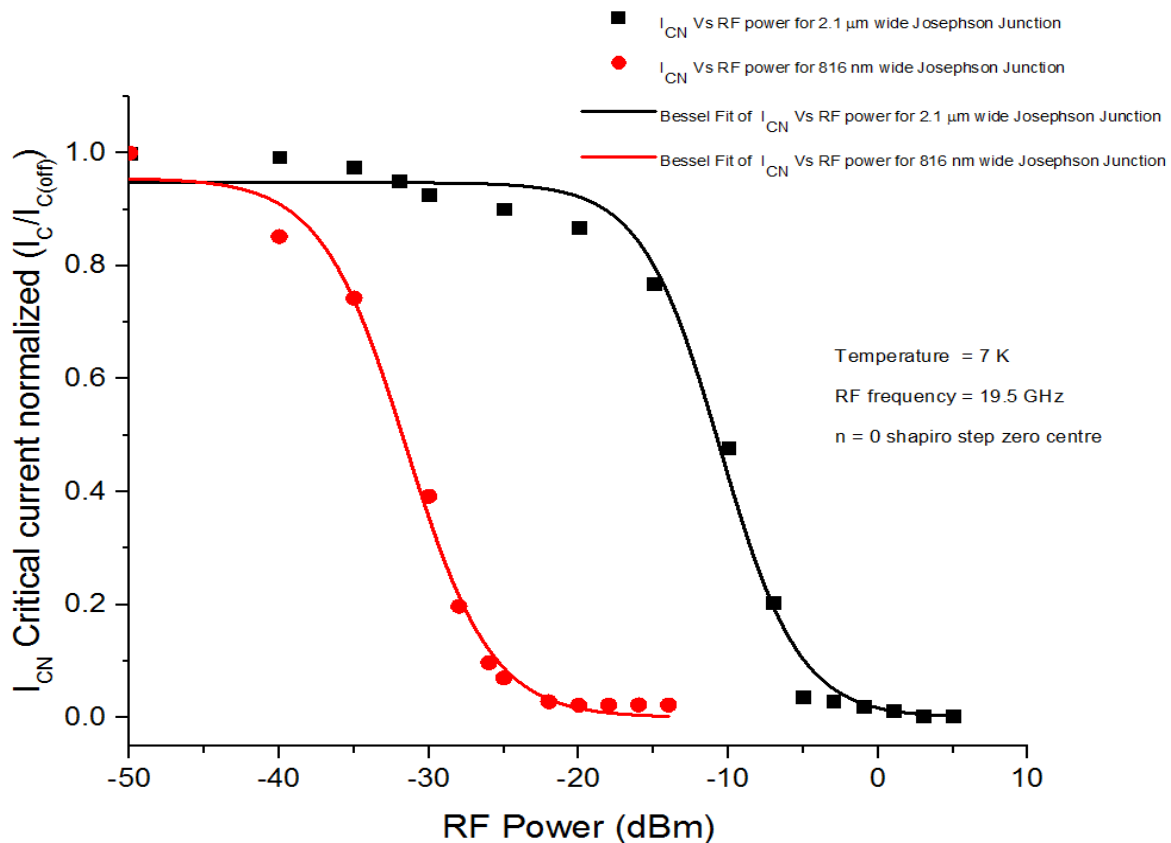


Figure 190 Power dependence of the normalized Critical Current  $I_{CN}$  for the first shapiro step  $n = 0$ , for the two Josephson junctions 816 nm and 2.1  $\mu\text{m}$  at a temperature of 7 K and signal frequency 19.5 GHz.

With further analysis of the curves in figure 190, we notice that the narrow 816 nm sub-micron junction has sharp cusps [4] in the minima trajectory which indicates the presence of a diffusive S-**N**-S type junction while the wide 2.1  $\mu\text{m}$  micron junction has a smooth transiting minimum which indicates the presence of a S-**s'**-S constriction type junction.

### 6.3 CONCLUSION

In conclusion two Josephson junctions were successfully fabricated, the first a micron sized junction and the second a sub-micron sized junction using the femtosecond laser technique. Both junctions responded to the presence of an RF power signal showing Shapiro steps and critical current suppression when the RF power level is increased which proves the a.c Josephson effect. When the normalized critical current is plotted against RF power for both junctions on the same axis, the curves fit the expected Bessel function. These curves show two minima with the narrow junction arriving at the first minimum before the wide junction, which again confirms the a.c Josephson Effect. The normalized critical current Vs RF power for the narrow junction has sharp (cusps) transitions in the minima proving the presence of the diffusive S-**N**-S type Josephson junction [3] while the normalized critical current Vs RF power graph for the wider junction shows smooth transiting minima proving an S-**s'**-S constriction type Josephson junction.

## 6.4 REFERENCES

1. J. Du, T. Zhang, Y.J. Guo, and X.W Sun, "A high-temperature superconducting monolithic microwave integrated Josephson down-converter with high conversion efficiency", *Applied Physics letters*, 102, (2013), 212602.
2. M. Veldhorst, M. Snelder, M. Hoek, T. Gang, V. K. Guduru, X. L.Wang, U. Zeitler, W. G. van derWiel, A. A. Golubov, H. Hilgenkamp, and A. Brinkman, "Josephson supercurrent through a topological insulator surface state", *nature material letters*, 11, 417-421, (2012).
3. Barzykin, V. & Zagoskin, A. M. Coherent transport and nonlocality in mesoscopic SNS junctions: Anomalous magnetic interference patterns. *Super lattices. Microstructures.* 25, Issues (5-6), pages 797-807, (1999).
4. S Shapiro, A R. Janus, and S Holly, *Rev. Mod. Phys.* 36, 223,(1964).

# CHAPTER 7

## SUPERCONDUCTIVE BRIDGES THAT DID NOT SHOW THE JOSEPHSON EFFECT; LIMITATIONS.

In this chapter, we discuss the constrictions fabricated with the femtosecond laser technique that show a measurable superconductive critical current flowing through them but do not show the a.c Josephson-like effect. I-V characteristics were used to determine the critical current  $I_C$  of the constrictions at 77 K. The width of the constrictions was determined at the narrowest point using SEM (Scanning electron microscope). Three micron sized constrictions were tested in this chapter with the following widths; 2.88  $\mu\text{m}$ , 1.72  $\mu\text{m}$ , and 1.69  $\mu\text{m}$  and lengths of approximately 5  $\mu\text{m}$ . Based on the width and length of these constrictions in relation to the coherent length ( $\xi$ ) of the YBCO it was determined that these constrictions should geometrically conduct supercurrent by Abrikosov vortices and hence show the Josephson-like effect. The SEM images of these samples show that the femtosecond laser heats the samples beyond the geometric boundary [1], damaging the superconductive phase of the YBCO constrictions partially. The partial heat damage causes inhomogeneities on the constriction material, leading to the pinning of the coherent motion of the Abrikosov vortices. This prevents the a.c Josephson-like effect from being observed on the samples. However, there is still “superconductive patches” inside the constriction which give rise to a measurable critical current probably produced by one-dimensional de-pairing effects since these junction are quiet long. Before delving into superconductive bridges that do not show the Josephson effect, i first described what the I-V characteristics of a superconductive, resistive and an open constriction would look like, using a (659.5 nm) sub-micron, (1.49  $\mu\text{m}$ ) micron and a (1.36  $\mu\text{m}$ ) micron sample respectively in the following sections.

## **7.1 CURRENT – VOLTAGE CHARACTERISTICS OF ELECTRONICALLY SUPERCONDUCTIVE, RESISTIVE AND OPEN CONSTRICTIONS.**

The current-voltage characteristics are used to determine the electronic nature of the constriction. From analysis of the I-V characteristics of a constriction, it can be categorised as either superconductive, resistive or open. A constriction that is superconductive but does not show the Josephson Effect is referred to as a bridge and a constriction, which is both superconductive and shows the Josephson Effect, is referred to as a junction. A constriction, which is having a high resistance, is referred to as resistive and one that is clipped can be said to be open.

### **7.1.1 SUPERCONDUCTIVE CONSTRICTION**

#### **7.1.1.1 SUB-MICRON BRIDGE (659.5 nm)**

The I-V curve in figure 191 shows the I-V characteristics of a superconductive constriction. In the centre of the curve where the voltage offset is approximately null, the constriction is superconductive. Slightly offset from the null voltage centre the constriction is no longer superconductive but becomes normal and has a resistance along each point on the curve. The normal resistance of the constriction can be measured at the end of the voltage sweep when the normal resistance has stabilized and remains constant for the specific temperature of 77 K at which the measurement was made.

The sub-micron bridge fabricated has a width of 659.5 nm, which is determined from the SEM image of the constriction in figure 192. The I-V curve in figure 191 shows the critical current of the constriction to be 9.26 mA. For a constriction of sub-micron, size such as 695 nm this current is quiet high. This leads us to believe that the localized heating effects of the laser did not damage most of the crystalline nature of the constriction. That is the geometric width of the constriction and the superconductive phase are the same and most of the superconductive phase conducts this current.

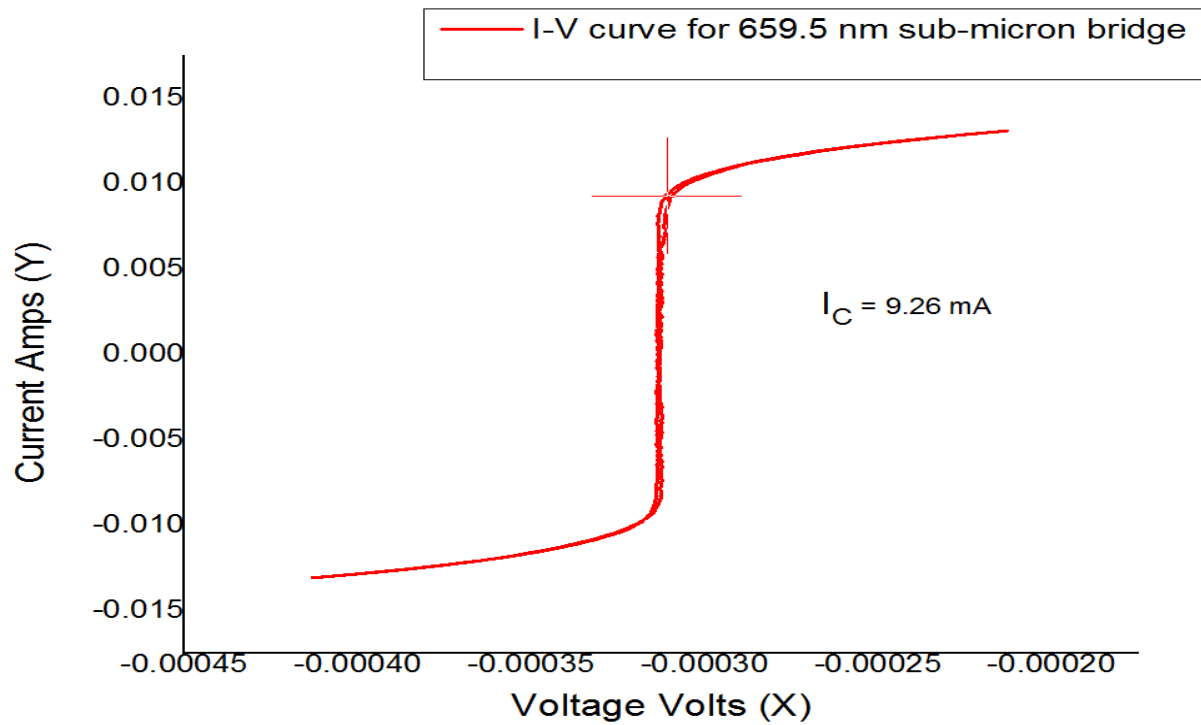


Figure 191 I-V characteristic of the superconductive sub-micron bridge (659 nm).

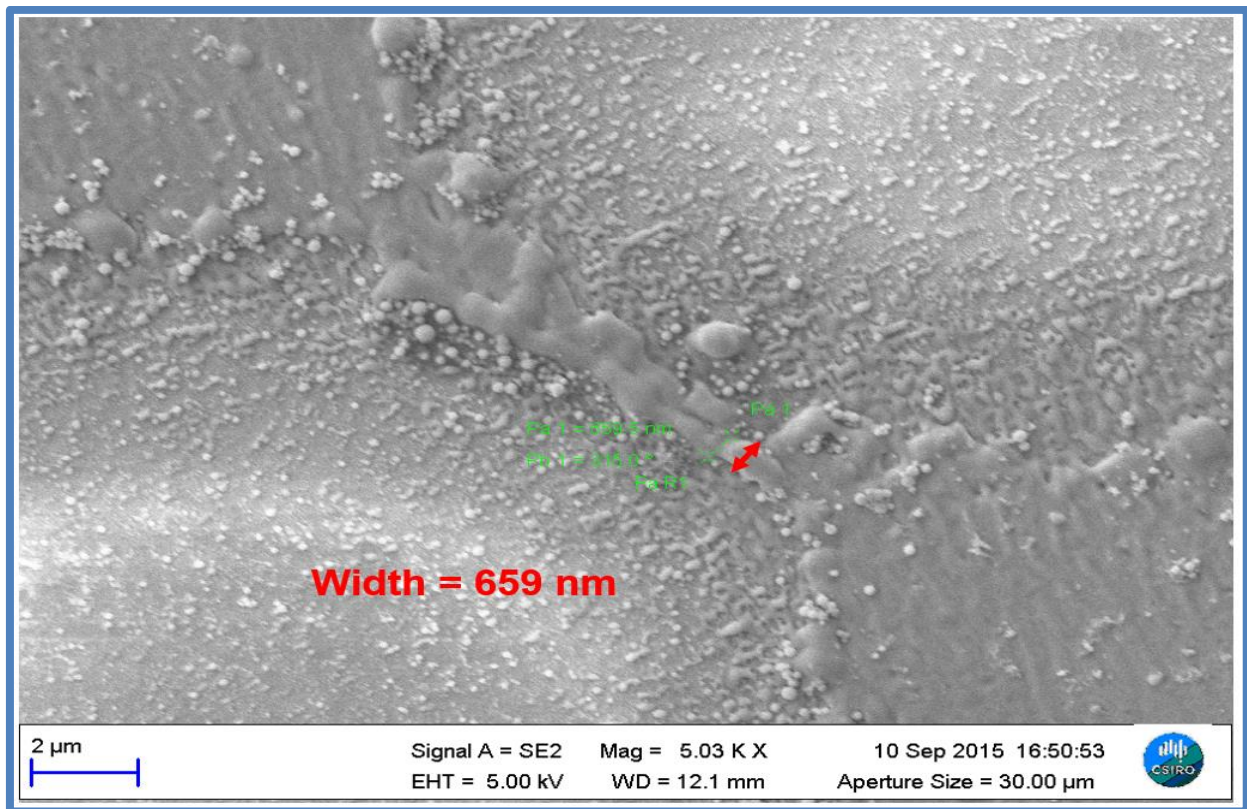


Figure 192 SEM image of the 659 nm sub-micron bridge.

## 7.1.2 RESISTIVE CONSTRICTION

### 7.1.2.1 MICRON CONSTRICTION (1.49 $\mu\text{m}$ )

The I-V curve in figure 193 shows a straight line, which indicates the micron constriction, in this case is resistive. During the fabrication of this constriction, the local heat from the femtosecond laser changed the superconductive state of the YBCO thin film to a normal resistive material. The constriction is purely resistive and its normal resistance  $R_N$  is 21.6  $\text{k}\Omega$ , which can be obtained from the gradient of the curve. The SEM image shown in figure 194, is that of the resistive constriction. The damage to the YBCO material in this case could also have been caused by poor storage conditions and delay in analysing the structures after fabrication. The YBCO thin films have a limited lifetime. That is after fabrication of constrictions using the laser they should not be stored for longer than 3 months before analysis of the constrictions.

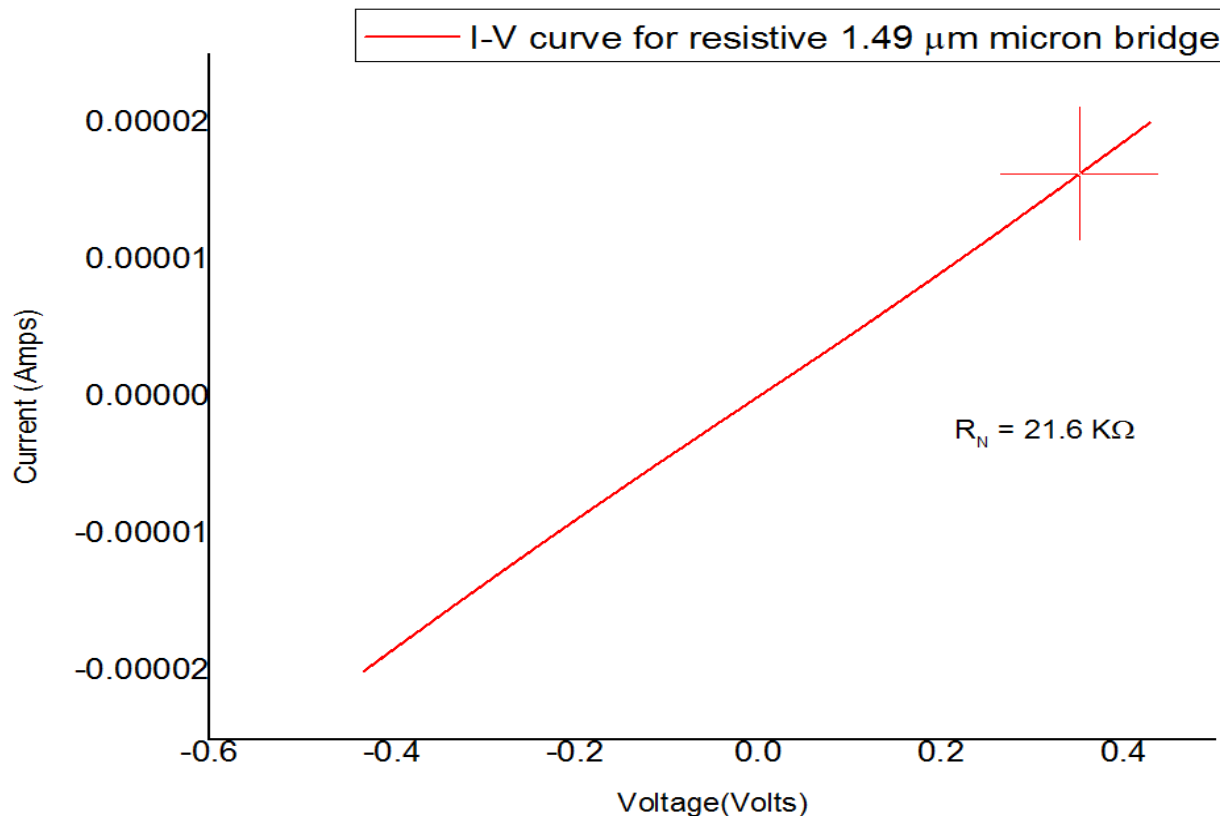


Figure 193 I-V curve for the resistive micron constriction 1.49  $\mu\text{m}$  showing a straight line.

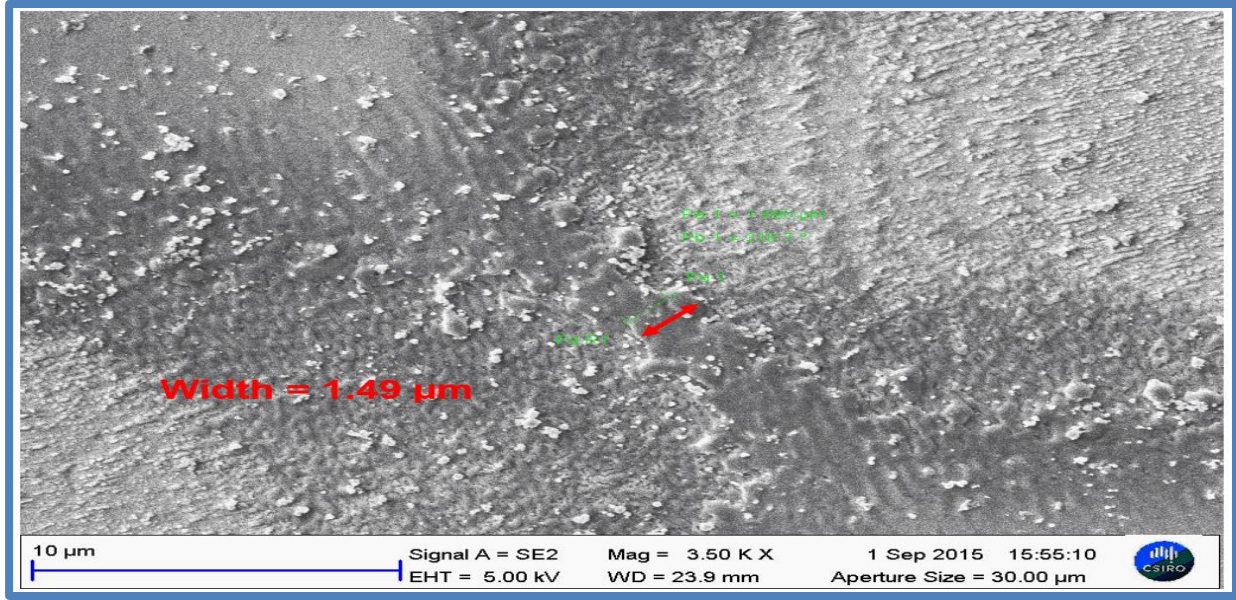


Figure 194 SEM image of the resistive micron constriction 1.49  $\mu\text{m}$ .

The appropriate way of storing fabricated Josephson junctions and SQUID devices can be seen in figure 195. This involves using an enclosure such as a glass cabinet and circulating nitrogen gas through the cabinet. The cabinet would have an inlet and outlet for the nitrogen gas to pass through. The nitrogen gas is inert and slows down the natural degradation of YBCO crystalline thin films because of the absorption of moisture from air.



Figure 195 Appropriate method of Storing fabricated Josephson junctions and SQUID devices.

### 7.1.3 ELECTRONICALLY OPEN CONSTRICTION

#### 7.1.3.1 MICRON CONSTRICTION (1.36 $\mu\text{m}$ )

The I-V curve in figure 196 shows a hysteresis loop, which indicates the micron sized constriction 1.36  $\mu\text{m}$ , is electrically open. In this case, the localized heating from the laser badly damages the superconductive state of the YBCO thin film. As a result, the constriction becomes highly resistive or electrically open. Although the constriction seems to be geometrically continuous, as can be seen in the SEM image in figure 197. Electrically the resistance is extremely high, thus one can say it is an open constriction. Calculation of the normal resistance in this case from the gradient of the hysteresis loop gives a value of 10.71 M $\Omega$ , which proves the constriction is open.

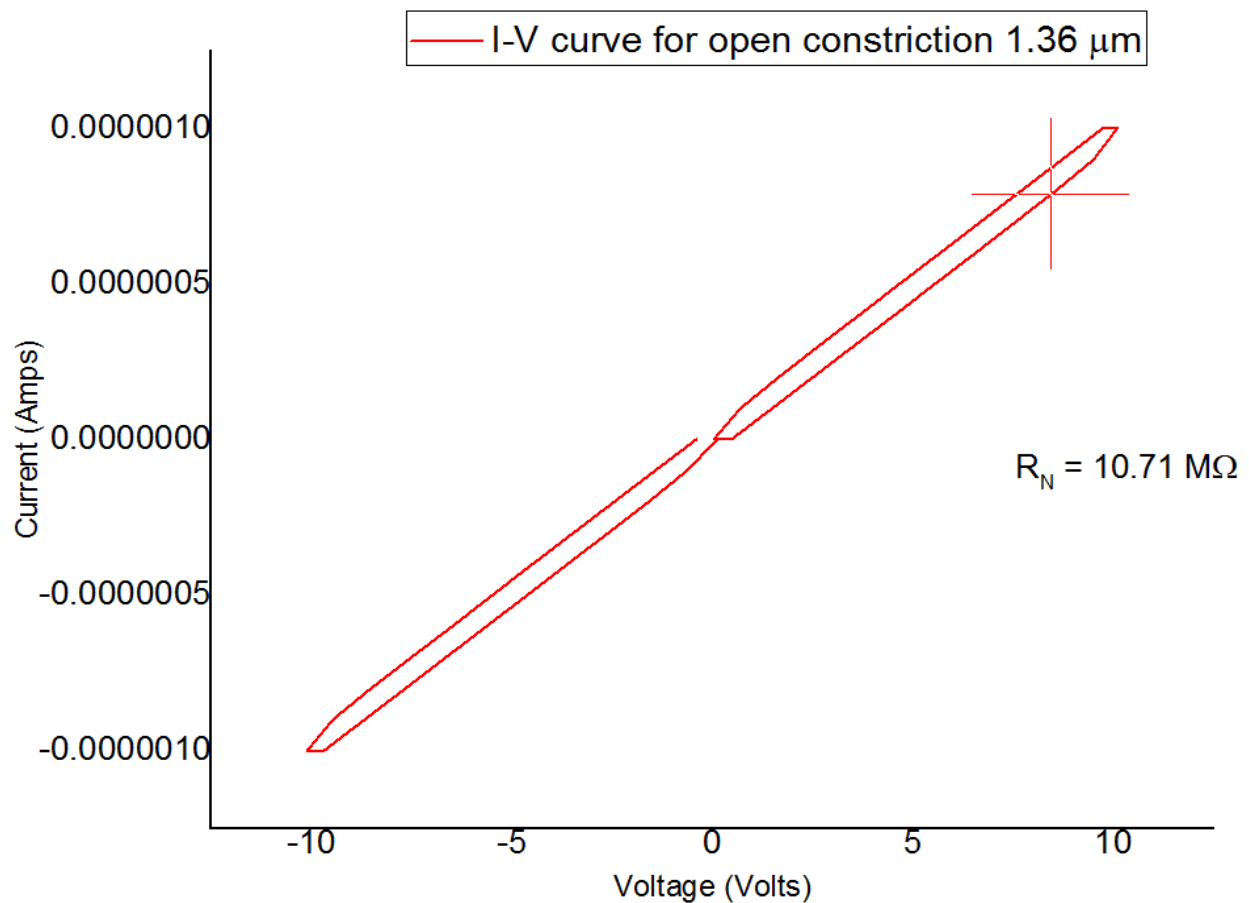


Figure 196 I-V curve for the open micron constriction 1.36  $\mu\text{m}$  showing a hysteresis loop.

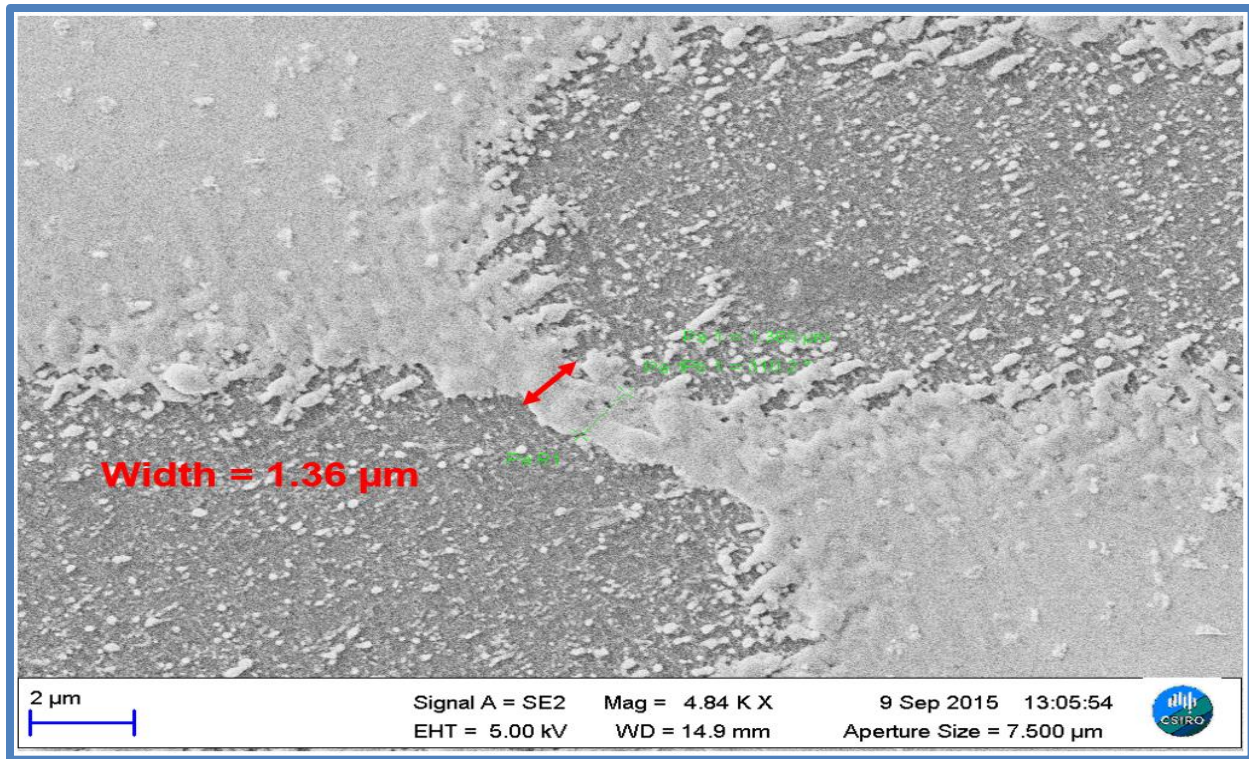


Figure 197 SEM image of the electrically open micron constriction 1.36  $\mu\text{m}$ .

The lens that was used to focus the laser in this case caused the excessive heating on the sample. An objective Plano convex lens of numerical aperture 0.25 was used to focus the laser beam. The burnt objective lens was used to fabricate this constriction. As a result, the laser beam was not well focused but slightly dispersed. The constriction was heated by the dispersed laser beam, therefore making it electrically open.

In this sub-section, we have shown the current-voltage characteristics (I-VC's) of the superconductive, resistive and electrically open constrictions fabricated on the YBCO thin film. The SEM images of these constrictions were also illustrated.

## 7.2 CLASSIFICATION OF THE SUPERCONDUCTIVE BRIDGES

Superconducting micron sized bridges are very useful for applications such as Bolometers [2-6], Fault current limiters [7] and microwave mixing [8] etc. In fact, YBCO, based bolometers can reach a theoretically predicted phonon noise-limited noise equivalent power (NEP) of  $3\text{pW}/\text{Hz}^{0.5}$  [9]. Micron sized constrictions on YBCO thin films were fabricated using a novel femtosecond laser technique shown in the previous

chapters in micro patterning of YBCO HTS films, since this laser has never been used before for this purpose.

Superconducting bridges can show similar a.c like behaviour as Josephson junctions, depending on their geometric dimension and hence can be classified according to their geometric dimensions. Following Likharev et al [10], we have that in the limit of a short and one dimensional bridge  $\left(w, \frac{l}{\xi(77K)} < 3.49\right)$  [10] where  $w$  is the width of the bridge,  $l$  is the length of the bridge and  $\xi$  is the coherent length of the YBCO thin film. In the condition above the bridge behaves similarly to a tunnel Josephson Junction as can be seen in figure 198. When the bridge length is increased with the same  $T$  (temperature) and the same width such that  $\left(w, \frac{l}{\xi(77K)} > 3.49\right)$  [10]. Then one-dimensional depairing effects characterizes the current flowing through the bridge. Finally, when increasing the bridge width to values  $\left(l, \frac{w}{\xi(77K)} > 4.44\right)$  [10] keeping the length the same, the maximum critical current density is now not given by depairing effects but by Abrikosov vortices (this is valid in the homogenous limit). That is in the case where the YBCO crystal remain homogenous (undamaged) at the constriction. According to [11] the coherent length ( $\xi$ ) of YBCO nanostructures is 2 nm in the limit of zero temperature. Using equation 1 and values from [12] the calculated coherent length ( $\xi$ ) for YBCO is 7 nm at a temperature of 4.2 K.

$$\xi = \frac{\hbar V_f}{\pi E_g} \quad (1)$$

Where,  $\hbar$  is Plancks constant,  $V_f$  is the fermi velocity and  $E_g$  is the Energy band gap of the YBCO thin film.

Using the value of 7 nm in our case for the coherent length of YBCO as an approximation at a temperature of 77 K. The widths of our constrictions range from (1.6  $\mu\text{m}$  to 3  $\mu\text{m}$ ) and the length is approximately 5  $\mu\text{m}$ . Then our bridges fabricated by the femtosecond laser technique should fall into the category, where the maximum current density is produced by Abrikosov vortices according to the diagram in figure 198.

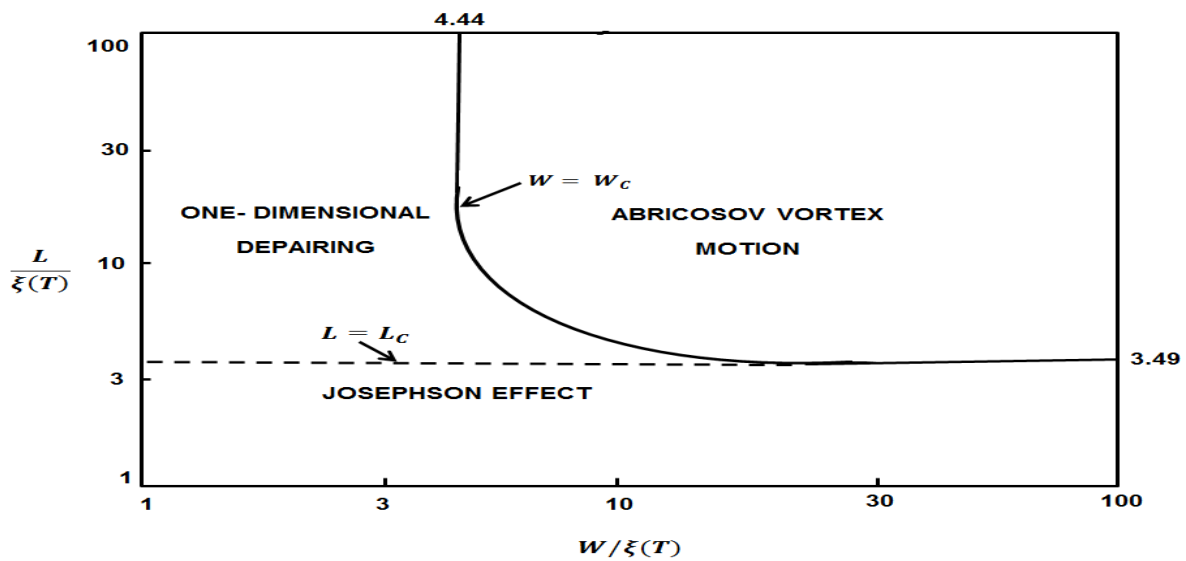


Figure 198 Variety of possible sizes of dirty weak links and causes of the flow of supercurrent through them [10].

However, for the coherent motion of the Abrikosov vortices to develop the constrictions fabricated must be absent of any inhomogeneities. If there are no inhomogeneities of any form on the YBCO constrictions, then synchronization of the coherent motion of the Abrikosov vortices to the external microwave field will occur by phase locking and Shapiro-like steps [13] should have been observed in these samples, showing an a.c Josephson-like behaviour. However, in these micron structures this did not occur due to the local heating from the laser, which partially damages the superconductive phase on the YBCO constrictions. The partial heat damage produces inhomogeneities on the YBCO constriction, pinning the coherent motion of the Abrikosov vortices and hence the Josephson-like a.c effects are not observed in these samples. Although there is laser heat damage and inhomogeneities are produced, there are superconductive patches inside the constriction where the superconductive phase survives giving rise to a measurable critical current. This critical current could not be modulated by the microwave radiation due to the defects on the constriction. In addition, the large value of the critical current measured in (mA) in relation to the low microwave radiation frequency (GHz) may have prevented Shapiro steps from being observed. Due to the inhomogeneities produced by heat damage, the current densities in these samples do not occur by virtue of Abrikosov vortices but probably due to the one-dimensional depairing mechanism.

### 7.3 I-V CHARACTERIZATION OF THE CONSTRICTIONS

The three constrictions discussed in this chapter did not show the a.c Josephson Effect, namely; 2.88  $\mu\text{m}$ , 1.72  $\mu\text{m}$ , and 1.69  $\mu\text{m}$  wide constrictions. Table 9 summarizes all the laser parameters related to the fabrication of these constrictions.

Table 9 Laser cutting parameters for each bridge.

Constriction width	$S_W$ laser separation distance	Laser ablation spot size	Lens used for fabrication	Substrate
(a) 2.88 $\mu\text{m}$	24 $\mu\text{m}$	20.9 $\mu\text{m}$	Spherical convex lens of 45 mm focal length	LAO
(b) 1.72 $\mu\text{m}$	18.3 $\mu\text{m}$	17 $\mu\text{m}$	Spherical convex lens of 45 mm focal length	LAO
(c) 1.69 $\mu\text{m}$	11.8 $\mu\text{m}$	10.5 $\mu\text{m}$	Objective Plano convex lens of numerical aperture 0.25	MgO

The method used to perform the I-V measurements and hence determine the critical current of each sample is summarized in the block diagram shown in figure 199. The software used to plot the I-V curves is called “SQUID” from national instruments.

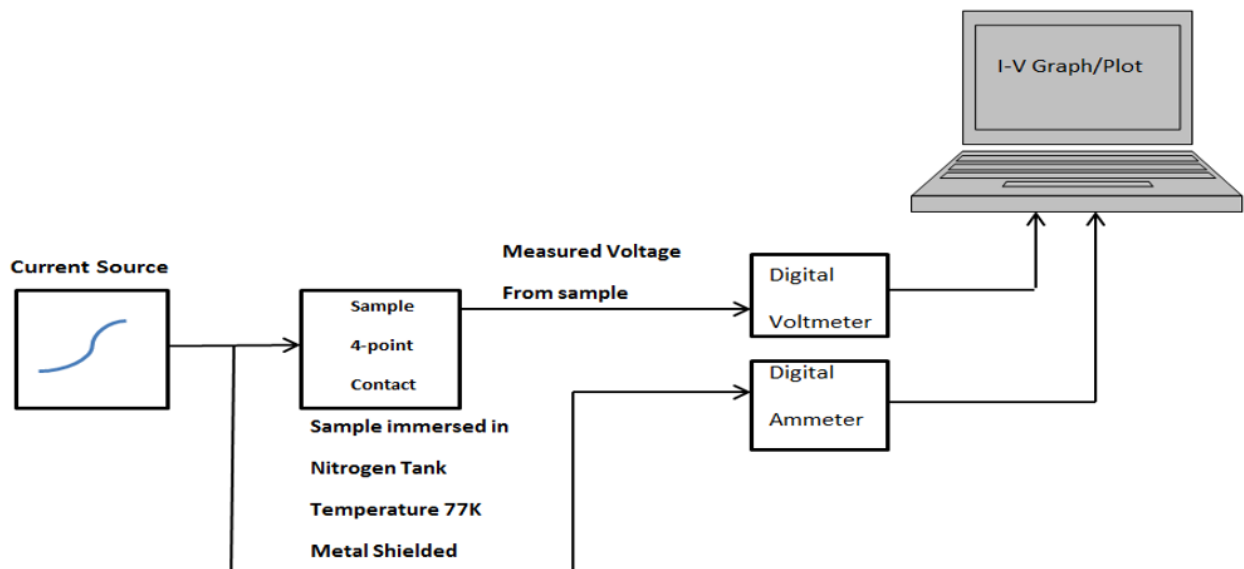


Figure 199 Set up for I-V measurement on the micron bridge samples using the circuit analysis software “SQUIDS” from national instruments.

As previously described 4-point gold contacts are placed on, the sample and then wire bonded to the PCB holder. The PCB holder together with the sample is mounted onto a probe. The probe is then immersed into a liquid nitrogen tank in order to take the sample to a temperature of 77 K. A d.c current source is used to pass current through the sample via two of the point contacts and the voltage produced is measured across the second two of the point contacts using the d.c voltmeter. The d.c ammeter, which gets a reference signal from the current source and the d.c voltmeter, are connected to the computer via a parallel interface, which with the aid of the “SQUID” software interface plots the I-V curves.

## 7.4 RESULTS: BRIDGES THAT DO NOT SHOW THE A.C JOSEPHSON-LIKE EFFECT.

Micron constrictions with different widths and lengths were fabricated using the femtosecond laser [14-15] as discussed in previous chapters. A few of these constrictions that did not show the Josephson-like effect were chosen and listed in table 10. The reason why they did not show the Josephson Effect was explained in the later sections. The widths of the constrictions were measured using the SEM at the narrowest points.

Table 10 Constrictions sizes and their corresponding critical current.

Constriction Name	Constriction width	Constriction Length	Measured critical current
(a) Micron	2.88 $\mu\text{m}$	5 $\mu\text{m}$	4.81 mA
(b) Micron	1.72 $\mu\text{m}$	5 $\mu\text{m}$	1.77 mA
(c) Micron	1.69 $\mu\text{m}$	5 $\mu\text{m}$	15.2 mA

### 7.4.1 MICRON (a) CONSTRICTION

The micron size (a) constriction shown in the SEM image in figure 200 is 2.88  $\mu\text{m}$  wide, measured at the narrowest point of the constriction. Figure 201 shows its I-V characteristic curve with a critical current  $I_c$  of 4.81 mA. The critical current was measured by taking a value of current at a voltage offset of 20  $\mu\text{V}$ , which is tending to the zero limit of voltage.

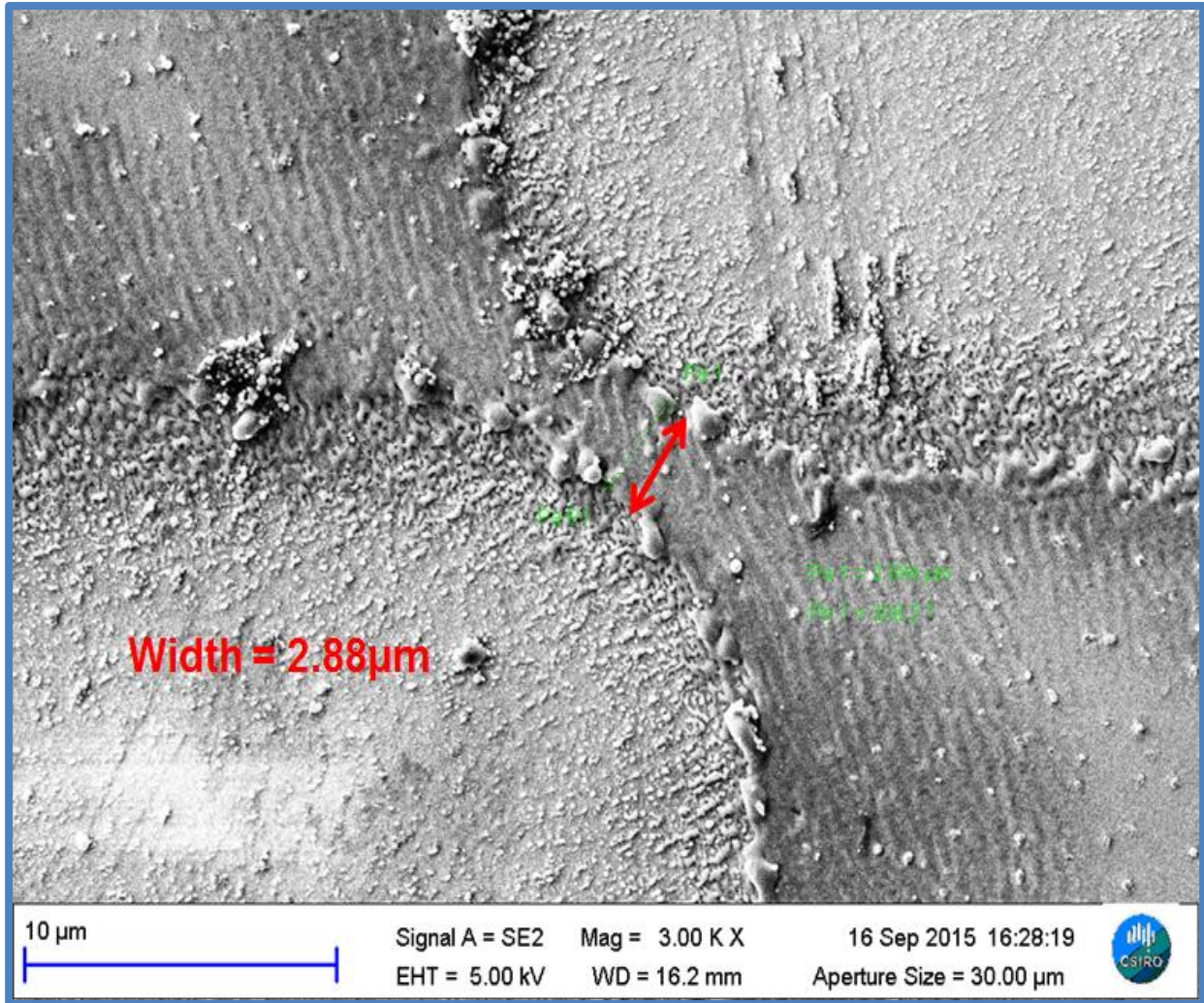


Figure 200 SEM image of 2.88 μm micron bridge.

As can be seen from figure 200, which is an SEM image of the sample. There is local heating from the femtosecond laser, which produces some re-deposited particles on the geometric edge of the constriction. A shadow is formed around the edge of the micron constriction. The shadow is the damaged superconductive material that changes to non-superconductive form. Hence, the real superconductive phase of the sample is smaller than the geometric size. There is a section in the constriction that conducts the measured critical current. However, this current on the sample does not conduct by the coherent motion of Abrikosov vortices due to the inhomogeneities produced by the heat damage. If the current was produced by Abrikosov vortices, then an a.c Josephson-like effect (Shapiro steps) could have been observed on this sample. The damage prevents response to microwave radiation and Shapiro steps are not observed.

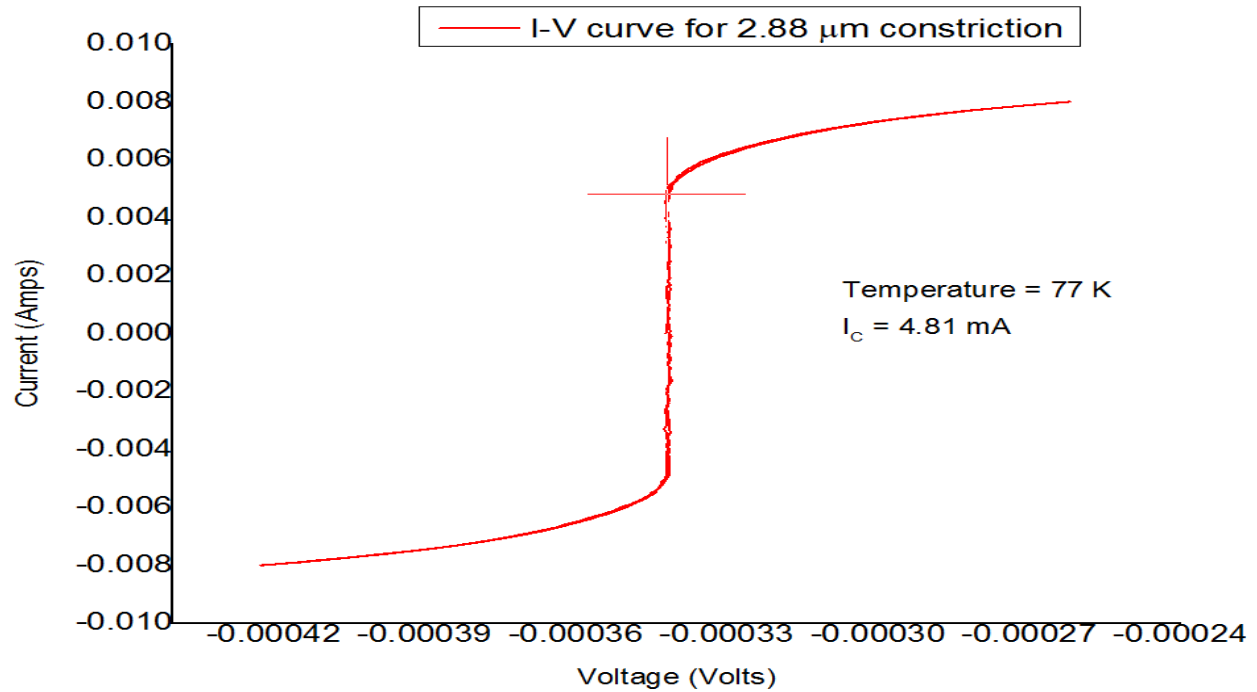


Figure 201 I-V characteristic for the 2.88 $\mu\text{m}$  constriction (a) showing critical current to be 4.81 mA.

The average height of the re-deposited particles after ablation was measured using an AFM profilometer for the specific sample and determined to be approximately 173 nm from the 3-D image in figure 202. It is believed that the re-deposited particles are insulating due to the laser heat damage and do not contribute to the measured critical current.

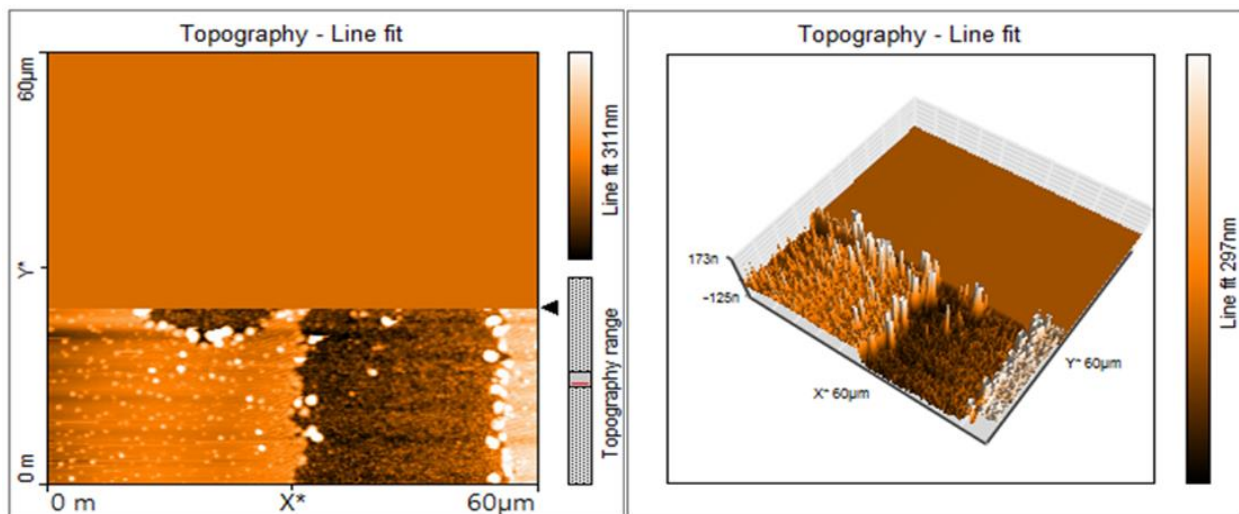


Figure 202 AFM profile of the 2.88  $\mu\text{m}$  constriction (a) showing the approximate height of the re-deposited particles to be 173 nm.

### 7.4.2 MICRON (b) CONSTRICTION

The width of constriction (b) was determined using SEM to be  $1.72\ \mu\text{m}$  wide as can be seen in figure 203. The critical current can be seen in figure 204 to be  $1.77\ \text{mA}$ . Again, the constriction is heated beyond the geometric boundary and some of the superconductive phase is damaged. Due to the heat, damage from the laser the crystalline structure of the YBCO constriction is not homogenous, for the coherent motion of Abrikosov vortices to develop and hence show the a.c Josephson-like effect.

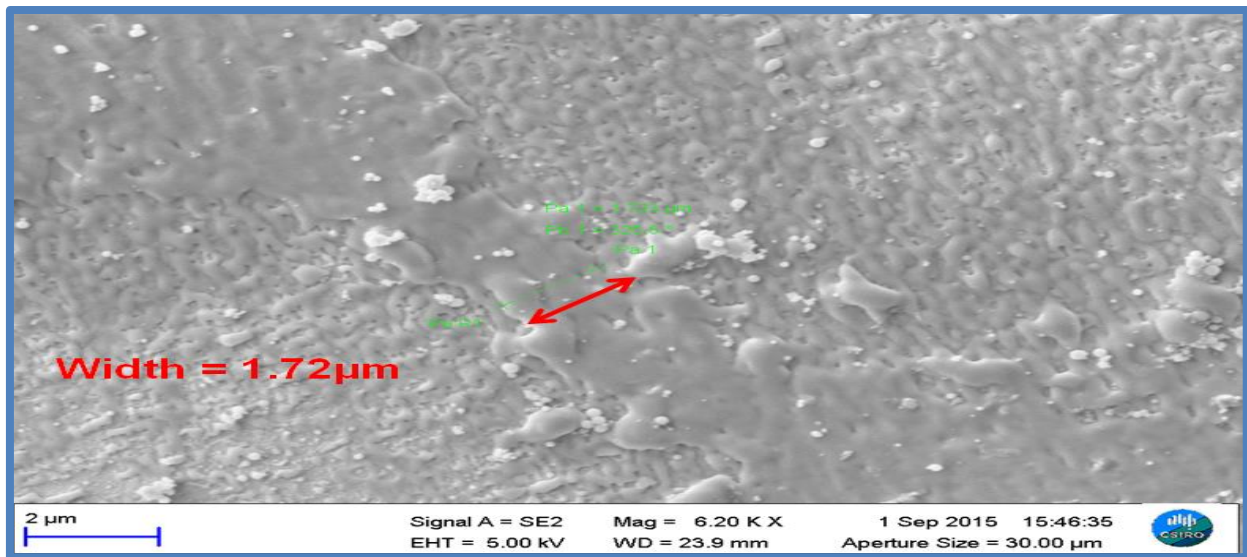


Figure 203 SEM image of constriction (b) showing the width to be  $1.72\ \mu\text{m}$ .

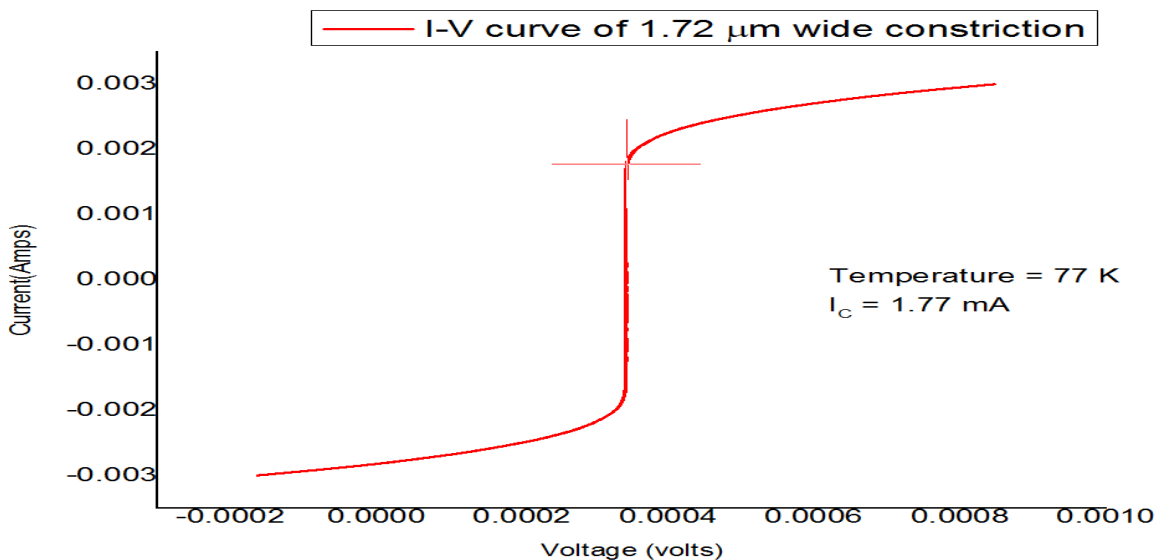


Figure 204 I-V characteristic for the  $1.72\ \mu\text{m}$  wide constriction (b) showing the critical current to be  $1.77\ \text{mA}$  at a temperature of  $77\ \text{K}$ .

The AFM 3-D profile of the 1.72  $\mu\text{m}$  wide constriction (b) can be seen in figure 205. The height of the re-deposited particles is 151 nm. The shadowed area of the constriction represents the heating damage from the laser. It is believed that the re-deposited particles are heat damaged and hence do not contribute to the measured current.

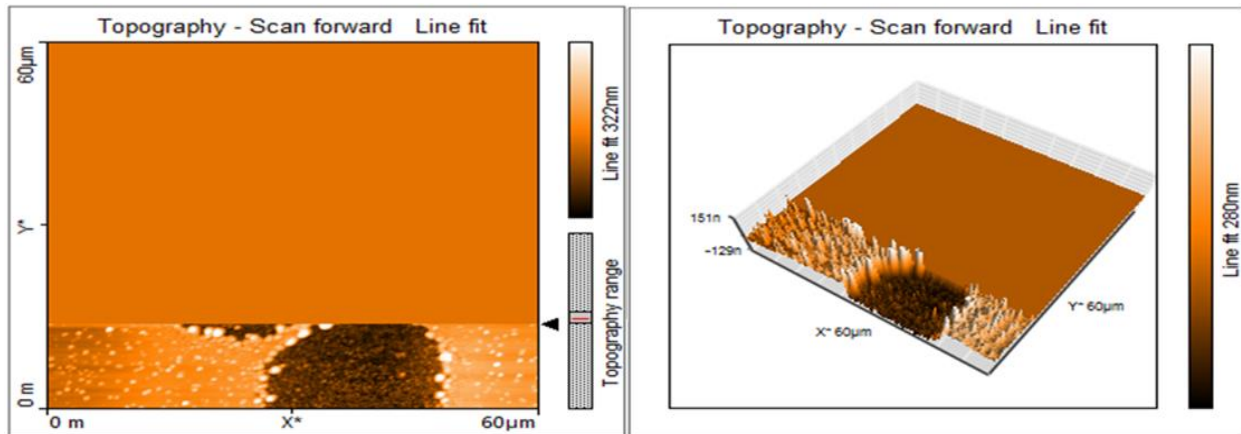


Figure 205 AFM profile of 1.72  $\mu\text{m}$  wide constriction (b) re-deposited particles height is 151 nm.

### 7.4.3 MICRON (c) CONSTRICTION

The width of constriction (c) is 1.69  $\mu\text{m}$  as can be seen in the SEM image of the sample in figure 206. The I-V curve in figure 207 shows that the sample has a critical current of 15.2 mA. This critical current is very large compared to the small geometric size of constriction (c), since both constriction, (b) and (c) are of similar geometric dimensions. The reason for this can be explained using the SEM image in figure 206. From this image, it can be seen that there is not much heat damage to the YBCO thin film on the constriction. The crystalline nature is largely untouched beyond the geometric boundary. The reason for this is that an objective lens was used at the terminal point in the shaping or focusing of the laser beam in this case. The objective lens has a numerical aperture of NA 0.25 and a X10 magnification. Therefore, it has a very high focusing power that enables the laser beam spot to be reduced to a very small laser ablation spot as seen in table 7-1 (10.5  $\mu\text{m}$ ). This laser ablation spot cuts right on the edges of the constriction without passing the geometric boundary of the constriction into the superconductive phase of the YBCO sample. The measured critical current is therefore quite large because most of the superconductive phase within the geometric boundary still conducts

the current. If you compare sample (b) and (c) with respect to their similar dimensions they should produce a similar critical current. However, in sample (b) the superconductive phase is highly damaged by the heat of the laser. This is due to the fact that in sample (b) a conventional spherical convex lens is used of focal length 45 mm to focus the laser beam before cutting. This lens can produce a poorly shaped ablation spot that damages the sample beyond the geometric boundary into the superconductive phase, hence the small critical current produced. Sample (c) on the other hand has a large measured critical current because by using the objective Plano convex lens the superconductive phase is not damaged beyond the geometric boundary.

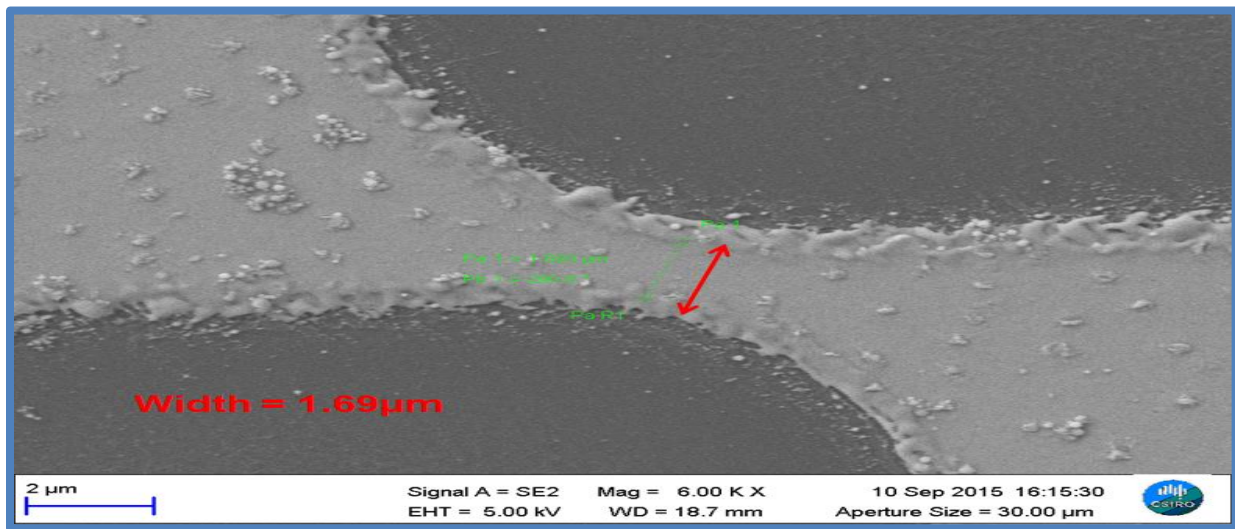


Figure 206 SEM image of the 1.69  $\mu\text{m}$  wide constriction (c).

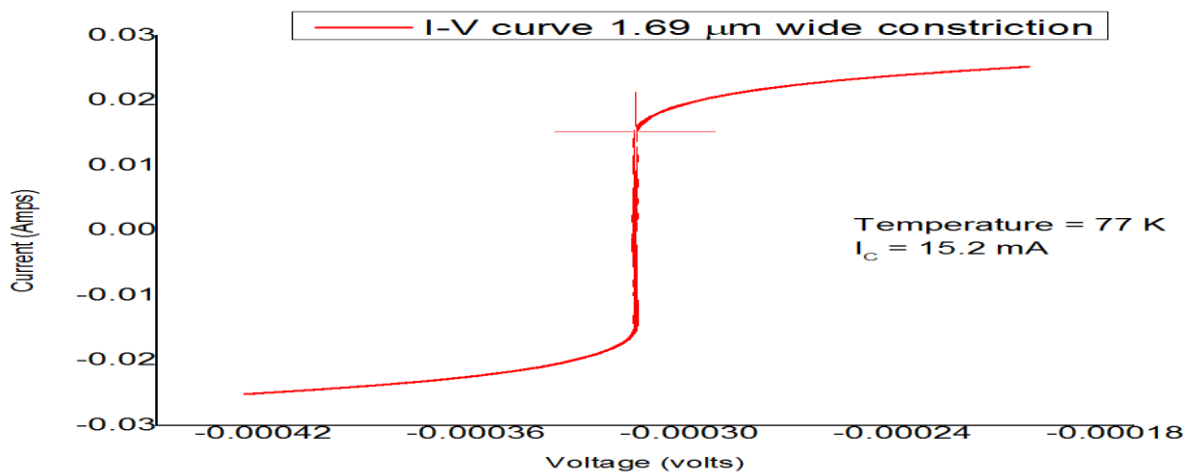


Figure 207 I-V curve of the 1.69  $\mu\text{m}$  constriction (c), showing the critical current to be 15.2 mA at a temperature of 77 K.

Sample (c) does not have any inhomogeneities on the constriction such that the crystalline structure of the YBCO is still intact and therefore the coherent motion of the Abrikosov vortices are able to develop. However, the critical current measured is very high 15.2 mA. The microwave radiation source used in our experiments with a frequency of 20 GHz will produce ( $\mu\text{A}$ ) size step currents, as calculated from equations in [13]. This ( $\mu\text{A}$ ) steps would not be visible in a (mA) current sweep. A terahertz frequency source could enable the shapiro steps produced in this case to be seen in the large current sweep of 20 mA.

## **7.5 LIMITATIONS OF THE FEMTOSECOND LASER METHOD AND POSSIBLE IMPROVEMENTS**

The main limitation or drawback in using the femtosecond laser technique is in the rigorous process of shaping the laser beam spot to the optimum size for micro-patterning processes. The laser spot size coming from the source is approximately 9 mm wide. To achieve micro patterning the laser ablation spot has to be reduced to at least 10  $\mu\text{m}$ . This requires mirrors, apertures, beam collimation (cylindrical lenses), which introduce spherical aberration and focusing lenses. All these have to be aligned and well-focused for the set up to work at optimum. Any change in alignment and focusing will change the size of the laser ablation spot. Hence the difficulty in reproducing the same results. When the laser beam is not well-focused due to spherical aberration, it transgresses the geometric boundary planned for cutting and damages the superconductive phase of the sample producing defects. This is the reason for the shadow around the geometric boundary. In addition, overlapping of the laser ablation spots occurs, clipping the constriction during the fabrication of very small structures and nanowires. For example, to easily fabricate a constriction of sub-micron width of 600 nm, the laser ablation spot size has to be of a relative size of at least 1  $\mu\text{m}$  to avoid clipping the constriction. One possible solution or recommendation is to make use of the objective lens with a high numerical aperture (NA) at the terminal point of focusing. This can help reduce the laser ablation spot to a relatively small dimension. In addition, the high focusing power of this lens will prevent the laser beam from straying beyond the geometric boundary of the constriction in the form of shadows.

## 7.6 CONCLUSION

In this chapter, we discussed three micron-sized superconductive constrictions of width 2.88  $\mu\text{m}$ , 1.72  $\mu\text{m}$ , and 1.69  $\mu\text{m}$  that did not show the Josephson Effect. The reason these constrictions did not show the Josephson-like Effect was explained. According to the condition  $\left(l, \left(\frac{w}{\xi(77K)}\right) > 4.44\right)$ , which is met in these samples, the current density should be due to the coherent motion of Abrikosov vortices. Localized heating effects from the laser create inhomogeneities on the constrictions that prevent Abrikosov vortices from developing and a.c Josephson-like effect from being observed. Constriction (c) could possibly show the a.c Josephson-like effect but due to the low frequency of the microwave radiation used (20 GHz) and the high measured value of the critical current, synchronization does not occur between the current and the microwave radiation source. Shapiro steps cannot be made visible on a current sweep of 20 mA using a gigahertz frequency source. A terahertz frequency source would be deemed necessary.

## 7.7 REFERENCES

1. U buttner, GL Hardie, R Rossouw, V V Srinivasu and W J Perold, "Fabrication of submicron YBCO Josephson junctions by a sample mosaic navigation assisted laser etching process", superconducting science and technology journal, 20, (2007), S426-S429.
2. M.Sc Thesis, Ali Bozbey, "YBCO edge transition bolometers: effect of superconductivity transition on the phase and magnitude of the response", Bilkent University, Turkey, 2003.
3. Philippe Mérel, Philips Laou and Franklin Wong, "YBCO micro bolometers for Infrared detection: Enhancement of performances with regionally thinned micro bridges", Technical Memorandum DRDC Valcartier TM 2006-496, 2009.
4. Mikael Lindgren, Marc Currie, Student Member, IEEE, Carlo A. Williams, Student Member, IEEE, Thomas Y. Hsiang, Philippe M. Fauchet, Senior Member, IEEE, Roman Sobolewski, Steven H. Moffat, Robert A. Hughes, John S. Preston, and Frank A. Hegmann, "Ultrafast Photoresponse in Microbridges and Pulse Propagation in Transmission Lines Made from High- Superconducting Y–Ba–Cu–O Thin Films", IEEE Journal of selected topics in quantum electronics, 668, vol. 2, NO. 3 1196.

5. Chen H.Z, Chow T.C, Hong M.T, Lin T.L, Lin K.S, Cheng Y.F, Chen Y.C, Chou H, "The broad band optical detection of precipitational free YBCO thin films", *Physica C*, 1197, vol.274, pp. 24-32.
6. Boris S. Karasik, Andrei V. Sergeev, and Daniel E. Prober, "Nano bolometers for THz Photon Detection", *IEE transactions on terahertz science and technology* 97, VOL. 1, 2011.
7. J A Lorenzo Fernandez, MR Osorio, JA Veira and F Vidal, *Superconductivity Science and Technology*, 22, 025009, (2009).
8. K. S. Il'in and M. Siegel, "Microwave mixing in micro bridges made from YBa<sub>2</sub>Cu<sub>3</sub>O<sub>7-x</sub> thin films", *Journal of applied physics*, 361, Volume 92, 2002.
9. Q. Hu, and P. L. Richards, "Design analysis of a high T<sub>c</sub> superconducting microbolometer," *Appl. Phys. Lett.* vol. 55, n.23, pp.2444-2446, Dec. 1989
10. Book Chapter, K.K Likharev, "Superconducting weak links", *American Physical Society*, 1979.
11. G.Papari, F.Carillo, D.Stornaiuolo, L.Longobardi, F.Beltram, F.Tafari, "High critical-current and scaling of phase-slip processes in YBCO nanowires", *Superconductor Science and Technology*, 25, 035011, 2012.
12. Nir Hass, D. Lizyca, G. Deutscher G. Desgardin, I. Monot and M. Weger, „Sharp Gap Edge and Determination of the Fermi Velocity in YtBa<sub>2</sub>Cu<sub>3</sub>O<sub>7-d</sub> by Point Contact Spectroscopy", *Journal of Superconductivity*, Vol. 5, No. 2, 1992
13. Vallabhapurapu V. Srinivasu, Willem Jacobus Perold, "Observation of Shapiro-Steps in AFM-Plough Micron-Size YBCO Planar Constrictions", *IEEE transactions on applied superconductivity*, Vol. 19, NO. 3, JUNE 2009.
14. Moritz Grehn, Thomas Seuthe, Michael Hofner, Nils Griga, Christoph Theiss, Alexandre Mermillod-Blondin, Markus Eberstein, HansEichler, and Jorn Bonse, "Femtosecond-laser induced ablation of silicate glasses and the intrinsic dissociation energy", *Optical Materials Express*, 4(4), 689-700, (2014), <http://dx.doi.org/10.1364/OME.4.000689>.
15. F.korte, J.Serbin, J.koch, A. Egbert, C. Fallnich, A. Ostendorf, B.N Chichkov, "Towards Nano structuring with femtosecond laser pulses", *Applied Physics A*, 77(2), 229-235, (2003).

# CHAPTER 8

## CONCLUSION

In order to conclude all the work done in the preceding chapters the problem statements made in chapter one will be answered.

1. A novel femtosecond laser technique was utilised to fabricate Josephson Junctions in two categories based on their width namely; the Josephson Junctions in the near nano size category (500 – 800 nm) and the Josephson Junctions in the micron size category (1 – 2  $\mu\text{m}$ ). These Josephson junctions were all fabricated on high  $T_C$  superconducting  $YBa_2Cu_3O_{7-x}$  thin films based on the LAO substrate. The Josephson Effect in these junctions was proven by the use of D.C I-V characteristics, A.C Shapiro steps and the microwave radiation effect on the critical current  $I_C$  of the junctions.
2. Initially it was assumed that due to the low pulse duration of the femtosecond laser 130 fs, the junctions fabricated by this method would not experience thermal degradation from the laser. However, from all the experimental work conducted, namely: I-V characterization, microscope scans, it is concluded that the femtosecond laser does heat the samples and thermal degradation occurs to some extent. The reason for this can be explained as follows; the femtosecond laser has a low pulse duration of 130 fs intrinsically, due to its own nature. However, during the fabrication process other factors combine to change how long the constriction is exposed to the laser heat. These factors include the laser frequency or pulse repetition rate which is 1 kHz (1000  $\mu\text{s}$ ) and the laser feed rate in this case (333  $\mu\text{ms}^{-1}$ ). The laser feed refers to how fast the translation stage is moved during the fabrication of the constriction. With these factors combined the sample would still be exposed to the laser heat for a much longer period than femtoseconds, and hence thermal degradation would occur to some extent. Therefore, the sub-micron sized 816 nm wide Josephson junction showed S-N-S type junction behaviour due to heating effects on the narrow constriction while the micron sized Josephson junction showed more of the S-s'-S type junction behaviour because of its wider

dimension. This tells us that the heating effects from the laser vary depending on how close the laser ablation spots are brought to each other during fabrication. It is recommended that in order to reduce the localized heating effects of the laser beyond the geometric boundary of the constriction, it is better to utilize the objective Plano convex lenses of numerical apertures (0.25, 0.40, and 0.65) to focus the laser beam rather than the conventional spherical lenses of relative focal lengths. As the former will produce sharper well define edged constrictions.

3. Several nanoscale constrictions that could act as superconductive bridges were achieved as seen in the previous chapters.
4. Novel S-shaped constrictions were designed by using the G-code program to move the translation stage during the fabrication of the constrictions. The S-shaped constriction is novel in that its shaped like the letter “S” and compared to standard constriction shapes, with the S-shaped constriction it is possible to regulate both the length and width of the constriction at the same time. The complete “S” shaped design was developed using a novel algorithm written in the G-code programming language for control systems. This algorithm is described in chapter 3 and the G-code program can be found in the [appendix](#).
5. Lastly, a laser beam shaping and collimation process was developed in order to optimize the laser beam spot for the machining process of the junctions. The laser beam shaping process involved blowing up (expanding) the laser beam spot and then collimating it by using cylindrical lenses. This was done to convert the elliptical spot shape to a spherical spot shape by expanding the X-direction of the spot. The beam collimation was done to expand the laser beam spot before converging it to the smallest spot possible, by using either the conventional spherical lenses or the objective lens.

## 8.1 FUTURE WORK AND RECOMMENDATION

1. After all the work done in this PhD, including optimising the laser beam shape, designing the S-shaped constrictions, determining the laser ablation threshold of YBCO thin film, fabricating constrictions, analysing the I-V curves, analysing Shapiro steps, etc. The main action that can be taken in the future to fabricate Nano Josephson junctions using the femtosecond laser without heating the constriction would be to optimize the laser beam shape using beam collimation processes and to use the objective plano convex lenses of high numerical aperture such as (NA 0.25, 0.40, and 0.65) to focus the beam. This lens would focus the laser ablation spot to the smallest ablation spot possible that can facilitate the fabrication of Nano Josephson Junctions. The objective lens would also prevent the laser beam from overlapping the geometric edge designed and hence the laser would not heat the superconductive phase of the constriction. This is only possible if the objective plano convex lens is not damaged and in good working order.
2. Another factor that can facilitate reducing the thermal heating of the constriction by the laser would be to increase the translation stage feed rate from (20 mm/min)  $333 \mu\text{ms}^{-1}$  to (30 mm/min)  $500 \mu\text{ms}^{-1}$ . This would reduce the exposure time of the sample to the laser heating effects.
3. A recommendation to improve the yield rate when fabricating Josephson Junctions would be to store the samples made, using inert nitrogen gas. The samples should be stored in in cylinders with inert nitrogen gas freely flowing across the samples. This can help to improve the life span of the junctions made.
4. Standard laser patterning techniques, applied to a multielement, highly anisotropic and chemically reactive YBCO often result in structures with fuzzy edges as seen in some AFM images in the previous chapters. In addition it produces degraded (oxygen –deficient) chemical composition, lowering the performance of fabricated devices such as Josephson Junctions. A laser patterning technique described in [1, 2] involves protecting the YBCO thin films by fabricating bilayer structures consisting of YBCO thin films with in-situ deposited insulating  $\text{SrTiO}_3$  (STO) coating. This bilayer structures can be used to fabricate planar constrictions

consisting of well defined, uniform superconducting YBCO regions free of surface contamination and edge degradation. The STO layer is used to protect the YBCO thin film during the laser patterning of the film. The laser-induced, non-invasive diffusion of oxygen atoms through the STO top layer, does not damage or degrade the YBCO layer by creating an oxygen deficient YBCO.

5. Based on the critical current temperature dependence graphs in chapter 5 for the micron and sub-micron sized Josephson Junctions. I determined the critical current density for the micron-sized Junction to be 9.5 Amps/cm<sup>2</sup> at 77 K and the sub-micron sized Junction to be 36.8 Amps/cm<sup>2</sup> at 77 K. These values are small at 77 K for fabricated Josephson Junctions. This occurs because of the thermal heating effects from the laser. However, these devices at lower cryogenic temperatures such as 8 K tend to have improved performance, becoming more superconductive at lower temperatures. This again indicates that their reduced performance is caused by thermal degradation from the laser. Hence, if the recommendations listed above are applied, then it would be possible to achieve reduced thermal degradation from the femtosecond laser and improved performance from the Junctions.
6. The femtosecond laser and the G-code algorithm designed for the fabrication of Josephson Junctions can be used in the future with a few alterations to the algorithm to fabricate RF micro strip lines, antennas and antenna patches that can be used in the field of RF electronics.

## 8.2 REFERENCES

- [1] R. Sobolewski, W. Xiong, W. K. R. Gavaler, and R. Sobolewski, "Laser patterning of Y-Ba-Cu-O thin-film devices and circuits Laser patterning of Y-Ba-Cu-O thin-film devices and circuits," vol. 643, pp. 1–4, 1994.
- [2] J. Talvacchio, "Laser patterning of YBa/sub 2/Cu/sub 3/O/sub x/ thin films protected by in-situ grown SrTiO/sub 3/ c - Applied Superconductivity, IEEE Transactions on," vol. 5, no. 2, pp. 1177–1180, 1995.

## APPENDIX

### **G-CODE PROGRAM TO FABRICATE THE S-SHAPED CONSTRICTIONS.**

;CUTS CONSTRICTIONS THAT YOU CAN CONTROL THE WIDTH AND THE  
LENGTH

DVAR \$xzero ;initial xvalue at beginning of EACH pad

DVAR \$xval ;next x value

DVAR \$yzero ;initial yvalue

DVAR \$yval ;next yvalue

DVAR \$zval ;initial z value - kept constant

DVAR \$zoutfocus ;an initial value for z out of the laser beam focus

DVAR \$iter ;iterator

DVAR \$l ;Length of rectangle

DVAR \$width ;width of rectangle

DVAR \$nrepsablation ;number of times to cut around rectangle ablation

DVAR \$nrepsconstriction ;number of times to make constriction

DVAR \$ax

DVAR \$bx

DVAR \$cx

DVAR \$ay

DVAR \$by

DVAR \$cy

BoundAxesMask = BoundAxesMask BOR 0x7 ; This task now takes control of the X axis

G90 ;Absolute mode

G71 ;METRIC MODE

G75 ;UNIT/MIN

G84 X Y ;ROTATION OFF FOR X Y

ENABLE X Y Z

RapidFeedRate.X=20 ;SET FEEDRATE FOR G0 COMMANDS

RapidFeedRate.Y=20

F100 ; Set feedrate

\$zval=-1.0 ; focal point

\$zoutfocus=5

\$Il=5

\$width=1

\$nrepsablation=10

\$nrepsconstriction=6

G82

;HOME X Y Z

\$xzero=1

\$yzero=5.5

G92 X\$zero Y\$zero ; Set these coordinates as the origin

; BLOCK BEAM!!

;DWELL 10

G1 X0 Y0 Z\$zoutfocus ;go to starting point

;DWELL 5

G1 X0 Y0 Z\$zval ;bring into focus

; OPEN BEAM!!

DWELL 10

; -----

; cut rectangle

; -----

; lower left corner of rectangle

\$xval=-\$l

\$yval=-\$width/200

G1 X\$xval Y0 Z\$zval ;go to lower left bottom of rectangle 1 ;lower half

G1 X\$xval Y\$yval Z\$zval ;go to lower left corner of rectangle

REPEAT \$nrepsconstriction

REPEAT \$nrepsablation

\$xval=\$xval+\$ll ;calculate new x position 2

G1 X\$xval Y\$yval Z\$zval ;shift to new x position

\$yval=\$yval-\$width/200

G1 X\$xval Y\$yval Z\$zval ;cut along x direction

\$xval=\$xval-\$ll ;calculate new x position 3

G1 X\$xval Y\$yval Z\$zval ;shift to new x position

\$yval=\$yval-\$width/200

G1 X\$xval Y\$yval Z\$zval ;cut along x direction

\$xval=\$xval+\$ll ;calculate new x position 4

G1 X\$xval Y\$yval Z\$zval ;shift to new x position

\$yval=\$yval-\$width/200

G1 X\$xval Y\$yval Z\$zval ;cut along x direction

\$xval=\$xval-\$ll ;calculate new x position 5

G1 X\$xval Y\$yval Z\$zval ;shift to new x position

\$yval=\$yval-\$width/200

G1 X\$xval Y\$yval Z\$zval ;cut along x direction

$\$xval = \$xval + \$ll$  ;calculate new x position 6

G1 X $\$xval$  Y $\$yval$  Z $\$zval$  ;shift to new x position

$\$yval = \$yval - \$width / 200$

G1 X $\$xval$  Y $\$yval$  Z $\$zval$  ;cut along x direction

$\$xval = \$xval - \$ll$  ;calculate new x position 7

G1 X $\$xval$  Y $\$yval$  Z $\$zval$  ;shift to new x position

$\$yval = \$yval - \$width / 200$

G1 X $\$xval$  Y $\$yval$  Z $\$zval$  ;cut along x direction

$\$xval = \$xval + \$ll$  ;calculate new x position 8

G1 X $\$xval$  Y $\$yval$  Z $\$zval$  ;shift to new x position

$\$yval = \$yval - \$width / 200$

G1 X $\$xval$  Y $\$yval$  Z $\$zval$  ;cut along x direction

$\$xval = \$xval - \$ll$  ;calculate new x position 9

G1 X $\$xval$  Y $\$yval$  Z $\$zval$  ;shift to new x position

$\$yval = \$yval - \$width / 200$

G1 X $\$xval$  Y $\$yval$  Z $\$zval$  ;cut along x direction

$\$xval = \$xval + \$ll$  ;calculate new x position 10

G1 X\$xval Y\$yval Z\$zval ;shift to new x position

\$yval=\$yval-\$width/200

G1 X\$xval Y\$yval Z\$zval ;cut along x direction

\$xval=\$xval-\$II ;calculate new x position 11

G1 X\$xval Y\$yval Z\$zval ;shift to new x position

\$yval=\$yval-\$width/200

G1 X\$xval Y\$yval Z\$zval ;cut along x direction

ENDRPT

\$xval=\$xval+\$II ; extra to remove block

G1 X\$xval Y\$yval Z\$zval

\$yval=\$yval-\$width/200

G1 X\$xval Y\$yval Z\$zval ;cut along x direction

\$xval=\$xval-\$II ;extra TO REMOVE BLOCK

G1 X\$xval Y\$yval Z\$zval

\$xval=\$xval+\$II/2.003004507 ;calculate new x position halfway point

G1 X\$xval Y\$yval Z\$zval ;shift to new x position

$\$yval = \$yval - \$width / 2.010050251$

G1 X\$ $xval$  Y\$ $yval$  Z\$ $zval$  ;cut along x direction enter y width constriction 20um

$\$yval = \$yval + \$width / 2.010050251$

G1 X\$ $xval$  Y\$ $yval$  Z\$ $zval$  ;cut along x direction enter y go BACK

$\$xval = \$xval + \$l / 1.997004493$  ; full way

G1 X\$ $xval$  Y\$ $yval$  Z\$ $zval$  ;shift to new x position

$\$yval = \$yval - \$width$

G1 X\$ $xval$  Y\$ $yval$  Z\$ $zval$  ;cut along x direction enter Y ACROSS

$\$xval = \$xval - \$l / 2.003004507$  ;calculate new x position  
HALF WAY DOWN

G1 X\$ $xval$  Y\$ $yval$  Z\$ $zval$  ;shift to new x position

$\$yval = \$yval + \$width / 2.010050251$

G1 X\$ $xval$  Y\$ $yval$  Z\$ $zval$  ;cut along x direction enter y WIDTH  
CONSTRICTION

$\$yval = \$yval - \$width / 2.010050251$

G1 X\$ $xval$  Y\$ $yval$  Z\$ $zval$  ;cut along x direction enter y OUT WIDTH  
CONSTRICTION

$\$xval = \$xval - \$l / 1.997004493$  ;calculate new x position FULL  
DOWN WAY DOWN

G1 X\$ $xval$  Y\$ $yval$  Z\$ $zval$  ;shift to new x position

ENDRPT

\$xval=\$xval-\$lI ;move to the top ;upper half

G1 X\$xval Y\$yval Z\$zval

\$yval=\$yval+9

G1 X\$xval Y\$yval Z\$zval ;move across 9mm

\$xval=\$xval+\$lI

G1 X\$xval Y\$yval Z\$zval ;go down

\$yval=-\$width/200

G1 X\$xval Y\$yval Z\$zval ;start going across

REPEAT \$nrepsconstriction

REPEAT \$nrepsablation

\$xval=\$xval-\$lI ;calculate new x position 2

G1 X\$xval Y\$yval Z\$zval ;shift to new x position

\$yval=\$yval-\$width/200

G1 X\$xval Y\$yval Z\$zval ;cut along x direction

$\$xval = \$xval + \$ll$  ;calculate new x position 3

G1 X $\$xval$  Y $\$yval$  Z $\$zval$  ;shift to new x position

$\$yval = \$yval - \$width / 200$

G1 X $\$xval$  Y $\$yval$  Z $\$zval$  ;cut along x direction

$\$xval = \$xval - \$ll$  ;calculate new x position 4

G1 X $\$xval$  Y $\$yval$  Z $\$zval$  ;shift to new x position

$\$yval = \$yval - \$width / 200$

G1 X $\$xval$  Y $\$yval$  Z $\$zval$  ;cut along x direction

$\$xval = \$xval + \$ll$  ;calculate new x position 5

G1 X $\$xval$  Y $\$yval$  Z $\$zval$  ;shift to new x position

$\$yval = \$yval - \$width / 200$

G1 X $\$xval$  Y $\$yval$  Z $\$zval$  ;cut along x direction

$\$xval = \$xval - \$ll$  ;calculate new x position 6

G1 X $\$xval$  Y $\$yval$  Z $\$zval$  ;shift to new x position

$\$yval = \$yval - \$width / 200$

G1 X $\$xval$  Y $\$yval$  Z $\$zval$  ;cut along x direction

$\$xval = \$xval + \$ll$  ;calculate new x position 7

G1 X $\$xval$  Y $\$yval$  Z $\$zval$  ;shift to new x position

$\$yval = \$yval - \$width / 200$

G1 X\$ $xval$  Y\$ $yval$  Z\$ $zval$  ;cut along x direction

$\$xval = \$xval - \$ll$  ;calculate new x position

8

G1 X\$ $xval$  Y\$ $yval$  Z\$ $zval$  ;shift to new x position

$\$yval = \$yval - \$width / 200$

G1 X\$ $xval$  Y\$ $yval$  Z\$ $zval$  ;cut along x direction

$\$xval = \$xval + \$ll$  ;calculate new x position

9

G1 X\$ $xval$  Y\$ $yval$  Z\$ $zval$  ;shift to new x position

$\$yval = \$yval - \$width / 200$

G1 X\$ $xval$  Y\$ $yval$  Z\$ $zval$  ;cut along x direction

$\$xval = \$xval - \$ll$  ;calculate new x position

10

G1 X\$ $xval$  Y\$ $yval$  Z\$ $zval$  ;shift to new x position

$\$yval = \$yval - \$width / 200$

G1 X\$ $xval$  Y\$ $yval$  Z\$ $zval$  ;cut along x direction

$\$xval = \$xval + \$ll$  ;calculate new x position

11

G1 X\$ $xval$  Y\$ $yval$  Z\$ $zval$  ;shift to new x position

$\$yval = \$yval - \$width / 200$

G1 X\$xval Y\$yval Z\$zval ;cut along x direction

ENDRPT

\$xval=\$xval-\$lI ; extra to remove block

G1 X\$xval Y\$yval Z\$zval

\$yval=\$yval-\$width/200

G1 X\$xval Y\$yval Z\$zval ;cut along x direction

\$xval=\$xval+\$lI ;extra TO REMOVE BLOCK

G1 X\$xval Y\$yval Z\$zval

\$xval=\$xval-\$lI/2.003004507 ;calculate new x position half way

G1 X\$xval Y\$yval Z\$zval ;shift to new x position

\$yval=\$yval-\$width/2.010050251

G1 X\$xval Y\$yval Z\$zval ;cut along x direction enter y width constriction 20um

\$yval=\$yval+\$width/2.010050251

G1 X\$xval Y\$yval Z\$zval ;cut along x direction enter y go BACK

\$xval=\$xval-\$lI/1.997004493 ;calculate new x position half way point

G1 X\$xval Y\$yval Z\$zval ;shift to new x position

$\$yval = \$yval - \$width$

G1 X\$ $xval$  Y\$ $yval$  Z\$ $zval$  ;cut along x direction enter Y ACROSS

$\$xval = \$xval + \$l / 2.003004507$  ;calculate new x position  
HALF WAY DOWN

G1 X\$ $xval$  Y\$ $yval$  Z\$ $zval$  ;shift to new x position

$\$yval = \$yval + \$width / 2.010050251$

G1 X\$ $xval$  Y\$ $yval$  Z\$ $zval$  ;cut along x direction enter y WIDTH  
CONSTRICTION

$\$yval = \$yval - \$width / 2.010050251$

G1 X\$ $xval$  Y\$ $yval$  Z\$ $zval$  ;cut along x direction enter y OUT WIDTH  
CONSTRICTION

$\$xval = \$xval + \$l / 1.997004493$  ;calculate new x position FULL  
DWN WAY DOWN

G1 X\$ $xval$  Y\$ $yval$  Z\$ $zval$  ;shift to new x position

ENDRPT

**THIS IS THE END OF THE PHD WORK!!!**